Decentralised Control and Stability Analysis of a Multi-Generator Based Electrical Power System for More Electric Aircraft

Fei Gao (BSc, MSc)

Submitted to the University of Nottingham
for the degree of Doctor of Philosophy

August 2016

Abstract

The more electric aircraft initative results in significant challenges in the design of aircraft electrical power systems. Different power system architectures are currently being studied by the engineering community. In this thesis, a promising single DC bus-based, multiple-source multiple-load power system is investigated in terms of power management and stability.

Due to its inherent modularity and ease of implementation, droop control, as a decentralised control method, has been widely used to cope with power sharing among parallel sources in the studied architecture. The thesis proposes a comparative study of different droop control approaches by focusing on steady-state power sharing performance and stability.

- Different droop control methods may lead to different stability margins. Until now, the effect of different droop control schemes on system stability has not been fully investigated. The thesis presents the control scheme for current-mode and voltage-mode systems, derives the corresponding output impedance of the source subsystem and analyses the stability of the power system. Based on the developed mathematical model, comprehensive modal analysis of the power system is performed.
- A generalised analytical impedance analysis is extended to a multi-source multi-load power system. To facilitate the analysis, the thesis proposes the concept of “global droop gain” as an important factor to determine the V-I bus characteristic and the stability behaviour of a parallel sources based DC system.
- Considering the tradeoff between voltage regulation and power sharing accuracy in droop control, this thesis proposes an improved voltage regulation method in multi-source based DC electrical power system. Due to the absence of additional controllers or communication lines, the proposed approach can be relatively easily implemented in a small scale DC electrical power system. The proposed approach effectively improves the load sharing

accuracy under high droop gain circumstances with consideration of cable impedance. Optimal droop gain settings are investigated and the selection of individual droop gains has been described in order to reduce the distribution losses.

Finally, the above-mentioned analytical results are confirmed by time-domain simulations and experimental results.

Acknowledgement

I would like to express my deepest gratitude to my supervisors Dr. Serhiy Bozhko, Prof. Greg Asher, Prof. Pat Wheeler, and Dr. Alessandro Costabeber for their support and expert guidance during the journey. Also, thanks to Prof. Chris Gerada for reviewing my annual reports and giving me valuable suggestions on my topic.

Moreover, special thanks are given to Dr. Patrick Norman and Dr. Michael Galea for sparing their time to be my examiners. I would like to thank Dr. Xiancheng Zheng from Northwestern Polytechinical University, China for his general guidance and help as well.

I also would like to express my sincere gratitude to the University of Nottingham for funding my PhD study through the Dean of Engineering Research Scholarship.

In addition, many thanks for a lot of help and support from the knowledgeable research fellows and PhD students in the PEMC group, Dr. Seang Yeoh, Dr. Chintan Patel, Dr. Tao Yang, Dr. Christopher Hill, Dr. Ponggorn Kulsangcharoen, Dr. Mohamed Rashed, Dr. Shuai Shao, Dr. Bilal Arif, Dr. Adane Solomn, Dr. Chao Ji, Dr. Xiang Wang and all other friends I have met here during my PhD study.

At last but not least, I would like to express my heartfelt appreciation to my parents for their understanding and support throughout my life. Also, I would like to thank my wife for her love and encouragement on the way.

List of Publications

The contents presented in this thesis have been published or accepted in the following peer-reviewed journal articles and conference proceedings:

Journal Articles

[J1] **F. Gao**, S. Bozhko, A. Costabeber, C. Patel, P. Wheeler, C. I. Hill, and G. Asher, "Comparative stability analysis of droop control approaches in voltage source converters-based DC microgrids," *IEEE Trans. Power Electron*., vol. 99, no. 99, pp. 1-1, 2016.

[J2] **F. Gao** and S. Bozhko, "Modeling and impedance analysis of a single DC bus based multiple-source multiple-load electrical power system," *IEEE Trans. Transp. Electrif.*, vol. 2, no. 3, pp. 335–346, Sep. 2016.

[J3] **F. Gao**, S. Bozhko, G. Asher, P. Wheeler, and C. Patel, "An improved voltage compensation approach in a droop-controlled DC power system for the more electric aircraft," *IEEE Trans. Power Electron.*, vol. 31, no. 10, pp. 7369–7383, Oct. 2016.

[J4] **F. Gao**, X. Zheng, S. Bozhko, C. I. Hill, and G. Asher, "Modal analysis of a PMSG-based DC electrical power system using eigenvalues sensitivity in the more electric aircraft," *IEEE Trans. Transp. Electrif.*, vol. 1, no. 1, pp. 65–76, Jun. 2015.

Conference Papers

[C1] **F. Gao**, S. Bozhko, and P. Wheeler, "An enhanced secondary control for voltage restoration in MEA electrical power systems," *SAE Technical Paper* 2016-01-1985, Sep. 2016.

[C2] **F. Gao,** X. Zheng, and S. Bozhko, "Stability assessment of a droop-controlled multi-generator system in the more electric aircraft using parameter space approach," in *Proc. ECCE 2016, IEEE Energy Conversion Congress & Expo*, Milwaukee, USA, Sep. 2016, pp. 1-8.

[C3] **F. Gao**, S. Yeoh, T. Yang, and S. Bozhko, "Stability assessment of a high speed permanent magnet machine based aircraft electrical power system," in *Proc. EPE'16-ECCE Europe, 18th European Conference 2016*, Karlsruhe, Germany, Sep. 2016, pp. 1–10.

[C4] **F. Gao**, S. Bozhko, G. Asher, and P. Wheeler, "Comparative stability study of DC current control strategies for a droop-controlled PMSG system," in *ECCE 2015, IEEE Energy Conversion Congress & Expo*, Montreal, Canada, Sep. 2015, pp. 6246–6253.

[C5] **F. Gao**, S. Yeoh, S. Bozhko, and G. Asher, "Coordinated control of a DC electrical power system in the more electric aircraft integrated with energy storage," in *ECCE 2015, IEEE Energy Conversion Congress & Expo*, Montreal, Canada, Sep. 2015, pp. 5431–5438.

[C6] **F. Gao**, S. Bozhko, G. Asher, and P. Wheeler, “Comparative study of power sharing strategies for the DC electrical power system in the MEA,” *SAE Technical Paper* 2015-01-2410, Sep. 2015.

[C7] **F. Gao**, X. Zheng, S. Bozhko, and C. I. Hill, “Permanent-magnet machine based DC electrical power system: modal analysis and eigenvalues sensitivity,” in *ISIE 2015, International Symposium on Industrial Society*, Brazil, Jun. 2015, pp. 1–8.

[C8] **F. Gao**, S. Bozhko, G. Asher, and P. Wheeler, “An improved voltage compensation method for droop-controlled system in DC microgrids,” in *Proc. IECON 2014, 40th Annual Conference of the IEEE*, USA, Nov. 2014, pp.1240–1246.

[C9] **F. Gao**, Y. Gu, S. Bozhko, G. Asher, and P. Wheeler, “Analysis of droop control methods in DC microgrids,” in *Proc. EPE'14-ECCE Europe, 16th European Conference*, Finland, Aug. 2014, pp. 1–9.

[C10] **F. Gao**, S. Bozhko, G. Asher, and P. Wheeler, “Stability of multi-source droop-controlled electrical power system for more-electric aircraft,” in *Proc. Intelligent Energy and Power Systems (IEPS), 2014 IEEE Conference on*, Ukraine, Jun. 2014, pp.122–126.

[C11] **F. Gao**, S. Bozhko, and G. Asher, “Drooping strategies for paralleling sources and their effect on electric power system stability,” *SAE Technical Paper 2014-01-2113*, Sep. 2014.

[C12] **F. Gao**, S. Bozhko, S. Yeoh, and G. Asher, “Control design for PMM starter-generator operated in flux-weakening mode,” in *Proc. Power Engineering Conference (UPEC), 2013 48th International Universities'*, Ireland, Sep. 2013, pp. 1–6.

[C13] S. Bozhko, S. Yeoh, **F. Gao**, and C. Hill, “Aircraft starter-generator system based on permanent-magnet machine fed by an active front-end rectifier,” in *Proc. IECON 2014, 40th Annual Conference of the IEEE*, USA, Nov. 2014, pp. 2958–2964.

[C14] S. Bozhko, S. Yeoh, **F. Gao**, T. Yang, and C. Hill, “Control design for electric starter-generator based on a high- speed permanent-magnet machine fed by an active front-end rectifier,” *SAE Technical Paper* 2014-01-2139, 2014.

[C15] X. Zheng, **F. Gao**, and S. Bozhko, “Stability study of a DC electric power system with paralleled generators for more-electric aircraft,” *SAE Technical Paper* 2014-01-2114, 2014.

[C16] S. Yeoh, **F. Gao**, S. Bozhko, and G. Asher, “Control design for PMM-based starter generator system for more electric aircraft,” in *Proc. EPE'14-ECCE Europe, 16th European Conference*, Finland, Aug. 2014, pp. 1–10.

Technical Reports

[R1] S. Bozhko and **F. Gao**, “Report on the possible, viable and optimized solutions for MEA electrical power systems for radical architecture designs and operation,” Cleansky II Program SGO ITD Systems for Green Operations D.2.4.2, 2015.

Table of Content

List of Figures

List of Tables

List of Acronyms

AC	Alternative Current
AEA	All Electric Aircraft
AEGART	Aircraft Electrical Generation Active Rectifier Technology
AFE	Active Front End
APU	Auxillary Power Unit
AR	Active Rectifier
ATRU	Automatic Transformer Rectifier Unit
CCL	Constant Current Load
CF	Constant Frequency
CIL	Constant Impedance Load
CPL	Constant Power Load
DC	Directive Current
DCL	Digital Communication Link
DFIG	Doubly-fed Induction Generator
DG	Distributed Generation
DSP	Digital Signal Processor
ECS	Environmental Control System
EHA	Electro-hydrostatic Actuators
EM	Electrical Machine
EMF	Electromotive Force
EMI	Electromagnetic Interference
EPS	Electrical Power System

ESAC	Energy Source Analysis Criterion
ESS	Energy Storage System
FPGA	Field Programmable Gate Array
FW	Flux Weakening
GaN	Gallium Nitride
GMPM	Gain Margin and Phase Margin
GVF	Global Voltage Feedback
GNC	Generalised Nyquist Criterion
HP	High Pressure
IGBT	Insulated Gate Bipolar Transistor
IM	Induction Machine
IPM	Interior Permanent Magnet
LP	Low Pressure
LVF	Local Voltage Feedback
LHP	Left Half Plane
MEA	More Electric Aircraft
MG	Microgrid
MLG	Minor Loop Gain
MTDC	Multi-terminal DC
PCC	Point of Common Coupling
PLL	Phase-Locked Loops
PMSG	Permanent Magnet Synchrounous Generator
PoC	Point of Connection
PV	Photovoltaic

PWM	Pulse Width Modulation
RAT	Ram Air Turbine
RESC	Root Exponential Stability Criterion
RF	Radio Frequency
RHP	Right Half Plane
S/G	Starter/Generator
SiC	Silicon Carbide
SRM	Switched Reluctance Machine
SMPMM	Surface-Mounted Permanent Magnet Machine
TRU	Transformer Rectifier Unit
VF	Variable Frequency
VSC	Voltage Source Converter
VSCF	Variable Speed Constant Frequency
VSI	Voltage Source Inverter
VSVF	Variable Speed Variable Frequency
WBG	Wide Band Gap
WIPS	Wings Ice Protection System

List of Symbols

C_{dc}	Equivalent DC side capacitor
e_d	*d*-axis point of common coupling voltage
e_q	*q*-axis point of common coupling voltage
f_{osi}	oscillation frequency of the i^{th} eigenvalue
G_{cc}	First-order lag to mimic the inner current loop
G_{Dy_CM}	DC current control dynamics
G_{Dy_VM}	DC voltage control dynamics
G_{Idc}	Transfer function of the DC current controller in current-mode
G_{P_C}	Plant of the DC current controller in current-mode
G_{P_V}	Plant of the DC voltage controller in voltage-mode
G_{Vdc}	Transfer function of the DC voltage controller in voltage-mode
I_{ac}	AC side current of converter
I_c	maximum continuous collector current
I_{CPL}	Current source of a linearised CPL
I_{CPLt}	Total equivalent current source of the parallel CPLs
i_d	*d*-axis component of stator current
i_{dc}	DC current before the capacitor
I_{dc}^{*}	DC current reference
I_{dc}^{ref}	DC current reference
I_i	i^{th} DC terminal current
I_i^{*}	i^{th} DC terminal current reference

i_{Lc}	DC line current
I_{Lt}	total DC link current
i_o	load current after the capacitor
i_o^*	DC current reference
i_q	*q*-axis component of stator current
I_{sc}	Short circuit current
k	Droop gain
k_1	Droop gain for source #1
k_2	Droop gain for source #2
k_3	Droop gain for source #3
$\mathrm{K_c}$	Coeffcient of the Clarke's transformation matrix
k_i	Droop gain for the i^{th} source
k_{idc}	Integral gain of the the DC current controller in current-mode
K_{idi}	Integral gain of the *d*-axis current controller
K_{idp}	Proportional gain of the *d*-axis current controller
K_{ioi}	Integral gain of the DC current controller
K_{iop}	Proportional gain of the DC current controller
K_{iqi}	Integral gain of the *q*-axis current controller
K_{iqp}	Proportional gain of the *q*-axis current controller
k_{iVdc}	Integral gain of the the DC voltage controller in voltage-mode
k_{pdc}	Proportional gain of the the DC current controller in current-mode
k_{pVdc}	Proportional gain of the DC voltage controller in voltage-mode
k_t	Global droop gain
$k_{\mathrm{t\_optimal}}$	Optimal droop gain

K_{vci}	Integral gain of the flux weakening controller
K_{vcp}	Proportional gain of the flux weakening controller
L_d	*d*-axis inductance
L_{DC}	Inductor of the buck converter
L_q	*q*-axis inductance
L_s	Synchronous inductance
m_d	*d*-axis modulation indices
m_q	*q*-axis modulation indices
N	Number of sources
n_i	load sharing percentage among all parallel sources
P	Active power
P_{c_loss}	Converter loss
$P_{c\_loss\_parallel}$	Generalised converters loss of N parallel converters
P_{cpl}	total power of the CPL
P_{CPLi}	power of i^{th} CPL
p_{ki}	Participation factor of the k^{th} variable in the i^{th} mode
$P_{loss\_parallel}$	Total loss of N parallel converters
$P_{Lossmin}$	Minimum distribution loss
P_{res}	total power of the resistive load
Q	Reactive power
r	Raio between the power of CPL and CIL
R_{CPL}	Impedance of a linearised CPL
R_{CPLt}	Total equivalent impedance of the parallel CPLs
R_{dc}	equivalent DC line resistance connecting from each converter to the

	bus bar
R_{DC}	Resistance of the buck converter
R_i	Cable resistance between the i^{th} source to the main bus
R_S	stator resistance
R_{source}	Equivalent source resistance
$T_{\alpha\beta 0}$	transformation matrix from natural reference frame to stationary frame
v_b	Main dc bus voltage
V_c	AC voltage
V_{CES}	maximum collector-emitter voltage
v_d,	*d*-axis component of stator voltage
v_{dci}	Local dc terminal voltage
v_i	right eigenvector corresponding to eigenvalue λ_i
V_i	i^{th} DC terminal voltage
V_i^*	i^{th} DC terminal voltage reference
v_{ik}	k^{th} element in the right eigenvector corresponding to the i^{th} eigenvalue
V_o	Nominal bus voltage
V_{oc}	Open circuit voltage
v_q	*q*-axis component of stator voltage
w_i	left eigenvector corresponding to eigenvalue λ_i
w_{ki}	k^{th} element in the left eigenvector corresponding to the i^{th} eigenvalue
x_{abc}	quantity in the natural reference frame
X_{id}	State variable of the *d*-axis current controller
X_{ioi}	State variable of the DC current controller
X_{iq}	State variable of the *q*-axis current controller

X_{vci}	State variable of the flux weakening controller
$x_{\alpha\beta0}$	quantity in the stationary reference frame
$Z_{s\_P\_GVF}$	Equivalent source impedance for the parallel soruces using GVF
$Z_{s\_P\_LVF}$	Equivalent source impedance for the parallel soruces using LVF
$Z_{s\_P\_VF}$	Equivalent source impedance for the parallel soruces using voltage-mode
λ_i	i^{th} eigenvalue
ξ_i	Damping ratio of the i^{th} eigenvalue
φ_m	flux linkage of permanent magnet
ω_e	electrical rotor angular velocity
ω_{Idc}	Bandwidth of the DC current control loop
ω_{Vdc}	Bandwidth of the DC voltage voltage loop

Chapter 1 Introduction

1.1 Background

Over past years, aircraft has been widely accepted as a convenient way to travel as they permit long distance, high speed travel and become a more fuel efficient mode of transportation in some circumstances. The aerospace industry is growing at a phenomenal rate. By 2030, it is estimated that there will be around 27,000 new aircrafts in the sky. It is an industry that is essential to today's global community, bringing cultures together and enabling strong annual economic growth worth $425bn in GDP worldwide.

However, aircrafts have environmental and climate impacts beyond fuel efficiency considerations. They are also relatively noisy compared to other forms of travel. In the competitive world of airline economics, where low-cost carriers are driving down profit margins on airline seat-miles, techniques for reducing the environmental impact and direct operating costs of aircrafts are in great demand. Tomorrow's aerospace industry will need to deliver more flights, operate more efficiently and be ever more respectful of the environment in which it evolves, whilst also remaining competitive. Indeed, a significant threat for the aerospace industry is that if future emissions are not improved, severe sanctions could be placed on the industry, pushing airline ticket prices up and reducing the competitiveness of air travel versus other transport tools such as rail, etc. Higher energy efficiency, lower CO_2 and NOx emissions, and low audible noise for aircrafts have become critical issues that need to be addressed due to threats on quality of life and even survivability of our future generations.

Based on this background, the aerospace engineering industry is placing greater emphasis on the use of technology to achieve more efficient and greener solutions. Due to the rapid development of electrical and electronic engineering, the move towards more electric aircraft (MEA) or all electric aircraft (AEA) is the tendency nowadays. The MEA and AEA concepts can potentially lead to significant reduction of the dependency on fossil fuels and pollutant emissions, as the electrification technologies expedite a paradigm shift towards a more sustainable air travel.

1.1.1 Conventional Aircraft

For the sake of comparison between conventional aircraft and MEA, it is of interest to introduce the conventional aircraft system first. Traditionally, there were two energy sources (primary source + secondary source) on conventional aircrafts. The primary source is the engines on the aircraft. The secondary source includes electric, hydraulic, pneumatic, and mechanical systems powered by the primary source. Figure 1.1 shows the conventional aircraft power source distributions which consist of pneumatic, hydraulic, mechanical, and electrical sources.

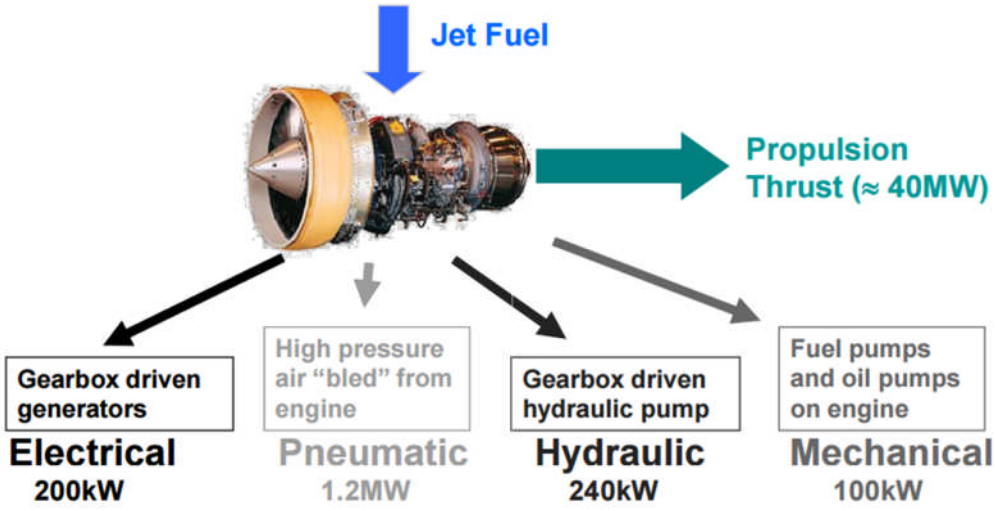

Figure 1.1. Power sources distribution in conventional aircraft [1].

Pneumatic power is used to power the ECS (Environmental Control System) and supply hot air for WIPS (Wings Ice Protection System) [2]. WIPS has two working modes: Anti-Icing and De-Icing. The Anti-Icing mode is preemptive and is turned on before the flight enters icing conditions, while the de-icing mode is reactive and used

after there has been significant ice built up. The main drawbacks of the pneumatic power are low efficiency and a difficulty in detecting leaks [3].

Hydraulic power is transferred from the central hydraulic pump to the actuation systems for primary and secondary flight control and to the landing gear for deployment, reaction, and braking. Hydraulic systems have a very high power density and are very robust. However, a heavy and inflexible infrastructure and the potential leakage of dangerous and corrosive liquids are the main drawbacks [3].

Mechanical power is transferred, by means of the gearboxes, from the engines to central hydraulic pumps, to local pumps for engine equipment and other mechanically driven subsystems, and to the main electrical generator [4]. The drawbacks of the mechanical system are the use of a heavy gearbox and its associated maintenance cost [4].

Electrical power in the aircraft is generated by the gearbox driven generators and distributed throughout the aircraft for avionics, cabin electronics, utility actuators, lighting and galleys. It can be seen from Figure 1.1 that the electrical power occupies a small amount/value among all power sources in the conventional aircrafts.

In contrast with the drawbacks of the pneumatic, hydraulic, and mechincal power, the electrical power system has many outstanding advantages such as high efficiency, low maintenance, good controllability and advanced diagnostics. Due to the abovementioned advantages, the use of more electrical power has become an inevitable trend. The concept of a “more electric aircraft” (MEA) is proposed which aims at increased penetration of electrical power in aircraft systems and becoming a major trend in modern aerospace engineering.

1.1.2 More Electric Aircraft

MEAs are advanced aircraft that make more use of electrical power to reduce the use of non-propulsive power such as mechanical, hydraulic, and pneumatic. As illustrated in Figure 1.2, the idea of the MEA is based on the fact that many devices, such as electric pumps, electric heaters, electrically driven air compressors etc, can be driven by electricity. Thus, the mechanical system and the pneumatic system in

conventional aircraft can be replaced by electrical power systems. Additionally, if the conventional hydraulic actuators were modified to become electro-hydraulic actuators (EHA), implying the use of electrical power as the prime power to drive the hydraulics, even the hydraulic system can be in more electric mode. In future, the hydraulics might be completely removed by employing electro-mechanical actuators (EMA).

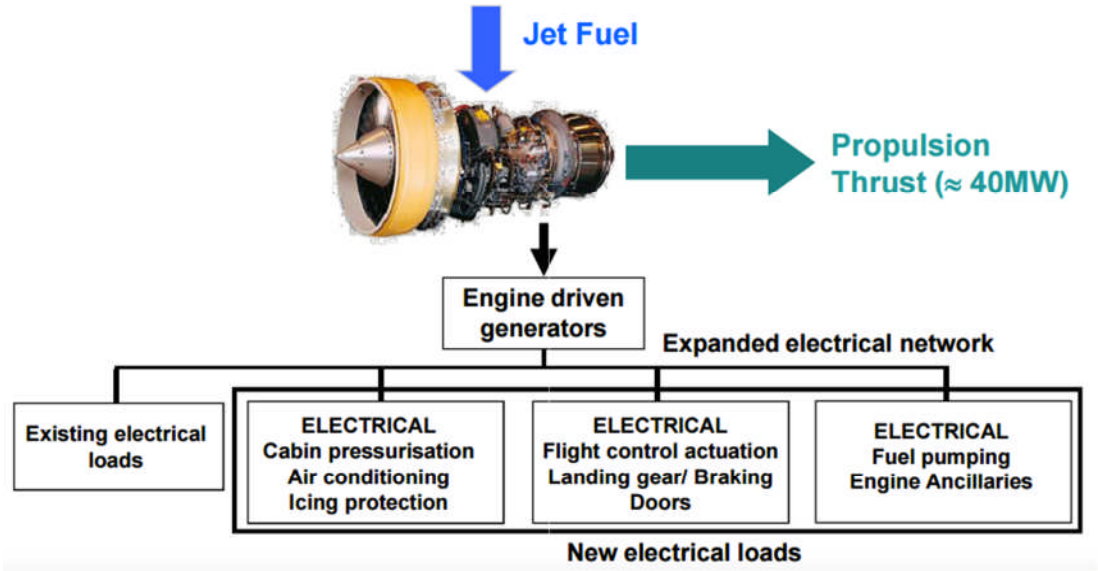

Figure 1.2. Power sources distribution of MEA [1].

The benefits of MEA compared to conventional aircraft can be summarised as follows [5]:

(1) Removal of hydraulic and pneumatic systems which are costly, not easily maintained and susceptible to leakage. This measure reduces the weight, cost and complexity of the system and improves the reliability and efficiency.

(2) Use of an electrical starter/generator (S/G) for the starting process of the aero-engine. If the S/G is embedded in the engine, this eliminates the engine tower shaft and gears, power take-off shaft, accessory gearboxes and reduces the engine starting power especially in cold conditions and aircraft front area.

(3) A fan shaft generator is used for emergency power generation instead of a ram air turbine (RAT) which is inefficient. This also increases system reliability and robustness against the engine contingency.

As can be concluded here, adopting MEA will revolutionise the aerospace industry. By means of significant improvements in terms of weight, cost, and fuel consumption, better maintainability and system reliability will be achieved.

However, MEA poses some challenges for the aircraft electrical system, in the significantly increased amount of power and in the management of this power. Table 1-1 lists the on-board electrical power evolution trend for civil aircraft. It can be seen that the generation power rating of aircrafts has increased over the years. The onboard power capability is over 800 kVA for Airbus A380 while it reached 1400 kVA for Boeing B787.

Table 1-1 Power generation capability in the existing aircrafts [6]

Aircraft	Electric Power Generation Capability
B717	2*40 kVA
B737NG	2*90 kVA
B767-400	2*120 kVA
B777	2*120 kVA and 2*20 kVA backup
A340	4*90 kVA
B747-X	4*120 kVA
A380	4*150 kVA and 2*120 kVA APU
B787	4*250 kVA and 2*225 kVA APU

1.2 Challenges of Moving Towards MEA

MEA applications demand high reliability and high power density while aiming to reduce weight, costs, fuel consumption, and environmental impact [3], [7].

One of the major challenges is the weight. Studies have shown that MEA can considerably reduce fuel burned, but MEA is generally heavier with the technologies that we have today. This is partially due to the heavy power electronics box, where

the staggering weight of the EMI filters comprises about 25%-40%. Nowadays, the rapid improvement of power electronics and the associated cooling and controls will bring down the size, weight of the electrical components.

Another challenge with MEA is that the design of the electrical systems and electrical components needs to be done simulatenously with the aircraft design. Since additional electrically-powered components increase the system's complexity, new designs for electric power systems need to behave according to certain properties or requirements determined by physical constraints or performance criteria.

From the electrical power system point of view, new power electronics, cooling, controls, and system level design pose a challenge to the safety, robustness, stability, reliability of MEAs. This puts tremendous technical, cost, resources, and schedule risks to the development of MEA. This means that challenges exist in all fields of electrical engineering covering power electronics (power devices, converters), electric machines (machine design and electric drive), and power systems (power system architectures and power management).

1.2.1 Power Electronics

Recent developments on wide bandgap (WBG) semiconductors, such as Silicon carbide (SiC) or Gallium nitride (GaN), will allow high-temperature (~250°C) operation with subsequent cooling device optimisation and power integration due to the characteristics of their high temperature, low losses, and high switching capabilities [8]. SiC is particularly attractive in terms of thermal conduction and technological maturity, while GaN would be the future low-cost device. Some studies show that GaN based power devices can offer performance that is comparable to SiC but at much lower cost [9]. Switching and conduction losses are also reduced with respect to classical silicon devices. Thus, the innovation of WBG power devices will be helpful for reducing losses, weight, and volume.

The challenges are to still run these converters and keep the high performance of power converters, including drivers and sensors, in higher temperatures and in a reliable fashion. In recent years, significant research has been carried out to make

power converters more reliable. This includes not only the reliability of power switches and drivers, but also fault-tolerant converters, real-time fault detection, and dynamic reconfiguration of power electronic converters. All of these techniques will inevitably affect the development of the next-generation power converters in the MEA.

1.2.2 Electrical Machines

Electrical machines (EMs) are one of the most important components in the MEA EPS. There is growing acceptance that conventional drive systems cannot meet the reliability requirement and hence a level of redundancy is essential. However, the number of fault tolerant drive systems which have been implemented is still small and no fault tolerant drives have actually been used in a production aircraft.

Due to the high switching capability of WBG devices, higher speed machines or a higher number of pole machines are feasible.

High speed, high power density, high torque density machines are the trends of electrical machines applicable to the MEA. Emerging high-speed machines provide new opportunities to improve the power density of the total drive system. In order to achieve minimum drive-system weight (high power density), the following measures can be considered:

- New electrical machine topologies
- Machine design by utilizing advanced materials
- Advanced control and manufacturing
- Thermal management.

Similarly, in terms of the machine design, the ways of improving the torque density can be listed as follows:

- Outer rotor configuration
- High pole number
- Unequal wound and unwound tooth widths
- Halback magnet arrangement

- High grade soft magnetic material
- Open slot design.

In alignment with the trend of increased operating voltages and reduced system losses, a new set of power quality and electromagnetic interference (EMI) requirements has been created to satisfy both quality and performance issues [11]. The significant increase in the number of installed EMs poses challenges on using this equipment on the new platforms. Therefore, it is necessary to increase the power density of the new-generation machines and improve the overall system performance. Cost is an additional driver that must be addressed as the new platforms must be affordable.

1.2.3 Power Systems

The MEA poses more demand on the aircraft electrical power system in fields of power generation and reliability, fault tolerance, power management and stability of the DC and AC power systems [7]. These entail innovations in power generation, distribution, processing, and management systems. Meanwhile, this trend increases the challenges for aircraft electrical power system (EPS) design [3]. Many architecture paradigms are currently a focus of engineering studies [12]. With the increasing number of power electronic loads, a MEA with a classical AC network includes a high number of AC–DC rectifier stages (Automatic Transformer Rectifier Unit, ATRU), which would have to comply with the AC quality standard (ABD100 for Airbus) [13]. A system solution for mass reduction would be to prefer a high-voltage DC (HVDC) network with an optimised association consisting of a generator, a rectifier unit (RU), a filter and a generator control unit. Several studies have been carried out, especially in the framework of the more open electrical technologies (MOET) EU project [14], emphasising the interest in such architecture. The HVDC network would facilitate generator–load coupling with possible regenerative load acceptance [15]-[17]. The evolution of power generation, distribution and the utilisation system will be overviewed in details in Chapter 2.

It has been shown that the HVDC distribution systems are applied in a large variety of applications, consequently, different architectures have been proposed such as

single bus, multi-bus, ring bus configuration. Due to its simplicity, as shown in Figure 1.3, such a “single bus” EPS architecture is one of the promising candidates for future MEA. Twin engine-driven generators provide the electrical power to the single DC bus through Active Rectifiers (ARs).

In order to achieve the following are required in such architecture:

- ways of ensuring an appropriate power sharing among the sources
- good dynamic performance
- high power quality
- stability in the presence of non-linear loads.

Relevant technologies that will need to be developed are listed below:

- Power electronic converters including WBG, new topologies to achieve efficient power conversion and advanced control technologies
- New types of machine including increased fault tolerance capability

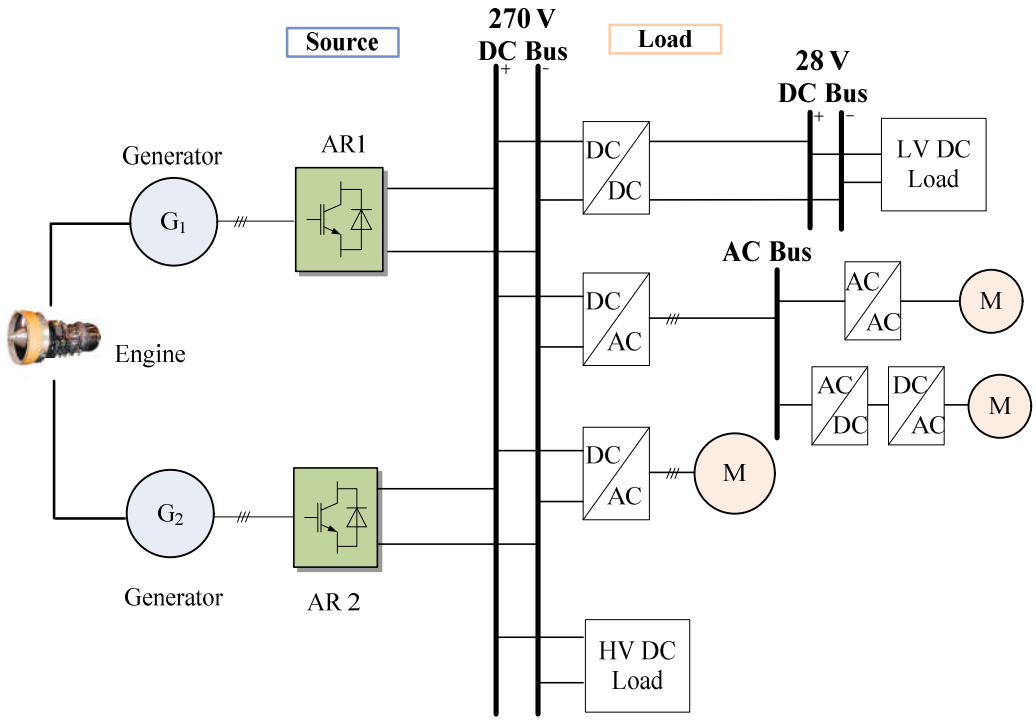

Figure 1.3. Single bus power system architecture.

1.3 Challenges of the Single Bus Power System Architecture

One of the expected benefits of using parallel energy sources is improvements in power system redundancy [18], [19]. In such defined “single bus” HVDC EPS candidates, the following issues are of main concern to the power system designer:

- DC bus voltage maintenance
- Load sharing among parallel sources
- System stability
- Power quality

1.3.1 Voltage Control

For the single-source based system, there is just the one source which regulates the bus voltage. In the presence of multiple sources and multiple converters working in parallel, at least one converter is responsible for regulating the DC bus voltage and all others could be operated in active power control mode. It is desirable that following an outage of one or more converters, the remaining ones should share the resulting power deficit in a certain appropriate proportion. Thus it would be good for all converters to operate in the DC link voltage control mode (or as slack converters [20]) rather than strictly trying to follow their respective active power references. However, set values of DC link voltage references at all converters could be conflicting unless they are modified properly depending on the reference and actual values of the active power and DC link voltage.

Therefore, most of the parallel sources need to participate in the control of the bus voltages, which implies the need for cooperative voltage control amongst all sources.

1.3.2 Load Sharing

An aircraft power system consists of an aircraft engine with a plurality of engine spools, a plurality of AC generators driven by at least one engine spool. In a specific

condition, as shown in Figure 1.4, one aero-engine connects twin generators through the low pressure (LP) shaft and the high pressure (HP) shaft.

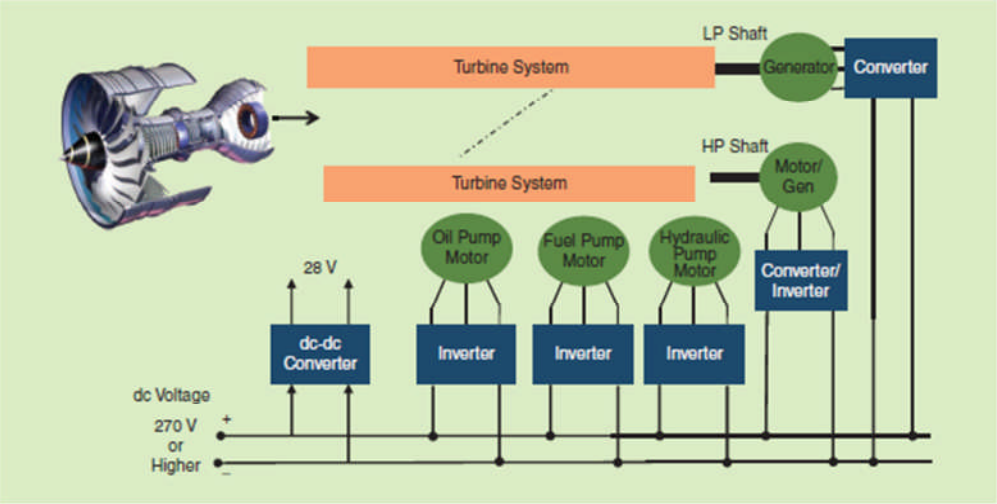

Figure 1.4. A MEA EPS with twin generators mounted on HP and LP shaft [6].

Traditionally, the electrical power is extracted from a high-pressure (HP) engine spool in a gas turbine engine. The high and relatively constant operating speed of the HP engine spool, compared to that of the low-pressure (LP) engine spool, makes it an ideal source of mechanical power to drive electrical generators connected to the engine [21], which can be made to be smaller and more compact due to the high speed. However, this added load placed on the HP engine core, can have a detrimental effect on engine performance under certain conditions. Combining with increasing demand for on-board electrical power generation, this could lead to the need to draw more power from any available source, including the LP shaft which can provide this alternate source of power [21]. Considering the abovementioned factors, it would be beneficial to provide a system and method for selectively controlling the extraction of electrical power from either the HP or LP engine spools, as desired, to optimize benefits in engine performance.

Parallel sources are expected to share the load power demand according to the rated power ratio. In such a multi-source multi-load power system, appropriate load sharing is of importance according to the source capacity. The details about the load sharing methods will be discussed in Chapter 2.

1.3.3 Stability Issue

In electrical power systems, there are three load categories: constant impedance loads, constant current loads, and constant power loads (CPLs). Typical constant impedance loads include resistive load, resistor-inductor load and other load types whose impedance is invariant to the operating condition. Constant current loads draw the constant current from the source where the voltage of the load could change. Tightly controlled power electronic converters and motor drives often behave like CPLs which show the constant power characteristic [22].

CPLs have negative incremental impedance characteristics [23] (will be discussed in Chapter 2 in detail), which can lead to an undesirable destabilising effect, oscillations, and eventual instability. This destabilising effect is not only a great threat to system stability, but also an obstruction to system optimisation, such as reducing size and saving weight. Thus, instability induced by CPLs is a great concern for the MEA EPS.

1.4 Aims and Objectives

1.4.1 Aims

Following an overview of potential opportunities and challenges of the “single bus” EPS architecture for potential applications in future MEA, this work aims to develop new knowledge regarding a proper power management and power distribution between the multiple sources, to analyse and establish EPS stability conditions, and to investigate solutions for guaranteeing DC bus voltage control.

1.4.2 Objectives

The aim of this research can be achieved through the following objectives:

1. To develop principles and methods of load sharing among the multiple parallel sources in the “single-bus” electrical power system. In the multi-source multi-load system, appropriate power sharing among the sources is of

importance since it will affect the stable and efficient operation of the whole system. Considering that the power sharing accuracy is sometimes influenced by the cable parameters, after reviewing different power sharing methods, an effective control strategy that can provide good sharing performance against the cable resistance variation should be clarified.

2. To investigate a stability condition of different droop control approaches. Different droop control approaches may yield different stability properties. It is worth investigating the impact of key parameters on stability under different droop control approaches. Based on the developed model of the studied "single-bus" electrical power system, the stability can be assessed using the state-space model approach and frequency domain approach.
3. To propose voltage compensation approaches to improve the voltage regulation of the DC bus. Since there is a trade-off between power sharing ratio and voltage regulation, secondary control approaches which provide voltage support to the EPS can be used. Conventional secondary control methods are based on the communication link and/or additional controllers, it is of interest to propose approaches to eliminate the voltage deviation in the absence of additional controllers and communications.

Although the context of the work is based on an aircraft's on-board power system, it can be also considered to be a challenging case of DC microgrids (MGs) in islanding mode and marine power systems. Thus, the analysis presented afterwards can be applied to design and control of other terrestrial DC MGs or shipboard DC power systems as well.

1.5 Contributions

The main contributions of this work can be summarised as follows:

- Presentation of modal analysis of the power system using participation factor and eigenvalues sensitivity (Chapter 3). Based on the developed state-space model in small signal, critical modes are identified and the impacts of some key parameters on the stability are discussed by observing the movement of

the eigenvalues.

- Proposal of a comparative stability analysis of a multiple source multiple load DC power system under different droop control approaches. Among several droop control methods in DC EPS, an impedance based approach is developed to show the system stability against parameters variations (Chapter 4-5).
- Proposal for a concept of global droop gain to facilitate the analysis of the main bus V-I characteristic and analysis of the stability of parallel source operation (Chapter 6). Similar to the droop characteristic of each individual module at the DC terminal, the main bus of the multi-source system also has the droop characteristic for the DC bus voltage and total load current. The global droop gain is derived to show the main bus V-I characteristic and favours the stability analysis of the multi-source multi-load system.
- Proposal of a novel voltage compensation approach to eliminate the bus voltage deviation which is independent from the communication line and meanwhile improves the power sharing performance (Chapter 7). In addition, an optimal droop gain setting principle in order to minimise the distribution line losses is proposed (Chapter 7). Considering the existing tradeoff between voltage regulation and power sharing accuracy in the droop control, a secondary control approach can provide the voltage support to eliminate the voltage deviation under a large droop gain. Meanwhile, the power sharing accuracy is improved automatically since the droop gain is set to be much larger than the cable resistance.

1.6 Thesis Structure

The research report presented in this thesis is organised in the following chapters.

Chapter 2 reviews the electrical power systems of MEA, discusses the electrical starter/generator system and possible electrical machine candidates. The paralleling of generation channels feeding the same DC bus is introduced and possible load sharing methods are overviewed. In addition, stability analysis methods are reviewed to lay the basement for the following chapters.

Chapter 3 performs the modal analysis of the single generator based EPS in order to show the importance of the cable modeling in subsequent analysis. A detailed mathematical model of the multiple generators-based single bus EPS candidate is developed and comprehensive EPS modal analysis is performed. Eigenvalue sensitivity and participation factors are utilised in order to assess the effect of machine and control parameters, as well as system operating conditions, on EPS stability. Furthermore, the chapter also presents comparative analyses of EPS models with and without taking into consideration the system cabling. This crucial analysis shows that the tendencies in stability behaviour can be significantly different with and without cabling. It is shown that the cable modelling is crucial for the subsequent analysis of power management and stability studies.

Chapter 4 deals with power management strategies and steady-state performance of the multi-source EPS. Due to the modularity and reliability of the droop control, two droop control approaches in DC systems are highlighted: current-mode and voltage-mode droop control. Current-mode system uses the I-V droop characteristic to control the DC current depending on the DC voltage whilst voltage-mode system employs the V-I droop characteristic to regulate the DC voltage according to the current feedback. The power sharing performance, including the sharing accuracy and influence of cable impedance, is presented in this chapter. Additionally the fault scenario is dicussed and investigated by time domain simulations.

Chapter 5 deals with the stability assessment of the EPS candidate by using the impedance-based approach. Firstly, the impedance-based model for a single source system using different droop approaches has been developed. The corresponding output impedance of the source subsystem and input impedance of the load subsystem has been derived and stability boundaries for different droop methods are presented.

Chapter 6 extends the impedance-based analysis to a generalised multiple source multiple load based EPS. The concept of global droop gain is proposed and the impact of a power sharing ratio among the parallel sources on the stability and power losses are discussed in this chapter.

Chapter 7 proposes a novel voltage compensation method in the multi-source based DC EPS to eliminate the DC bus voltage deviation. Optimal droop gain settings have been proposed based on the transmission loss minimisation and the selections of individual droop gains as well as the proportional power sharing ratio have been described. In addition, the stability of the proposed method has also been assessed to show the performance and robustness of this method.

Chapter 8 deals with the experimental support of the analytical results of previous chapters. The chapter presents the experimental platform and lab prototype setup. Experimental results are shown to support the analytical results of previous chapters.

Chapter 9 summarises the findings and contributions of the thesis and shows consideration of future work.

Chapter 2 Electrical Power System in the MEA

This chapter provides a literature review of the electrical power system in the MEA, covering power generation, distribution and utilisation. Load sharing methods are reviewed and stability analysis approaches are addressed to cope with the stability issue caused by CPLs.

2.1 Introduction

The aircraft electrical power systems have made much progress in recent years as the aircraft depends more and more on electricity.

Overall, the increase in the amount of required electrical energy onboard future MEA leads to new challenges for the design of the EPS including generation, distribution and utilisation. The power generation, distribution and utilisation will be reviewed in detail.

2.2 Power Generation

In large commercial aircrafts, one generator per engine typically performs electrical generation. Depending on the aircraft type, there could be more than one generator connected to each engine, such as back-up generators, in order to meet redundancy and extended range twin-engine operations performance standard (ETOPS) [24]. An additional source of electric power on an aircraft is an auxiliary power unit (APU),

which is essentially a small gas turbine-driven generator that can be used as an additional power source. APU typically provides power when the aircraft is on the ground and can also provide power while in the air under emergency conditions. Various batteries exist in the aircraft to start the APU and to provide back-up power for critical equipment in the cockpit as well as other important functions such as the emergency lighting for the aisles [26].

The 115 VAC at 400Hz constant frequency (CF) aircraft system started in the 1960s. This generation of electrical networks was equipped with fixed frequency (115/200 VAC 400Hz) integrated drive generators as on the A320, A330, and A340. With this architecture, the generator is connected to the main engine via a mechanical drive, which keeps the mechanical speed, and hence the electrical frequency, constant on the aircraft's electric bus. The variable-frequency (VF) generations have appeared since the 1990s. In order to simplify the constant-speed mechanical gearbox, the variable-frequency generators are preferred, as on the A380 and on the next A350, for which the voltage standard is doubled (230/400 VAC) with respect to the increase in electrical power needs. Variable-speed constant-frequency (VSCF) aircraft appeared in the 2000s. This new system contains a range of harmonics due to the existence of power electronic converters. To meet the harmonic contents standards, passive filters [1] and active power filters [2], [5] are used. Due to the introduction of variable frequency generation, several power loads supplied at fixed frequency, such as induction motor driven pumps, have been replaced with power electronics controlled loads compatible with variable frequency standards (360–900Hz). For example, this was the case for flight control actuation systems in which electro-hydrostatic actuators (EHAs) were embedded on the A380 for hydraulic network backup.

As discussed above, the power generation system gradually evolves from 115 VAC 400Hz constant frequency, variable speed constant frequency, to variable speed variable frequency. Table 2-1 lists the power generation types of recent civil and military aircrafts.

Table 2-1 Power generation type for recent aircrafts [8]

Generation type	Civil aircrafts		Military aircrafts	
CF	B777	2*120kVA	Eurofighter Typhoon	
	A340	4*90kVA		
	B737NG	2*90kVA		
	MD-12	4*120kVA		
	B747-X	4*120kVA		
	B717	2*40kVA		
	B767-400	2*120kVA		
VSCF (cycloconverter) 115VAC/400Hz			F-18C/D	2*40/45 kVA
			F-18E/F	2*60/65 kVA
VSCF (DC Link) 115 VAC/400Hz	B777 (Backup)	2*20 kVA		
	MD-90	2*75 kVA		
VF (115VAC/380-760Hz)	Global Ex	4*40 kVA		
	Horizon	2*20/25 kVA		
	A380	4*150 kVA	Boeing JSF	2*50 kVA
VF 230VAC	B787	4*250 kVA		

As can be seen from Table 2-1, the power generation system gradually evolves from CF to VSVF. This subsection will review these power generation architectures and working principles in detail.

2.2.1 Constant Frequency (CF)

Conventional civilian aircrafts (Airbus A340, Boeing B717, B737NG, B747, B767-400, B777, MD-12) use a complex mechanical gearbox which keeps the mechanical speed, and hence the electrical frequency, constant on the aircraft's electric bus, as shown in Figure 2.1. This system can therefore provide constant output speed while the input speed (e.g.engine shaft speed) can vary depending on engine. This constant speed shaft drives a generator to give a constant frequency electrical supply, typically at 400Hz. However, the cost of purchase and maintainence of the gearbox can be high due to the complexity of the hydro-mechanical drive system [27]. In addition, the use of the gearbox reduces the reliability of the system. Hence, this topology appears not to be the best choice.

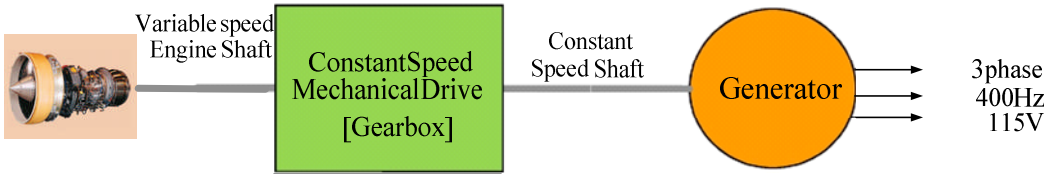

Figure 2.1. A constant frequency generation system using a mechanical gearbox [28].

2.2.2 Variable Speed Constant Frequency (VSCF)

Figure 2.2 presents an alternative technique for generating a constant frequency supply with the generator connected directly to the engine shaft. The output of the generator is of a variable frequency related to the speed of the turbine. This electrical frequency, which changes during phases of flight in response to changing engine operational mode, is processed by a regulated AC/AC power converter and filter to produce a fixed frequency supply for the aircraft's EPS. The AC/AC power conversion can be realised using different power converter topologies including matrix converters or a cycloconverter (see Figure 2.2(a)) or back-to-back converters with DC-link (see Figure 2.2(b)). The architecture of a VSCF with a cycloconverter is mainly used on military aircraft. The VSCF with a DC-link has been used in the B777 (backup) and MD-90. The DC-link is beneficial for feeding high voltage loads and charging batteries through DC/DC converters whilst the bulky DC-link capacitor will increase the size and weight of the system.

In such a VSCF generation system, no gearbox is needed between the gas turbine shaft and the generator; however, the drawback is that this power converter must process all the generated power and, therefore, must have the full power rating and high reliability to get the required level of safety from the aircraft design. In such systems, the power electronic converters will be the bottle-neck of reliability.

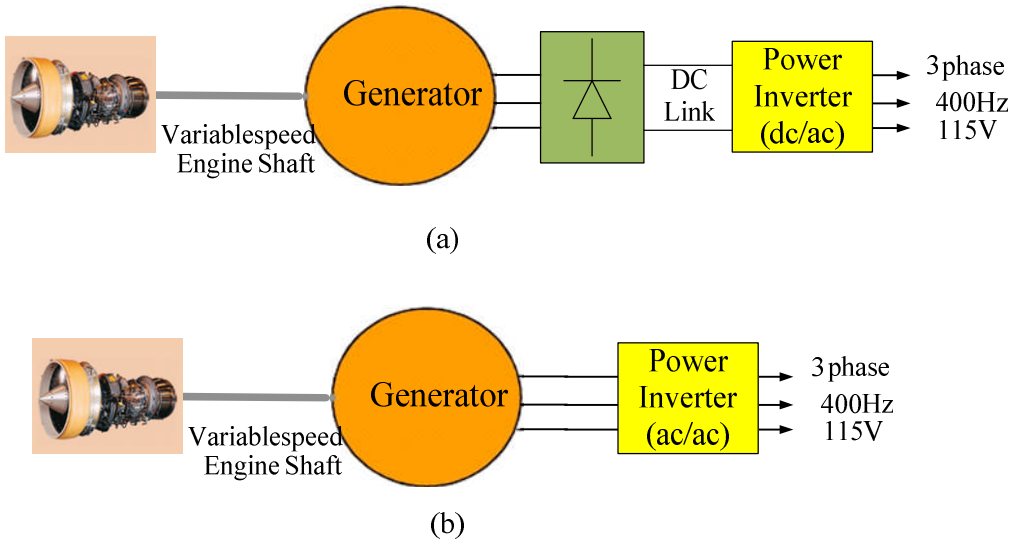

Figure 2.2. A variable speed constant frequency generation system with (a) cycloconverter (b) DC link [28].

2.2.3 Variable Speed Variable Frequency (VSVF)

If the electrical system and associated loads can be adapted to operate with a variable frequency, then it is possible to link a generator directly to the engine shaft, as shown in Figure 2.3. The electrical output of the generator provides a variable-frequency supply with the frequency related to the speed of the gas turbine, typically in the range 360 to 900Hz. EPS architectures with such variable frequency distributions are known as “frequency-wild” systems. The key advantage of these is the direct connection between the generator output and the electrical power system, giving a simple and potentially very reliable configuration. The drawback is that nearly all aircraft loads will require power converters for control, as the variable-frequency supply cannot be used directly by some onboard loads. However, many loads, for example, actuators, require this power conversion stage for control even when operated from a fixed frequency supply. Having many distributed power converters gives more options for a safe aircraft system design as redundancy can be built-in at

the systems level, avoiding any single points of failure within the design [28]. In new aircrafts such as the Boeing 787, Airbus A380 and A350, this VSVF architecture has been employed [29]. In these aircrafts, while the voltage is regulated at either 115 (A380) or 230 VAC (B787), the frequency changes with the engine speed and typically varies between 320 and 900Hz [32]. This change in paradigm leads to establishing power conversion for many loads, including motor drives. As a result, power electronic converters are needed locally.

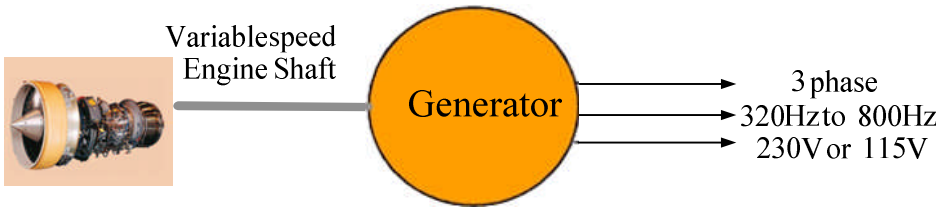

Figure 2.3. A variable frequency generation system (with AC distribution) [28].

Comparing to AC systems and used primarily on military vehicles and military aircraft, variable frequency generation with high voltage DC (HVDC) distribution structure is shown in Figure 2.4. The difference is that the generated electrical power is rectified to the DC bus for further distribution which has a HVDC bus bar (270 V or 540 V).

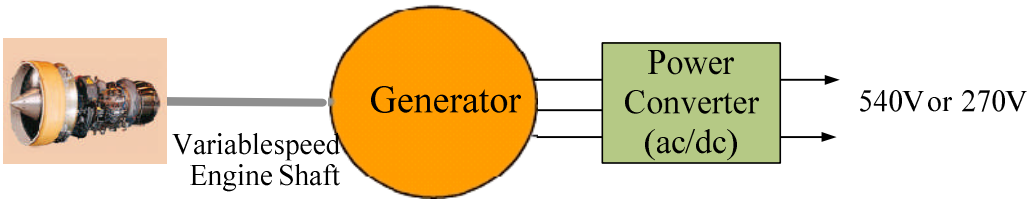

Figure 2.4. A variable frequency generation system (with DC distribution) [28].

The benefits of variable frequency generation with HVDC distribution can be summarised as follows:

- Lower losses in the power transmission cables. This is due to the fact that only two conductors are required in HVDC distribution, whereas three conductors are required in AC distributions. The HVDC system shows about 67% reduction compared to the conventional system (115 V constant frequency) and about 33% compared to the HVAC system;

- The reduction of skin effect in HVDC can also reduce the power losses and also significantly reduce the dielectric losses in the power cables [12];
- Less corona effect with DC compared to AC conductors [12].
- No need for any reactive power compensation equipment: the capacity of wires and devices can be reduced because it does not need to distribute/process the reactive power [12].

2.2.4 DC Generation

DC power generation systems use generators to develop a DC voltage to supply aircraft system loads. The voltage is normally 28 VDC for low power DC loads and 270 VDC for high power loads and further power conversion. For DC generator systems, the stator field can be controlled by varying the stator resistance which influences the output voltage seen in Figure 2.5. The variation of resistance takes into account the amount of connecting loads and engine speed. The DC generators are controlled to supply constant DC voltage even with varied engine speed and electrical loads. Also, the voltage regulation needs to be in accordance with the standard used to specify aircraft power generation systems, namely MIL-STD-704F [33]. This standard specifies the voltage at the point of regulation and the nature of the acceptable voltage drops throughout the aircraft distribution, protection and wiring system [34].

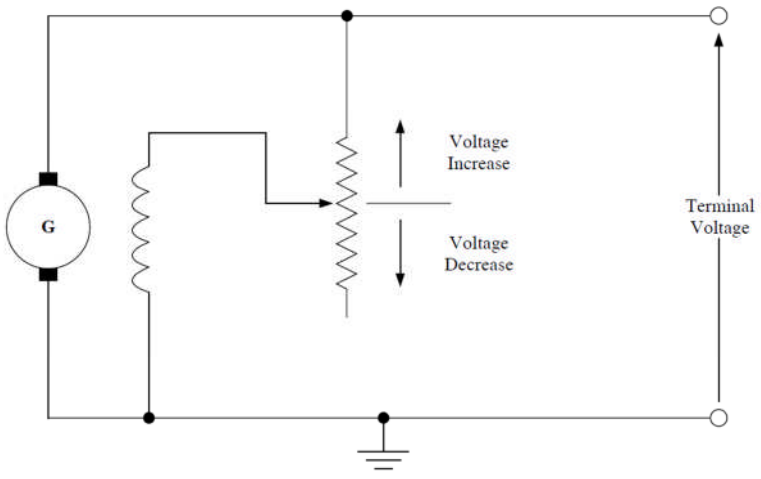

Figure 2.5. DC voltage regulator [34].

In these DC generation systems high power generators output 270V DC power, some of which is then converted into 115 VAC 400Hz or 28V DC required to feed specific loads. This approach has been adopted on the Lockheed Martin F-22 and F-35 aircraft. It is claimed to be more efficient than conventional methods of power generation where the required power conversion stages are significantly reduced with accompanying benefit of weight savings.

However, there are some limits for 270V DC systems which are explained below [34]:

1) The current cannot exceed 400A, otherwise, the size of conductors and switchgears to carry the necessary current becomes prohibitive.

2) The brush wear on brushed DC generators becomes excessive with resulting maintenance costs if the current exceeds 400A or the power per channel is over 12kW.

3) Conventional circuit breakers cannot be used at such high voltages 270 VDC and as a consequence, 270 VDC protection devices need to be developed [34].

2.2.5 Electric Starter/Generator

Electric starter/generator is beneficial to facilitate electric engine crank, assist the engine in reaching the desired idle speed, generate power to drive the onboard auxiliaries, and improve the overall system efficiency [35]. Figure 2.6 shows the architecture of the electric starter/generator system. In the motoring mode, the machine is driven by a bi-directional power converter and uses the power coming from the supply bus to accelerate the aircraft engine. Since the control target in the motoring mode is the machine speed, as can be seen, the speed signal is sensored and the control system regulates the machine speed to its reference value. This mechanical energy can be harnessed to the engine shaft and cause the engine to spool up to a speed where the combustion ignites and the engine becomes self-sustaining. In the generating mode, the engine acts as a source of mechanical power that is converted by machine and converter into the electrical power to supply on-board loads.

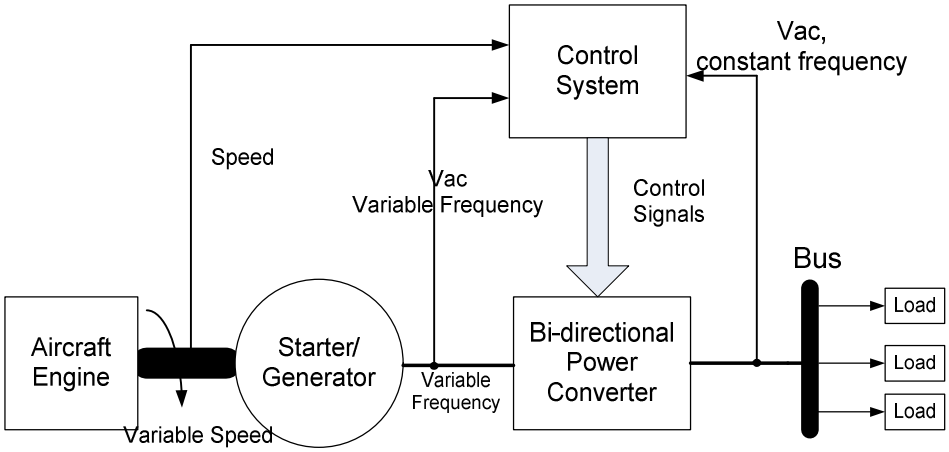

Figure 2.6. Electric S/G system.

Figure 2.7 shows the torque-speed characteristic of the aircraft S/G. The machine runs as a motor during engine start period and is required to supply constant torque (T_{start}) from standstill to ω_b. The machine operates in the constant torque region where the maximum torque of the machine can be achieved. Between ω_b to ω_{min} the machine provides a constant power to accelerate the engine until the engine is fired and becomes self-sustaining. When the machine reaches ω_{min} the engine is considered to have become self-sustaining and the generator operation is initiated. In generation mode, the machine is required to produce maximum constant power up to a maximum speed (ω_{max}).

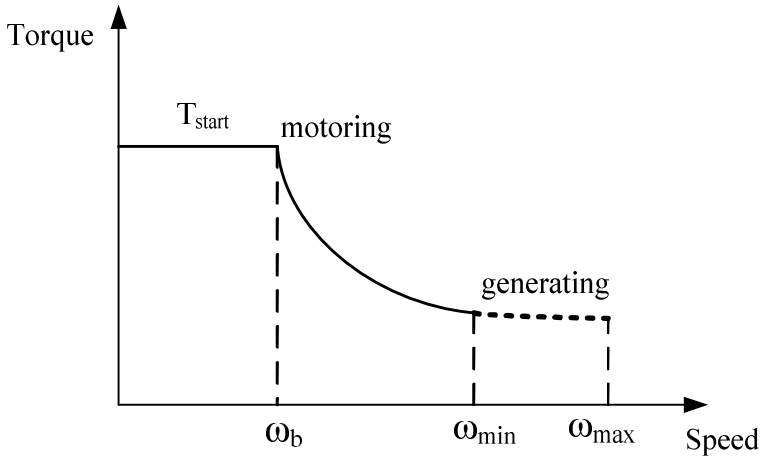

Figure 2.7. Torque-speed profile of the aircraft starter/generator [36].

2.2.5.1 Electrical Machines

The anticipated increase in electrical power generation requirements on MEA suggests that high power generators should be attached directly to the engine, mounted on the engine shaft and used for the engine start in the Integral Starter/Generator (IS/G) scheme [35]. Considering that the harsh operating conditions and the high temperatures may push most materials close to their limits, more innovations in materials, thermal management systems design, etc are required. Consequently, various types of electric machines have been considered for aircraft power systems in literature: induction machine (IM), switched reluctance machine (SRM) and permanent magnet machine (PMM) [37], [38].

Wound Field Synchronous Machine (WFSM)

The evolution of AC generators over the years has led to the state-of-the-art machine three stage wound field synchronous machine (WFSM). Figure 2.8 shows the equivalent electric structure of a typical, three stage WFSM. It is actually three electric machines using a common shaft in the same housing. It consists of a PMM (Stage 1), an exciter (Stage 2), and a main generator (Stage 3).

As the rotor turns, the PMM generates AC power because the rotating magnets induce AC power in the stator. The exciter consists of a rotor with AC armature and a stator with windings. The generator control unit (GCU) rectifiers the AC power into DC power for use in the GCU control circuits and provides main generator excitation via a DC/DC converter. Since the exciter rotor windings are three phase, the output power generated is continunous three phase AC. A rotating rectifier is included in Stage 2 to convert the exciter AC output to DC for presentation to the main generator. The main generator has a rotor with a DC winding and a stator with an AC winding. Thus, as the rotor rotates, it generates an EMF and produces power [39].

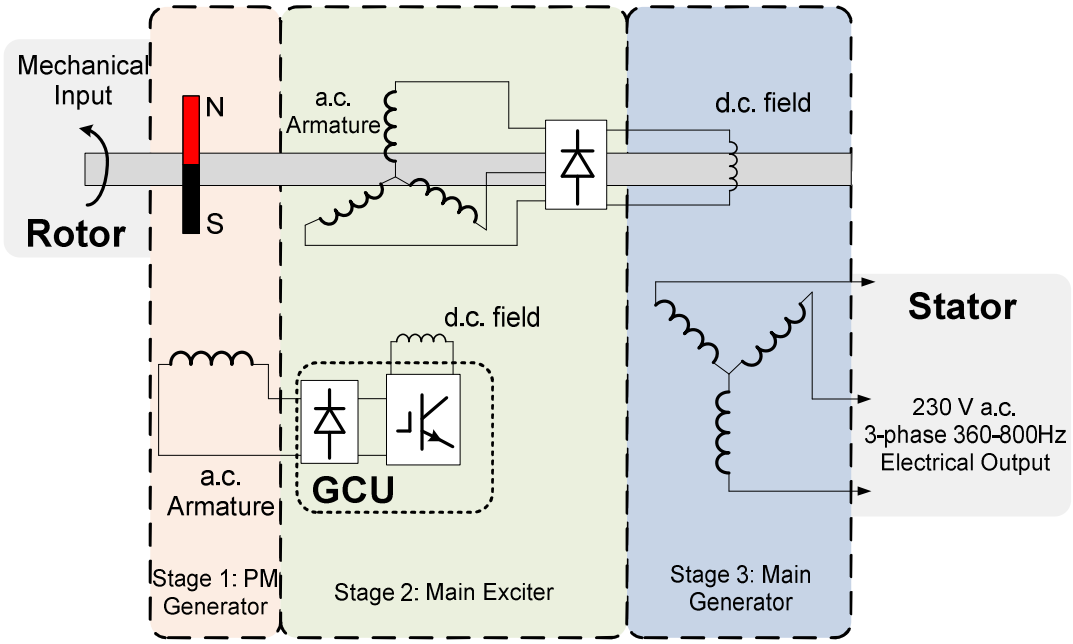

Figure 2.8. Three-stage wound-field variable frequency generator.

Induction Machine (IM)

IMs are robust, have fault tolerant capability, and can operate at high temperatures. References [40] and [41] present an S/G operation with resonant converter fed IM. With the use of a DC machine to mimic the aircraft engine, experimental results showed the feasibility of operation of the IM as an S/G. In [42], a direct-flux vector control scheme of an asymmetrical six-phase IM is implemented. The overload capabilities and post-fault operations of the multi-phase IM have been demonstrated experimentally. Further work would include assessing the S/G in an actual aircraft operating environment to determine its limitations. The limitation of this topology may lie in the cooling system since heat is generated both in the rotor and stator side. Also, IM has a low power density, large end windings and excitation problem at high speeds [43]. Although IMs are used for automotive electric propulsion, induction generators have not been used in aircraft power generation. With active rectifier and field orientation control, the use of an IM as an embedded starter/generator needs to be further explored for aircraft applications.

Switched Reluctance Machine (SRM)

For the aircraft applications, high power density, wide speed range, wide operating temperature range, low volume, high reliability and easy control are required. SRM matches the requirements. The magnetic and electric independence of the machine phases and the absence of permanent magnets provide fault tolerance and also improve reliability. The mechanical integrity of the rotor permits high-speed and high-power-density operation. The SR S/G system is considered a prime candidate technology that meets the requirements and constraints of the embedded generation in aircraft applications. SRM has been considered and investigated as a S/G in [44]-[47]. Since 1995, the SRM has been used in the S/G system. A comparative study of a high speed SRM with and without a resolver is conducted in [44]. A 100 kW 13.5 krpm modular rotor SRM is designed and the reduction in loss is achieved [45]. In [46], the design and realisation of an SRM as an S/G in the hybrid electric vehicle application has been presented. It is shown that a higher number of stator and rotor poles is more appropriate for active power utilisation. It also proves that the SRM is a suitable candidate for high specification applications. Reference [47] presented an angle and speed estimation algorithm to realise the sensorless control strategy for the SRM and results showed that the S/G can operate with full-torque sensorless operation from zero speed to engine ignition speed.

The main features of this SRM-based system include fault tolerance, suitability to operate at high speeds and in harsh environments, and relatively high power density. However, SRM has limited high speed capability and a high torque ripple is the limitation factor. Due to the acoustic noise and torque pulsations of SRMs, the use of SRMs for aerospace applications is still restricted to some extent.

Permanent Magnet Machine (PMM)

PMMs have dominated the traction motor market for electric vehicle (EV)/hybrid electric vehicle (HEV) application recently [47]. They can be designed to operate over wide torque speed range with superior torque density and power density. Today, the interior PM (IPM) synchronous motor is widely used in automotive propulsion because of its high efficiency, high torque, high power density, and relative ease of field weakening operation [48].

In [49], an enhanced control strategy of an open-winding PMM as an S/G with the inverter-rectifier topology was proposed to overcome the shortcomings of a traditional PMM such as narrow speed range and low power factor. In [50], an optimal multidomain design with the combination of finite-element and an analytical model was proposed for the IPM for the S/G applications. In [51] two S/Gs with surface-mounted PMM and IPM were developed. It is shown that the eddy current loss reduces with a thinner sleeve as long as the skin depth is still larger that the sleeve thickness. In [52] an optimal design and control of the PMM-based S/G was proposed to allow a wide constant power zone operation with relatively high efficiency. In [53] a new PMM has been designed and implemented as S/G for HEVs. Due to the unique feature of hybrid excitations to produce the magnetic field, the proposed PMM can accomplish various operating modes (engine cranking, battery charging, and torque boosting).

Due to the abovementioned advantages, the focus of this thesis is on the PMM-based S/G system and the generation mode will be highlighted in the following chapters.

However, there are still limitations of this topology such as cost and availability of rare-earth material used in permanent magnet. Also, its vulnerability to high temperatures is another disadvantage. The limit temperature of the permanent materials is about 300ºC. In addition, the PMMs are not inherently fault tolerant. Since the flux is generated by the permanent magnet and cannot be disengaged electrically. The back electromechinical force (EMF) is in presence until the machine stops spinning. As a result, an excessive short-circuit current may be fed to the point of failure and the braking torque arises. A key requirement for many aircraft and automotive generation systems is a degree of fault tolerance, i.e., an ability to continue operating at or near rated power in the event of a single point fault in the electric machines or its associated power converter [54]. One way of achieving fault tolerance is to isolate the phase windings physically, magnetically, and electrically. Three-phase or multiple-phase machines can be an option, where each phase of the machine is fed separately by a single-phase bridge converter [54]. As a consequence, a fault in one phase will not readily propagate to the adjacent phases. In addition, each phase winding is designed to have one per-unit self-reactance to limit the short-circuit current to its rated value at fault conditions.

2.2.5.2 AEGART Project

The work presented in this thesis is based on the "Aircraft Electrical Generation with Active Rectification Technology" (AEGART) project, a part of the Clean Sky JTI ITD EU FP7 framework program [55]. The project has conducted an intensive trade-off study of potential S/G topology candidates and, due to the advantages of the PMM, the topology of surface-mounted PMM (SMPMM) fed by an active front end rectifier has been chosen. Figure 2.9 shows the lab prototype of the AEGART project for the electric S/G studies.

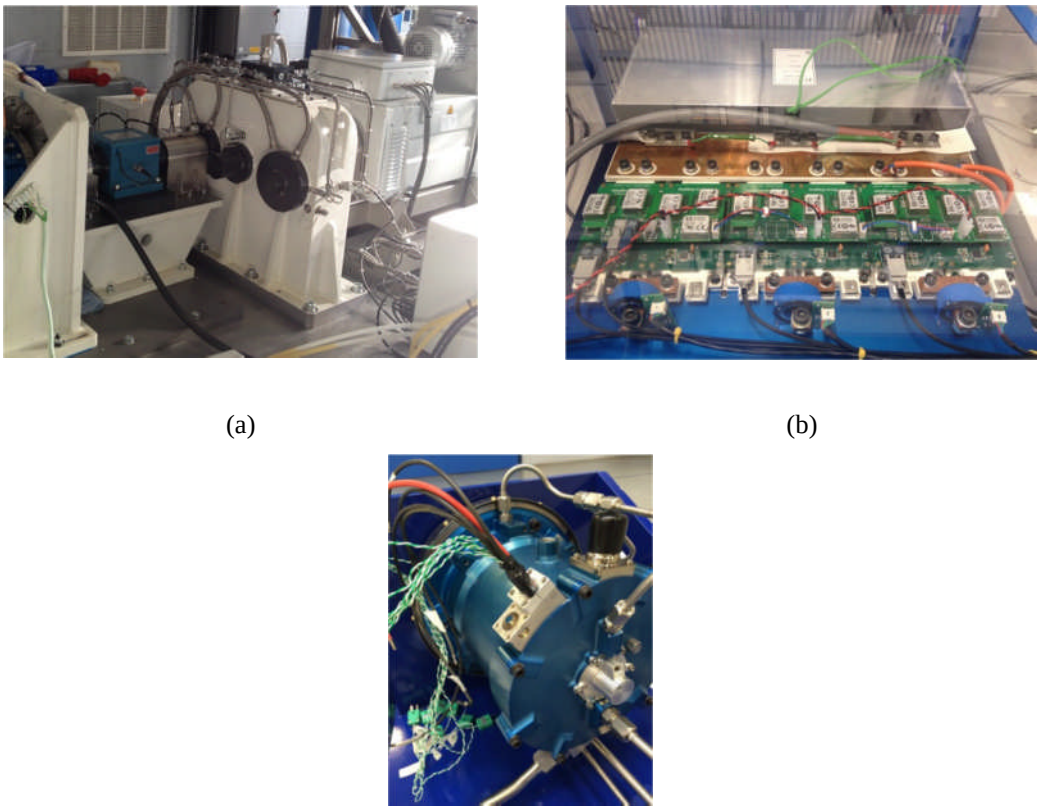

(a) (b)

(c)

Figure 2.9. Lab prototype of AEGART project. (a) aircraft engine emulator; (b) bi-directional power converter; (c) starter/generator (SMPMM).

This PhD research starts with the control design of the generator-active rectifier system and extends the analysis to the multiple generators-based electrical power system including power sharing performance, stability assessment, etc. As shown in Figure 2.10, fundamental vector control is used in the core system. The reference frame transformation is discussed in detail in Appendix A.

After transforming measured currents to rotating frame, the linear control (conventional PI controller) adjusts current in the synchronously rotating reference frame (*dq* domain) and outputs *dq* voltage demands. Voltage demands are inversely transformed into 3-phase demand modulation indexes for PWM. Then the core system can be fully controlled by using both *dq* current demands.

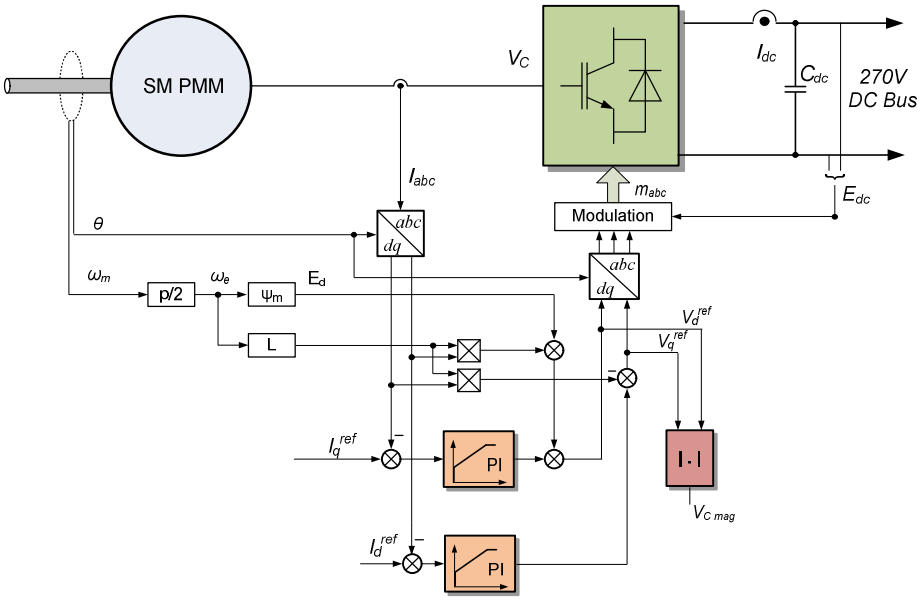

Figure 2.10. Inner current loop control of the PMM-based S/G (core system).

Figure 2.11 shows the outer loop of the S/G. Since the designed PMM is for high speed operation (32 krpm), the flux weakening controller needs to be taken into account when the machine speed exceeds the base speed. For the starter mode, speed controller and flux weakening controllers are employed to generate the *q*-axis current reference and *d*-axis current reference. When the stator voltage is less than its maximum value, the output of the flux weakening controller is saturated to zero. The controller starts to work when the stator voltage exceeds the maximum voltage limit. With the outer voltage regulation loop (V_c loop), the flux-weakening control is fulfilled by injecting the negative *d*-axis current.

For the generator mode, conventional PI controllers are used to deflux the machine (*d*-axis) at high speed and control the output DC current (*q*-axis). The stator current references in the *d* and *q* axes are obtained from the output of the flux weakening controller and I_{dc} controller respectively. The reference of the AC voltage (V_c) is

dependent on the DC voltage. The DC current reference (I_{dc}^{ref}) is determined by the desired droop characteristic.

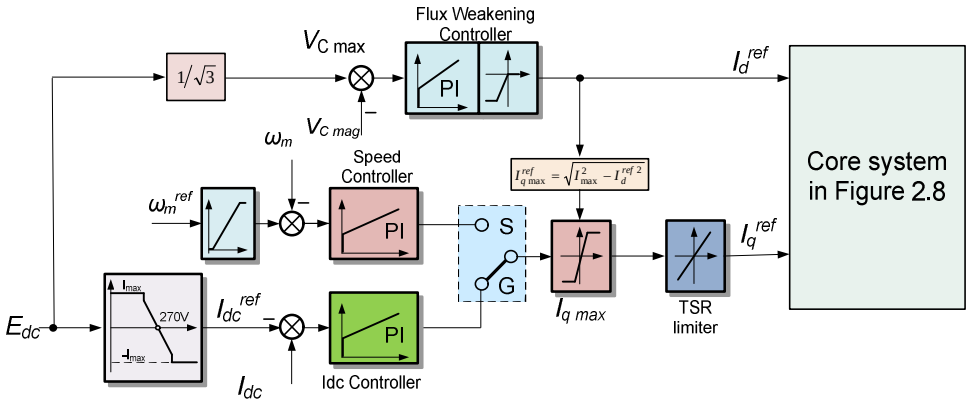

Figure 2.11. Outer loop control for AEGART S/G system.

The control design lays the foundation of the modelling, with analysis in the subsequent chapters.

2.3 Power Distribution

After the electrical power is generated by the generators, it is distributed throughout the aircraft. The power distribution system of the most in-service civil aircrafts is composed of hybrid AC/DC topologies. For instantce, an AC supply of 115V/400Hz is used for large loads such as galleys, while the DC supply of 28V DC is used for flight control, avionics, and battery-driven vital services [5]. In the traditional aircraft model, all of the electrical power is generated remotely from engines-driven main generators (next to the engines) and APU-driven generator (in the aft area). Such traditional architecture is illustrated by Figure 2.12(a) and is referred to as a centralised power system distribution. The generated electrical power is then routed to the front of the aircraft for protection and control.

One advantage that the move to MEA brings is the flexibility to generate and distribute power efficiently near to where it is being consumed. In an MEA, the new solid-state power controllers and contactors with communication allow for the possibility to eliminate the configuration in favor of remote distribution. This results in increased efficiency of the power distribution system, as line losses are decreased

due to shorter distances between generation and consumption. Moreover, significant weight and volume savings may be realised, as the power rating of the main conductors may be reduced. These weight savings and rating reductions contribute both to improved fuel efficiency of the aircraft and a lower total cost, as the lower rated equipment may be provided at a reduced price. Additionally, the distributed power system configuration realises maintenance cost savings. The Boeing 787 is an example of this modern network configuration and is shown in Figure 2.12(b).

As can be concluded, modern MEAs provide the flexibility to generate and distribute power efficiently near to where it is being consumed.

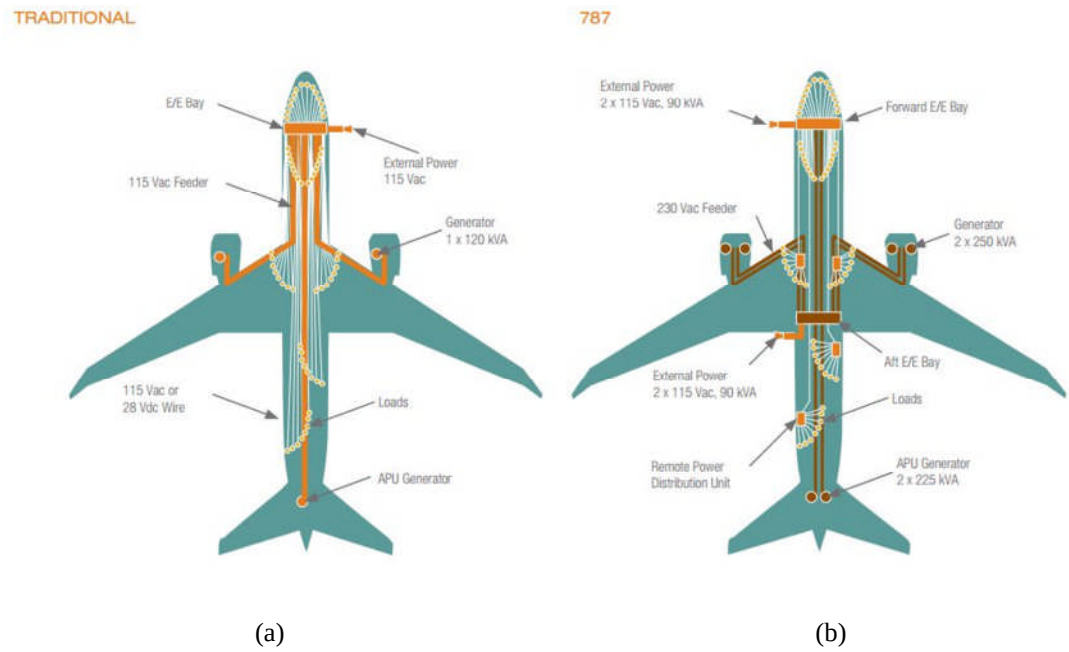

(a) (b)

Figure 2.12. Comparison between the power distribution of conventional aircraft and the MEA [7].

2.3.1 Power Distribution in Conventional Aircrafts

Electrical power system in conventional aircrafts often consists of two or more engine-driven generators to power AC loads. The engine driven-generators are connected to the distribution buses in some civil aircraft configurations (i.e. each generator is responsible for a specific numbers of buses). In the event that one generator fails it is automatically isolated from its respective busbar and all busbar loads are then taken over by the alternative generator. As shown in Figure 2.13, in

conventional aircraft systems, the synchronous generator supplies AC voltage at constant frequency to the AC loads throught the aircraft. AC/DC rectifiers are used to convert the AC voltage with fixed frequency at the main AC bus to DC voltage at the secondary buses which provides electrical power to DC loads.

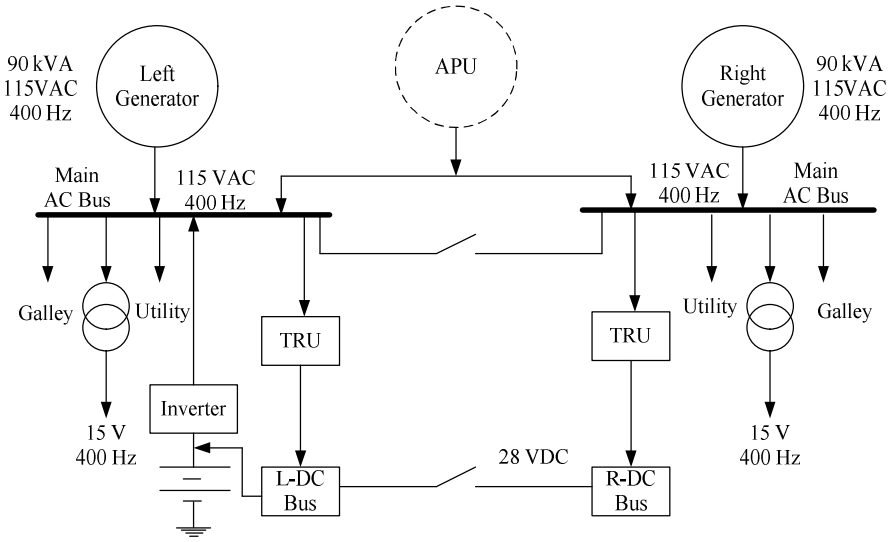

Figure 2.13. Power distribution system in conventional aircraft B767 [29].

2.3.2 Power Distribution in Modern MEA

With the development of high voltage technologies, there is a trend for using only high voltage DC power distribution system in MEA. Several factors encouraging this trend can be listed as follows [5]:

- recent advancements in the areas of interfacing power electronic circuits, control strategies and protections,
- adopting the new generation options as variable frequency,
- the advantages of the high voltage DC distribution system in reducing the weight, size and losses, while increasing the levels of the transmitted power.

For modern MEA, a new power distribution system is employed. Figure 2.14 shows the power distribution system in a B787. It has 2*250 kVA S/G per engine, resulting in 500 kVA of generated power per channel. In addition, 2*250 kVA APU S/G are on board. Instead of 115V 400Hz (fixed frequency) bus, the main bus is high voltage (230 VAC) variable frequency ranging from 360Hz to 800Hz.

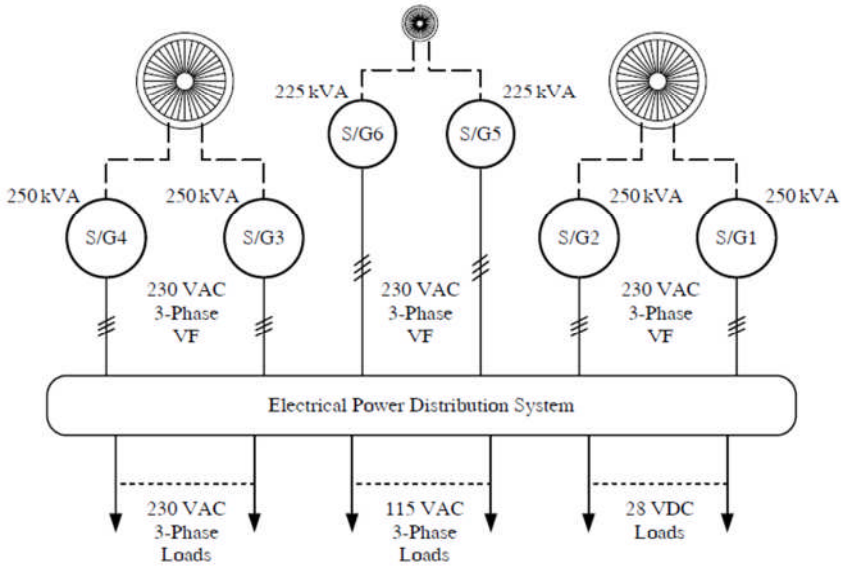

Figure 2.14. Power distribution system in a modern aircraft B787 [30].

Compared to the B787, the A380 has four engines, each of which drives one VF generator (370-770 Hz). Figure 2.15 shows the AC power system architecture. The two APU generators are driven by their respective APUs. Each main generator supplies power to the appropriate AC bus under the control of the GCU. Each main AC bus can also accept a ground power input for servicing and support activities on the ground. Since the aircraft generators are variable frequency and the frequency of the AC power depends upon the speed of the appropriate engine, the primary AC buses cannot be paralled. Although VF generators are reliable, they cannot offer a no-break power capability.

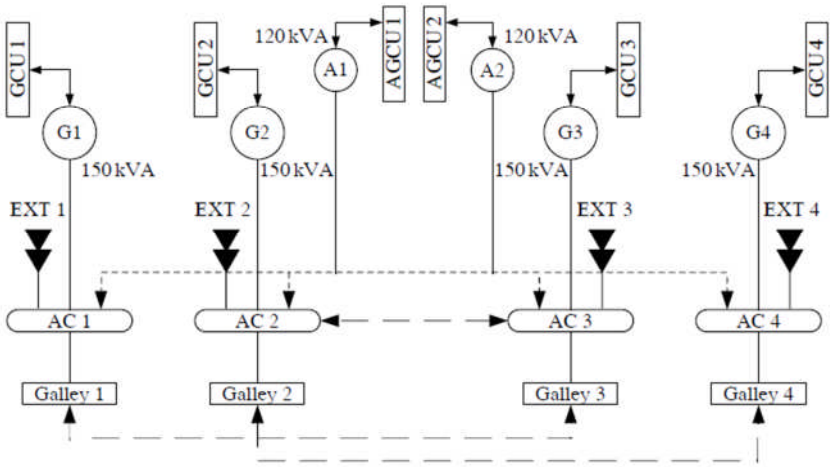

Figure 2.15. A380 AC power distribution architecture [30].

Figure 2.16 shows the DC distribution system of A380 which provides a no-break power capability. Key aircraft systems can operate without power interruption during reconfigurations. Since most control comupters are DC powered and the use of DC paralleling techniques facilitates the provision of no-break power for these crucial elements. It consists of three 300 A battery charge regulator units (BCRU), one 300 A TRU, three 50 Ah batteries, and one static inverter [30].

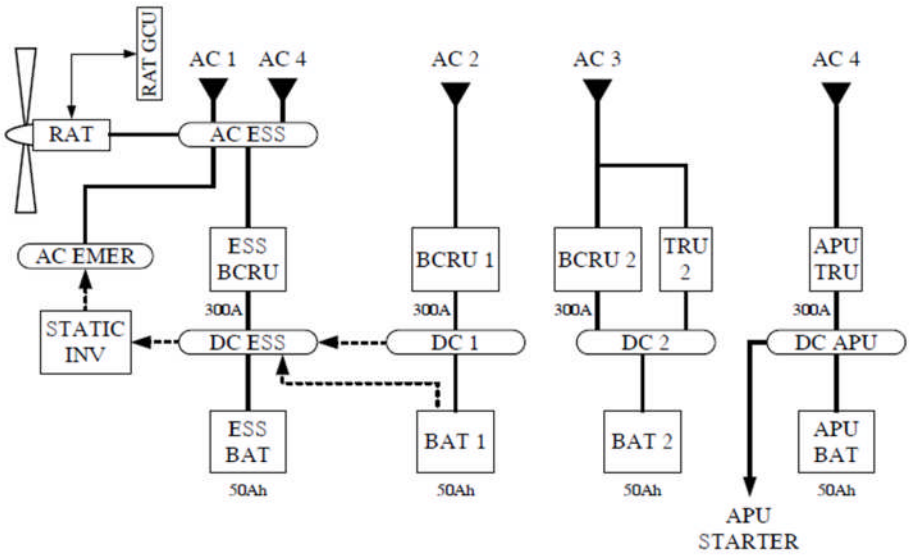

Figure 2.16. A380 DC power distribution architecture [30].

2.4 Power Consumption (Aircraft Electric Loads)

After the electrical power has been generated and distributed throughout the aircraft, it is available to the aircraft services i.e., power consumption. These electrical services/loads cover a range of functions [29]:

- lighting services
- heating devices
- motors and actuation
- subsystem controllers
- avionics systems

As is known to all, the availability of adequate lighting is of great importance to the safe operation of the aircraft. Lighting systems consist of internal lighting and

external lighting. Internal lighting includes cockpit/flight deck, passenger service and emergency/evacuation lighting. On the other hand, external lighting includes navigation, strobe, landing/taxi, formation, inspection, emergency evacuation and logo lights [29].

The heating load represents the power needed for WIPS (anti-icing or de-icing systems) which can easily consumes tens of kVAs.

Motors used onboard have the following application scenarios [29]:

- linear actuation: engine control, trim actuators for flight control systems
- rotary actuation: electrical position actuations for flap/slat operation
- valve operation: electrical operation of fuel, hydraulic, air and ancillary systems control valves
- engine starter: starting of the engine, APU and others to reach self-sustaining operation
- pumps: provision of motive force for fuel, hydraulic, auxiliary system pumps
- gyroscope devices: provision of power to run gyroscopes for flight instruments and autopilots
- fans: running of cooling fans for the provision of air to passengers or equipment.

2.5 Proposed Single Bus-based Multi-Generator Electrical Power System

After reviewing the power generation, distribution and utilisation system in the MEA, the proposed “single-bus” EPS architecture with multiple generators feeding to the same bus is highlighted in this section. The expected benefits of using parallel generation with single bus include improvements in power system redundancy, i.e., the parallel system can provide ‘no break’ power in the event of a generator failure. An example is shown in Figure 2.17. Two PMSGs are connected directly to the turbine shafts through active rectifiers (ARs) and can operate in variable speed mode. The two generators take power from the main engine through the high pressure (HP) and low pressure (LP) shafts, guaranteeing an efficient exploitation of

the power generated by the engine, and operate in parallel to transfer the power to the DC bus. Normally this 270V DC power can be derived from main engine-driven generators or through active rectification. Alternatively for ground starting of the engine, the 270V could also be obtained from a ground-based APU.

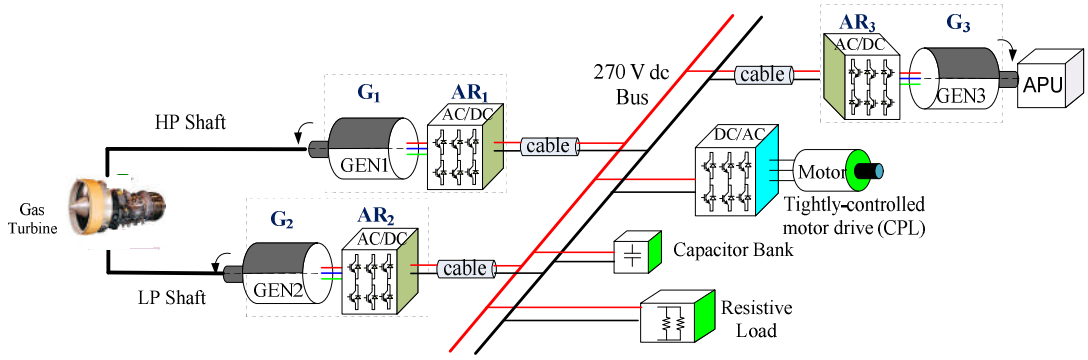

Figure 2.17. A single bus EPS architecture under study for future MEA applications.

As discussed in Section 1.3 Chapter 1, challenges exist in coordinated control of the multiple sources, proper power management and stability issue caused by the CPLs. The load sharing among the parallel sources andthe stability assessment methods will be reviewed in the following subsections.

2.6 Load Sharing Methods

After discussing the existing electrical loads in the MEA, it is important to manage the load power sharing in the multiple generator based single bus architecture, one of the challenges discussed in subsection 1.3.2.

As discussed before, the multiple generators based DC EPS can be regarded as a challenging case of islanded DC MG. Thus, the power sharing methods used in the DC MG can be applied in the studied aircraft's EPS. From the communication point of view, overall control of DC MGs can be divided into three categories: centralised control, decentralised control, and distributed control [57].

2.6.1 Centralised Control

As shown in Figure 2.18, centralised control can be implemented in distributed generation (DG) based DC EPS by employing a centralised controller and a digital communications network to connect it with sources and loads [58], [59].

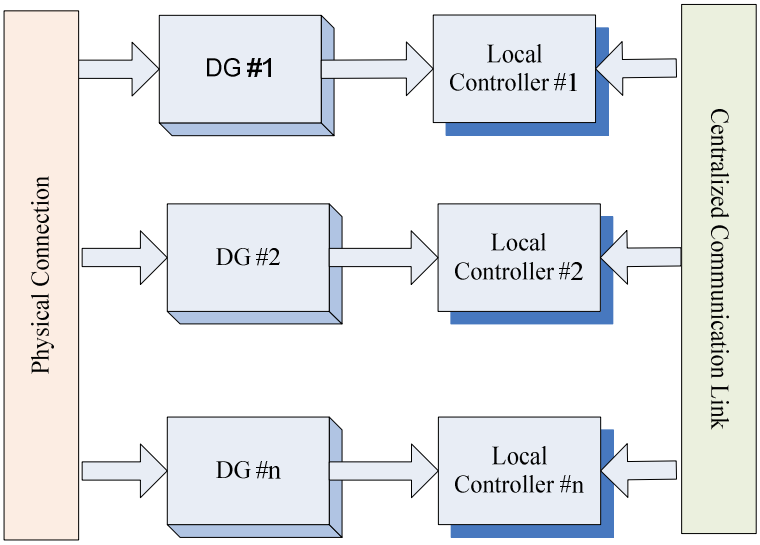

Figure 2.18. Operating principles of centralised control in DC EPS.

Master-slave control can be implemented by a module chosen as a “master” and remaining modules as “slaves”. Normally the module which has the largest capacity or is the most reliable, can be chosen as a “master”. The master module controls the load voltage and generates the current references for the remaining “slave” modules [62]-[64]. The typical block diagram of master-slave control is illustrated in Figure 2.19.

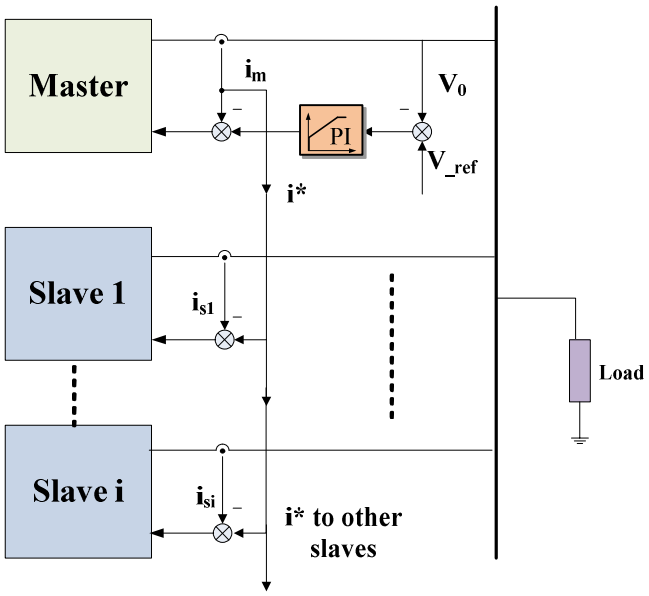

Figure 2.19. Control scheme of master-slave control.

For small-scale DC MGs, each unit can be directly controlled by the centralised controller that employs high-bandwidth communications using a master/slave approach [65], [66]. A master-slave current sharing control of a system with parallel DC-DC converters was studied in [67]. The current reference for the slave modules was generated by the master module and provided by the radio-frequency (RF) wireless transmission. However, for larger scale DC systems, hierarchical control is often a preferred choice since it introduces a certain degree of independence between different control levels. It is more reliable as it continues to be operational even in the case of failure of the centralised control. Hierarchical control is achieved by simultaneously using local converter and digital communication link-based coordinated control, which are separated by at least an order of magnitude in control bandwidth. Coordinated functions can include secondary/tertiary regulation of the DC voltage, power flow control, and different grid-interactive control objectives, such as unit commitment, changing operating modes, global optimisation aimed at maximising efficiency, minimising operating cost, etc. In [69], a multilayer supervision system is proposed to cope with power balancing and energy management in the PV penetrated microgrid. In [70], a comparison between centralised control and distributed control has been performed for building-environmental control systems.

The centralised control is easier to apply compared to the MS method but the load current needs to be measured so the current references for each power module are generated by splitting the load current according to the rated power ratio of sources [71]. The centralised control method is depicted in Figure 2.20.

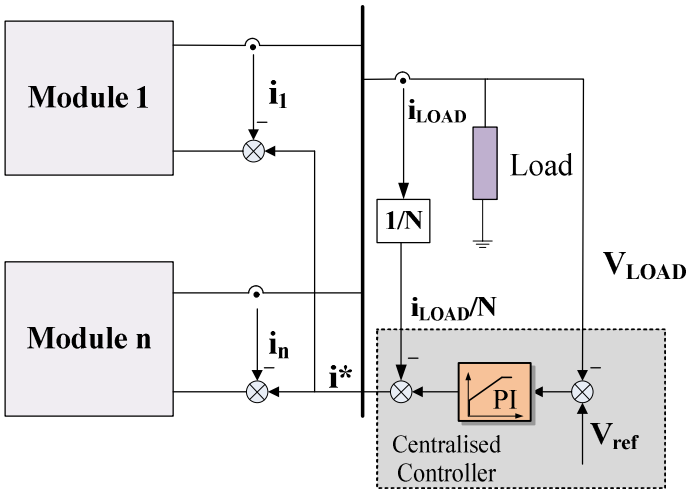

Figure 2.20. Control scheme of centralised control.

Although active load sharing has much better voltage regulation and current sharing performance, the requirement of communication restricts its application area so that it cannot be used in large-scale systems.

2.6.2 Distributed Control

Distributed control indicates the control principle whereby a central control unit does not exist and a communication line exists between the neighboring modules, as shown in Figure 2.21.

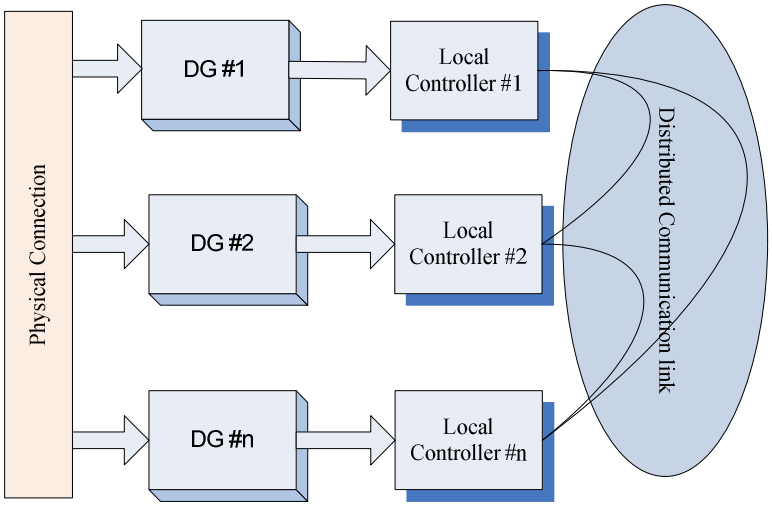

Figure 2.21. Operating principles of distributed control in DC EPS.

The main advantage of this approach is that the system can maintain full functionality, even if the failure of some communication links occurs, provided that the communication network remains connected. Therefore, distributed control is immune to a single point of failure [72]-[74]. The functionalities that can be achieved by this approach resemble those of centralised control and are also represented in the digital communication link-based coordination control.

However, differently from centralised control, the information directly exchanged between the local controllers can contain only locally available variables. In other words, if the two units are not connected directly by the communication link, they do not have direct access to each other's data and their observation of the whole system is limited. In order to overcome this problem, a consensus algorithm, which is a simple protocol installed within local controllers, can be used. It can be analytically proved that, if the communication network is connected, all variable values will converge to a common average after a certain amount of time.

In [75], a consensus algorithm is developed in modular DC-DC converters. The proposed cooperative control is implemented on a sparse communication graph across the MG, reducing the number of communication lines. Reference [76] proposed a dynamic consensus protocol. A noise-resilient DC voltage observer is employed to estimate the average voltage across the MG. A current regulator, which compares the local per-unit current of each converter with the neighbours', is used to

provide a second voltage correction term in order to ensure proportional load sharing. A dynamic consensus algorithm is proposed in [77] and the communication links are only required between neighbouring unbalanced systems. In [78] a complete DC MG model using a discrete-time approach with consideration of the consensus algorithm is proposed. The impact of communication topology and the communication speed are studied in detail.

2.6.3 Decentralised Control

Decentralised control uses local measurement to implement local regulation, as shown in Figure 2.22. If the outage of one module occurs, the remaining modules can still contribute to power sharing according to their local droop settings. Thus, the system reliability is increased [79]. Since communication links among the sources and an additional centralised controller are not needed, each parallel module can work independently relying on the local measurements and controllers.

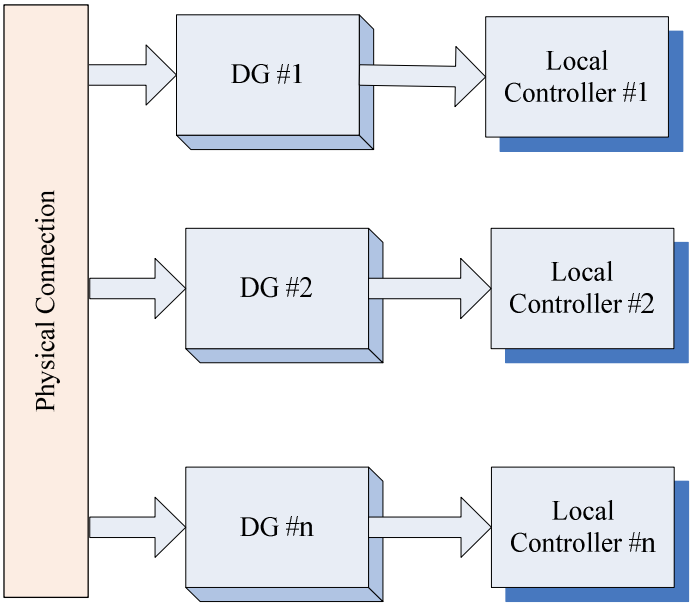

Figure 2.22. Operating principle of decentralised control in DC MGs.

Droop control has been widely accepted as a decentralised control method since there is no dependency on the communication lines. By introducing such a “droop” characteristic, desired power or current sharing conditions can be achieved. Usually, “droop control” is realised by adding a “virtual resistance” into the existing system.

The difference between this “virtual resistance” and “real resistance” is that the “virtual resistance” is an ideal value which will not be affected by its working condition, such as temperature, and no “real” power loss will be produced, whereas the “real resistance” is not a fixed value which could change with the environmental factors and will cause “real” power losses which should be minimised. This virtual resistance is also called droop gain, droop constant or droop coefficient.

Initially droop control was employed in AC systems, active power is highly dependent on the power angle δ, which is dynamically controlled by the frequency, and the reactive power is determined by the voltage V. Figure 2.23 shows the relationship between the P−Q circle of a DG unit and P−f and Q−E droops. So in AC systems, P-ω and Q-V droop are used and they can be expressed as follows [79]:

$$\omega = \omega^* - k_{P-f}(P - P^*) \tag{2-1}$$

$$V = V^* - k_{Q-V}(Q - Q^*) \tag{2-2}$$

where ω and V are the frequency and amplitude of the output voltage measurement; ω^* and V^* are the references; P and Q are the active power and reactive power measurements; P^* and Q^* are the references; $k_{\text{P-f}}$ and $k_{\text{Q-V}}$ are the proportional gain for the P-f and Q-V droop characteristics, respectively.

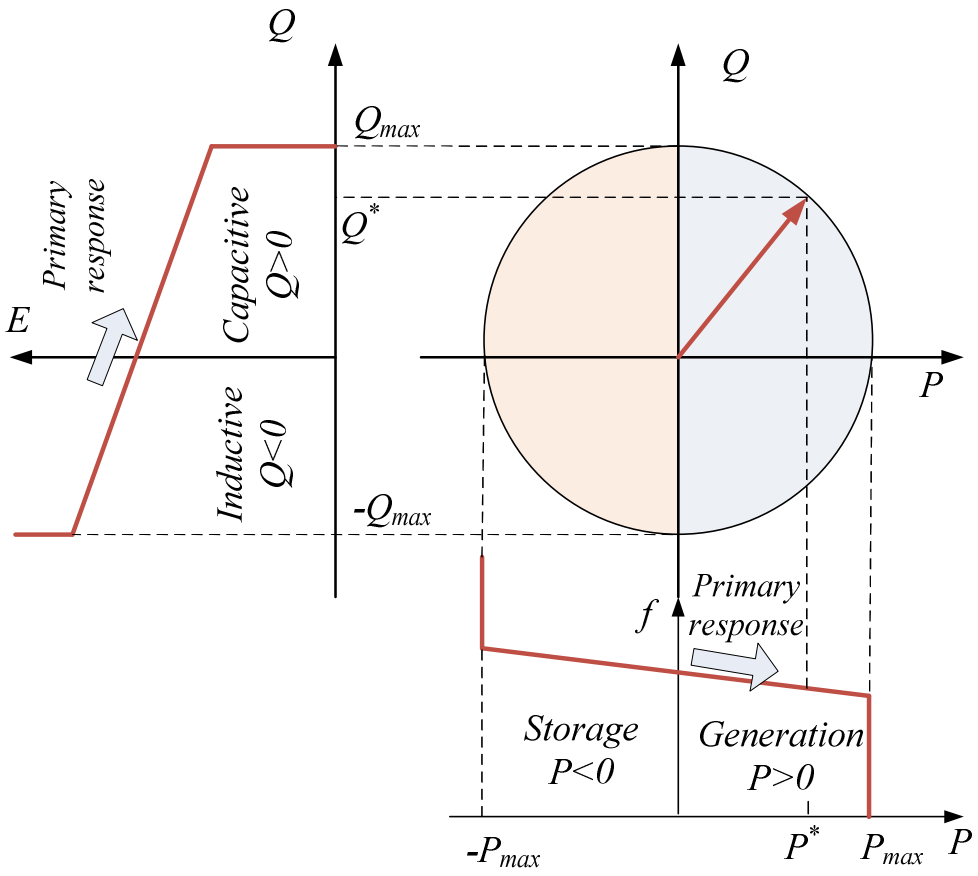

Figure 2.23. P-f and Q-V droop control relationship in AC MGs [80].

Similarly the droop concept has already been successfully used in DC systems. In contrast to the AC systems, the concept “reactive power” is not applicable and only active power can be transferred. The amount of active power transferred in the DC network can be defined by the voltage. Therefore, in DC systems a similar droop control can be built by setting a relationship between active power P and voltage V in order to achieve the desired load sharing by adjusting the voltage. Sometimes P-V droop can be formulated as I-V droop which is also a common DC droop type. The calculations of references for the voltage controller in the two aforementioned cases are as follows:

$$V_{dci}^{*} = V_{dc}^{*} - k_{dp} P_i \tag{2-3}$$

$$V_{dci}^{*} = V_{dc}^{*} - k_{di} I_{dci} \tag{2-4}$$

where V_{dci}^{*} is the output of the droop controller, i.e., the reference value of DC output voltage of the converter #i; V_{dc}^{*} is the rated value of DC voltage; k_{dp} and k_{di}

are the droop coefficients in power- and current-based droop controllers, while P_i and I_{dci} are the output power and current of the converter #i, respectively.

As a decentralised control method to realise desirable power sharing, droop control increases the system modularity and reliability.

However, a distribution line having some impedance will also affect the performance of droop control. Moreover, the cable resistance is subject to changes, such as temperature variation. In order to mitigate the side effect of the cable resistance, the droop gain should be adjusted correspondingly. However, there is a trade-off for the droop gain design. Taking the two parallel connected DC sources as an example, unequal load sharing due to small error in nominal voltages is illustrated by Figure 2.24. If a small droop gain is applied, the difference in source current, i.e., (I_{2o}−I_{1o}), is large. Alternatively, a larger droop gain can be used and the difference in source current reduces to ($I_2 - I_1$). However, the voltage regulation is large and may not be acceptable to loads. Therefore, for DC droop control there is an intrinsic trade-off between voltage regulation and current sharing. In spite of that, droop control is still a competitive solution for both large and small systems due to there being no requirement for communication links and but having a flexible configuration which is appropriate for distributed power system.

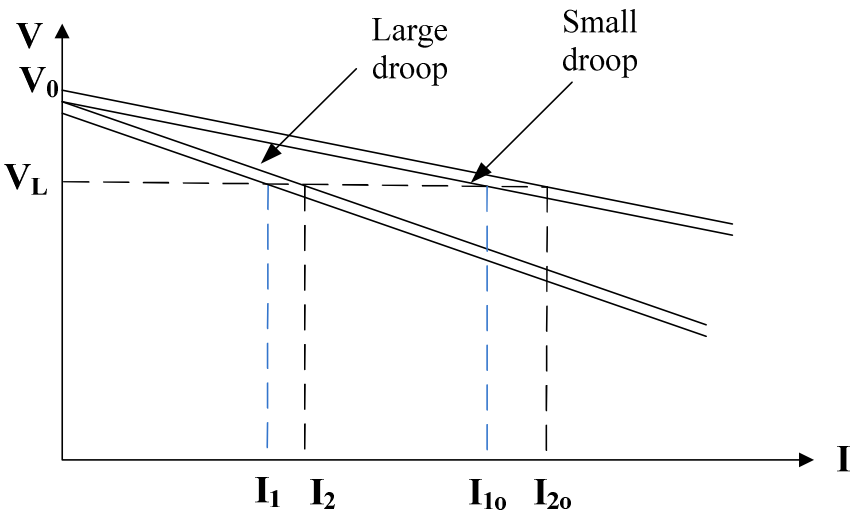

Figure 2.24. Trade-off between power sharing accuracy and voltage regulation.

In [81] the impact of DC line impedance on the power flow of multi-terminal DC (MTDC) and the effect of the droop gain on power balancing is analysed. In [82] an

adaptive droop control approach is proposed to deal with the power sharing according to the headroom (the difference between the rated capacity and present loading). This proposed approach can effectively avoid the over load condition. In [83] a gain-scheduling technique is proposed to adjust the droop constant. By checking the voltage error for different droop gain under various load conditions, the relationship between the load condition and droop gain are derived. This gain-scheduling method can improve voltage regulation and power sharing performance simultaneously without setting a high droop gain at the expense of high voltage regulation. However, the high dependency on the parameters is the main drawback. Reference [84] uses a large droop gain to minimize the load sharing error caused by potential inequality in nominal voltage and/or feeder resistance. By calculating the average current, the droop characteristic in each module will be shifted up by the same amount. Thus both accurate load sharing performance and low voltage regulation can be achieved.

Reference [85] proposed a three level control structure to achieve good load sharing and voltage regulation. Primary control includes conventional droop control and inner loops. Secondary control is used for voltage restoration (AC/DC system) and frequency synchronization (AC system). Tertiary control can provide the global optimization and dispatching, decides the scheduling generating power, etc. Reference [86] proposed a novel droop control method in which the nominal voltage is regulated to improve load sharing performance. Nevertheless, only equal sharing condition is considered which limits its application scenarios.

In summary, as a type of decentralized control methods, droop control can achieve appropriate power sharing amongst parallel sources with the information of local variables. The increased modularity and reliability of the system makes droop control a good candidate to cope with power sharing issue in DC systems.

2.7 Stability Analysis Methods

Control and stability are two important topics that interest researchers in aerospace engineering. This section will address the stability issue of the tightly controlled

power-electronic-interfaced systems and will provide an overview of stability analysis methods applied in the EPS.

As a good example of the CPLs, a DC/DC converter tightly controls the voltage of an electrical load with one-to-one voltage–current characteristics. For example, a resistor is a typical load which has a linear V-I characteristic. As can be seen from Figure 2.25, the controller tightly regulates the voltage; hence the voltage (V) is almost constant. For every voltage, there is only one corresponding current since the electrical load has a one-to-one V-I characteristic. Finally, for a constant voltage (V), current (I) is constant, and hence power (P= V*I) is also constant. Under the assumption that both the system efficiency and the load power are constant, the input power of the DC/DC converter will be constant as well [91]. Thus the DC/DC converter behaves as a CPL to the automotive power grid.

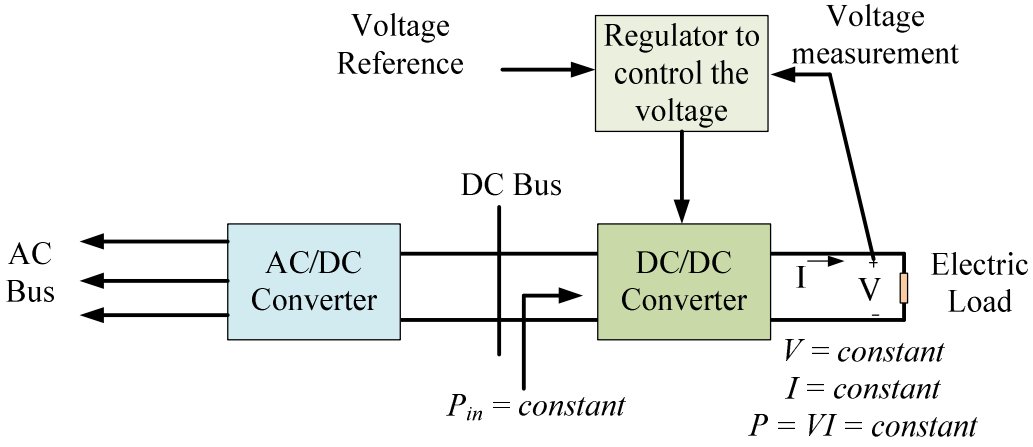

Figure 2.25. Constant power characteristic of DC/DC converters.

Similarly, the negative impedance behaviour of a CPL can also be shown through an example of a tightly controlled motor drive system, as shown in Figure 2.26. A DC/AC inverter drives an electric machine and tightly regulates the rotating speed. Therefore the speed (ω) is almost constant under this rigorous regulation. Since the rotating load has a one-to-one torque–speed characteristic, for every speed, there is only one corresponding torque. Hence, for a given constant speed (ω), torque (T) is constant and hence power (the multiplication of speed and torque) is also constant. Thus the tightly controlled DC/AC inverter and its associated motor drive present a CPL characteristic.

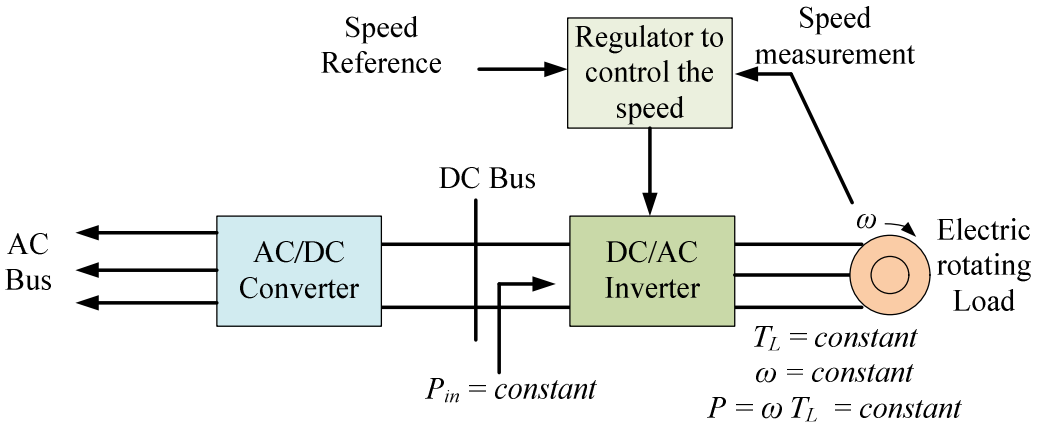

Figure 2.26. Constant power characteristic of motor drives [91].

The V-I characteristic can be illustrated in Figure 2.27. As can be seen, the slope of the tangent line at the operating point is negative, i.e. negative resistance in a small signal manner (negative incremental resistance).

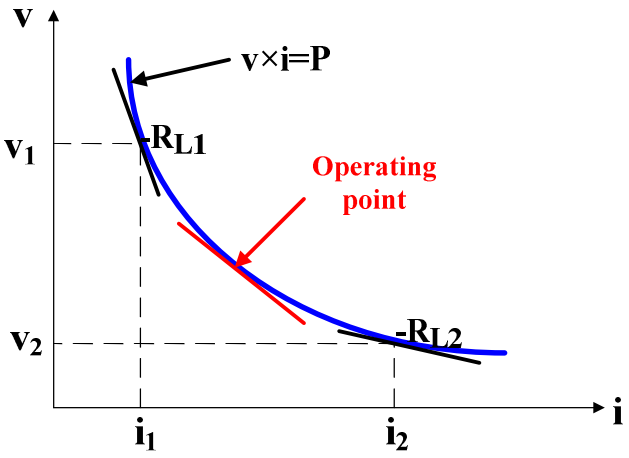

Figure 2.27. Negative impedance characteristic of a CPL.

As a consequence, CPLs have negative incremental impedance characteristics which can lead to interaction problem among subsystems, deteriorating system stability and power quality [91], [92]. Thus this undesirable destabilizing effect induced by CPLs is a great concern for the MEA EPS. The candidate architecture should be carefully examined for stability in order to guarantee safe EPS operation for a wide range of operation scenarios. Two types of stability analysis can be remarked here: large signal and small signal.

Large signal stability analysis investigates the ability of a power system to maintain stable operation and reach acceptable steady-state operating points when subjected to

large disturbances. The Lyapunov-based method has been popular in terms of large signal stability analysis, where nonlinear mathematical modelling is used instead of small signal linearisation [93], [94]. The main advantage of Lyapunov-based approaches is that a developed Lyapunov function allows the estimation of the attraction region of a stable operating point, thus providing an estimate of the size of disturbance that can be tolerated [95], [96]. In [97] the large-signal stability of a hybrid AC-DC aircraft power system has been studied. In particular, the effect of the DC-link capacitance size on system stability has been discussed. Similarly, reference [98] discusses the DC link voltage stability of the motor drives.

On the other hand, small signal stability ensures that the system can revert to its original equilibrium point when subject to a small signal disturbance. Thus, a linearised model around the system equilibrium point is used to study the stability. Linear analysis tools (Bode diagram, Nyquist diagram, and Routh–Hurwitz criterion) can then be employed to derive local stability conditions. These approaches are relatively easy and familiar to applied engineers.

Two dominant approaches for small signal stability analysis can be remarked on here. The first option is to consider the stability problem with a general state space model, design the control and evaluate the impact of different parameters by studying eigenvalues [100]-[102]. Alternatively the impedance method, which is based on an analysis of the output impedance of the source and equivalent load impedance, has also been widely used. The contribution of each component to the system's stability can be assessed in the frequency domain. In addition, the output impedance of the components or subsystems can be reshaped to stabilise the overall power system using an active damping method, an impact of connection of new converters that can be easily assessed. For these reasons, the impedance-based method has been successfully applied in power system stability analysis [103], [104].

2.7.1 Eigenvalue Method

The flow chart of the eigenvalue method is illustrated in Figure 2.28.

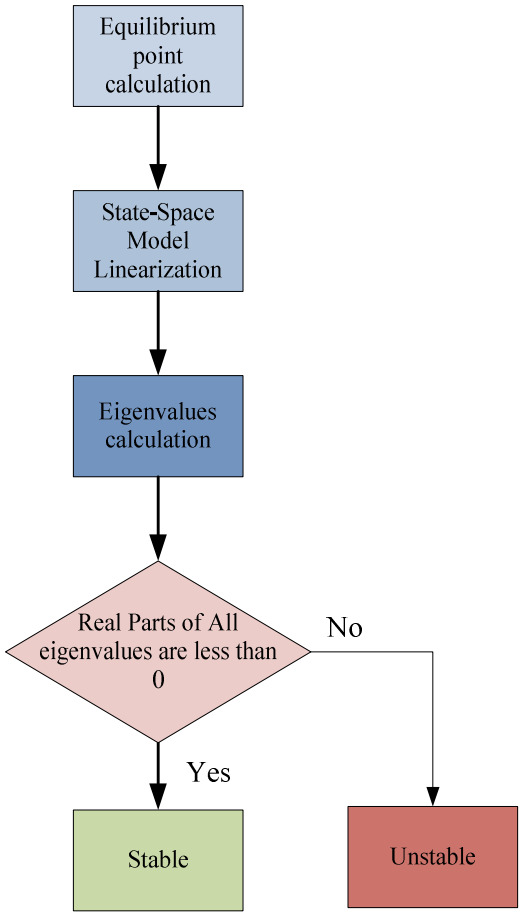

Figure 2.28. Flow chart of the eigenvalues method for the stability assessment.

The steps of the eigenvalue method are discussed as follows:

Step 1) Equilibrium point calculation

For a complex non-linear system, equilibrium point calculation is the first step. The operating point can be calculated by solving the set of equations from the system modelling at steady-state. In terms of the linear system, the equilibrium point with *n* unknown parameters can be calculated by solving *n* linear equations. In addition, the limitation due to the practical operation scenario and ratings of the equipment (e.g. the current ratings of the converters) should be taken into account to obtain the feasible operating point.

Step 2) Model linearisation

For a non-linear system, a linearised state-space model in small signal can be developed according to the specific equilibrium point using the model linearisation approach.

Step 3) Eigenvalue calculation of the state-space matrices

The eigenvalues of the small signal model for the particular equilibrium point can be calculated to evaluate the stability. The corresponding equilibrium point is stable only if the real parts of all eigenvalues of the state matrix are negative [105]:

$$\forall i,\ \mathrm{Re}\left[\lambda_i\right] < 0 \tag{2-5}$$

otherwise, the system at this specific equilibrium point is unstable.

In [106] the stability of a fault-tolerant PMG based AC/DC active rectification system was discussed by applying the eigenvalue method. Reference [107] studied the small signal stability of a typical hybrid more electric power system by evaluating the eigenvalues of the system Jacobian matrix. Reference [108] analyzed the stability of a three-phase frequency-wild AC power system under some key parameters variations such as frequency variations, bus voltage control bandwidth, DC-link parameters etc. In [109] the stability of a three-phase frequency-wild AC power system with a CPL fed through an uncontrolled diode rectifier has been performed and the generalised state-space model in the synchronously rotating frame *dq* has been presented. Small-signal stability of a switched reluctance generator based 270V DC power system for MEA applications has been investigated in [110].

2.7.2 Impedance Based Method

As mentioned above, impedance based methods have been widely accepted for system stability assessment [111]-[114]. Models of individual components are assembled into a full system model which is then typically broken down into two subsystems at a DC point of interest, i.e. a load subsystem and a source subsystem, as shown in Figure 2.29. Consequently, analytical expressions are derived for input impedance of the load $Z_{\mathrm{in\_L}}$ and output impedance of the source $Z_{\mathrm{o\_s}}$ subsystems. The input of the full system is V_{in} and output is V_{o}. The voltage at the breaking point for the subsystem is V_{bus}.

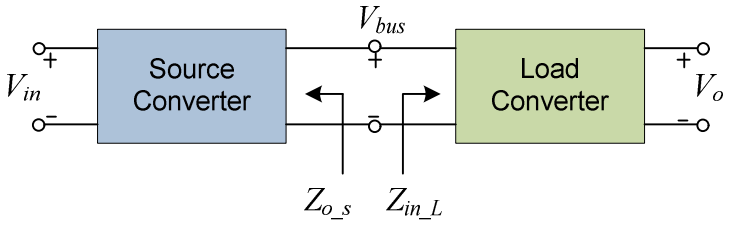

Figure 2.29. Typical cascaded system.

The total input-to-output transfer function of the cascaded subsystems can be written by

$$V_o = V_{in}\frac{Z_{in\_L}}{Z_{in\_L}+Z_{o\_s}} = \frac{V_{in}}{Z_{in\_L}}\frac{1}{1+T_{MLG}} \tag{2-6}$$

where the the ratio Z_{o_s}/Z_{in_L}, which is often referred to as the minor loop gain [111], T_{MLG} can be given by

$$T_{MLG} = \frac{Z_{o\_s}}{Z_{in\_L}} \tag{2-7}$$

If each of the two subsystems is individually properly designed with good dynamic performance, the influence of their interaction can then be studied by looking into the minor loop gain. In particular, in order to preserve the stability, it is mandatory that minor loop gain meets the Nyquist stability criterion [111]. It should also be noted that if the detailed information about source and load systems is not available and the respective impedances cannot be analytically constructed then they should be measured online [112], [113]. Since the source and load converter are assumed to be stable standalone, the minor loop gain term in (2-7) is the one responsible for stability. Therefore, a necessary and sufficient condition for stability of the system can be obtained by applying the Nyquist Criterion to T_{MLG}, i.e. the interconnected system is stable if, and only if, the Nyquist contour of T_{MLG} does not encircle the (−1, j0) point.

Compared to classical stability analysis tools used in large power systems, the impedance based approach has the following key feature: it allows definition of stability criteria for every individual subsystem through convenient impedance specifications. The first specification was proposed by Middlebrook in 1976 who

introduced a set of input-filter designs for regulated converters [111] and many others followed it up in subsequent years [114]-[116].

As shown in Figure 2.30, apart from the well-known Middlebrook's criterion, the other stability criteria for DC power systems are: Gain Margin and Phase Margin (GMPM) Criterion [117], Energy Source Analysis Criterion (ESAC) [116], Root Exponential Stability Criterion (RESC) [118], Opposing Argument Criterion [119], [120], Three-Step Impedance Criterion [115] and Passivity-Based Stability Criterion [121]. For the convenience of comparison, the boundaries for different criteria between forbidden and allowable regions are also presented in Figure 2.30. The forbidden regions are the ones that contain the (−1, 0) point. System stability can be ensured by keeping the contours of T_{MLG} outside of the forbidden regions. Based on the definition of the forbidden regions, design formulations and design criteria can be specified. Note that these criteria give only sufficient, but not necessary stability conditions. Therefore, the minor loop gain may lie in the forbidden region while the system is still stable. For example, Figure 2.31 shows several Nyquist contours of the minor loop gain. The system shown in Figure 2.31(a) is stable since the contour lies within the unit circle and matches the Middlebrook's critierion. Since the Nyquist contour does not encircle (-1, j0), the system represented by Figure 2.31(b) is still stable although the contour does not strictly lie within the unit circle. The system whose Nyquist contour shown in Figure 2.31(c) is unstable since it breaks the Middlebrook's criterion and Nyquist stability criterion.

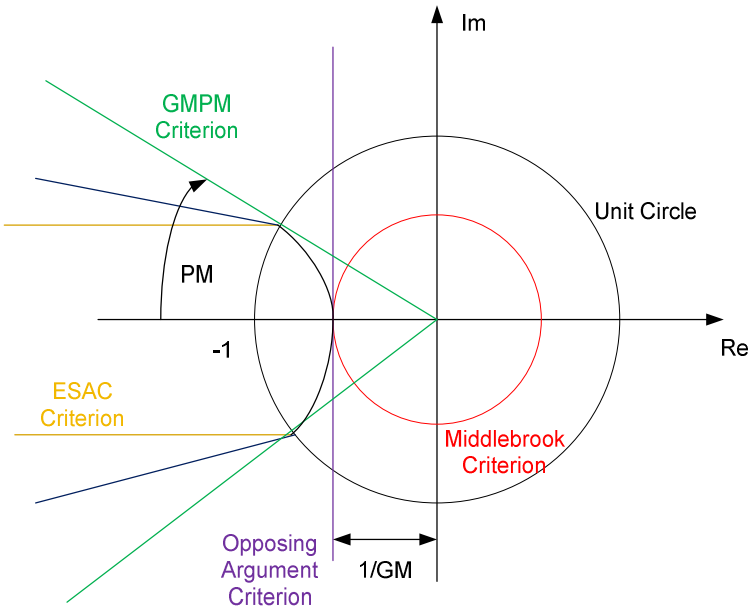

Figure 2.30. Stability criteria for DC power systems [121].

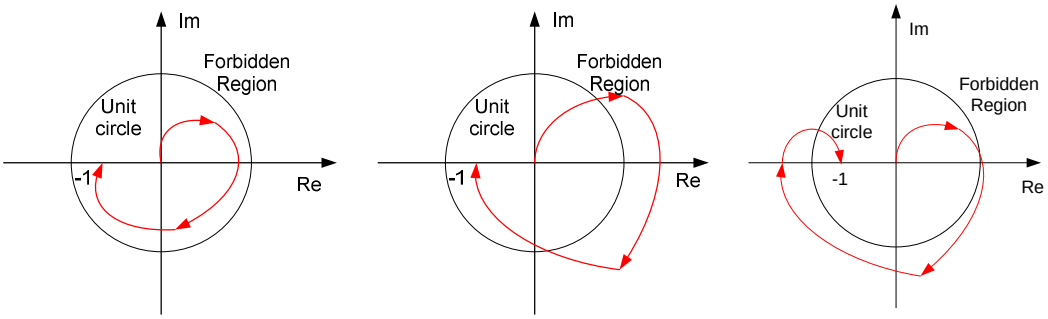

(a) (b) (c)

Figure 2.31. Nyquist contours of the minor loop gain (a) stable; (b) stable; (c) unstable.

Nevertheless, the stability results for impedance criteria rely on the selection of the point in the system where it is broken into load and source subsystems. A different selection of subsystems may show different stability margins moreover, the criteria provide only sufficient stability conditions. In cases where these conditions are not met, a full order state space approach can be used as an alternative.

Unlike the abovementioned stability criteria, the Nyquist stability criterion is the sufficient and necessary condition to judge the system stability. So far there are quite a few published works on the system stability using an impedance-based approach.

In [122] small signal stability of a three-phase AC system consisting of voltage source converters (VSCs) and voltage source inverters (VSIs) has been analysed using the generalised Nyquist criterion (GNC). The output impedance of the source converter and the input impedance of the load converter were derived in the *dq* frame before the GNC was applied. The synchronisation instability in a VSC system was analysed in [123] with the impedance-based approach. Using a small-signal mode of phase-locked loops (PLLs), the grid-tied inverters' impedance was derived. It was shown that a proper PLL design of the VSI can play an important role in stabilising the system. In [124] the impedance-based analysis was employed in the islanding detection of a grid-tied VSI system. The minor loop gain was derived using the output impedance of the source subsystem and input impedance of the load subsystem. Reference [125] presented the analysis of a *dq* small-signal impedance of grid tiered inverters. The negative incremental resistive characteristic of q-q channel impedance was shown and the effect of PLL bandwidth on the system stability under weak grid conditions was discussed.

This thesis uses the Nyquist criterion based impedance method to analyse the system stability. Chapters 5 and 6 will present the impedance based stability analysis in detail.

2.8 Chapter Summary

This chapter reviewed the evolution of aircraft electrical power systems including power generation, distribution and utilisation. The different electric power generation options are highlighted and reviewed. The candidates of the power generation system, electric machines for the starter/generator have been presented and compared. The AEGART project is reviewed and the control strategy is explained in detail.

In addition, this chapter provides a review of the control strategies of the DC power system and power sharing methods among the parallel generation sources. According to the requirements of the communication link, centralised control, distributed control and decentralised control are presented and discussed. A

comparison between the three control approaches is listed. As one can see, a Digital Communication Link (DCL) is required for centralised and distributed control. This will reduce the reliability of both control strategies. Especially for the centralised control, the potential single point of failure exists in the centralised controller.

Considering all this, it can be clearly seen that decentralised control can achieve high reliability, modularity and only depends on the local variables. It is perceived to be a highly effective methodology for mitigation of source contingencies and communication breakdown.

Table 2-2 Comparison among different control approaches

	Centralised control	Distributed control	Decentralised control
Communication medium	DCL	DCL	Power line
Centralised controller	Yes	No	No
Modularity	Low	High	High
Reliability	Low	Medium	High
Single point of failure	Yes	No	No
Advantages	Proper coordination and leadership	Improved immunity to single point of failure	Local measurement and regulation
Disadvantages	Single point of failure	Complex interaction network	Lack of global information

The stability issue caused by the CPL is highlighted here and dominant approaches for stability analysis are introduced in this chapter. Large signal stability using the

Lyapunov-based approach and small signal stability using eigenvalues and impedance-based methods are analysed and reviewed in this chapter.

The Middlebrook criterion is very design oriented and has infinite phase margin, which is the most conservative criterion. The GMPM criterion is less conservative than the Middlebrook criterion since it defines a smaller forbidden region. The Opposing Argument Criterion is applicable to systems with multiple loads. Both methods provide design criteria for load impedance for a given source impedance. The ESAC criterion provides a less conservative stability with a desired gain and phase margin. It has been shown to be less sensitive to component grouping. However, it does not provide easy design formulation and a computer toolbox is needed to conduct the stability analysis.

It is worthy to be noted that all the abovementioned stability criteria offer sufficient conditions for system stability. In other words, when the criteria are met, the system is stable. However, the system can be still stable when the criteria are violated.

Alternatively, the Nyquist criterion offers the sufficient and necessary conditions for system stability. It means that if/when the Nyquist criterion is violated, the system is unstable. Therefore, in the subsequent stability analsysis in Chapter 5 and 6, the Nyquist criterion is utilized to analyse system stability.

Overall, this chapter addressed the challenges of the power system under study and presented the state-of-art research covering the power system’s architecture, power management, and stability assessment.

Chapter 3 Modal Analysis of the DC Electrical Power System

This chapter will perform the modal analysis of the single-bus based DC electrical power system using the participation factor and eigenvalue sensitivity. Based on the developed small signal state-space model, an overview of the impact of the key parameters on the stability is presented and the importance of cable modelling is investigated in the chapter, laying the foundation of the necessarity of cable modelling in the subsequent chapters.

3.1 Introduction

The modal analysis method [126]-[131] such as participation factor, damping ratio and oscillation frequency provides an efficient tool to identify the physical nature of modes, extract the critical modes and analyse the dynamic response of the system. It has been widely applied to power grids [126] and doubly-fed induction generator (DFIG) based wind power generation systems [127]-[131]. Participation factor analysis is beneficial for identifying the mode type and for analysing the participation degree of state variables on the given eigenvalues [128], [131].

As discussed in Chapter 2, the eigenvalues-based method can be utilised to analyse system stability. System stability can be judged by the location of all the eigenvalues. However, in order to get the small signal stability information of a wide range operation scenario the repetitive eigenvalues calculation needs to be performed according to different operating points. This is not a convenient and efficient solution for small signal stability analysis.

In contrast, eigenvalue sensitivity analysis which avoids repeat computation for the eigenvalues with varying parameters, has wide applications in power system modeling and analysis [132]-[138]. This method not only predicts the movement of the dominant modes of the system but also reduces the computation burden, especially in a large-scale power system. The eigen-sensitivity theory was introduced in [132] and was used as a small signal stability assessment tool in a turbine/governor system. In [134] comprehensive modal analysis including participation factor and eigenvalue sensitivity analysis with respect to machine and control parameters is performed for a DFIG-based wind turbine system. In [135] the small signal stability of an EPS with increased photovoltaic (PV) generation is examined using eigenvalue sensitivity with respect to system inertia. It shows that increased PV and DFIG-based penetration generation may render the system unstable as the damping of the critical modes is reduced. The study of sensitivity provides useful guidance for analysis, planning, and operation of power systems. It was successfully applied for optimal tuning of control parameters [136], [137], determining the locations of compensating devices, for damping improvement and stability enhancement such as capacitor compensation and FACTS devices [138].

Reference [97] presents the large-signal stability analysis of a hybrid AC-DC power system. An 18-pulse ATRU is used instead to realise the rectification from AC to DC. The EPS shown in [97] is different from the power system under study in this thesis. Hence, one cannot simply apply the results obtained from [97] to this chapter.

Permanent magnet machines have been widely used in aircraft and hybrid electric vehicles due to their high power density, high efficiency, fast dynamic response and improved reliability. Compared to a DFIG-based generation system, permanent magnet synchronous generators (PMSGs) have some unique properties which can be summarised as below:

1) a constant flux linkage is established by the permanent magnets,
2) control strategies for high speed PMSG-interfaced converters are also different,
3) varying machine speeds, which define the generated AC frequency and may impact the system stability,

4) transmission lines are not negligible in such MG structures and may influence the system dynamic and steady-state performance.

Thus the effect of abovementioned factors on stability is uncertain without systematic analysis. One cannot simply apply the results obtained from a DFIG system to the targeted PMSG-based MEA EPS. Several publications have studied the stability of the EPS in the MEA using small-signal analysis [139]-[141]. In [140] small signal stability analysis of a hybrid EPS for the MEA is presented. The effect of control bandwidth, circuit component parameters and operating conditions on stability is discussed using the eigenvalue loci. However, the eigenvalues need to be calculated repetitively with varying parameters. So far there are few published reports dealing with comprehensive modal analysis using eigenvalue sensitivity and participation factors for the MEA EPS, especially for the potential DC EPS. A systematic analysis and a design framework are required to ensure EPS stability, desired performance and robustness. To fill this gap, this chapter will investigate the importance of the cable modelling in stability analysis looking at the system mode's behaviour [142].

3.2 System Modelling

The example MEA EPS architecture with DC-distribution used for this initial study is shown in Figure 2.14. It includes two main PMSGs off-taking power from the main engine and APU-driven PMSG. Depending on the flight scenario and EPS operational regime the system can be operated with only one active source, or with multiple sources feeding the same DC bus. Before moving to the complex system with multiple generators, it is necessary to investigate the system characteristics with single source as shown in Figure 3.1. The PMSG provides power through an active front-end (AFE) rectifier, utilises the engine mechanical power and converts it to the electric power to supply the EPS DC bus. The detailed control strategy is discussed in Section 2.2.5. The on-board loads are represented by a combination of conventional resistive loads and by CPLs typically driven by tightly controlled power-electronic, as overviewed in Section 1.3.2.

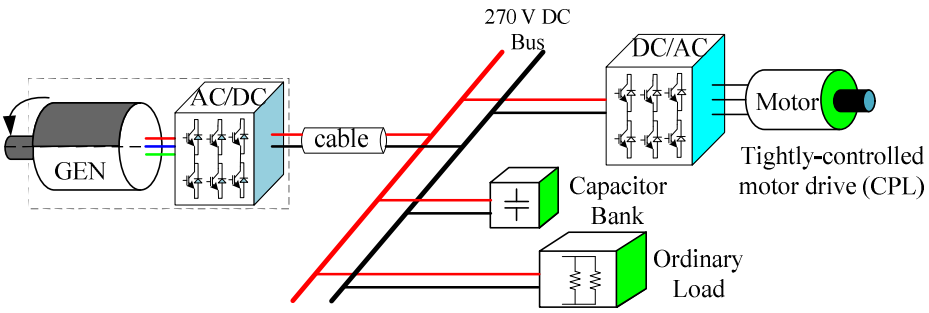

Figure 3.1. Configuration of the studied system in the MEA.

Non-switching functional models of the EPS will be developed in the subsequent subsections.

3.2.1 PMSG Model

The PMSG has been modelled synchronously and a rotating reference frame has been widely adopted for electric machines modelling, including PMSG [143], [144]. The dynamic equations for PMSG in the *dq* frame are as follows [145]:

$$\begin{cases} \dfrac{di_d}{dt} = \dfrac{1}{L_d}(-v_d - R_s i_d + \omega_e L_q i_q) \\ \dfrac{di_q}{dt} = \dfrac{1}{L_q}(-v_q - R_s i_q - \omega_e L_d i_d - \omega_e \phi_m) \end{cases} \tag{3-1}$$

where v_d, v_q: *d*-axis, *q*-axis component of stator voltage; i_d, i_q: *d*-axis, *q*-axis component of stator current; L_d, L_q: *d*-axis, *q*-axis inductance; R_S: stator resistance; φ_m: flux linkage of permanent magnet; ω_e: electrical rotor angular velocity.

In this study, a surface-mounted PMSG is used, thus the machine inductances in the *d*-axis and *q*-axis are identical ($L_d = L_q = L_S$) [146]. The machine speed and torque (i.e. *q*-axis current) will define the *d*-axis current in order to limit the machine voltage by appropriate defluxing.

Maximum allowable phase currents are determined by the inverter and machine ratings. Maximum voltage is dependent on the available DC-link voltage and modulation method. The voltage and current limitations can be written as follows by neglecting stator resistance and the transient terms [145]:

$$\begin{cases} \omega_e \sqrt{(L_s i_q)^2 + (L_s i_d + \varphi_m)^2} \le v_c^{\max} \\ \sqrt{i_d^2 + i_q^2} \le i_c^{\max} \end{cases} \tag{3-2}$$

where $v_c^{\max}$ and $i_c^{\max}$ are the maximal phase voltage amplitude at the fundamental frequency and maximal phase current, respectively.

3.2.2 Converter Model

The converter is also modelled in *dq* frame. The converter's AC voltage v_c can be expressed as follows:

$$v_c = \sqrt{v_d^2 + v_q^2} \tag{3-3}$$

As shown in Figure 3.2(a), the *d*-axis and *q*-axis components of the AFE AC-side terminal voltage can be written as [147]:

$$v_d = \frac{1}{2} m_d v_{dci}, \quad v_q = \frac{1}{2} m_q v_{dci} \tag{3-4}$$

where m_d, m_q are the modulation indices in corresponding directions.

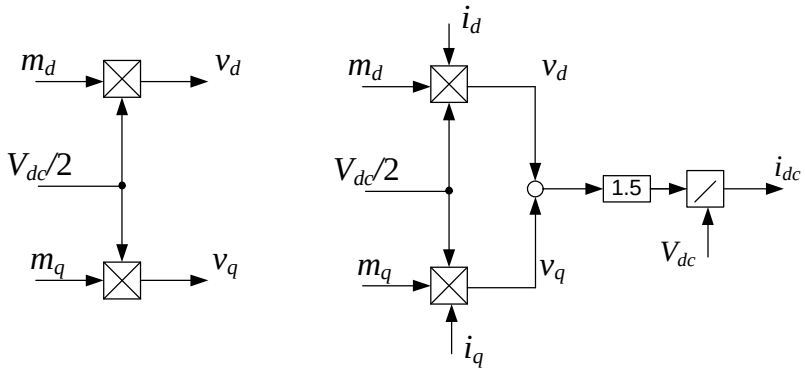

Figure 3.2. Model of the two-level AFE in *dq*-frame [147].

The AC-side terminal real power of the two-level AFE can be formulated as

$$P = \frac{3}{2}(v_d i_d + v_q i_q) \tag{3-5}$$

If neglecting the power losses of the converter, as shown in Figure 3.2(b), the power

balance between the DC and AC side yields:

$$v_{dc} i_{dc} = \frac{3}{2}(v_d i_d + v_q i_q) \tag{3-6}$$

where i_{dc} is the output DC current flowing into the capacitor.

3.2.3 DC-Link Model

The dynamics on the DC-link (see Figure 2.10) can be expressed as:

$$\frac{dv_{dc}}{dt} = \frac{1}{C_1}(i_{dc} - i_o)\,. \tag{3-7}$$

If the impedance of the DC cable between the converter and the main DC bus is ignored, v_{dc} is equal to the main bus voltage (v_b). The nominal voltage of the main bus is 270V, but the acceptable steady state range is between 250V and 280V as defined in MIL-STD-704F [33]:

$$250\,\mathrm{V} \le V_b \le 280\,\mathrm{V} \tag{3-8}$$

3.2.4 Load Model

As mentioned above, the load is represented by a combination of resistive load and constant power load:

$$P_L = P_{res} + P_{cpl} = \frac{v_b^2}{R_{res}} + P_{cpl} \tag{3-9}$$

where P_{cpl} and P_{res} are the total power of the CPL and resistive load, respectively. Hence, one can derive:

$$i_o = \frac{v_b}{R_{res}} + \frac{P_{cpl}}{v_b} \tag{3-10}$$

3.2.5 Overall Model

Figure 3.3 shows the control block diagram of the PMSG-AFE. $X_{vci}, X_{ioi}, X_{idi}, X_{iqi}$ are the states associated with the PI controllers for the flux weakening, DC current, and *dq*-axes current controllers, respectively:

$$\begin{cases} \dot{X}_{vci} = v_c^{\max} - v_c \\ \dot{X}_{ioi} = i_o^* - i_o \\ \dot{X}_{idi} = K_{vci} X_{vci} + K_{vcp} v_c^{\max} - K_{vcp} v_c - i_d \\ \dot{X}_{iqi} = K_{ioi} X_{ioi} + K_{iop} i_o^* - K_{iop} i_o - i_q \end{cases} \tag{3-11}$$

Here i_o is the load current (from the bus capacitor); i_o^* is the reference of the DC current calculated by droop; K_{vci}, K_{vcp}, K_{ioi} and K_{iop} are the integral gains and proportional gains for the flux weakening controller, and DC current controllerrespectively (see Table 3-1).

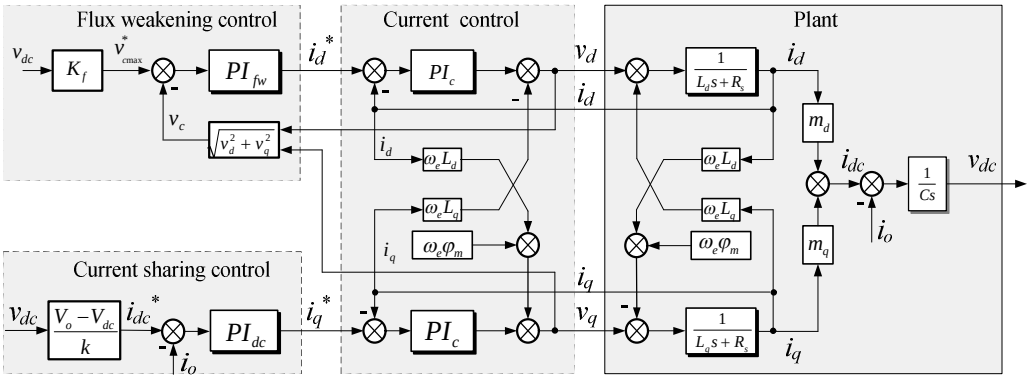

Figure 3.3. Control block diagram of the PMSG-AFE.

From (3-5)-(3-12), a set of state equations to represent the entire system can be established as:

$$\dot{X} = f(X, U) \tag{3-12}$$

where X and U are the vectors with respect to the state and input variables which are defined as $X=[v_{dc}, i_d, i_q, X_{vci}, X_{ioi}, X_{id}, X_{iq}]^T$. The nonlinear system equations are linearised around the equilibrium point to obtain a set of linearised dynamic equations. They can be formulated in state-space as follows:

$$\dot{\hat{X}} = A\hat{X}. \tag{3-13}$$

The derived system matrix A is of the 7th order and is shown in Appendix B. The system represented by (3-13) does not take the DC cable into consideration. However, in many practical cases the DC cable impedances cannot be neglected, especially in low voltage DC power networks. The simplified equivalent single line diagram of the EPS with cable included is depicted in Figure 3.4. Since the parasitic capacitance is much smaller than the bus capacitance (C_b) and the local capacitance (C_1), the cable parasitic capacitance can be combined with the local capacitance of the converter. Thus the cabling can be represented by series R_C-L_C branch [148]. Two more state variables (the line current i_{Lc} and bus voltage v_b) are added to the entire system and the corresponding equations can be derived:

$$\begin{cases} \dfrac{di_{Lc}}{dt} = \dfrac{1}{L_c}(v_{dc1} - R_c i_{Lc} - v_b) \\ \dfrac{dv_b}{dt} = \dfrac{1}{C_b}(i_{Lc} - i_o) \end{cases} \tag{3-14}$$

where v_{dc1} and v_b are the voltage across the local capacitor and bus capacitor, respectively.

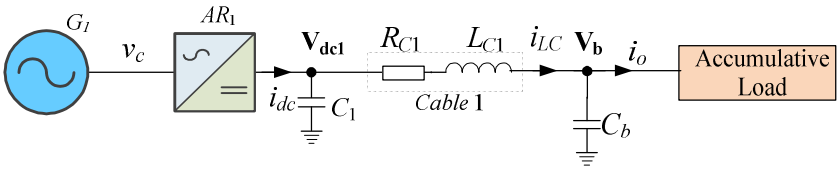

Figure 3.4. Equivalent single line diagram of the EPS with cabling included.

In this sense, the whole system shown in Figure 3.4 (with cabling included) becomes of the 9th-order and can be formulated as

$$\dot{\hat{X}}_C = A_C \hat{X}_C \tag{3-15}$$

where the vector of state variables is X_C=[v_{dc1}, v_b, i_{Lc}, i_d, i_q, X_{vci}, X_{ioi}, X_{id}, X_{iq}]^T and the system matrix $\boldsymbol{A_C}$ is as follows:

$$A_C = \begin{bmatrix} A & F_1 & F_2 \\ L & -\dfrac{R_{c1}}{L_{c1}} & -\dfrac{1}{L_{c1}} \\ 0 & \dfrac{1}{C_b} & -\dfrac{1}{C_b} * ((\dfrac{2}{R_{res}} - \dfrac{P_{cpl}}{V_b^2})) \end{bmatrix} \quad (3\text{-}16)$$

Here L=[1/L_{C1}, 0, 0, 0, 0, 0, 0], and F_1, F_2 are the column vectors consisting of control parameters and operating points. The full matrix is reported in Appendix B.

3.3 Modal Analysis

In practice, the system parameters such as generator and cables inductances and resistances, bus capacitors and EPS operating conditions (machine speed, load power, etc) vary during operation. Any such change affects the elements of the system matrix and consequently influences the eigenvalues. To obtain the eigenvalue change tendency, eigenvalues can be calculated repetitively with respect to specific parameter variations. Alternatively, in order to estimate the eigenvalue change tendency without calculating the eigenvalues repetitively, a sensitivity analysis can be applied as a convenient tool. This subsection deals with a comprehensive modal analysis of the generalised EPS architecture to show the influence of some key parameters on the stability.

Eigenvalues calculated from the state matrix may be real or complex. The complex eigenvalues can be expressed in conjugate pairs as follows:

$$\lambda_i = -\sigma_i \pm j\beta_i . \quad (3\text{-}17)$$

The damping ratio and oscillation frequency corresponding to mode λ_i (i^{th} eigenvalue) can be defined as

$$\xi_i = \frac{\sigma_i}{\sqrt{\sigma_i^2 + \beta_i^2}}, \quad f_{osci} = \frac{|\beta_i|}{2\pi} . \quad (3\text{-}18)$$

Participation factor analysis aids the identification of how each state variable affects

a given mode. It is a measure of the relative participation of the k^{th} state variable in i^{th} mode and can be computed from the eigenvector matrices as follows [127]:

$$p_{ki} = \frac{|w_{ki}||v_{ik}|}{\sum_{k=1}^{n}|w_{ki}||v_{ik}|} \tag{3-19}$$

where w_{ki} is the k^{th} element in the left eigenvector corresponding to the i^{th} eigenvalue and v_{ik} is the k^{th} element in the right eigenvector corresponding to the i^{th} eigenvalue. In general, the participation degree of the k^{th} variable in the i^{th} mode is measured by p_{ki}. As discussed in [134], p_{ki} can also be regarded as the sensitivity of λ_i with respect to the k^{th} diagonal element of the state matrix [126].

Eigenvalue sensitivity is used to measure the rate and direction of the mode movement due to variations in system parameters. The eigenvalue sensitivity of a mode (λ_i) with respect to an uncertain parameter μ can be calculated as follows:

$$\frac{\partial\lambda_i}{\partial\mu} = \frac{w_i^T(\partial A/\partial\mu)v_i}{w_i^T v_i} \tag{3-20}$$

where w_i is the left eigenvector corresponding to eigenvalue λ_i and v_i are the right eigenvector corresponding to eigenvalue λ_i, respectively.

The nominal system parameters used in this analysis are given in Table 3-1.

Table 3-1 The EPS Parameters

Category	Parameter	Symbol	Value
PMSG	Machine resistance	R_S	1.058 mΩ (1 p.u.)
	Machine	L_S	99 μH (1 p.u.)
	Permanent magnet	φ_m	0.03644 V*s/rad (1 p.u.)
	Number of poles	p	6
Cable	Local capacitor	C_1	1 mF
	Cable resistor	R_C	3 mΩ (0.6 mΩ/m)
	Cable inductor	L_C	1 μH (0.2 μH /m)
Main bus	Bus capacitor	C_b	0.5 mF
Droop characteristic	Nominal voltage	V_o	270 V
	Droop slope	k_D	8.5
Stator current loop	Proportional gain	K_{idp}, K_{iqp}	0.8785
	Integral gain	K_{idi}, K_{iqi}	3908
Flux weakening control	Proportional gain	K_{vcp}	0
	Integral gain	K_{vci}	5000
DC current control	Proportional gain	K_{iop}	0.4
	Integral gain	K_{ioi}	600

Table 3-2 lists the eigenvalues of the studied system and the corresponding damping ratio and oscillation frequency for each mode. From this table, it is obvious that for selected operational points the modes $\lambda_{1,2}$ are poorly damped and are the dominant modes in the system response. Table 3-3 illustrates the participation factor of the state variables.

Table 3-2 Eigenvalues, damping ratio and oscillation frequency of the studied system with cables

Mode	Eigenvalue	Damping ratio	Oscillation f_{osc}(Hz)
$\lambda_{1,2}$	-193.7±52355i	0	8333
$\lambda_{3,4}$	-5429±7719i	0.58	1229
$\lambda_{5,6}$	-2910±4838i	0.52	770
$\lambda_{7,8}$	-1797±1507i	0.77	240.3
λ_9	-1871	1	0

Table 3-3 Participation factors of the studied system with cables

Mode	$\hat{v}_{dc1}$	$\hat{v}_b$	$\hat{i}_{Lc}$	$\hat{i}_d$	$\hat{i}_q$	$\hat{X}_{vci}$	$\hat{X}_{ioi}$	$\hat{X}_{idi}$	$\hat{X}_{iqi}$
$\lambda_{1,2}$	0.13	0.34	0.48	0	0.03	0.01	0	0	0
$\lambda_{3,4}$	0.07	0.09	0	0.17	0.22	0.12	0.02	0.15	0.14
$\lambda_{5,6}$	0.07	0.06	0	0.2	0.23	0.08	0.03	0.14	0.19
$\lambda_{7,8}$	0.22	0.15	0	0.07	0.04	0.08	0.31	0.02	0.1
λ_9	0.08	0.05	0	0.21	0	0.33	0.25	0.08	0.01

It is seen that the DC state variables (v_{dc1}, i_L, v_b) exhibit substantial participations in the dominant modes, whereas the other states participate in $\lambda_{1,2}$ weakly. Cable parameters have a direct influence on the DC state variables: this explains why the cable impedance has a strong influence on the modes $\lambda_{1,2}$. The effect of cable impedance is assessed in the following subsection, together with the other aforementioned parameters.

3.3.1 Effect of Cable Impedance

Considering the distribution distance from the generators to the main distribution bus, the cable length is around 5 m. Nominal values of cable resistance and inductance are defined as 0.6 mΩ/m and 0.2 μH/m respectively [110]. Table 3-4 lists the eigenvalue sensitivities with respect to the cable inductance and cable resistance (calculated by (17)). The 2nd column in the table shows the standardised unit for the eigenvalue sensitivities calculation corresponding to the variable in the 1st column. For instance, the eigenvalue sensitivities of modes $\lambda_{1,2}$ with regards to a 1 μH increment of L_C are 1569 ± 26440i. This value means that an increase of 1 μH inductance will shift the real part of the eigenvalue in a positive direction (+1569). Therefore, cable inductance has a significant adverse impact on stability as the eigenvalues $\lambda_{1,2}$ will move towards to the right half plane (RHP) at a fast rate with increased L_C. In contrast, an increment of cable resistance is helpful for stabilising the system as better damping is obtained and the dominant eigenvalues move further

left from the imaginary axis. Figure 3.5(a) and (b) illustrate the movement of the critical eigenvalues with respect to varying cable inductance and resistance. The dominant modes ($\lambda_{1,2}$) change significantly compared to the other modes. Increasing cable inductance (L_C) results in the system being less damped (the poles move towards the RHP). It can be clearly seen that the eigenvalue plots in Figure 3.5(a) and (b) match the aforementioned analysis (see Table 3-4).

Table 3-4 Eigenvalues sensitivities for single generator system with cables.

Variable	Standardised unit	$\lambda_{1,2}$	$\lambda_{3,4}$	$\lambda_{5,6}$	$\lambda_{7,8}$	λ_{9}
L_C	1 µH	1569±26440i	-62.9±3.75i	-7.14±10.4i	1.45±2.41i	0.055
R_C	1 mΩ	-506.4±27.93i	5.2±3.7i	1.6±0.11i	0.022±0.026i	-0.46
L_S	1 µH	-22.99±0.4i	68.56±26.94i	22.57±3.1i	4.31±2.51i	9.5
R_S	1 mΩ	-7.55±21.09i	1.72 ±4.86i	-7.8±0.31i	2.47±4.64i	-5.4
φ_m	1 mV*s/rad	60.2±50.7i	-10±88.6i	-0.6±25.9i	-25.37±1.974i	19.9
K_{vcp}	1	-3280.2±8118.6i	8400.54±447.1i	-330.99±605.52i	1379.84±922.2i	-1614.2
K_{vci}	1	-0.05±0.02i	-0.13±0.56i	-0.24±0.09i	0.11±0.14i	0.14
K_{iop}	1	20.03±5040.51i	-100.83±2949.25i	1549.4±3035.6i	-4287.54±943.8i	5637.96
K_{ioi}	1	-0.08±0.02i	0.52±0.31i	0.4±0.10i	0.38±1.56i	-2.45
C_b	1 mF	225.44±87093i	-4404.5±1887.96i	-974.8±1094.77i	1324.5±494.12i	-424
P_{cpl}	1 W	0.01±0.06i	-0.02±0.00i	0.01±0.02i	-0.01±0.00i	0.01
P_{res}	1 W	-0.03±0.06i	-0.02±0.02i	0.01±0.03i	-0.02±0.01i	0.01
ω_e	1 rad/s	0.2±0.26i	0.06±0.02i	-0.3±0.11i	-0.01±0.07i	0.08

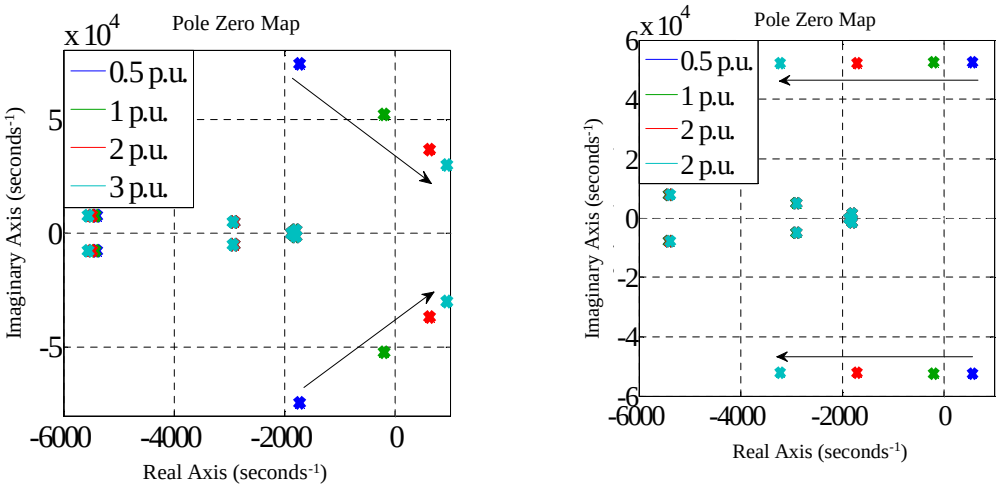

(a) (b)

Figure 3.5. Eigenvalue movement with respect to cable impedance variation. (a) Cable inductance (L_C) variation. (b) Cable resistance (R_C) variation.

3.3.2 Effect of Generator Parameters

The key parameters of the PMSG considered are the synchronous inductance (L_S), stator resistance (R_S) and flux linkage of permanent magnet (φ_m).

(1) Synchronous Inductance

As shown in Table 3-4, the eigenvalue sensitivities of modes $\lambda_{1,2}$ with regard to a 1 µH increment of L_S are -22.99 ± 0.4i. In other words, an increase of 1 µH inductance will shift the real part of the eigenvalue in a negative direction by -22.99. Hence, the EPS will be better damped and its stability margin will increase.

(2)Stator Resistance

From the results shown in Table 3-4, it can be concluded that the effect of PMSG resistance is not significant since the sensitivities of all eigenvalues with respect to R_S are relatively small compared to L_S. In other words, the eigenvalues are almost identical for differing R_S values. This can be explained by the fact that the stator resistance is typically quite small hence the voltage drop due to the stator resistance is much smaller than the voltage of coupling terms in (3-1). Thus its contribution to the operating point is insignificant compared to the machine inductance.

(3)Flux Linkage of Permanent Magnet

A small increment of flux linkage will significantly compromise the damping since the dominant modes ($\lambda_{1,2}$) will move towards RHP. It can be inferred from (3-2) that a more negative i_d is needed to keep the AC side voltage (V_c) constant in the high speed region if φ_m is increased. It is obvious that φ_m cannot be decreased arbitrarily for a manufactured machine; however this result may be useful for designers of electric machines for MEA EPS applications.

In summary, from the results in Table 3-4, it can be concluded that the machine parametric uncertainties, or parameter variations, significantly influence the EPS stability (except of stator resistance variations). The system stability margin improves with the increase of the machine inductance. On the other hand, a small decrease in the permanent magnet flux improves the stability margin of the entire system.

The eigenvalue sensitivity analysis above with respect to cable resistance and inductance is confirmed by the pole movement plots above shown in Figure 3.5. Figure 3.6 and Figure 3.7 show the eigenvalue plots with regard to varying synchronous inductance and permanent magnet flux linkage, respectively. It can be seen in Figure 3.6 that the dominant modes move to the left with increased L_S. Hence, the increase of *Ls* improves the stability margin, as is indicated by the eigenvalue sensitivity. On the contrary, the critical eigenvalues move into the RHP if the flux linkage of the permanent magnet is increased (see Figure 3.7). The eigenvalue plots match well to the detailed sensitivity analysis above (see Table 3-4). Again, this demonstrates the feasibility and efficiency of the eigenvalue sensitivity analysis. The pole movement with respect to the stator resistance variation is shown in Figure 3.8. The movement rate is much slower compared to the pole movement shown in Figure 3.6 and Figure 3.7. Again, this agrees with the values listed in Table 3-4.

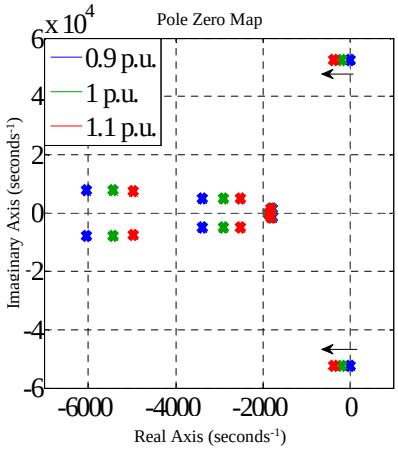

Figure 3.6. Eigenvalue loci with respect to varying synchronous inductance.

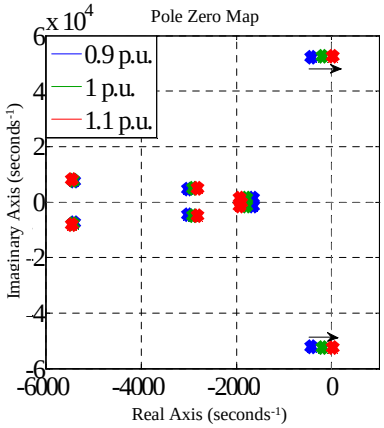

Figure 3.7. Eigenvalue loci with respect to varying flux linkage of permanent magnet.

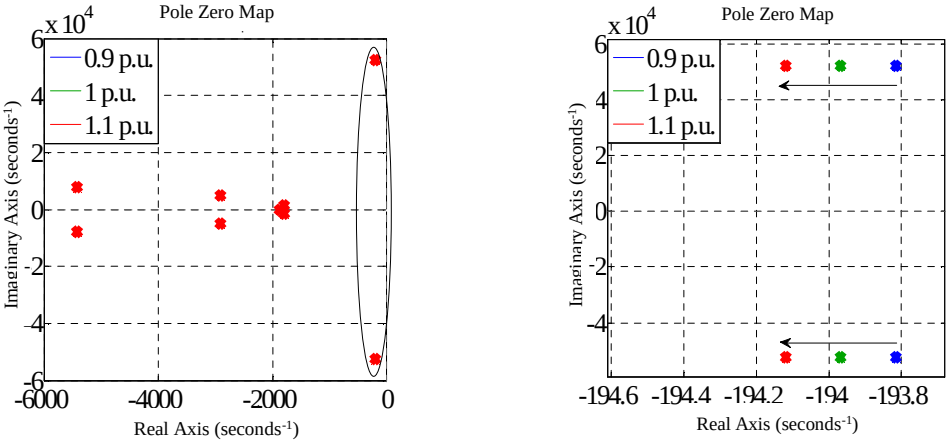

(a) (b)

Figure 3.8. Eigenvalue loci with respect to varying stator resistance. (a) overview. (b) zoomed area of dominant poles.

3.3.3 Effect of Control Parameters

Due to the required fast dynamic response of the core system shown in Figure 2.10 in Subsection 2.2.5, the inner current loops (i_d, i_q loops) are designed with a 1 kHz bandwidth and a 0.707 damping factor. Thus the analysis in this chapter is focused on flux-weakening control and DC current control. Table 3-4 displays the eigenvalue sensitivities with regard to the flux weakening (FW) controller parameters (proportional K_{vcp} and integral K_{vci} gains), and the DC current controller (K_{iop}, K_{ioi}). A small increment in the proportional gain of K_{vcp} leads to $\lambda_{1,2}$ shifting to the left. However, the increase of K_{vcp} is limited by the movement of $\lambda_{3,4}$ to the right hence limiting the stability margin. In the case of the DC current controller, the dominant modes will move towards the RHP with increase of K_{iop}. Overall, one can conclude that the proportional gains of the flux weakening and DC current controllers have a significant impact on the EPS stability.

3.3.4 Effect of Operating Parameters

Load power and generator speed are the key factors defining the EPS operating conditions. Their effects are analysed and the results given in Table 3-4. It can be seen that higher speed operation deteriorates the system's stability margin as $\lambda_{1,2}$ and $\lambda_{3,4}$ move towards the RHP with the increase of machine speed. The less damped modes, $\lambda_{1,2}$, will approach the RHP if the load power is increased. This matches with the well-known CPL property to compromise the EPS stability [91].

3.4 EPS Modal Analysis with Cables Neglection

In many research studies, cables are often neglected in order to simplify the modelling. However, it is still not evident whether this simplification would reflect the system's behaviour correctly. This subsection demonstrates that this assumption may lead to inaccurate and even incorrect conclusions. In order to show this, the EPS model without cabling has been derived from (3-1) to (3-11) in Section 3.2. Following this, it has been reassessed using the procedure similar to one used in Section 3.3. Based on the matrix in (3-13), the eigenvalues, the relevant damping

ratios and the oscillation frequencies are summarised in Table 3-5. In addition, Table 3-6 illustrates the corresponding participation factors. It can be seen that mode $\lambda_{1,2}$ is the least damped one (see Table 3-5) and is mainly associated with the DC link voltage and *q*-axis current. The mode $\lambda_{3,4}$ is more associated with the *d*-axis current and λ_7 is related to the FW controller and DC current controller.

Table 3-5 Eigenvalues of the studied system without cables

Mode	Eigenvalue	Damping	Oscillation f_{osc} (Hz)
$\lambda_{1,2}$	-1765 ± 10836i	0.16	1724
$\lambda_{3,4}$	-2823 ± 6034i	0.42	960
$\lambda_{5,6}$	-3034 ± 660i	0.98	105
λ_7	-1556	1	0

Table 3-6 Participation factors of the studied system without cables

Mode	$\hat{v}_{dc}$	$\hat{i}_d$	$\hat{i}_q$	$\hat{X}_{vci}$	$\hat{X}_{ioi}$	$\hat{X}_{idi}$	$\hat{X}_{iqi}$
$\lambda_{1,2}$	0.27	0.09	0.31	0.1	0.04	0.05	0.13
$\lambda_{3,4}$	0.05	0.38	0.06	0.18	0.01	0.24	0.08
$\lambda_{5,6}$	0.17	0.02	0.07	0.13	0.18	0.17	0.25
λ_7	0.08	0.1	0	0.1	0.7	0.02	0

Table 3-7 lists the eigenvalues sensitivities for the system without cables. It can be observed that the influence of some parameters on stability are the opposite of those found previously with cabling included, as will be discussed below.

Table 3-7 First-order eigenvalues sensitivities for single generator system without cables

Variable	Standardized unit	$\lambda_{1,2}$	$\lambda_{3,4}$	$\lambda_{5,6}$	λ_{7}
L_S	1 μH	70.4±64.85i	-6.84±12i	12.66±4.66i	1.16
R_S	1 mΩ	14.73±9.85i	-12.2±0.4i	1.65±5.51i	-3.67
φ_m	1 mV*s/rad	-33.68±200.73i	27.03±67.7i	-11.67±9.21i	10.84
K_{vcp}	1	12070.87±1852.2i	-178.46 ± 2411.1i	988.34 ± 543.24i	-1079.1
K_{vci}	1	0.07 ± 0.58i	-0.46 ± 0.11i	0.1 ± 0.05i	0.11
K_{iop}	1	5076.15±6544.32i	-577.36±3010.22i	-2907.7 ± 1408.3i	5537
K_{ioi}	1	1.24 ± 0.67i	0.03 ± 0.28i	-0.17 ± 1.71i	-2.19
C_i	1 mF	-1320.4±13176.1i	-3589.32±1772.45i	1751 ± 543.17i	-658
P_{cpl}	1 W	0.02 ± 0.04i	-0.02 ± 0.03i	0.02 ± 0.01i	-0.01
P_{res}	1 W	0.00 ± 0.02i	-0.01 ± 0.03i	-0.01 ± 0.02i	0.01
ω_e	1 rad/s	-0.27 ± 0.75i	0.18 ± 0.19i	-0.12 ± 0.08i	-0.03
k_D	1	350 ± 660i	-89.4 ± 2.22i	-40.24 ± 139i	0.82

3.4.1 Effect of Generator Parameters

In contrast to the system with cables included, the real part of the eigenvalue sensitivity of mode $\lambda_{1,2}$, with regards to the machine inductance (L_S), is now positive. Hence the system stability now degrades with an increase in stator inductance. As for the flux linkage, an increment of φ_m will now shift the eigenvalues to the left. This is contrary to the conclusions drawn from Table 3-4 for EPS when cables were taken into account.

3.4.2 Effect of Control Parameters

It is shown in Table 3-7 that the critical mode $\lambda_{1,2}$ quickly moves to the imaginary axis with even a small increment of K_{vcp}. In other words, a small increment in proportional gain for the FW controller will lead to instability. This is opposite to the cabled case in which a small K_{vcp} can stabilise the system (shown in Table 3-7).

3.4.3 Effect of Operating Parameters

As the machine speed affects the *d*-axis current when operating in the flux-weakening region, mode $\lambda_{3,4}$ is dominant since it is related to the machine speed. It can be seen that the participation factor of i_d in mode $\lambda_{3,4}$ is the largest among all the modes. Although increased machine speed renders less damping for $\lambda_{3,4}$, the damping of the critical modes $\lambda_{1,2}$ is increased. Overall, it is shown that the increment of the speed is beneficial for reinforcing the damping of the entire system. Note that this is opposite to the previous findings for the EPS when cabling is taken into account (Table 3-4).

3.5 Simulation Results

As discussed in [139], functional models (non-switching models) are well suited to tasks such as the investigation of EPS stability. Therefore, to support the analysis above, results of time-domain simulations are presented in this section. The model used has been developed in Section 3.2. The simulation scenario assumes the step-wise increase of load power each of 0.01 s as detailed in Table 3-8. Simulation studies have been carried out for the example EPS (defined in Section 3.2) with cables and without cables.

Table 3-8 Simulation events for CPL

Time (s)	Load (kW)	Time (s)	Load (kW)
0-0.01	0	0.05-0.06	41
0.01-0.02	10	0.06-0.07	42
0.02-0.03	20	0.07-0.08	43
0.03-0.04	30	0.08-0.09	44
0.04-0.05	40	0.09-0.10	45

3.5.1 Single Generator System without Cables

First, the simulations are carried out to test the system without cabling. The results to confirm the effect of the machine inductance (L_S) and permanent magnet flux linkage (φ_m) on EPS stability are shown in Figure 3.9 and Figure 3.10. The per unit values for the system are listed in Table 3-1. It can be seen from Figure 3.9 that if L_S is increased to 1.1 p.u. instability occurs when the load power exceeds 40 kW. However, under the same test, the system is stable with L_S set to 0.9 p.u.

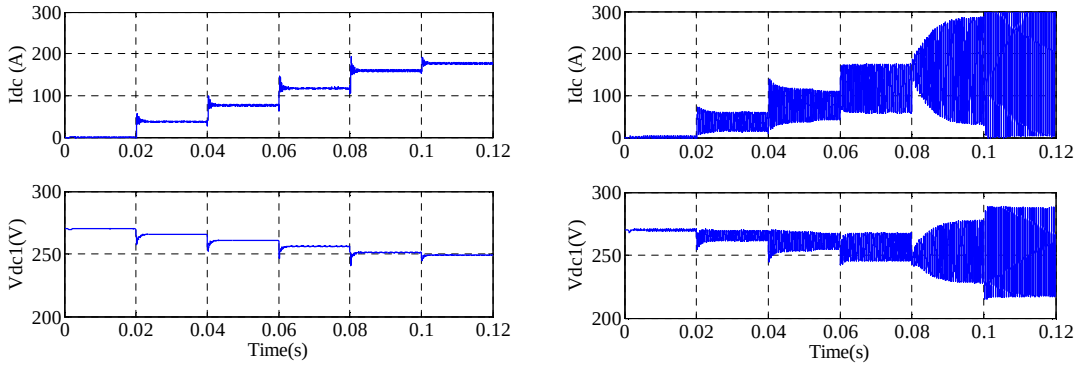

Figure 3.9. Simulation results for different machine inductances. (a) L_S = 0.9 p.u. (b) L_S = 1.1 p.u.

Figure 3.10 shows the results for variation of the permanent magnet flux linkage. It can be seen that at 0.9 p.u. the system becomes unstable under high load power (30 kW) whilst at 1.1 p.u. the system remains stable.

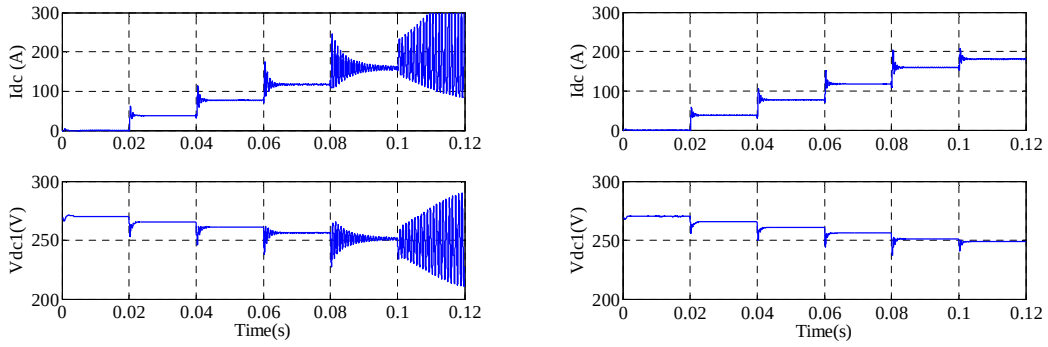

(a) (b)

Figure 3.10. Simulation results for different permanent magnet flux linkages. (a) φ_m = 0.9 p.u. (b) φ_m = 1.1 p.u.

Figure 3.11(a) and (b) show the dynamic responses obtained when varying the proportional gains of the FW and DC current controllers. As expected from the analytical analysis, the EPS is confirmed to be very sensitive to variations in the K_{vcp}. At t = 0.12 s instability occurs since K_{vcp} is increased from 0 to 3. From Fig. 12(b) it can be seen that the system becomes unstable when K_{iop} is increased from 0.4 to 0.8 at t = 0.14 s. It demonstrates that the increase of K_{vcp} and K_{iop} destabilises the system when the cabling is nelegcted as predicted from Table 3-8.

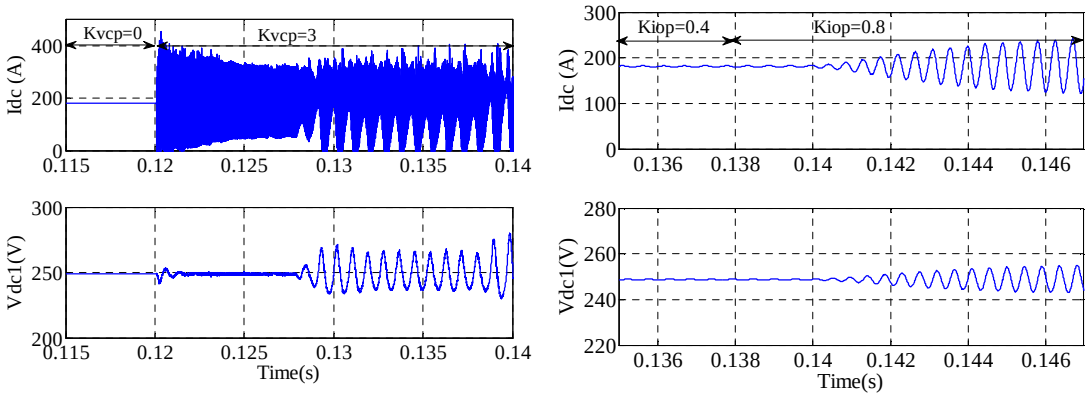

(a) (b)

Figure 3.11. Simulation results for control parameter variation (a). K_{vcp} is changed from 0 to 3. (b) K_{iop} is changed from 0.4 to 0.8.

Figure 3.12 shows the effect of generation speed on stability. In this case 0.5 mF is used for the local capacitor (C_1). Figure 3.12(a) shows the machine speed and the stator current in both *d* and *q* axes, while Figure 3.12(b) shows the DC link current

and voltage waveforms. Instability can be seen in Figure 3.12(a) at low generation speed (< 15 krpm), which confirms the findings in the analysis in Section 3.3.

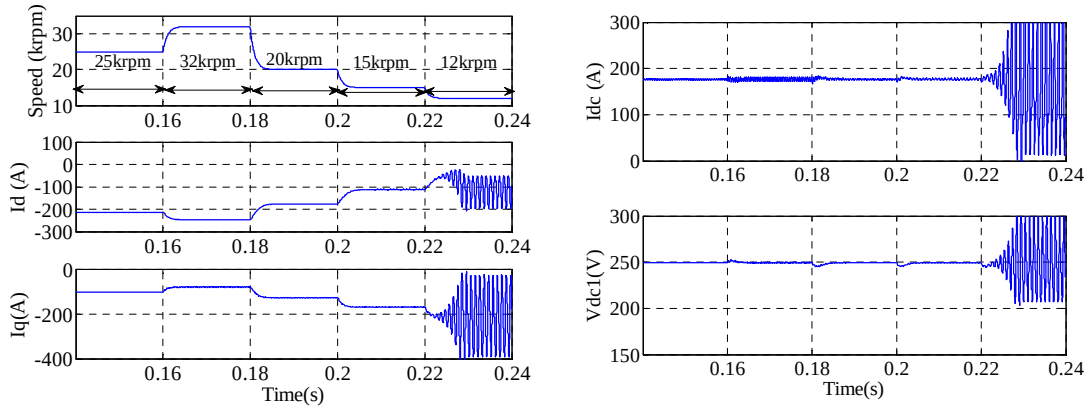

(a) (b)

Figure 3.12. Simulation results for machine speed variation (C_b = 0.5 mF). (a) machine speed and stator current in *dq* axes. (b) DC current and voltage.

3.5.2 Single Generator System with Cables

Simulations were also performed using the single generator EPS shown in Figure 3.4 with cables taken into account. Figure 3.13 and Figure 3.14 show the effect of the generator parameters on the EPS stability margins. The local capacitor (is set to 1 mF. A small bus capacitance (0.13 mF) is used within the example EPS model in order to demonstrate the effect of bus capacitance on system behaviour. Compared to the results in Figure 3.9, it can be seen that with L_S = 1.1 p.u, the system is stable when *Ls* is reduced to 0.9 p.u. the EPS becomes unstable under high loads. This is opposite to the case when cables are neglected and agrees with the expectations from the analysis in Subsections 3.3.2 and 3.4.1.

Figure 3.14 shows that the EPS with the flux of 0.9 p.u. remains stable under high power load, however if the flux is increased to 1.1 p.u. the EPS shows unstable behaviour under the loads close to full power (over t = 0.08 s in the simulation scenario). As before, this is contrary to the case when cables are ignored.

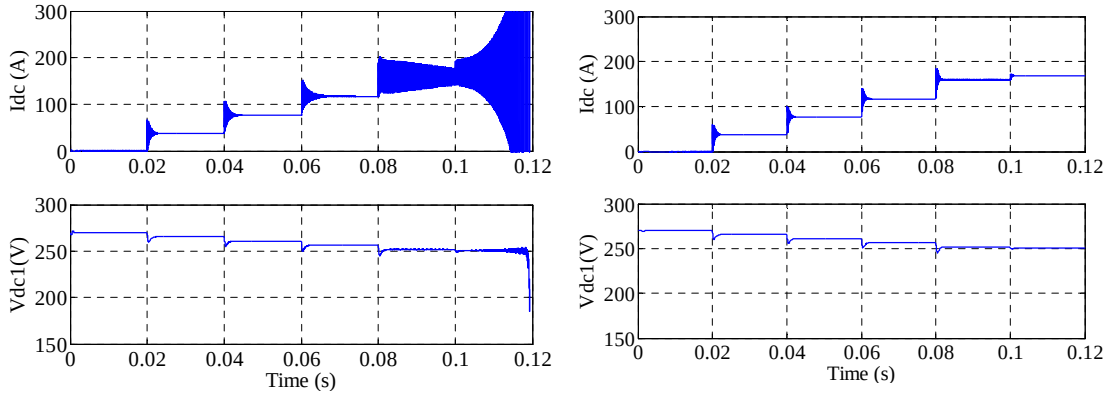

Figure 3.13. Simulation results for different machine inductances. (a) L_S = 0.9 p.u. (b) L_S = 1.1 p.u.

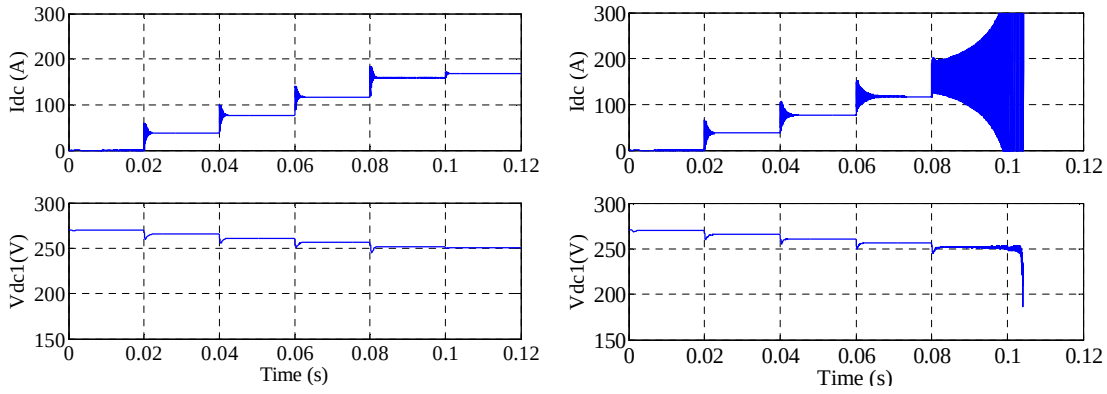

Figure 3.14. Simulation results for different permanent magnet flux linkages. (a) φ_m = 0.9 p.u. (b) φ_m = 1.1 p.u.

Figure 3.15 shows the results for a scenario with the generator speed gradually increased from 12 krpm to 32 krpm. It can be seen that in the high speed region the EPS is unstable. This, as in other cases, confirms the findings summarised in Table 3-4. Figure 3.16 demonstrates that the EPS can be stabilised at high speed by increased bus capacitance C_b (in the simulated case it has been increased to 0.5 mF). These simulation results emphasise that an appropriate bus capacitance should be carefully selected in order to establish appropriate damping of the entire EPS. This is consistent with the findings in subsection 3.3.4.

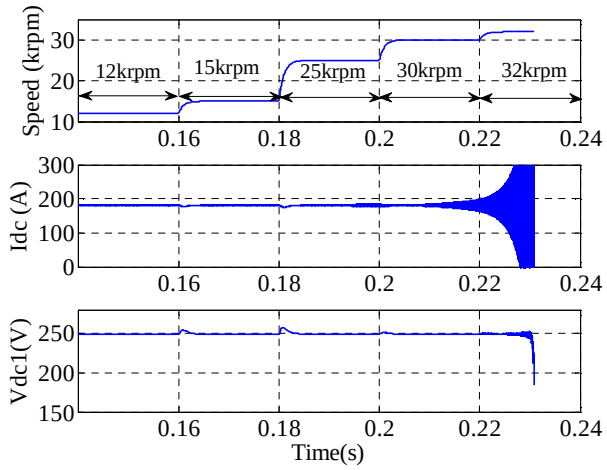

Figure 3.15. Simulation results for varying machine speeds (C_b = 0.13 mF).

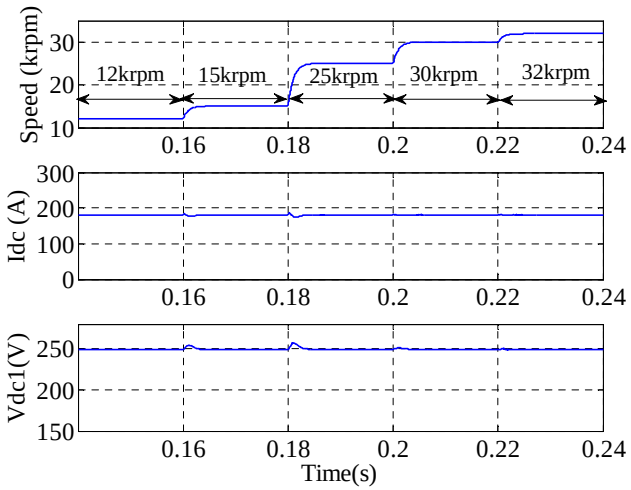

Figure 3.16. Simulation results for varying machine speeds (C_b = 0.5 mF).

3.6 Chapter Summary

A detailed modal analysis of a PMSG based MEA EPS has been performed in this chapter. The PMSG and PWM rectifier provide the electrical power from the primary source to the main DC bus. Analysis of participation factors, damping ratios and oscillation frequencies helps to understand the system characteristics. Within the analysis, the cable impedance was taken into consideration. The impact of different parameter variations on EPS stability was illustrated using the eigenvalue sensitivity. Unlike the conventional eigenvalue method which needs to calculate the system's eigenvalues according to each operating point, the applied method shows the

tendency of the eigenvalue's movement and significantly reduces the computation burden as repetitive calculation of eigenvalues is not needed. By utilisation of this technique, the effect of parameter variation on EPS behaviour, tendencies and direction of modal shift can be presented in a convenient and illustrative form. Generator parameters, control parameters and operating conditions were varied to demonstrate their effects on small signal stability. Time-domain simulations using a non-linear functional model of the example EPS have been carried out to verify analytical results.

The main finding of this chapter can be summarised as follows:

1) critical modes, which are identified by modal analysis, are mainly affected by DC state variables (DC voltage and current).

2) ignoring of EPS cables when analysing the system stability can lead to severely inaccurate results compared to the case when cables are duly considered by the EPS model.

3) the generator parameters, cable impedance, control parameters (control bandwidth, droop gain), and operating conditions (generator speed, load power) will affect the system stability. The increase of the cable inductance, flux linkage of permanent magnet, load power and generator speed will deteriorate the system stability whilist the appropriate increase of cable resistance and synchronous inductance will be beneficial to improve the stability. Chapters 5 and 6 will ananlyse the impact of key parameters in the frequency domain approach.

It can be concluded that in order to obtain accurate system characteristics, cable influence cannot be neglected. It proves that cable modelling is crucial to achieve satisfactory results as shown in the following chapters.

Chapter 4 Load Sharing Analysis

This Chapter reports the proposed droop control approaches in the multi-source based DC systems and analyses the steady-state performance of the load sharing under different droop approaches.

4.1 Introduction

Considering the studied future promising EPS architecture candidate (shown in Figure 2.17) with multiple sources and loads connected to the common bus, appropriate power sharing amongst the parallel sources is of concern. As discussed in Section 2.6, dominant control methods for power sharing can be grouped into three categories: centralised control, distributed control, and decentralised control. The common factor of the former two approaches is the need of communication among the parallel sources. The central controller and the presence of the communication line are vital for the system and the contingency of either one may result in the system failure. Therefore, recent research is focused on decentralised load sharing e.g., droop control [149] where parallel modules operate independently since no communication among them is needed. Since the outage of one source will not influence the normal operation of other modules, the system reliability is improved. Due to the absence of the communication link, the system cost could be reduced.

Existing droop control methods for voltage source converters (VSCs)-based DC MGs implement the basic concept of droop in different ways and can be grouped in two families namely current/power mode droop, including Current-Voltage (I-V) and Power-Voltage (P-V) strategies and voltage mode droop, including V-I and V-P

strategies. I-V/P-V droop controls the DC current/power depending on the DC voltage whilst V-I/V-P droop regulates the DC voltage based on the output current/power. Reference [151] and [152] show the system with I-V/P-V droop control whilst reference [153] and [171] present the usage of V-I/V-P droop control in a hybrid AC/DC microgrid. However, until now there are no reports to compare the abovementioned apporches in steady-state and dynamic performance.

This chapter will investigate the power sharing performance of different droop approaches. After addressing the importance of the cable modelling in a single source based EPS in Chapter 3, the DC distribution cable is taken into account and the effect of cable impedance on the sharing performance is also analysed.

4.2 Single Bus Multi-Source EPS Architecture

Figure 4.1 shows the studied topology of MEA EPS. It assumes that three sources (PMSGs) controlled by PWM active rectifiers (ARs) provide power to the 270V DC bus. The rated voltage of the main bus is 270V, but the acceptable steady state range is between 250V and 280V as depicted in the standard MIL-STD-704F [33]. Fundamental vector control in the *dq* frame associated with the rotor position is used and flux weakening is made to achieve a high speed operation region for the PMSGs. The detailed control strategy is discussed in Chapter 2 with regards to the AEGART project. Desired power sharing among the sources in EPS is achieved by droop control schemes.

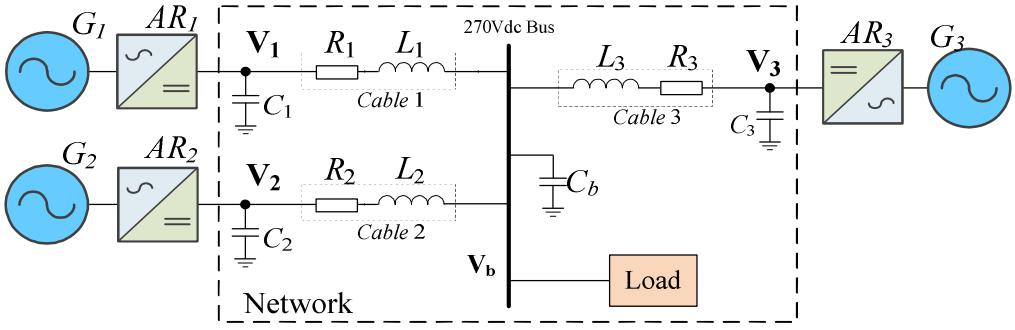

Figure 4.1. Equivalent system architecture of Figure 2.17.

4.3 Droop Control Schemes

The basic concept of droop control, as discussed above, is implemented by adding a "virtual resistance" into the existing local voltage controllers for the sources, enabling their parallel operation on common load(s). Due to the modularity and reliability, droop control has been successfully applied in DC systems [149].

For active front ends (AFEs)-based DC EPS, the basic droop control concept can be implemented either as current/power mode droop, including Current-Voltage (I-V) and Power-Voltage (P-V) strategies or as voltage mode droop, including V-I and V-P strategies [150]. The I-V and P-V droop methods are shown in Figure 4.2(a) and (b) [151]-[153]. In the implementation of these control methods, the DC voltage is measured and the injected current/power is controlled according to the droop characteristic. Alternatively, for the V-I and V-P methods shown in Figure 4.2(c) and (d), current or power is measured and the DC voltage is regulated accordingly [153].

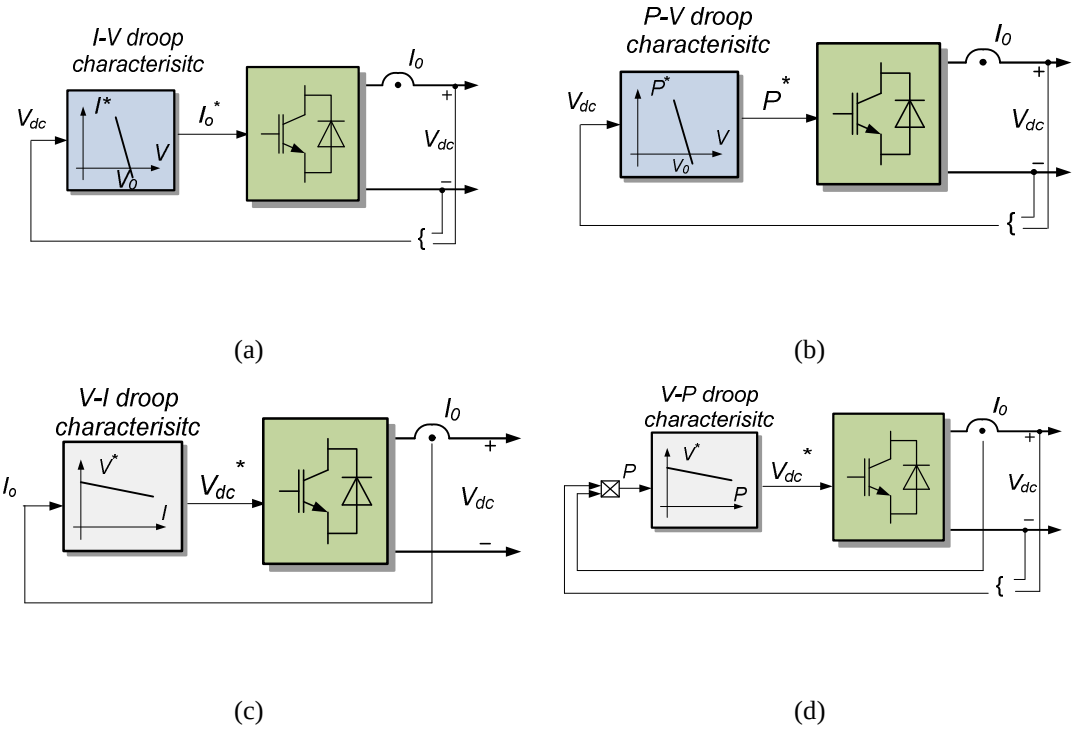

Figure 4.2. Droop characteristic employed in AFEs. (a) I-V droop. (b) P-V droop. (c) V-I droop. (d) V-P droop.

Figure 4.3 shows the voltage current/power characteristics for both power voltage and current voltage controlled terminals. It is obvious that both models are almost

equivalent with little difference when small voltage errors are considered. In [154], I-V and P-V demonstrated similar performance and for this reason only I-V droop is considered in this thesis as a representative of the current/power mode strategies. Similarly, only V-I droop is investigated within the voltage mode methods.

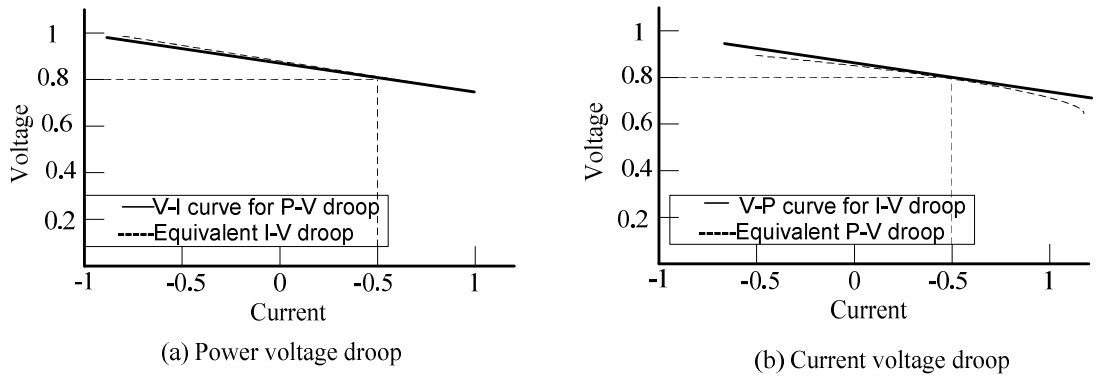

(a) Power voltage droop (b) Current voltage droop

Figure 4.3. Similarity validation of P-V droop and I-V droop [154].

4.3.1 Voltage-Mode Approach

Voltage-mode approach employs the V-I droop characteristic which uses the measured branch current to generate the terminal voltage reference.The control scheme for voltage-mode droop-controlled AFE is shown in Figure 4.4(b). As expressed in (4-1), the DC voltage reference is generated according to the branch output DC current using the V-I droop characteristic shown in Figure 4.4(a).

$$V_{dc}^{*} = V_{o} - kI_{dc} \tag{4-1}$$

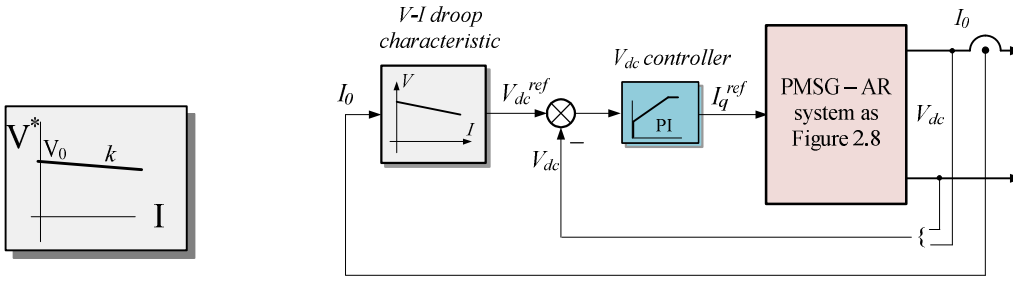

(a) (b)

Figure 4.4. Voltage-mode droop control scheme. (a) V-I droop characteristic. (b) Voltage-mode droop control scheme.

According to the EPS being studied, an equivalent voltage-mode droop-controlled system is shown in Figure 4.5. First-order lags are used to approximate the dynamics of a PMSG-AR system.

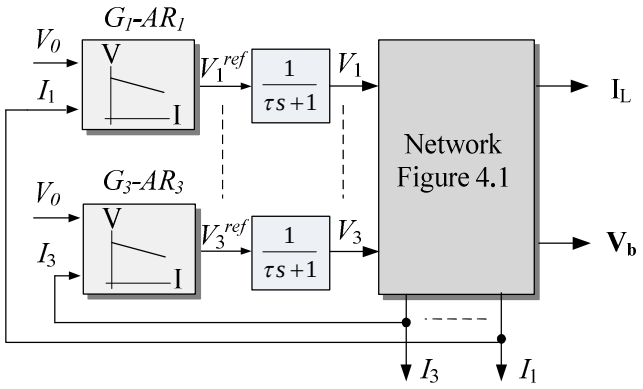

Figure 4.5. Paralleled voltage-mode droop-controlled system.

4.3.2 Current-Mode Approach

The current-mode approach uses the measured voltage to calculate the desired injecting DC current. The current-mode droop control scheme is shown in Figure 4.6(b), with the current reference derived from the I-V droop characteristic, based on the DC voltage measurement:

$$I_{dc}^{*} = \frac{V_o - V_{dc}}{k} \tag{4-2}$$

where V_o is the nominal bus voltage (270V); k is the droop gain; V_{dc} is the DC voltage measurement; I_{dc}^{*} is the generated DC current reference.

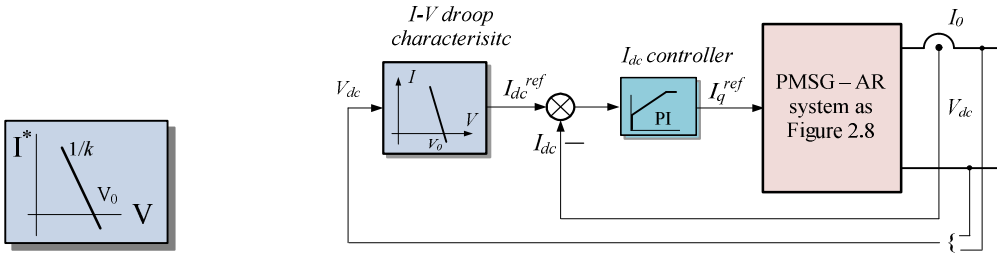

(a) (b)

Figure 4.6. Current-mode droop control scheme. (a) I-V droop characteristic. (b) Current-mode droop control scheme.

For the EPS being studied, paralleled configuration using the current-mode approach is shown in Figure 4.7. The I_{Si} shown in Figure 4.7 is regarded as a voltage controlled current source, which can be dependent either on the DC output voltage of each converter V_i (local voltage feedback, LVF) or on the main bus voltage V_b (global voltage feedback, GVF) [150].

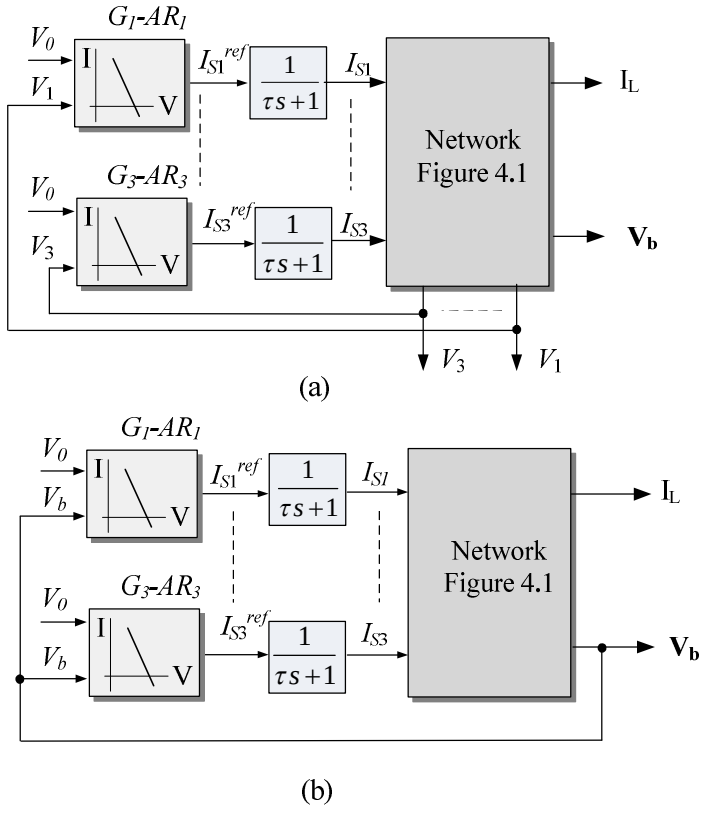

Figure 4.7. Parallel current-mode droop-controlled system (a) LVF. (b) GVF.

4.4 Steady-State Power Sharing Analysis

4.4.1 Voltage-Mode Approach

As discussed above, the voltage–mode droop approach assumes the operation of converters as voltage sources. The V-I droop characteristic shown in Figure 4.4(a) is used and the branch current is measured to generate the voltage reference for each module. The converter DC terminal voltage V_i is regarded as a current controlled voltage source, and can be expressed as follows:

$$V_i^* = V_o - I_i k_i, \quad i = 1, 2, 3 \tag{4-3}$$

Considering the voltage drop on the cables and neglecting the voltage control dynamics, the bus voltage in steady-state can be expressed as follows:

$$V_b = V_i - I_i R_i = V_o - I_i (k_i + R_i), \quad i = 1, 2, 3 . \tag{4-4}$$

The current sharing among the sources yields:

$$I_1 : I_2 : I_3 = \frac{1}{k_1 + R_1} : \frac{1}{k_2 + R_2} : \frac{1}{k_3 + R_3} \tag{4-5}$$

and given a k_1, the other droop gains can be computed by referring to,

$$k_i = \frac{k_1 + R_1}{n_i / n_1} - R_i \tag{4-6}$$

where n_i is the power sharing percentage of the i^{th} module among all the sources. It can be inferred that the existence of the cable resistance will affect the steady-state power sharing ratio, i.e., degrade the sharing accuracy especially when the droop gain and the cable impedance are similar.

4.4.2 Current-Mode Approach

Considering the LVF case, the output current reference is obtained by the local voltage measurement as follows,

$$I_i^* = \frac{V_o - V_i}{k_i} \tag{4-7}$$

The current sharing among the parallel branches can be derived in (4-8),

$$I_1 : I_2 : I_3 = \frac{1}{k_1 + R_1} : \frac{1}{k_2 + R_2} : \frac{1}{k_3 + R_3} \tag{4-8}$$

where k_1, k_2, k_3 are the droop coefficients for the three parallel modules individually.

Based on the aforementioned analysis, in the LVF current-mode and in voltage-mode droop-controlled systems the ratio of the source powers is not as desired due to cable resistances. Hence, cable resistance variation will degrade the power sharing accuracy and the droop gains need to be adjusted according to the cable resistance.

For a current-mode with GVF the output current reference for each module is given by (4-9),

$$I_i^* = \frac{V_o - V_b}{k_i} \tag{4-9}$$

In steady state, the current sharing ratio yields,

$$I_1 : I_2 : I_3 = \frac{1}{k_1} : \frac{1}{k_2} : \frac{1}{k_3} \tag{4-10}$$

It can be seen that current mode with GVF is independent of cable resistances. In other words, GVF approach is not affected by cable impedance and has improved the power sharing accuracy compared to LVF and voltage-mode approach.

4.4.3 Comparisons

Table 4-1 summarises the steady-state power sharing properties of current-mode and voltage-mode droop control strategies. Current-mode with GVF can realise accurate power sharing but it is dependent on the global voltage measurement. In contrast, voltage-mode approach and current-mode with LVF cannot guarantee precise power

sharing among the sources but these two methods rely only on local measurements. Hence additional sensors and potentially remote communications are not required.

Table 4-1 Comparison of possible power sharing strategies

Method	Accurate power sharing	Properties
Voltage-mode	No	Only dependent on local measurement
Current-mode (LVF)	No	Only dependent on local measurement
Current-mode (GVF)	Yes	Dependent on global voltage measurement

4.5 Simulation Results

To validate the power sharing performance among the proposed droop control approaches, the simulation for the multi-source based DC EPS shown in Figure 4.1 has been performed using Matlab/Simulink. Based on a business jet aircraft platform, considering the distance from the engine-driven generator-rectifier unit to the main dc bus (5m) and the APU-driven generator-rectifier unit to the main dc bus (20m), the system parameters are given in Table 4-2 and 4-3.

Table 4-2 EPS parameters

Parameter	Symbol	Value
Nominal voltage	V_o	270 V
Local shunt capacitor	C_i	1 mF
Main bus capacitor	C_b	1 mF
Droop coefficient for source #1	k_1	1/8
Droop coefficient for source #2	k_2	1/8
Droop coefficient for source #3	k_3	1/4

Table 4-3 Equivalent parameter for the DC cables

Cable	Resistance (R_i)	Inductance (L_i)	Length
Cable 1	5 mΩ	1 μH	5m
Cable 2	20 mΩ	4 μH	20m
Cable 3	5 mΩ	1 μH	5m

4.5.1 Normal Scenario

Considering the actual power ratings of the generators (G_1, G_2-main generators, and G_3-APU), the desired ratio of transmitted power among the three sources is set to be 2:2:1, which is in accordance with the individual droop gain settings. The load increases in steps of +5 kW every 0.2s.

As seen from Figure 4.8(a), for the voltage-mode method, the load sharing is affected by the resistance difference of the lines. Above t = 0.8 s, DC current flowing through the three converters is 23.61 A, 20.6 A, 12 A, respectively. Hence, the actual current sharing among the sources is 1.97:1.72:1. In Figure 4.8(b), the result of the local voltage feedback case for current-mode method shows similar sharing error issues as well. However, in a case of global voltage feedback shown in Figure 4.8(c), it can be seen that the accurate current sharing is achieved in steady-state: there is no error between I_{dc1} and I_{dc2} and the DC current flowing through the three converters satisfies the desired ratio (2:2:1). The results show that a global voltage feedback (GVF) case for the current-mode approach demonstrates a better power sharing performance than the other two methods.

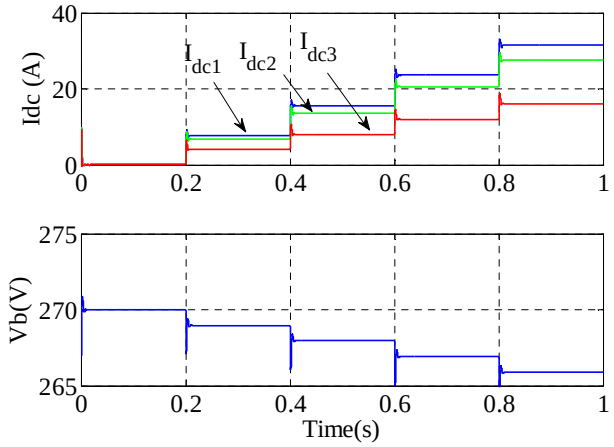

(a)

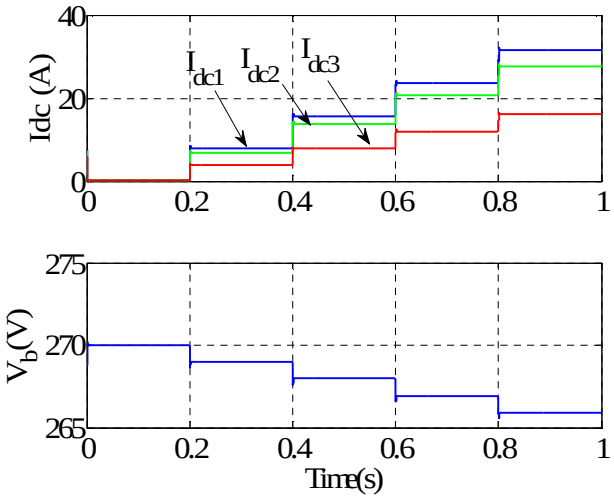

(b)

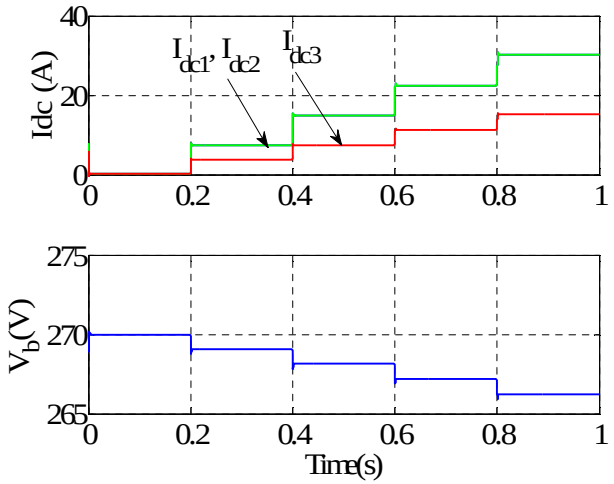

(c)

Figure 4.8. Simulation results for current sharing accuracy. (a) Voltage-mode strategy. (b) Current-mode strategy with LVF. (c) Current-mode strategy with GVF.

4.5.2 Fault Scenario

The fault scenario was simulated to test the robustness of the droop control approach. Figure 4.9 shows the fault scenario in the current-mode GVF system. Before t = 0.2 s, three sources are working in parallel to share the load power (20 kW CPL) as a desired ratio 2:2:1 ($k_1 = k_2 = 1/8$, $k_3 = 1/4$). At t = 0.3 s, source #3 G_3 is disconnected from the system and it can be seen that sources G_1 and G_2 take the full responsibility of providing power to meet the load demand after the loss of G_3 with the equal sharing amount (1:1). The outage of source #2 G_2 happens at t = 0.5 s. In this case, only the active source G_1 provides the power to feed the load. At t = 0.7 s, source 3 is reconnected to the system. It is seen that G_1 and G_3 share the load power as the original ratio 2:1.

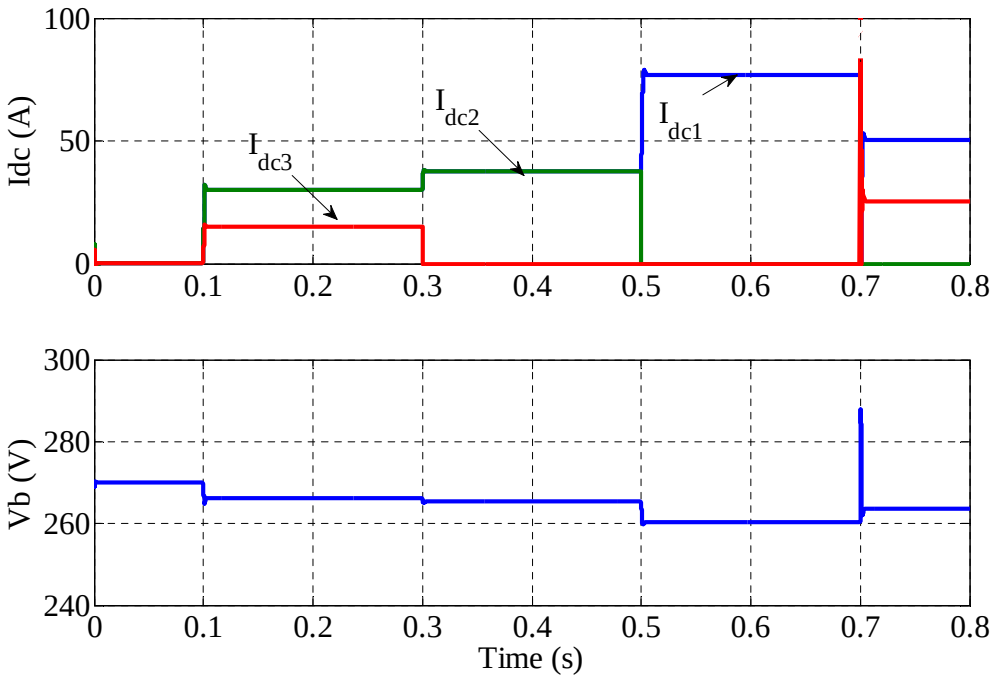

Figure 4.9. Simulation results for fault scenario (GVF).

Similarly, the current-mode LVF system is tested for the fault scenario. The simulation scenario is identical with Figure 4.10. Except for the load sharing inaccuracy due to the cable impedance, it can be seen that LVF droop approach is still invulnerable to source contingency.

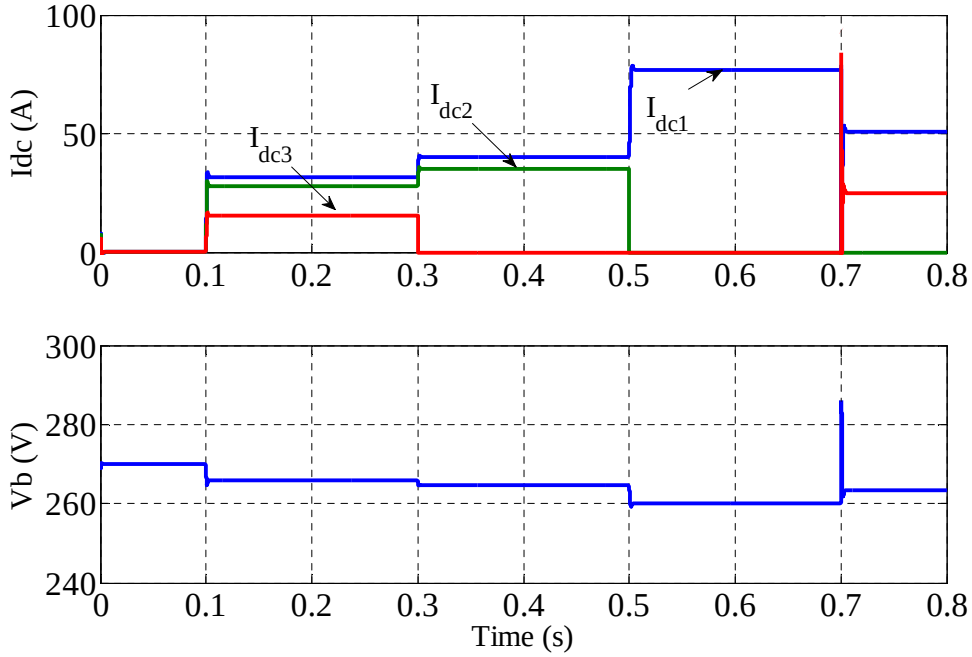

Figure 4.10. Simulation result for fault scenario (LVF).

Thus, it can now be confirmed that the droop control is robust to the failure of parallel sources. In the event of breakdown of any sources, other active sources will still share the power according to their individual droop gain settings.

4.6 Chapter Summary

This chapter considers droop control methods in the DC electrical power distribution system for the MEA. Voltage-mode and current-mode approaches are discussed with the inclusion of cable impedance. Global voltage feedback (GVF) and local voltage feedback (LVF) cases are addressed with respect to current-mode method. However, the accuracy of the power sharing using droop characteristic is affected by the cable impedance. The main findings reported in this chapter can be summarised as follows:

1) current-mode droop control uses a DC current controller to regulate the injected current from each terminal based on the voltage measurements. In contrast to the current-mode approaches, voltage-mode droop control regulates the terminal voltage based on current measurements.

2) following the comparison of the above-mentioned strategies, current-mode strategy with GVF is shown to be the best current sharing performance, which can attenuate the side effect of the cable impedance on the current sharing ratio

3) droop control is a type of autonomous control which can assure normal operation even if outage of source occurs. In such a fault scenario, other active sources will share the load according to their individual droop gain settings.

4) the stability analysis of voltage-mode and current-mode droop approaches will be discussed in subsequent chapters (Chapter 5 and 6).

Chapter 5 Stability Analysis of a Single Source-based DC EPS under Droop Control

In VSCs-based DC MGs, systems using different droop approaches (current/power mode or voltage mode) may show different stability boundaries. However, to the author's knowledge, until now there are no available reports, dealing with the performance comparison of the current-mode vs. voltage-mode droop-controlled systems in terms of stability. To fill this gap, after analysing the power sharing performance of the droop control approaches in Chapter 4, this chapter will investigate the stability of a single–source based DC EPS under droop control using impedance-based approach.

5.1 Introduction

Many loads within the MEA EPS are tightly controlled by power electronic converters and can often behave like CPLs. As discussed in Chapter 2 the negative input impedance characteristic of CPLs may result in oscillations of the system and, as a consequence, reduce power quality and lead to instability. Thus stability is a great concern for the MEA EPS. The candidate architecture should be carefully examined for stability in order to guarantee safe EPS operation for a wide range of scenarios.

In [154], I-V and P-V demonstrated similar performance and for this reason only I-V droop is considered in this paper as a representative of the current/power mode

strategies. For the current-mode droop control, the effect of the passive components (DC link capacitor, feeder impedance) and the power of CPLs on the stability margin have been investigated in [155], [156]. It is known that the stability margin increases with an increase of DC link capacitance, decrease of feeder inductance and decrease of load power. Nevertheless, the effect of local control bandwidth and droop gains on stability has not been fully investigated.

Similarly, only V-I droop is investigated within the voltage mode methods [153], [165]. A hierarchical control scheme using V-I droop characteristics for a parallel AC-DC converter interfaced hybrid MG is presented in [153]. Within [153] the effect of the delay between secondary control (voltage restoration) and primary control (local DC voltage) on system stability is investigated. However, the effect of local control bandwidth and droop gains on stability is not fully assessed as well. Stability of a low voltage DC system is studied including the cable effects in [165]. In that paper the sufficient condition for stable operation is discussed but the impact of different droop methods is not considered.

Following discussions in Chapter 2, in terms of stability analysis, two dominant approaches, namely, eigenvalues theorem and the impedance-admittance method have been widely used. Instead of systematically analysing the eigen properties of the state matrix as in state-space models, the impedance-based approach locally predicts the system stability at each point of connection (PoC) of the component. Thus, the formulation of the system matrices can be avoided, and the contribution of each component to the system stability can be readily assessed in the frequency domain. Also, the output impedance of the component or subsystem can be accordingly reshaped (“virtual impedance”, additional control loop, etc) to stabilise the overall power system. Therefore, this chapter will deal with more straightforward and design-oriented stability analysis using impedance-based method [157].

5.2 Control Schemes

5.2.1 Current-Mode Droop Control Scheme

Figure 5.1 shows the current-mode droop control scheme for AFEs in which the current reference is generated by the specified I-V droop characteristic.

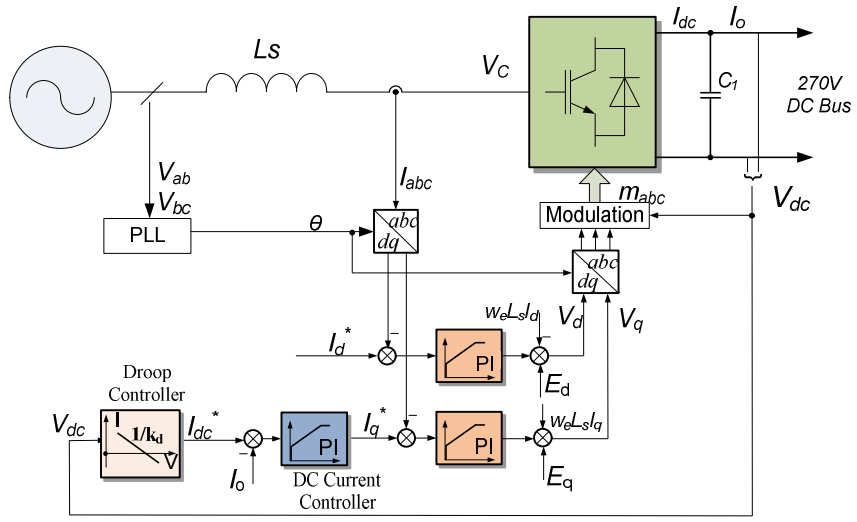

Figure 5.1. Current-mode droop control scheme for AFEs.

Figure 5.2 shows the equivalent control block diagram for this system. The output of the voltage droop controller is the DC current reference (I_{dc}^*) with the DC current being regulated by a PI controller G_{Idc}. The inner current loop, being much faster than the outer loop, is represented by a first-order lag G_{cc}(s).

$$G_{CC}(s) = \frac{1}{\tau s + 1} \tag{5-1}$$

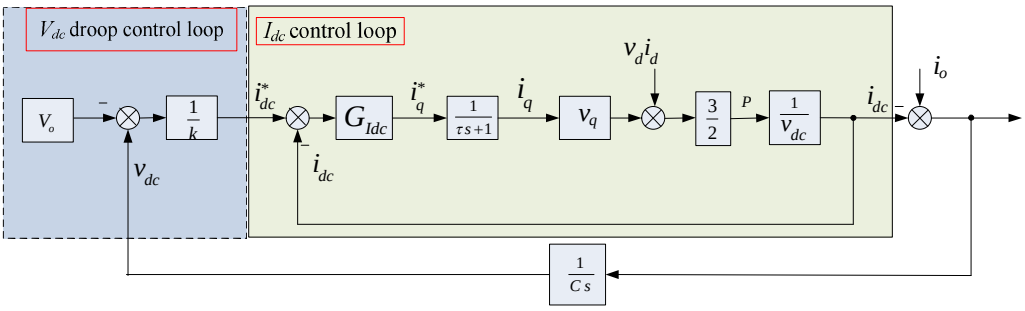

Figure 5.2. Control block diagram for the current-mode droop-controlled system.

Using the amplitude invariant for *abc* to *dq* transformation (see Appendix A), the active power of the system in the *dq* frame can be expressed as:

$$P = \frac{3}{2}(v_d i_d + i_q v_q) \tag{5-2}$$

where v_d and v_q are the converter AC terminal voltage components in the *dq* axes and i_d and i_q are the AC currents.

Using the classical vector control [143], the *d*-axis and *q*-axis stator voltages yield:

$$\begin{cases} v_d = (R_s + L_s s) i_d - \omega_e L_s i_q + e_d \\ v_q = (R_s + L_s s) i_q + \omega_e L_s i_d + e_q \end{cases} \tag{5-3}$$

where e_{dq} is the point of common coupling (PCC) voltage; R_s is the stator resistance; ω_e is the grid frequency in rad/s; L_S is the AC side inductance of the machine. In this project, the *q*-axis is used to regulate the active power. Thus, e_d is controlled to be zero and e_q is the magnitude of the phase voltage vector.

According to (5-3), the linearised *q*-axis voltage, v_q, can be expressed as:

$$\triangle v_q = (R_s + L_s s) \triangle i_q + \omega_e L_s \triangle i_d \tag{5-4}$$

Equation (5-2) can be linearised about an operating point (indicated with the subscript “o”):

$$\triangle P = \frac{3}{2}(\triangle v_q i_{qo} + \triangle i_q v_{qo} + \triangle v_d i_{do} + \triangle i_d v_{do}) \tag{5-5}$$

By substituting (5-4) into (5-5), the active power in small signal can be written as:

$$\begin{aligned} \triangle P &= \frac{3}{2}[((R_s + L_s s) i_{qo} + v_{qo} - \omega_e L_s i_{do}) \triangle i_q + ((R_s + L_s s) i_{do} + v_{do} + \omega_e L_s i_{qo}) \triangle i_d] \\ &\approx \frac{3}{2}(L_s i_{qo} s + R_s i_{qo} + v_{qo} - \omega_e L_s i_{do})) \triangle i_q \end{aligned} \tag{5-6}$$

Figure 5.3 shows the linearised control block diagram for the current-mode droop-controlled system. The transfer function of Δi_{dc} to Δi_q^* (G_{P_C}) can be expressed as:

$$G_{P\_C} = \frac{\Delta i_{dc}}{\Delta i_q^*} = \frac{1.5(i_{qo}L_s s + R_s i_{qo} + v_{qo} - \omega_e L_s i_{do})}{V_{dco}(\tau s + 1)} \tag{5-7}$$

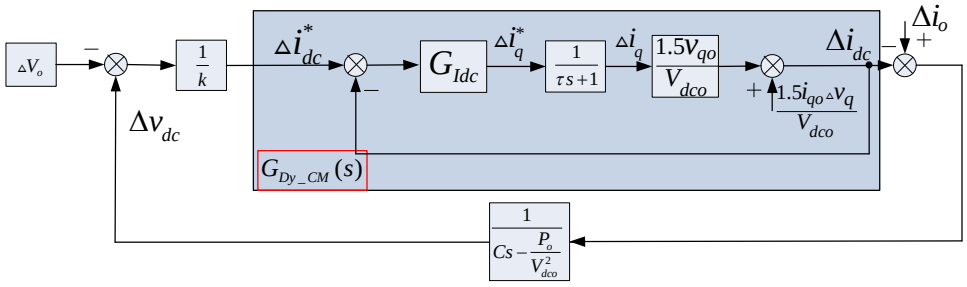

Figure 5.3. Linearised control block diagram of the current-mode droop-controlled system.

The I_{dc} control dynamics G_{Dy_CM} can be derived as

$$\begin{aligned} G_{Dy\_CM} &= \frac{\Delta i_{dc}(s)}{\Delta i_{dc}^*(s)} = \frac{G_{Idc}G_{P\_C}}{1 + G_{Idc}G_{P\_C}} \\ &= \frac{(k_{pdc}s + k_{idc})(L_s i_{qo}s + R_s i_{qo} + v_{qo} - \omega_e L_s i_{do})}{\frac{2}{3}v_{dco}s(\tau s + 1) + (k_{pdc}s + k_{idc})(L_s i_{qo}s + R_s i_{qo} + v_{qo})} \end{aligned} \tag{5-8}$$

where k_{pdc} and k_{idc} are the PI control parameters for the I_{dc} controller G_{Idc}(s).

Due to the term ($L_s i_{qo}s+R_s i_{qo}+v_{qo}-\omega_e L_s i_{do}$) in the control-to-output transfer function (i_{qo} is negative and v_{qo} is positive at the operating point for the generating mode), a positive right half plane (RHP) zero exists in the I_{dc} control loop (G_{Dy_CM}) which can be expressed as

$$z = -\frac{v_{qo} + R_s i_{qo} - \omega_e L_s i_{do}}{L_s i_{qo}} \tag{5-9}$$

This RHP zero will pose some challenges to system stability, as will be discussed in later subsections.

Considering the DC bus voltage dynamics, the relationship between DC current and voltage can be written as

$$\begin{aligned} C\frac{d\triangle v_{dc}}{dt} &= \triangle i_o - \triangle i_{dc} = \triangle i_o - (\frac{\triangle P}{v_{dco}} - \frac{P_o}{v_{dco}^2}\triangle v_{dc}) \\ &= -\frac{1}{v_{dco}}\triangle P + \frac{P_o}{v_{dco}^2}\triangle v_{dc} + \triangle i_o \end{aligned} \tag{5-10}$$

In the Laplace domain, (5-10) can be rewritten as

$$\triangle v_{dc} = \frac{1}{(Cs - \frac{P_o}{v_{dco}^2})}\triangle i_o - \frac{1}{(Cs - \frac{P_o}{v_{dco}^2})}\triangle i_{dc} \tag{5-11}$$

The overall closed loop transfer function of the V_{dc} droop control yields

$$\frac{\triangle v_{dc}}{\triangle v_o} = \frac{G_{Dy\_CM}}{G_{Dy\_CM} + k(Cs - \frac{P_o}{V_{dco}^2})} \tag{5-12}$$

By substituting (5-8) into (5-12), the closed loop transfer function of the V_{dc} loop for the current-mode droop-controlled system is expressed as follows:

$$\frac{\triangle v_{dc}}{\triangle v_o} = \frac{(k_{pIdc}s + k_{iIdc})(L_s i_{qo}s + R_s i_{qo} + v_{qo} - \omega_e L_s i_{do})}{(k_{pdc}s + k_{idc})(L_s i_{qo}s + R_s i_{qo} + v_{qo} - \omega_e L_s i_{do}) + k(Cs + \frac{P_o}{V_{dco}^2})\frac{2}{3}V_{dco}(s(\tau s + 1) + (k_{pIdc}s + k_{iIdc})(L_s i_{qo}s + R_s i_{qo} + v_{qo} - \omega_e L_s i_{do}))} \tag{5-13}$$

It can be inferred from (5-13) that the droop gain will not only affect the steady-state voltage deviation but also influence the voltage loop bandwidth.

5.2.2 Voltage-Mode Droop Control Scheme

Figure 5.4 shows the voltage-mode droop control scheme for AFEs. In contrast to the current-mode droop control scheme shown in Figure 5.1, the control target is the DC terminal voltage and the reference value is obtained by the V-I droop characteristic.

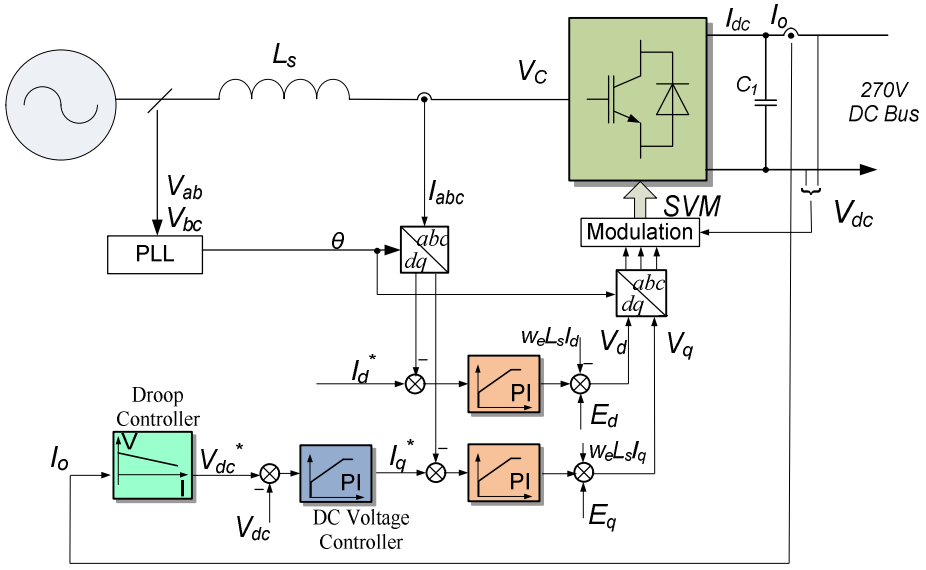

Figure 5.4. Voltage-mode droop control scheme for AFEs.

Figure 5.5 shows the control block diagram for the voltage-mode droop-controlled system. V_o is the no load voltage reference for the droop characteristic.

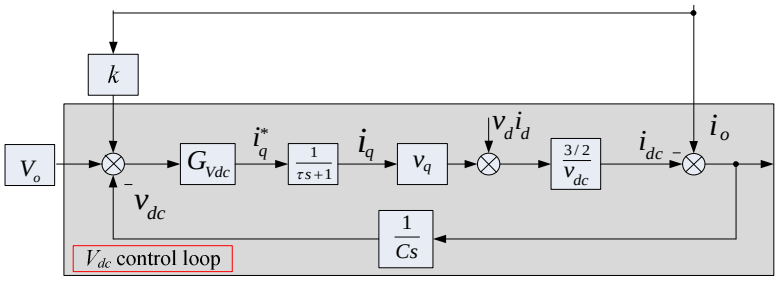

Figure 5.5. Control block diagram for the voltage-mode droop-controlled system.

Applying the same analysis developed for the current-mode system, the linearised block diagram of Figure 5.5 is shown in Figure 5.6. The plant for the V_{dc} controller (transfer function of Δv_{dc} to Δi_q^* $G_{p\_V}(s)$) yields:

$$G_{P\_V}(s) = \frac{\Delta v_{dc}}{\Delta i_q^*} = \frac{1.5(i_{qo}L_s s + R_s i_{qo} + v_{qo} - \omega_e L_s i_{do})}{V_{dco}(\tau s + 1)(Cs - \frac{P_o}{V_{dco}^2})} \qquad (5\text{-}14)$$

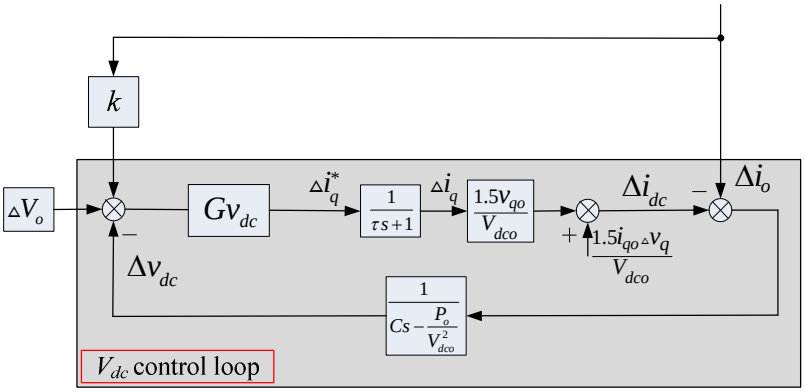

Figure 5.6. Linearised control block diagram for the voltage-mode droop-controlled system.

Due to the RHP zero in (5-14) it can be observed that a faster bandwidth (high gains) within the V_{dc} control will challenge stability. In comparison with the current-mode droop control diagram, a small droop gain k applied to the voltage-mode droop does not impose limitations to stability, as the droop gain k appears as a feedforward term in the block diagram.

As can be seen from Figure 5.6, the voltage control dynamics G_{Dy_VM} can be expressed as

$$\begin{aligned} G_{Dy\_VM} &= \frac{\Delta v_{dc}}{\Delta v_o} = \frac{G_{Vdc}G_{P\_V}}{1+G_{Vdc}G_{P\_V}} \\ &= \frac{1.5(i_{qo}L_s s + R_s i_{qo} + v_{qo} - \omega_e L_s i_{do})(k_{pVdc}s + k_{iVdc})}{s(\tau s+1)(V_{dco}Cs - \frac{P_o}{V_{dco}}) + 1.5(i_{qo}L_s s + R_s i_{qo} + v_{qo} - \omega_e L_s i_{do})(k_{pVdc}s + k_{iVdc})} \end{aligned} \quad (5\text{-}15)$$

where k_{pVdc} and k_{iVdc} are the proportional and integral gains of the V_{dc} controller G_{Vdc}, respectively. It can be inferred that the voltage dynamics are mainly determined by the controller bandwidth rather than the droop gain.

5.3 Impedance Analysis

The impedance and stability properties of the two droop techniques will be investigated within a single source scenario. The system can be represented in a cascaded way: source subsystem and load subsystem. Assuming that the source and load subsystems are individually stable, when the output impedance of the source

subsystem Z_S is less than the input impedance of the load subsystem Z_L in the entire frequency range, the stability of the cascaded system can be guaranteed based on Middlebrook's criterion [111].

However, it has been shown that the minor loop gain (impedance ratio Z_S/Z_L) needs to be examined carefully in the voltage-source and the current-source systems, i.e., if the converter of the source susbsystem is controlled as a voltage source, the impedance ratio should be Z_{o_s}/Z_{in_L}, whereas if the converter of the source susbsystem is controlled as a current source, the impedance ratio will be Z_{in_L}/Z_{o_s} [158], [159]. However, not all DC EPS can be treated simply as a voltage-source or current-source system. Thus the existing impedance-based stability criteria may not be adequate in some particular applications.

Reference [160] shows the principle of selecting the numerator and denominator of the minor loop gain. In general, the impedance on the numerator has to be the internal impedance of the subsystem containing the voltage source or sink, and the impedance on the denominator has to be the internal impedance of the subsystem containing the current source or sink [160], [161]. In addition, the voltage-source or current-source should also be an independent source and should not be related to other variables (controlled source). For the current-mode droop-controlled system as shown in Figure 4.6, the DC current reference is still dependent on the voltage and the control target is needed to regulate the DC terminal voltage in proportion to the load (see Figure 5.2). Hence, the minor loop gain for the current-mode approach should still be Z_S/Z_L when using the impedance-based approach [162], [163].

5.3.1 Load Impedance

As mentioned previously, tightly controlled power electronic converters and motor drives in the EPS can behave like CPLs. Consequently the input impedance of the load subsystem can be seen as a negative resistance. This subsection will begin with an introduction of modelling the CPLs [92]. In order to facilitate the analysis of the load impedance, the cable between the load to the DC bus can be regarded as part of the cables in the source subsystem.

The V-I relationship of a CPL is shown in (5-16):

$$i = \frac{P}{v} \tag{5-16}$$

As discussed in [92], for a given operating point, the rate of change in current can be expressed as follows by linearising (5-16):

$$\frac{\partial i}{\partial v} = -\frac{P}{V^2} \tag{5-17}$$

Therefore the curve representing the current versus voltage for a CPL can be approximated by a straight line tangent to the curve at the operating point. The equation for this line can be expressed as:

$$i = -\frac{P}{V^2} v + 2\frac{P}{V} \tag{5-18}$$

thus, as shown in Figure 5.7, a linearised CPL can be approximately expressed by a negative impedance ($-R_{CPL}$) in parallel with a current source (I_{CPL}) [164], [165].

$$R_{CPL} = \frac{V_b^2}{P_{CPL}}, \quad I_{CPL} = 2\frac{P_{CPL}}{V_b} \tag{5-19}$$

where P_{CPL} is the power absorbed by the CPL.

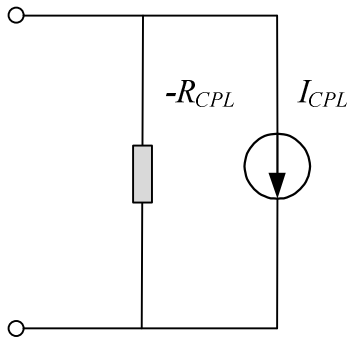

Figure 5.7. The linearised model of a CPL.

5.3.2 Source Impedance

A representative DC power system, consisting of one generating unit feeding the load, is analysed in this section to investigate the worst conditions from the stability point of view.

Since the DC terminal voltage is droop controlled and can be expressed as follows:

$$V_i = V_i^* G_{Dy\_VM} = (V_o - k_i I_i) G_{Dy\_VM} \tag{5-20}$$

where G_{Dy_VM} is the voltage control dynamics defined in (5-15). The impedance-based model for the voltage-mode approach is depicted in Figure 5.8.

It can be seen that the DC terminal is modelled as two voltage sources in which one is an ideal voltage source and the other is a current-controlled voltage source. Cable is modelled as an R-L branch and the cable capacitance is combined with the bus capacitance C_b. As discussed in Section 5.3.1, a single CPL is modelled as a negative resistance ($-R_{CPL}$) in parallel with a current source (I_{CPL}).

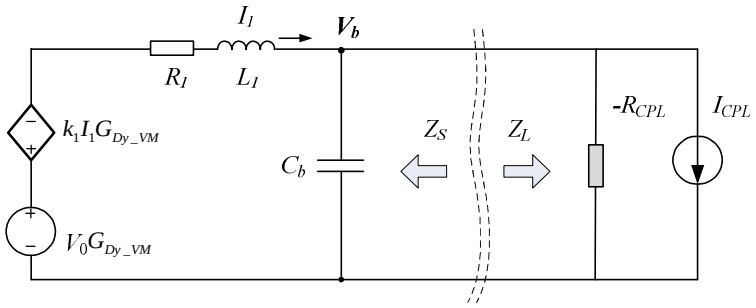

Figure 5.8. Equivalent circuit for voltage-mode droop approach.

LVF and GVF are shown in Figure 5.9. For the current-mode LVF approach, based on the DC current equation and shown as follows:

$$I_i = I_i^* G_{Dy\_CM} = \frac{V_o - V_i}{k} G_{Dy\_CM} \tag{5-21}$$

the source is modelled as a current source in parallel with a resistor. Meanwhile for the GVF approach, based on the DC current equation shown below:

$$I_i = I_i^* G_{Dy\_CM} = \frac{V_o - V_b}{k} G_{Dy\_CM} \tag{5-22}$$

the source is modelled as an ideal current source in parallel with a DC bus voltage-controlled current source.

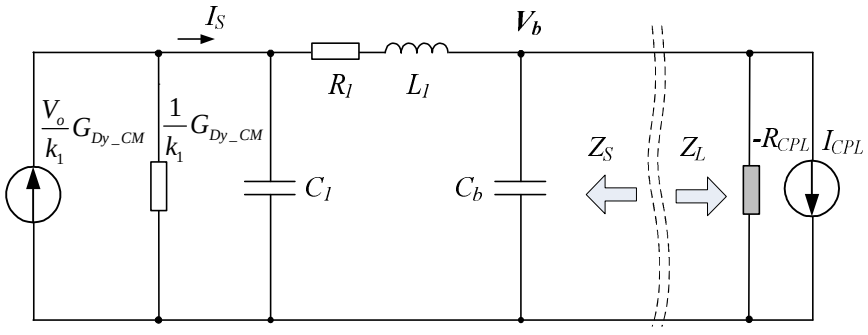

(a)

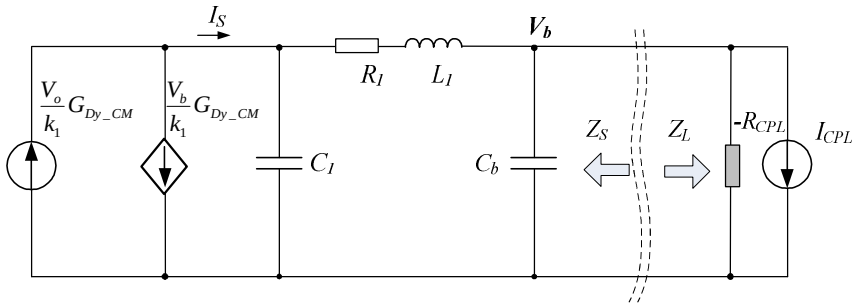

(b)

Figure 5.9. Equivalent circuit for current-mode droop approach. (a) LVF. (b) GVF.

According to the equivalent linearised circuits, the equivalent source impedances can be derived as follows:

$$\begin{cases} Z_{s\_LVF}(s) = \dfrac{k_1(L_1C_1s^2 + R_1C_1s + 1) + G_{Dy\_CM}(L_1s + R_1)}{k_1 s(L_1C_1C_bs^2 + R_1C_1C_bs + C_1 + C_b) + G_{Dy\_CM}(L_1C_bs^2 + R_1C_bs + 1)} \\ Z_{s\_GVF}(s) = \dfrac{k_1(L_1C_1s^2 + R_1C_1s + 1)}{k_1 s(L_1C_1C_bs^2 + R_1C_1C_bs + C_1 + C_b) + G_{Dy\_CM}} \\ Z_{s\_VM}(s) = \dfrac{(L_1s + R_1) + k_1G_{Dy\_VM}}{(L_1C_bs^2 + R_1C_bs + 1) + C_bk_1sG_{Dy\_VM}} \end{cases} \quad (5\text{-}23)$$

G_{Dy_CM} and G_{Dy_VM} are the DC current and DC voltage control dynamics for the current-mode (see (5-8)) and voltage-mode (see (5-15)) droop-controlled systems respectively.

Using the parameter values listed in Table 5-1, Figure 5.10 shows the Bode diagrams of the LVF and GVF source impedances. Since the frequency responses of the LVF and GVF are similar, it indicates that the stability characteristics for LVF and GVF are similar. In comparison to the GVF approach, the LVF is not an accurate solution

for power sharing performance (see the discussion in Section 4.4). However, its control scheme can be implemented using only local measurements. For the GVF approach, the main bus voltage needs to be measured, i.e. an extra voltage sensor and additional communication links between the common bus and the individual parallel modules would be required within a large DC MG. This would compromise the modular, decentralised feature of droop control. Hence, the LVF method is selected as a representative of the current-mode droop control approach for the subsequent analysis. Further, comparative stability analysis using the current-mode and voltage-mode approach will be presented in the following discussion.

Table 5-1 Parameters for Figure 5.10

Category	**Parameter**	**Symbol**	**Value**
Cable	Cable resistance	R_i	3 mΩ
	Cable inductance	L_i	5 μH
Droop characteristic	Nominal voltage	V_o	270 V
	Droop gain	k_1	1
Capacitor	Local capacitance	C_1	1.2 mF
	Bus capacitance	C_b	0.8 mF

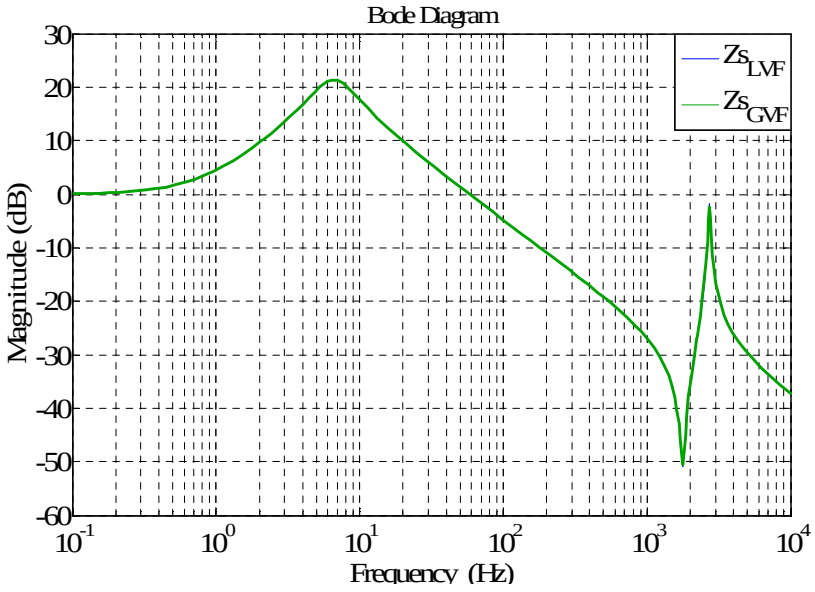

Figure 5.10. Source impedance for the current-mode droop control under LVF and GVF approach adopting the same control parameters.

5.4 Sensitivity Analysis (Parameteric Study)

Having derived the source impedance and load impedance, this section deals with stability of the single source system against parameter uncertainties. To provide an insight into how the parameters influence the system stability, the influence of operating parameters (generator speed), component parameters (local capacitor, cable impedance, cable length), and control parameters (control bandwidth, droop gain) on the impedance are presented below.

5.4.1 Effect of Capacitor

It is well known that larger bus capacitance corresponds to a stiffer DC voltage plant, better stability margins, and smoothed transients [166]. This conclusion can also be inferred from Figure 5.11 as a smaller source impedance magnitude is obtained with larger bus capacitance. According to the derived source impedance in (5-23), two positive resonance peaks and one negative peak value exist. The corresponding frequencies can be derived and approximated as follows:

$$f_{res1} \cong \frac{1}{2\pi\sqrt{\tau_i(C_i+C_b)}},\ f_{res2} \cong \frac{1}{2\pi\sqrt{L_iC_i}},\ f_{res3} \cong \frac{1}{2\pi\sqrt{L_1C_{dc}}} \tag{5-24}$$

where C_{dc} is given by:

$$C_{dc} = \frac{C_1C_b}{C_1+C_b} \tag{5-25}$$

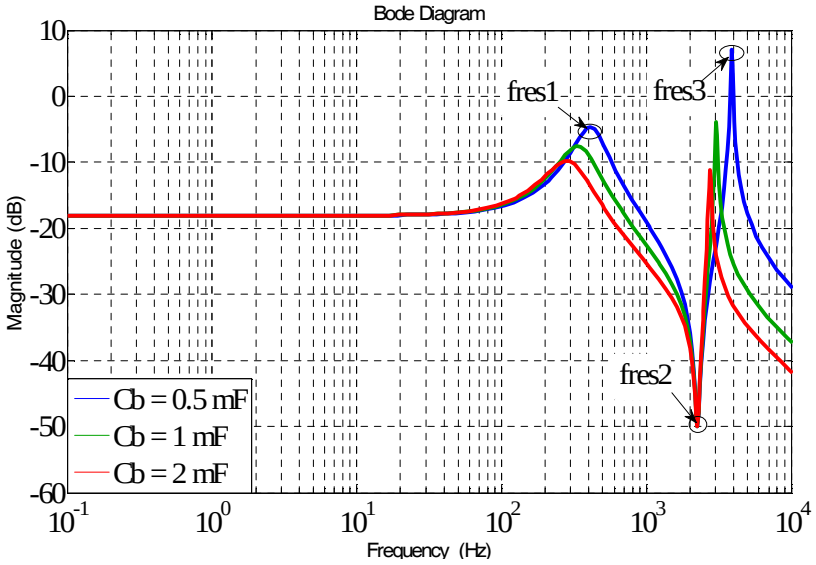

Figure 5.11. Bode plot of source impedance with different capacitances.

The second resonance peak at f_{res2} is in the negative position and therefore it does not influence the EPS' stability margin. Both positive resonance peaks will challenge the system stability, thus they are of concern in the following analysis. Although the resonance peaks at corresponding resonant frequencies are too complex to show here, the tendency of their change depending on parameters variation can be illustrated using the Bode plots. It can be seen from Figure 5.11(a) that increasing the local capacitance helps to damp the resonance peak at f_{res1} but increases resonance peak at f_{res3}. Hence there is a trade-off between damping at f_{res1} and f_{res3} by adjusting the local capacitance.

The resonance peak on the high-frequency domain f_{res3} decreases alongside the increase of the bus capacitance. A large filter capacitance provides a limited attenuation on the first and second resonant peaks, but it presents an effective attenuation on the high-frequency resonant peaks.

In comparison with the effect of a local capacitor, the resonance peaks on f_{res1} and f_{res3} can be damped simultaneously by increasing the main bus capacitance. This is in accordance with what is known from the practice stabilising effect of large bus capacitance. However, the bus capacitance cannot be simply increased to ensure system stability since cost, weight and volume also need to be taken into consideration. This applies for MEA EPS applications in particular.

5.4.2 Effect of Cable Impedance

Figure 5.12 and 5.13 analyse how the source impedance is influenced by cable inductance and cable resistance respectively. From Figure 5.12 it can be seen that the peak value of the source impedance at f_{res3} changes with the cable inductance. From Figure 5.13 it can be seen that the resonance peak at f_{res3} can be damped by increasing cable resistance. It is seen that the resonance frequency is invariant with respect to cable resistance variation, as is expected from the analysis of (5-24). However, increased feeder resistance will cause more voltage drop at the DC bus and more distribution losses will be introduced into the system. An equilibrium point criterion is used to formulate an upper limit for the output resistance of the source converter [167]: the equivalent load resistance must be higher than the source converter output resistance. Overall, the source resistance should satisfy the following inequality,

$$R_{source} < \frac{V_b^2}{4P_{CPL}} \tag{5-26}$$

where R_{source} consists of the cable resistance, the resistance of contactors, switches and parasitic resistance on the passive components on the DC side. The impedance on the contactors, connectors, etc is smaller compared to the cable impedance. Overall, the value of the source impedance is much smaller than the droop gain settings. Thus, the impedance on the contactors, terminals, and swichgears show less influence on the system stability and it is not considered in the thesis.

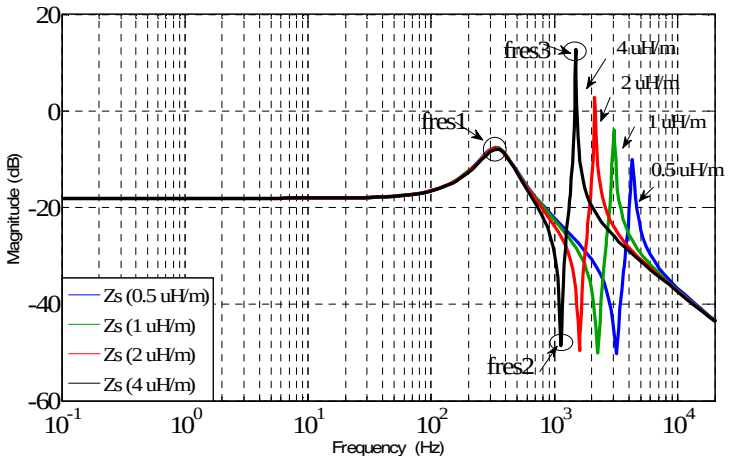

Figure 5.12. Bode plot of source impedances with cable inductance fluctuation.

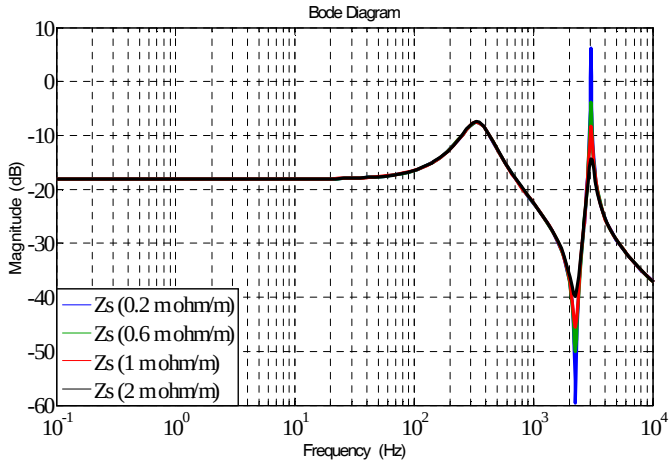

(a)

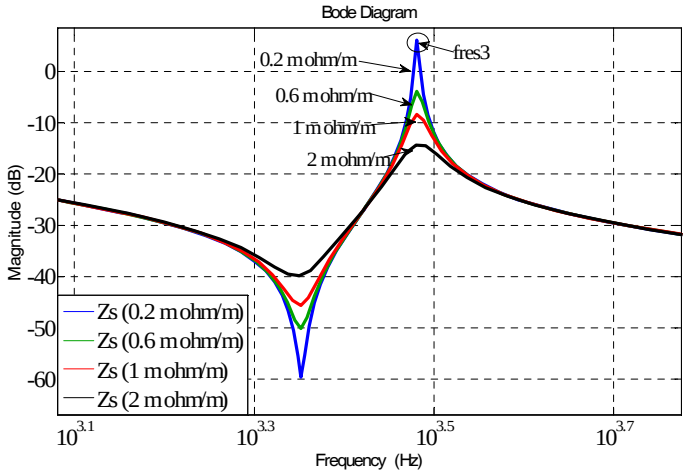

(b)

Figure 5.13. Bode diagram of source impedances with different values of cable resistance. (a) Overview. (b) Zoomed part around f_{res3}.

In conclusion, the resonance peak at f_{res3} can be relieved by increased cable resistance or bus capacitance, as well as by reduced cable inductance or local capacitance.

5.4.3 Effect of Cable Length

Considering typical geometry of civil aircraft, the cable length in this study is varied from 5m to 30m. The Bode diagram of the source impedance with different cable lengths is depicted in Figure 5.14. It shows that resonant frequencies f_{res2} and f_{res3} decrease with the increase of cable length, and can be predicted from (5-24), whilst

the resonant peak at f_{res3} is not influenced. Thus, it can be concluded that the cable length does not affect the system stability noticeably.

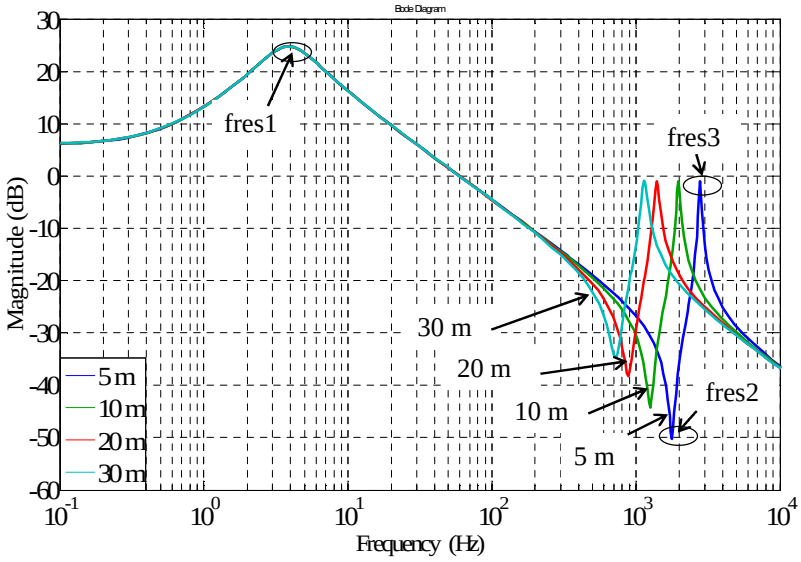

Figure 5.14. Bode plot of the source impedance with variation of cable length.

5.4.4 Effect of Generator Speed

The Bode diagram of source impedance under different AC fundamental frequencies is shown in Figure 5.15. A frequency of 50 Hz AC corresponds to the LP generator frequency whilst 400 Hz corresponds to the HP shaft generator frequency. It can be seen that the magnitude of the source impedance increases with the AC fundamental frequency (generator speed). 50 Hz AC frequency corresponds to a generator running at low speed whilst 400 Hz corresponds to a generator operating at high speed. This indicates that the system stability margin will be reduced with higher generator speed, and agrees with the eigenvalue sensitivity analysis with respect to the generator speed discussed in Chapter 3.

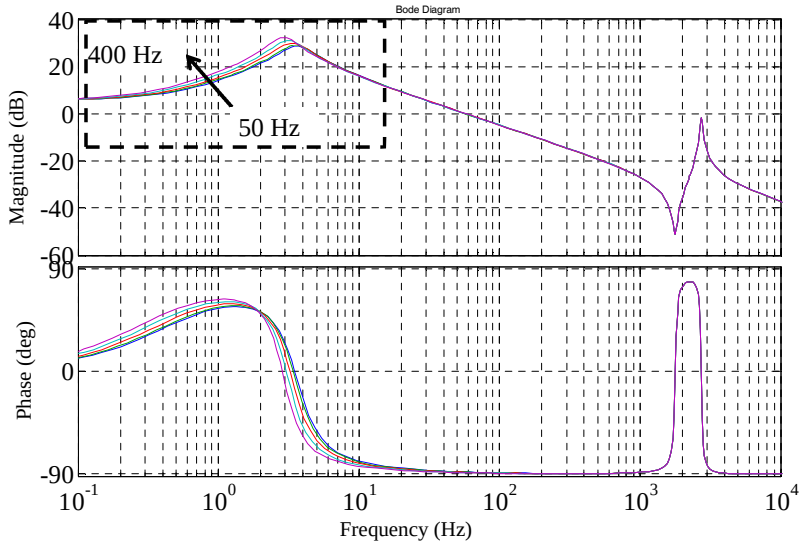

(a)

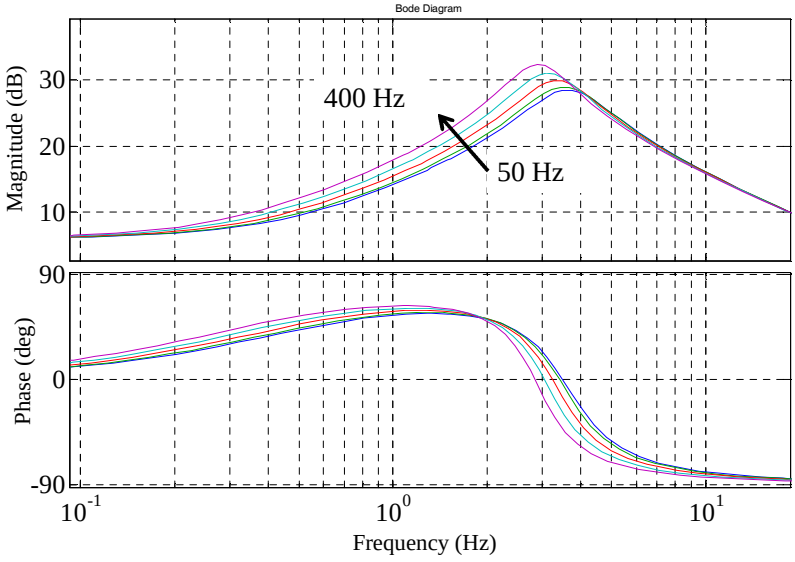

(b)

Figure 5.15. Bode diagram of source impedances with different AC fundamental frequency from 50Hz to 400Hz (a) Overview; (b) Zoomed view of selected area.

5.4.5 Effect of Control Bandwidth

The effect of control bandwidth on the source impedance is investigated in this subsection.

5.4.5.1 Current-Mode Droop-Controlled System

In the current-mode droop-controlled system, as can be seen from Figure 5.3, there are three control loops: voltage droop control, I_{dc} control loop, and inner current loop. If the second loop, the I_{dc} control loop, is simplified to be a first-order system with bandwidth ω_{Idc} and the inner loop is simplified to be a unit gain, the voltage loop (shown in Figure 5.3) can be rewritten as:

$$\frac{\triangle v_{dc}}{\triangle v_o} = \frac{\omega_{Idc}}{k_1 C_1 V_{dco}(s^2 + (\omega_{Idc} - \frac{P_o}{C_1 V_{dco}^2})s + \frac{\omega_{Idc}}{C_1}(\frac{1}{k_1 V_{dco}} - \frac{P_o}{V_{dco}^2}))} \tag{5-27}$$

Based on (5-27), the voltage-loop bandwidth can be expressed as:

$$\omega_{Vdc} = \sqrt{\frac{\omega_{Idc}}{C_1}(\frac{1}{k_1 V_{dco}} - \frac{P_o}{V_{dco}^2})} \tag{5-28}$$

then, the damping ratio of the voltage-loop can be derived as

$$\zeta = (\omega_{Idc} - \frac{P_o}{C_1 V_{dco}^2}) / 2\omega_{Vdc} \tag{5-29}$$

It can be inferred from (5-27) that decreasing the droop gain, k_1, increases the voltage-loop bandwidth for the current-mode droop-controlled system. Meanwhile the system damping decreases.

Using the Routh-Hurwitz stability criterion, in order to ensure stability, the simplified DC current loop bandwidth ω_{Idc} should satisfy:

$$\omega_{Idc} > \frac{P_o}{C_1 V_{dco}^2} \tag{5-30}$$

For the load susbsystem, the buck converter is tightly regulated as a CPL [168] and the control scheme is shown in Figure 5.16. According to the control scheme, the buck converter can be tightly controlled to follow the power reference P^*.

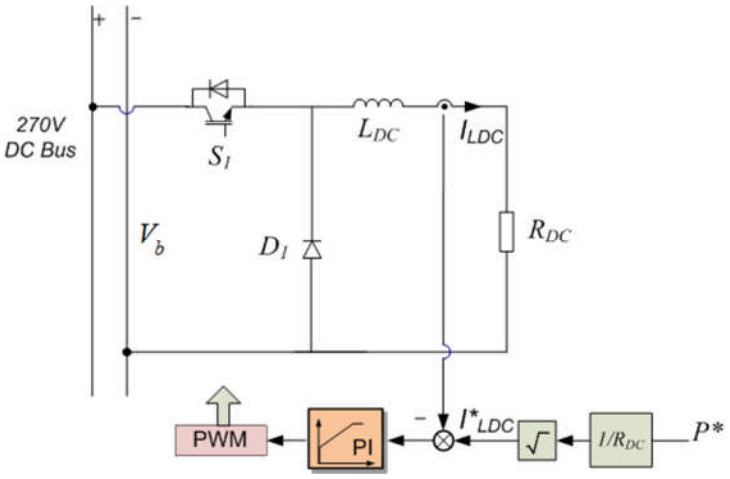

Figure 5.16. Control scheme of the buck converter.

The droop gain of the source subsystem is set to 2 and the power of the buck converter is regulated to 3 kW. Figure 5.17 shows the source impedance of the current-mode system with a different I_{dc} control bandwidth. Meanwhile the input impedance of the buck converter (load impedance Z_L) is also shown to see the interaction between the source and load subsystem.

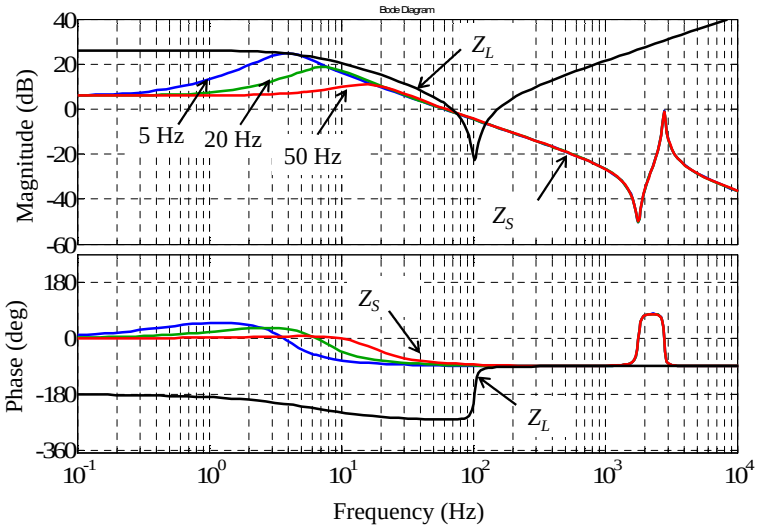

Figure 5.17. Bode diagram for the current-mode droop-controlled system with different I_{dc} control bandwidth.

It can be seen that slow I_{dc} control dynamics (5Hz bandwidth) will challenge the stability since the magnitude of source impedance hits the load impedance at around 3Hz while the phase difference between source and load impedances exceeds 180°.

Increasing the I_{dc} control bandwidth can attenuate the peak magnitude of the source impedance and consequently increase the stability margin. However it should be noted that the RHP zero in (5-9) could impose severe stability limitations, including high gain instability and restricted closed-loop bandwidth [169]. It is well-known from classical root-locus analysis that as the feedback gain increases towards infinity, the closed-loop poles migrate to the positions of the open-loop zeros. In other words, in the presence of the RHP zero, the gains of the controller/compensator cannot exceed certain values, otherwise the system eigenvalues will be moved to the RHP with the appearance of instability. It can be seen that the RHP zero migrates closer to the origin and results in strict limitations on the feasible bandwidth of the DC current loop. According to [169], the feasible bandwidth should be approximately limited:

$$\omega_{Idc} < \frac{z}{2} = \frac{-(v_{qo} + R_s i_{qo} - \omega_e L_s i_{do})}{2 L_s i_{qo}} \tag{5-31}$$

In practical cases the DC current loop bandwidth cannot exceed the upper limit due to the cascaded control structure.

5.4.5.2 Voltage-Mode Droop-Controlled System

The voltage-mode droop-controlled system consists of two loops: the V_{dc} control loop and the inner current loop, as shown in Figure 5.5. Droop control is implemented as a feedforward link while Figure 5.18 shows the source and load impedance with a different V_{dc} control bandwidth. It can be seen in Figure 5.18 that with a 5Hz V_{dc} control bandwidth the source impedance magnitude hits the load impedance and the phase discrepancy is larger than 180º, indicating that the system is unstable. With a higher control bandwidth (10 or 20Hz), the magnitude of the source impedance is always lower than the load impedance. Therefore system stability is guaranteed when the V_{dc} control bandwidth is increased (in this example - to 10 or 20Hz).

Similar to the current-mode system, it should be noted that the RHP zero in (5-9) could impose severe stability limitations, including high gain instability and restricted closed-loop bandwidth [169]. Therefore, in the presence of the RHP zero,

the gains of the controller/compensator cannot exceed certain values, otherwise the system eigenvalues will be moved to the RHP and the instability appears.

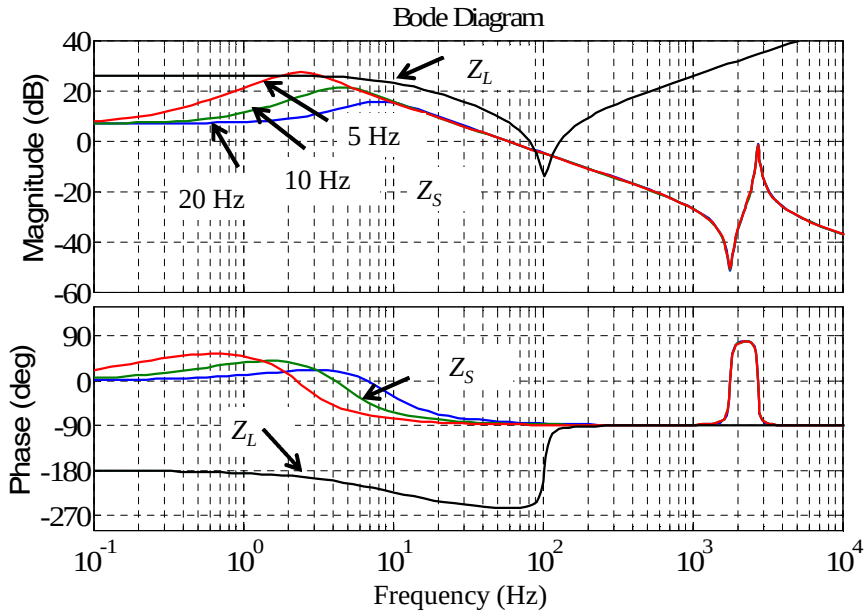

Figure 5.18. Bode diagram for the voltage-mode droop-controlled system with different V_{dc} control bandwidth.

5.4.6 Effect of Droop Gain

5.4.6.1 Equilibrium Point-Upper Limit

It is known that a larger droop coefficient will cause more voltage deviation and therefore the system needs to be designed carefully in order to ensure that the equilibrium point is achievable according to the load power. As shown in Figure 5.19, the V-I characteristic of the main bus can be expressed as

$$V_b = V_o - (k_i + R_i) I_o \tag{5-32}$$

For the load side a CPL creates a hyperbolic line which can be expressed as:

$$P_{CPL} = V_b I_o \tag{5-33}$$

where P_{CPL} is the power of CPL and I_o is the load current. The system can operate normally only if the two curves have an intersection point (equilibrium point). The stable equilibrium point can be derived as follows:

$$V_b = \frac{1}{2}(V_o + \sqrt{V_o^2 - 4(k_i + R_i)P_{CPL}}), \quad I_o = \frac{1}{2k_i}(V_o - \sqrt{V_o^2 - 4(k_i + R_i)P_{CPL}}) \tag{5-34}$$

Figure 5.19(a) shows that a larger droop constant will cause larger bus voltage deviation and might result in there being no intersection point between the source curve and CPL curve (for example the k_3 curve). As a consequence, no steady-state solution can be found, leading to instability. Using (5-34), the maximum droop gain can be derived as

$$k_i < \frac{V_o^2}{4P_{CPL}} - R_i \tag{5-35}$$

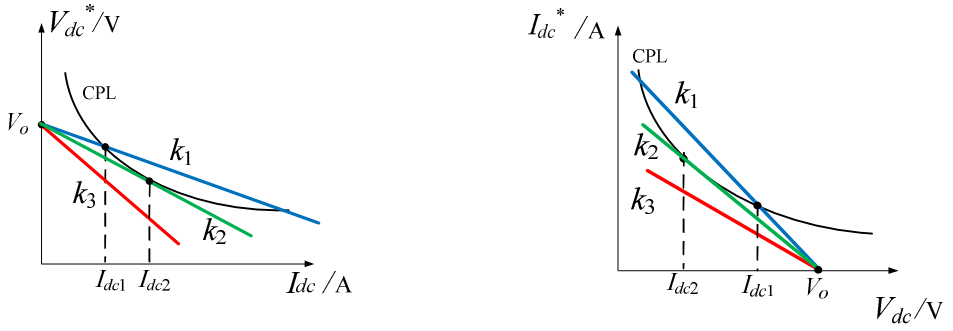

(a) (b)

Figure 5.19. Interaction between the droop-controlled source system and CPL. (a) Voltage-mode. (b) Current-mode.

5.4.6.2 Source and Load Impedance Interaction-Upper Limit

The droop coefficient will also influence the source and load impedance and consequently affect the system stability. For the current-mode droop approach, the Bode diagram of the impact of droop gain on the source and load impedance is shown in Figure 5.20. With an increase in the droop coefficient, the source impedance magnitude increases (especially at low frequencies). The DC bus voltage will reduce and, as a result, the magnitude of the load impedance will decrease

according to (5-19) (see Figure 5.19(b)). Overall, the system stability margin decreases with increased droop gain.

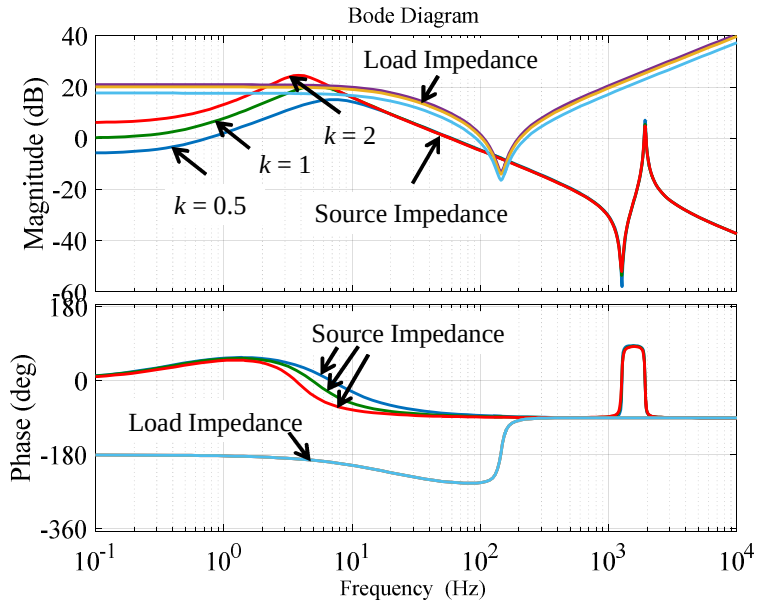

(a)

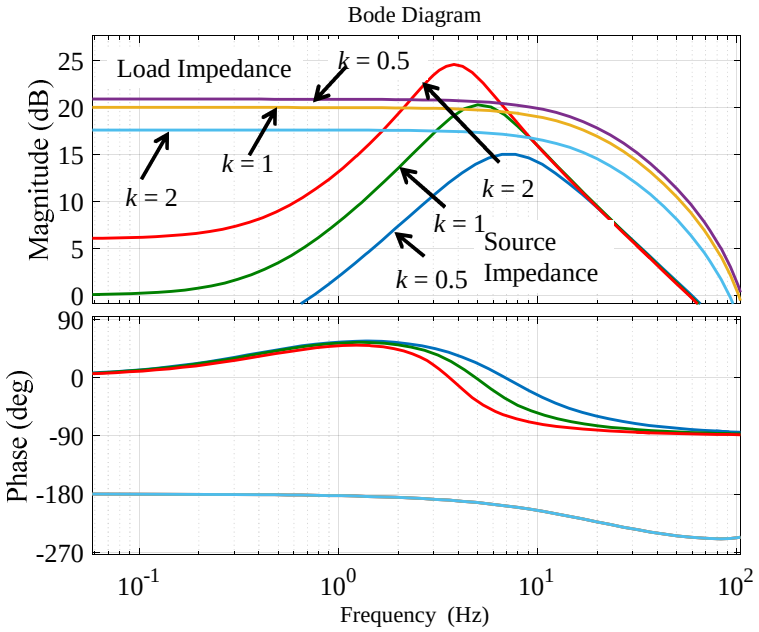

(b)

Figure 5.20. Bode diagram of source/load impedances with different values of droop gain using the voltage-mode droop control approach (6 kW CPL). (a) Overview. (b) Zoomed part of the load impedances.

The Bode plot of the source and load impedance in the voltage-mode droop-controlled system is shown in Figure 5.21. Similarly to the current-mode system, the source impedance magnitude in the low frequency range also increases with an increase in the droop gain whilst the load impedance magnitude decreases. Therefore, the stability of the voltage-mode system is also degraded with the increase in the droop gain. However it is worth noting that, in contrast with the current-mode approach, the frequency peak within the voltage-mode approach is quite similar under different droop gains and the peak can be attenuated by increasing the voltage loop bandwidth (see Figure 5.18).

In summary, the upper boundary of the droop gain is limited by two factors: existence of the equilibrium point and source and load impedance interaction. Hence the upper threshold value of the droop gain has to be set in order to ensure that the steady-state operating point is achievable, according to the specific system loads, and in order to avoid interaction of the source/load impedance.

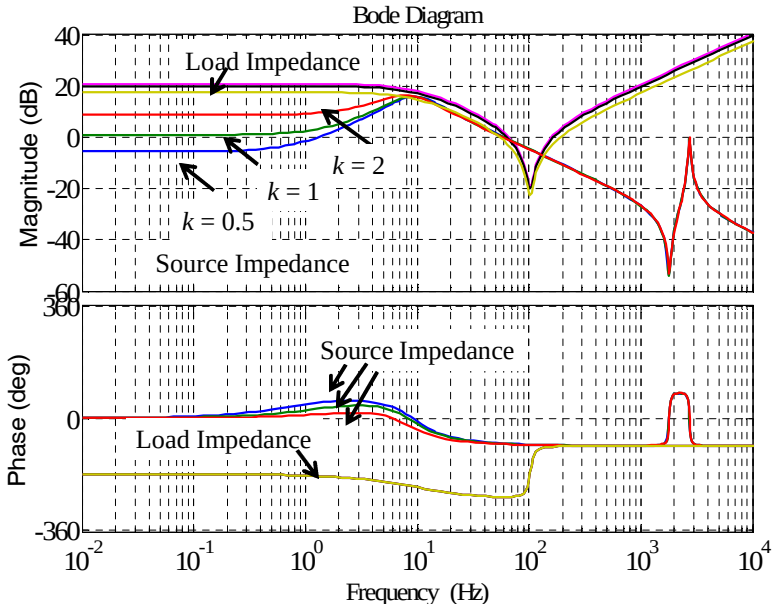

(a)

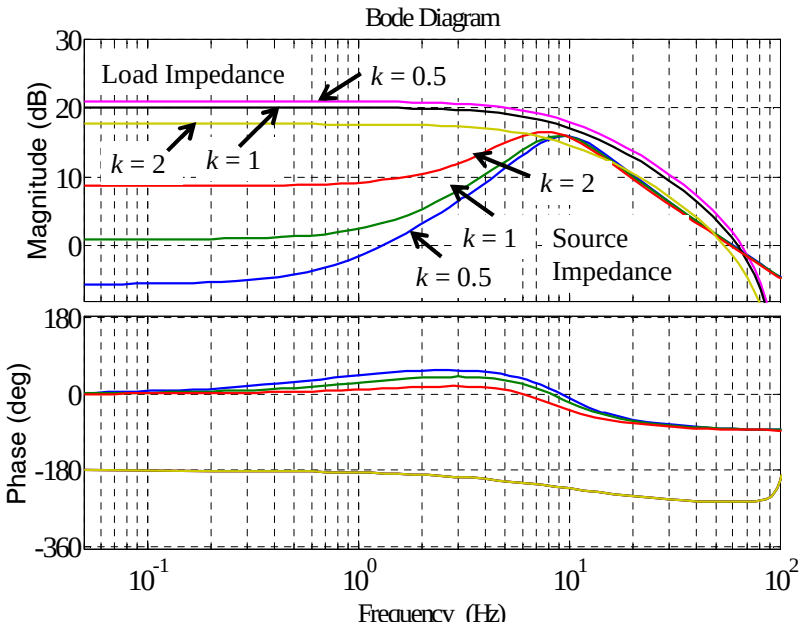

(b)

Figure 5.21. Bode diagram of source/load impedances with different values of droop gain using the voltage-mode droop control approach (6kW CPL). (a) Overview. (b) Zoomed part of the load impedances.

5.4.6.3 Non-minimum Phase Property-Lower Limit

For the current-mode droop approach, as discussed in Section 5.4.6.1, decreasing the droop gain *k* reduces the steady-state DC voltage error and increases the voltage-loop bandwidth. However this also reduces the damping and robustness of the system, leading to a lower boundary for the droop gain.

Figure 5.22 shows the layout of the poles and zeros of the source impedance of current-mode system derived in (5-23). It is clearly seen that poles in the RHP appear if the droop gain is set to be less than 1/40 and, therefore, the source subsystem is not stable in stand-alone condition. Hence, decreasing the droop gain can also lead to the instability phenomenon. As the load impedance is equivalent to a negative resistance, the impedance ratio of source impedance and load impedance has RHP poles, which reveals the non-minimum phase property of the system.

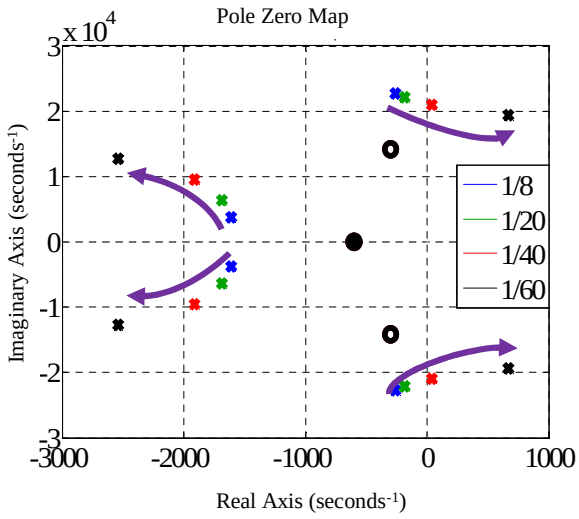

Figure 5.22. Pole-zero plot of source impedances with droop gain variation.

This effect can be also explained from the standpoint of control design. Droop gain is effectively a proportional controller: as shown in Figure 5.23, the droop gain reciprocal can be regarded as the proportional gain of the DC voltage controller. Following discussion in the previous section, due to the presence of the RHP zero in control dynamics of the current-mode system G_{Dy_CM} (see(5-8)), a high proportional gain (i.e. inverse of the droop gain, 1/k) will push the non-minimum phase system to instability due to the movement of some system eigenvalues into the RHP. Figure 5.24 shows the root contour with respect to the proportional gain (1/k), demonstrating that the system is unstable when the inverse of droop gain 1/k is higher than 40 (k is lower than 1/40).

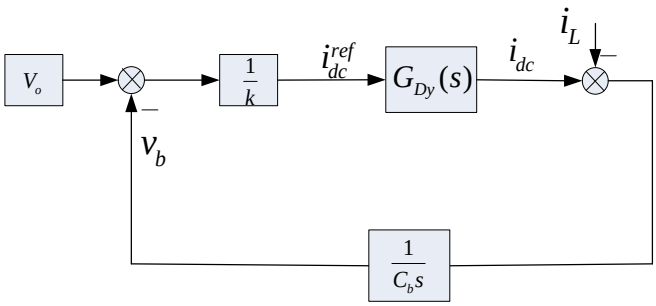

Figure 5.23. Equivalent control block diagram.

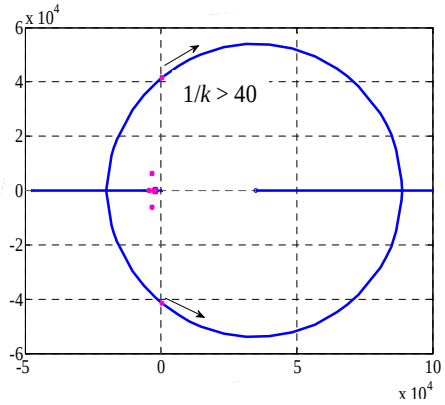

Figure 5.24. Root contour with respect to droop coefficient.

A distinct characteristic of the voltage-mode droop approach is that the droop gain lies in a feedforward term, as discussed in subsection 5.2. Hence a small droop gain k does not deteriorate the system stability. This is a significant advantage of voltage-mode droop over current-mode droop.

A comparison of the control properties of current-mode and voltage-mode droop control is listed in Table 5-2. Comparing the control schemes in Figs. 7 and 9, three control loops exist in the current-mode system whilst only two cascaded loops exist in the voltage-mode system. The local control bandwidth (I_{dc} control bandwidth for current-mode system / V_{dc} bandwidth for voltage-mode system) are limited by the non-minimum phase property (upper boundary) and source/load impedance interaction (lower boundary).

Table 5-2 Comparison of the control properties under current/voltage mode droop control

Control bandwidth / Droop mode	**Upper Limit**	**Lower Limit**	**Control loops**
Current-mode	Non-minimum phase property (Eq. (24))	Source/load impedance interaction (Eq. (23))	DC voltage control + DC current control + Inner current control
Voltage-mode	Non-minimum phase property	Source/load impedance interaction	DC voltage control + Inner current control

The limitations on stability imposed by the droop gain are summarised in Table 5-3. For current-mode droop control, the RHP zero in G_{Dy_CM} imposes a tighter lower limit for the droop gain and restricts the system stability. In contrast, voltage-mode droop control can operate with a wider range of droop gain or even with zero droop gain, i.e. constant voltage control. However, for both droop approaches a larger droop gain will reduce the stability margin, introduce more voltage deviation and even cause non-operability of the system due to the absence of a steady-state operating point. Furthermore, in the current-mode system, the droop gain will infuence the DC voltage control dynamics. Meanwhile, in the voltage-mode system the DC voltage dynamics are not affected by the droop gain (see Section II-B).

Table 5-2 Comparison of upper and lower limit for the droop gain under current/voltage mode droop control

Droop gain / Droop mode	Upper Limit	Lower Limit	Control block diagram	Influence on DC voltage dynamics
Current-mode	Equilibrium point + Source/load impedance interaction	Non-minimum phase property	Proportional controller in forward channel	Yes
Voltage-mode	Equilibrium point + Source/load impedance interaction	Not less than 0	Feedforward term	No

5.5 Simulation Results

Having investigated the influence of some key parameters in the single source based system, simulation has been carried out in Matlab/Simulink for the system with single source to validate the effect of the above mentioned components/control parameters on the system stability.

5.5.1 Effect of Cable Impedance

Figure 5.25 shows the results of time-domain simulations of the single source EPS

for different values of cable impedance. The power of the CPL increases step wise at +5kW every 0.01 s since t = 0.02 s. It can clearly be seen from Figure 5.25(b) that larger cable inductance will lead to instability. Figure 5.25(c) shows the stabilising effect of the increased feeder resistance. In other words, increased cable resistance will increase the system damping in order to compensate for the negative resistance characteristics of the CPL.

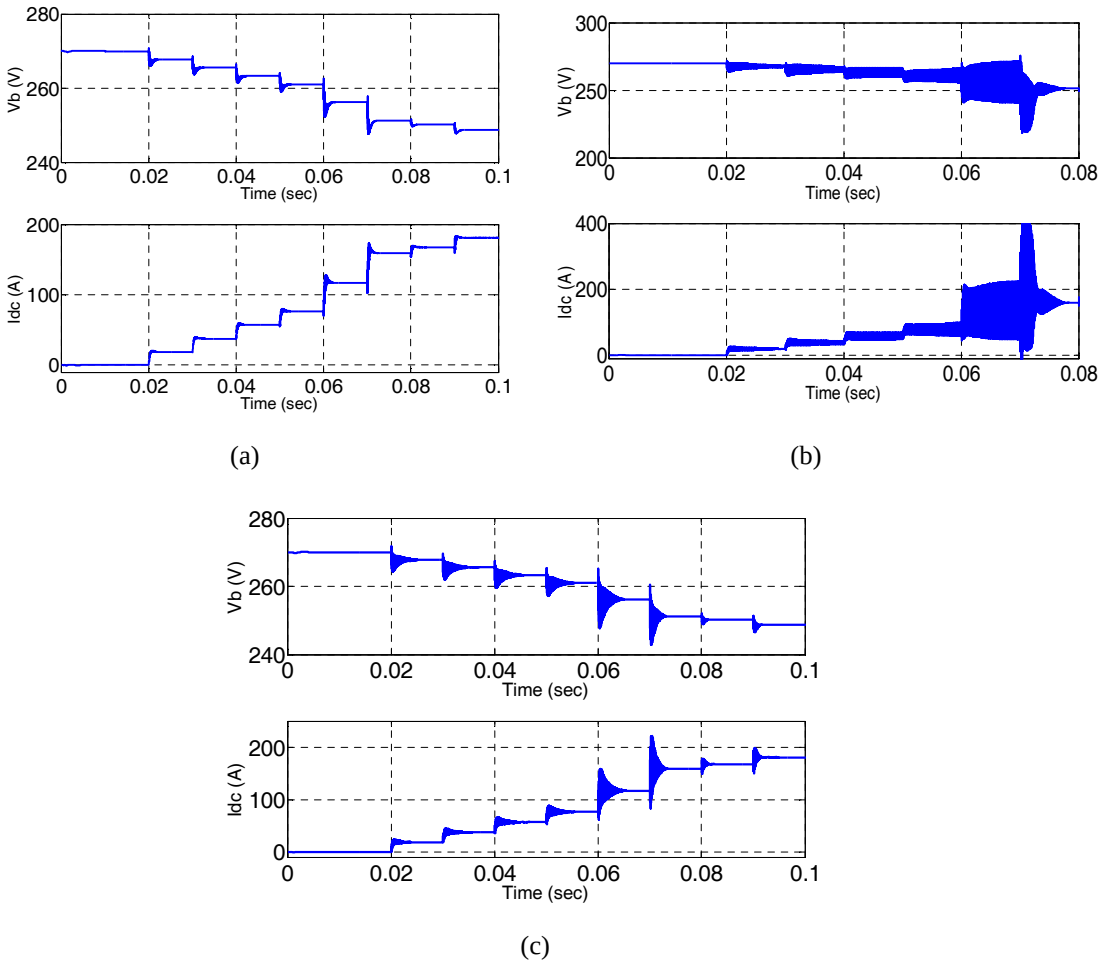

Figure 5.25. Bus voltage and DC current for cable impedance variations. (a) 1 mH+3 mΩ. (b) 4 mH+3 mΩ. (c) 4 mH+6 mΩ.

5.5.2 Effect of Local Capacitor

Simulation results for varying bus capacitance are shown in Figure 5.26. Stable operation under full load (40kW) is achieved with 0.3 mF bus capacitance. However, at lower bus capacitance (0.06 mF) instability occurs when a CPL of (25 kW) is applied.

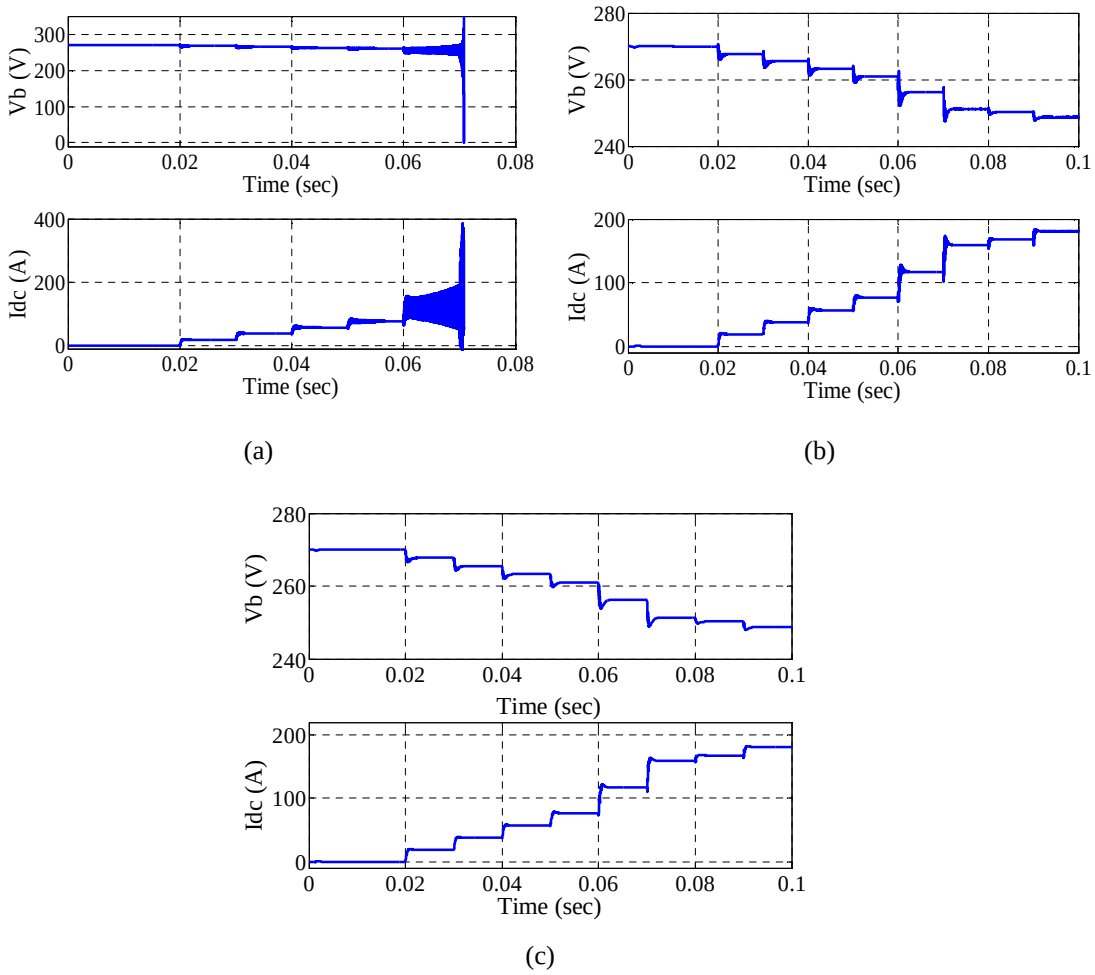

Figure 5.26. Bus voltage and DC current at different bus capacitance. (a) 0.06 mF. (b) 0.1 mF. (c) 0.3 mF.

5.5.3 Effect of Droop Coefficient

Simulations reported in Figure 5.27 shows the effect of droop gain on stability. The bus capacitance is set to 0.3 mF. It can be seen that normal operation can be guaranteed when a small droop gain (1/8.5) is applied. The oscillation appears at t = 0.2 s when the droop gain is reduced to 1/50 which confirms the destabilising effect of the decreased droop gain. Above t = 0.25 s, the system restores stable operation when the droop gain is adjusted to 1/10. However, the system tends to be unstable again when the droop gain is set to 1/4. A large voltage drop on the DC bus is also visible from Figure 5.27 at the heavy load above t = 0.3 s. These results are consistent with the impedance analysis in Section 5.7.5.

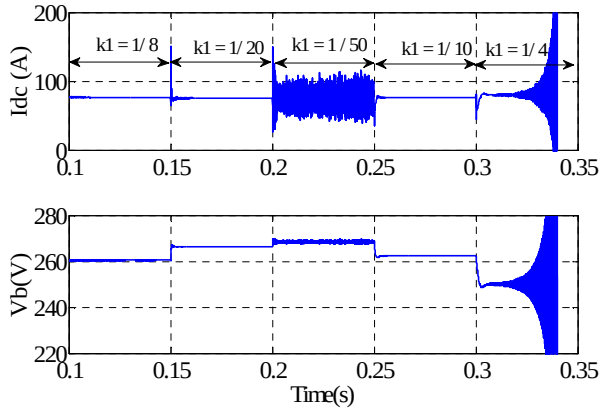

Figure 5.27. Bus voltage and DC current for varying droop gains in current-mode system.

5.5.4 Effect of DC Current Control Bandwidth

Simulation results for the single source system with a 10Hz control bandwidth of DC current in current-mode system is shown in Figure 5.28. The CPL increases step-wise every 0.1 s. Significant oscillation can be observed above t = 0.4 s when the system is working under full load. In comparison, the system with a 50Hz control bandwidth is simulated again, as illustrated in Figure 5.29. The system can be stabilised by properly increasing the control bandwidth and the dynamic response is also improved. Also, these results match the effect of control bandwidth on stability discussed in Subsection 5.7.4.

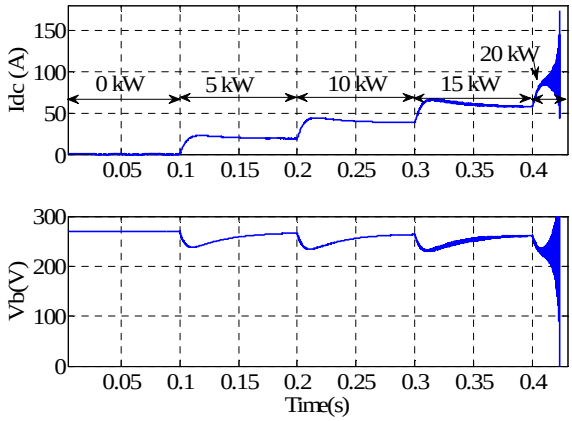

Figure 5.28. Simulation results for 10Hz DC current control bandwidth.

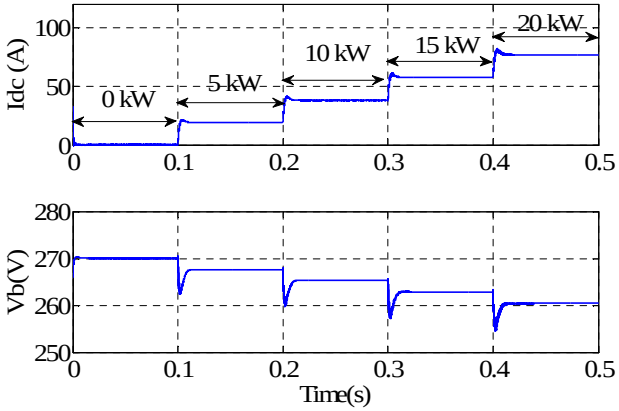

Figure 5.29. Simulation results for 50Hz DC current control bandwidth.

5.6 Chapter Summary

This chapter considered the stability study of single source EPS under different droop control approaches. Firstly, a comparative study of the ideal system without inclusion of control dynamics has been conducted using impedance-based criterion. This shows that the current-mode GVF approach has the most critical condition in terms of stability although it shows best performance in power sharing.

The main findings of this chapter can be summarised as follows:

1) among the current-mode droop control schemes, GVF shows better power sharing performance but additional sensors or communication lines are needed which compromise the modularity and reliability of droop control. LVF and GVF methods display similar stability performance when taking the converter dynamics into account

2) when utilising current-mode droop control, increased DC current control bandwidth is helpful for stability enhancement of the system since it avoids source/load impedance interactions. However the upper boundary of DC current control bandwidth is limited by the RHP zero. For the current-mode droop-controlled system, the DC voltage dynamics are affected by the DC current control bandwidth and the droop gain. It has been demonstrated that increasing the droop gain will reduce the voltage loop bandwidth

3) for the voltage-mode approach, the RHP zero causes high gain instability within the V_{dc} controller, i.e. the system will easily become unstable when the V_{dc} controller has a high gain. When utilising voltage-mode droop control, the voltage loop bandwidth is mainly determined by the voltage controller rather than the droop gain.

4) assuming the existence of a steady state operating point and the absence of source/load impedance interactions, an upper boundary for the droop gain can be defined in both techniques. Under current-mode droop control, a lower boundary is imposed due to the RHP zero, whilst voltage-mode droop control is feasible for wider droop gain settings even under zero droop gain (constant DC voltage control).

5) depending on the practical application, the required droop method can be chosen appropriately. If constant nominal voltage control is not required, and the main control objective of the AFEs is to inject/absorb current/power, then current-mode droop control is preferred. In this case, the DC voltage will reduce according to the load and the reduction rate will be related to the droop slope. Nevertheless, the nominal voltage (270 V in this study) can not be obtained when the system is loaded since the current-mode droop control approach is not feasible under zero droop gain. In contrast, if the DC voltage needs to be tightly regulated, and the nominal voltage is required in full load conditions, then voltage-mode droop control is recommended.

Chapter 6 Stability Analysis of Multi-Source DC EPS Under Droop Control

Following the impedance-based stability analysis of single source DC EPS in Chapter 5, this chapter will extend the stability analysis to a generalised system consisting of multiple sources and loads.

6.1 Introduction

A generalised EPS structure composed of multiple sources and multiple loads is illustrated in Figure 6.1. This chapter will extend the impedance analysis, discussed in previous chapters, to the general case of multi-source single bus EPS topology with multiple loads of different natures. By investigating the equivalent source and load impedances, a stability assessment of parallel source operation including the impact of power sharing ratio and number of paralleled modules has been performed in this chapter. The main contribution of this chapter can be summarised as follows:

- The equivalent source impedance under current-mode (LVF and GVF) and voltage-mode droop control has been derived and comparative Nyquist contours have been shown to analyse the system with multiple sources and loads;

- In addition, the concept of global droop gain has been proposed to analyse the system stability with multiple sources and loads. Employing the proposed concept, the main bus V-I characteristic can be analysed and dynamic stability of the parallel sources can be analysed in an explicit way.

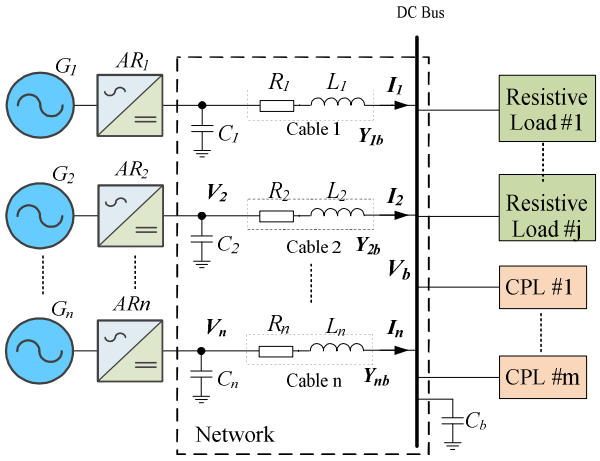

Figure 6.1. Generalised EPS structure with multi-generator feeding single DC bus with multiple loads.

6.2 Equivalent Source and Load Impedance

Equivalent source and load impedance for the multi-source multi-load system shown in Figure 6.1 is analysed in this subsection.

6.2.1 Equivalent Source Impedance

Taking the current-mode LVF approach (see Figure 4.7(a)) as an example, Figure 6.2(a) presents the generalised multi-source based source bank, with the desirable load power sharing realised by decentralised droop control. The cable admittance from the i^{th} source to the bus can be written as follows:

$$Y_{ib} = \frac{1}{R_i + L_i s} \tag{6-1}$$

Assuming that the control dynamics of n parallel modules are identical, the impedance-based model of the source bank is shown in Figure 6.2(b).

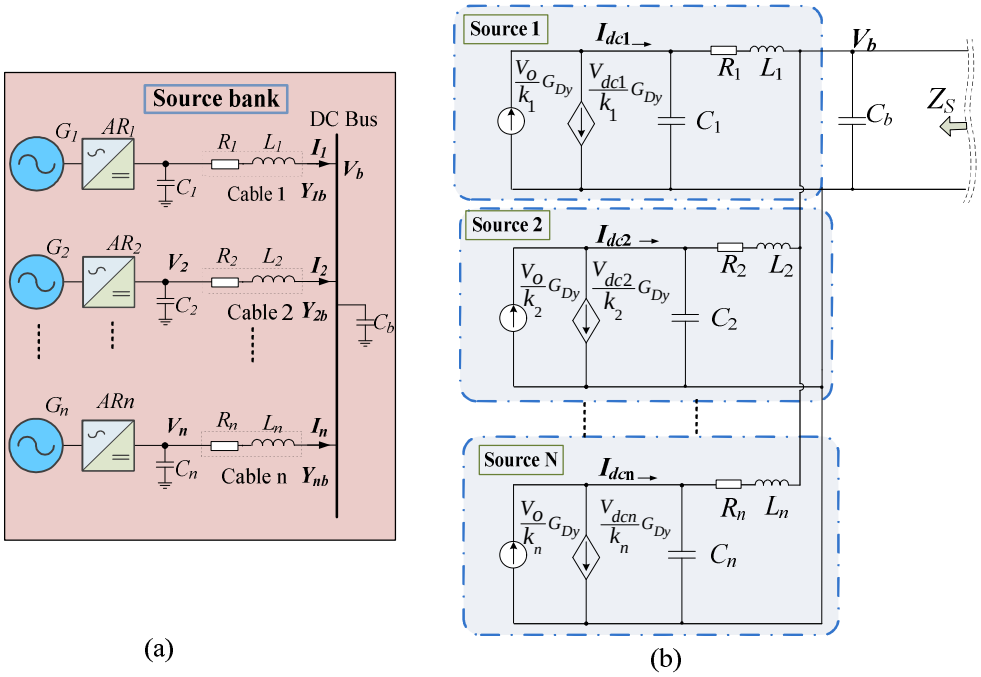

Figure 6.2. Multiple sources modelling. (a) Topology of multi-source feeding single bus. (b) Impedance model of parallel sources.

Similar to the derivation process in Chapter 5 for single-source EPS, the overall source impedance can be computed by the ratio of open circuit voltage and short circuit current of the bus bar. Based on Kirchhoff's law, open circuit voltage and short circuit current can be derived as follows:

$$V_{oc} = \frac{\sum_{i=1}^{n} \frac{Y_{ib} G_{Dy}}{k_i (Y_{ib} + C_i s)}}{\sum_{i=1}^{n} \frac{Y_{ib}(C_i s + \frac{G_{Dy}}{k_i})}{(Y_{ib} + \frac{G_{Dy}}{k_i} + C_i s)} + C_b s}, \quad I_{sc} = \sum_{i=1}^{n} \frac{Y_{ib} G_{Dy}}{k_i (Y_{ib} + C_i s)} \tag{6-2}$$

and the source impedance can be expressed as:

$$Z_{s\_P\_LVF} = \frac{1}{\sum_{i=1}^{n} \frac{Y_{ib}(C_i s + \frac{G_{Dy}}{k_i})}{(Y_{ib} + \frac{G_{Dy}}{k_i} + C_i s)} + C_b s} \tag{6-3}$$

Similarly, the source impedance for parallel sources using GVF approach (see Figure 4.7(b) in subsection 4.3.2) and voltage-mode approach can be written as in (6-4) and (6-5),

$$Z_{s\_P\_GVF} = \frac{1}{-\sum_{i=1}^{n} \frac{Y_{ib}(Y_{ib} - \frac{G_{Dy}}{k_i})}{(Y_{ib} + C_i s)} + C_b s + \sum_{i=1}^{n} Y_{ib}} \tag{6-4}$$

$$Z_{s\_P\_VF} = \frac{1}{\sum_{i=1}^{n} \frac{1}{(\frac{1}{Y_{ib}} + k_i G_{dyi})} + C_b s} \tag{6-5}$$

The equivalent source impedance of the multi-source system has been derived for the subsequent stability analysis.

6.2.2 Equivalent Load Impedance

In modern EPS, there are many power electronic interfaced loads which may behave like CPL as shown in Figure 6.3(a). From the viewpoint of impedance analysis, the paralleled CPLs can be modelled according to Figure 6.3(b) in small signal manner and thus a total input load admittance of the cumulative CPL can be equivalently depicted in Figure 6.3(c).

Based on this, the input admittance of CPL (Y_{CPL}) can be expressed as

$$Y_{CPLt} = \sum_{i=1}^{n} Y_{CPLi} = -(\frac{P_{CPL1}}{V_b^2} + \frac{P_{CPL2}}{V_b^2} + \cdots + \frac{P_{CPLm}}{V_b^2}) = -\frac{\sum_{i=1}^{m} P_{CPLi}}{V_b^2} \tag{6-6}$$

where P_{CPLi} is the power of i^{th} CPL. Hence the equivalent load can be represented as a negative impedance ($-R_{CPLt}$) in parallel with a current source (I_{CPLt}):

$$\begin{cases} -R_{CPLt} = -\dfrac{V_b^2}{\sum_{i=1}^{m} P_{CPLi}} \\ I_{CPLt} = 2\dfrac{\sum_{i=1}^{m} P_{CPLi}}{V_b} \end{cases} \tag{6-7}$$

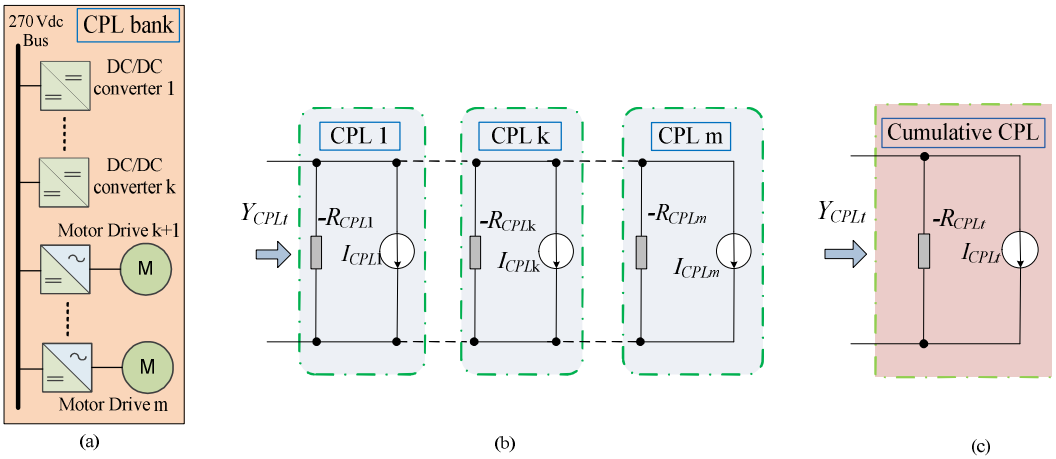

Figure 6.3. Multiple CPLs modelling. (a) Topology of single bus feeding multiple CPLs. (b) Impedance model of parallel CPLs in small signal manner. (c) Impedance model of cumulative CPL.

6.3 Global Droop Gain

Similarly to the droop characteristic of each individual module at the DC terminal, the main bus of the multi-source system also has the droop characteristic for the DC bus voltage and total load current. The global droop gain, which defines the main bus V-I characteristic, will be derived as below.

For a current-mode LVF and voltage-mode system, bus voltage can be expressed as follows:

$$V_b = V_o - I_1(k_1 + R_1) = V_o - I_2(k_2 + R_2) = \ldots = V_o - I_n(k_n + R_n) \tag{6-8}$$

The total load current can be written as

$$I_L = I_1 + I_2 + \ldots + I_n = (V_o - V_b)\sum_{i=1}^{n} \frac{1}{k_i + R_i} \tag{6-9}$$

Then equation (6-9) can be reformatted as

$$V_b = V_o - I_L \frac{1}{\sum_{i=1}^{n} \frac{1}{k_i + R_i}} \tag{6-10}$$

and the main bus voltage-current characteristic can be formulated as a linear line characterised by the droop gain as

$$k_{t-LVF} = k_{t-VM} = \frac{1}{\sum_{i=1}^{n} \frac{1}{k_i + R_i}} \tag{6-11}$$

The droop gain derived in (6-11) is defined as the "global droop gain" k_t.

For the current-mode GVF system, the global droop gain can be derived similarly as follows:

$$k_{t-GVF} = \frac{1}{\sum_{i=1}^{n} \frac{1}{k_i}} \tag{6-12}$$

The relationship between global droop gain and individual droop gain is depicted in Figure 6.4. It can be seen that the global droop slope k_t is stiffer than individual droop gain k_i. In other words, under the same load power the voltage drop at the main bus with multi-source operation is smaller than the voltage deviation under single source operation scenario.

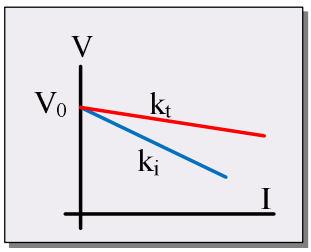

Figure 6.4. Relationship between global droop gain and individual droop gain.

6.4 Load Sharing Ratio Discussion

After analysing the global V-I characteristics at the main bus, the load sharing ratio among the parallel sources is of interest since it would affect the impedance and as a consequent, affect the stability of the overall system. Also, different power sharing ratio may yield different power loss, which it is well worth investigating.

6.4.1 Effect on Impedance

The power supplied to the DC bus by multiple sources can be adjusted by the ratio of the individual droop gain among the parallel modules.

The individual source droop gain setting can be defined as follows:

$$\begin{aligned} k_i &= k_t / n_i \\ \sum_{i=1}^{n} n_i &= 1 \end{aligned} \tag{6-13}$$

Assuming that the global droop gain is fixed, it can be observed from Figure 6.5 that the Nyquist contours are the same when the system is subjected to different power sharing ratios (1:1:1, 1:1.32:1.68, 1:1:2). It can be seen that the Nyquist contour does not encircle the critical point (-1, j0), indicating that the load sharing ratio hardly affects the overall system stability for current-mode LVF approach. For the other proposed droop control strategies, it is also found that the power sharing ratio does not influence the system stability.

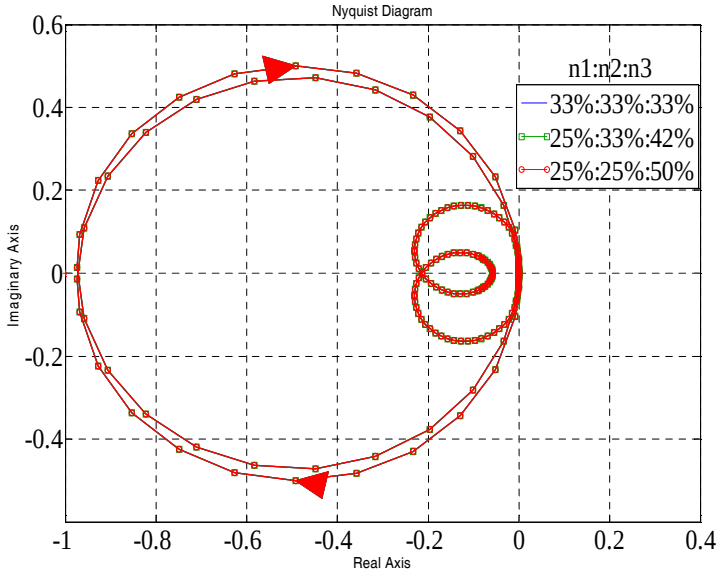

Figure 6.5. Nyquist contours for varying load sharing ratio using LVF approach.

As mentioned in Section 1.3.2, the parallel source can be from different shaft of the engine, i.e., LP and HP shaft. If the fundamental frequency of LP generator and HP generator are different (50Hz-LP and 400Hz-HP respectively), it is shown in Figure 6.6 that the total source impedance changes under different power sharing ratios. As discussed in Section 5.7.6, increase of the frequency has a detrimental impact on the system stability. Therefore, for a standalone operation, the low frequency source system is more stable than the high frequency source system if the other parameters of the system remain identical. It can be observed that the magnitude of the overall equivalent source impedance decreases if the low frequency system shares more power. It demonstrates that under the prerequisite that the load power does not exceed the ratings of the low frequency channel, the paralleling system will be more stable if the low frequency system provides more power to feed the load.

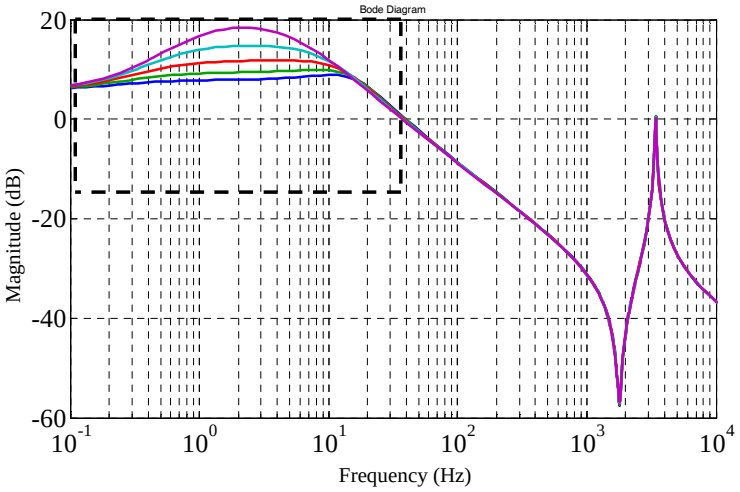

(a)

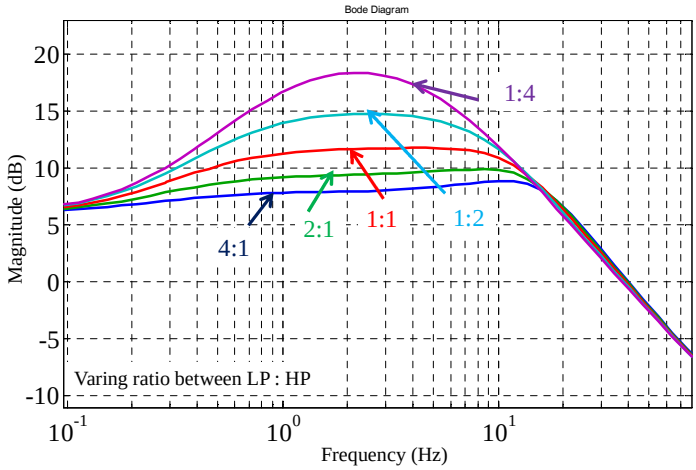

(b)

Figure 6.6. Bode plots of source impedance under different load sharing ratio LP (50Hz): HP (400 Hz). (a) Overview. (b) Zoomed area of low frequency area.

6.4.2 Effect on Power Loss

Power loss is also of concern in such EPS. The power losses include distribution loss, converter loss (switching loss and conduction loss). Cable modelling is highlighted in the thesis and the distribution loss is the main focus in this section. In order to minimise the distribution losses optimal power flow (OPF), which is discussed in multi-terminal DC grids [170], can be also investigated in this common bus architecture. If the cable length connecting each converter to the main bus is the same, the distribution losses can be expressed as follows:

$$\begin{aligned} & I_{Lt}^2 R_c (n_1^2 + n_2^2 + \cdots + n_n^2) \\ & Condition: \quad n_1 + n_2 + \cdots + n_n = 1 \end{aligned} \tag{6-14}$$

where n_i (i = 1, 2,…,n) is the load sharing percentage among all parallel sources. By solving the optimal issue developed in (6-14), the total distribution losses yield,

$$P_{Loss\min} = \frac{1}{n} I_{Lt}^2 R_c \tag{6-15}$$

where I_{Lt} is the total DC link current and R_{dc} is the equivalent DC line resistance connecting from each converter to the bus bar. Hence, it indicates that the losses can be minimised on the condition that each module shares the load current equivalently, i.e., (n_1 = n_2 =…= n_n). It can be inferred that the line losses in DC transmission/distribution lines are significantly reduced and further loss reduction could be obtained with more of parallel sources.

The abovementioned conclusion applies for the system with equal distribution cables. Without losing generality, the optimal power flow is also discussed below when the distribution cable length of modules is different. It is intuitive that distribution losses can be reduced if the module with long distribution line delivers less power and the one with short line provide more power to meet the load demand. Considering the EPS with two sources, optimal power flow can be formulated as follows:

$$\begin{aligned} & \min\{I_{Lt}^2 (n_1^2 R_1 + n_2^2 R_2)\} \\ & Condition: \quad n_1 + n_2 = 1 \end{aligned} \tag{6-16}$$

By solving (6-16), the optimal sharing proportion in symbolic form yields as follows:

$$n_1 = \frac{R_2}{R_2 + R_1}, n_2 = \frac{R_1}{R_2 + R_1} \tag{6-17}$$

It infers that the module with the higher resistance cable will provide a smaller portion while a lower resistance cable module will provide a higher portion to feed the load.

The converter losses which take switching loss and conduction loss into consideration can be examined as well. Based on a generalised converter loss expression in [171], [172], a single converter loss can be written as

$$P_{C-loss} = aI_{ac}^2 + bI_{ac} + c \tag{6-18}$$

where a, b, c is the coefficient defined in per unit [171] and I_{ac} is AC side current. The AC side current of each converter is reduced with the increase of the parallel converters. Assuming that the parallel sources share the power equally, the generalised converters loss of N parallel AFEs can be expressed as follows:

$$P_{C-loss\_parallel} = \frac{1}{N} aI_{ac}^2 + bI_{ac} + N * c \tag{6-19}$$

where I_{ac} is the total AC side current. Combining the line loss and converter loss shown in (6-15) and (6-19) respectively, the total loss of N parallel AFEs operation yields:

$$P_{loss\_parallel} = \frac{1}{N} I_{dc}^2 R_{dc} + (\frac{a}{N} I_{ac}^2 + bI_{ac} + N * c) \tag{6-20}$$

Figure 6.7 shows the power losses (line loss + converter loss) with respect to the number of sources/converters using (6-15), (6-19) and (6-20). It can be seen that the line losses keep reducing with the increase of the number of parallel AFEs. Alternatively, the converter losses reduce to a certain threshold value, with the initial increase of the number of parallel sources, and then increases with the number of sources. Therefore, with a correctly selected number of the multiple sources, parallel operation can effectively reduce the losses to some extent.

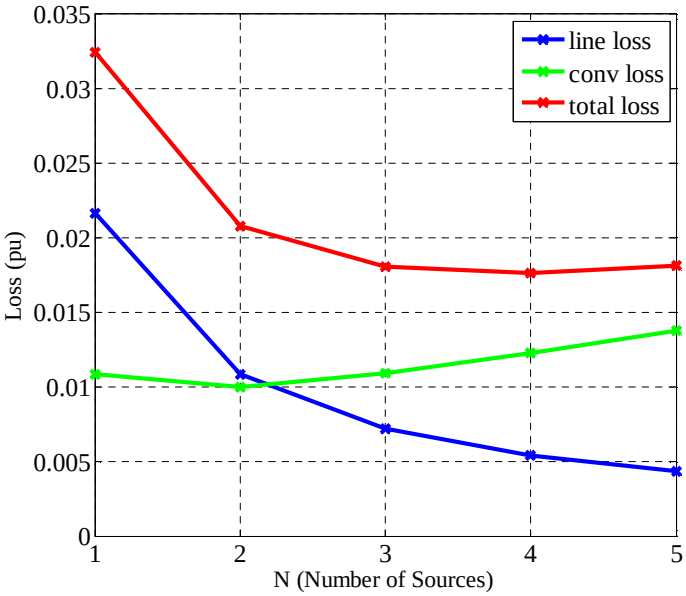

Figure 6.7. Power losses with respect to the number of sources.

6.5 Stability Assessment for Parallel Sources

This subsection will conduct the stability assessment of the parallel sources operation. The system stability with fixed and individual droop gain will be presented for the system using current-mode and voltage-mode approaches, respectively.

6.5.1 Current Mode System

Assuming that parallel sources have the same parameters and the global droop gain k_t is set to be fixed (1/8), the Bode plot of the equivalent source and load impedance of the system with parallel sources feeding multiple loads is shown in Figure 6.8. N stands for the number of parallel sources. If the global droop gain k_t is fixed, the V-I characteristic for the load subsystem is identical under the same CPL. It can be seen that within the 100 Hz control bandwidth of the load, the phase diagram shows -180°. It shows the negative impedance charactieristic within the load control bandwidth. It indicates that the bus voltage is invariant and consequently the load impedance is kept the same according to (6-6). It can be seen that parallel operation only slightly

changes the stability margin by increasing the number of parallel sources, as depicted in Figure 6.8. Since the droop gain is much larger than cable resistance, the impact of the droop gain dominates at the low frequency range response. As the global droop gain is fixed for parallel sources, the amplitude of the source impedance at low frequency is approximately the same.

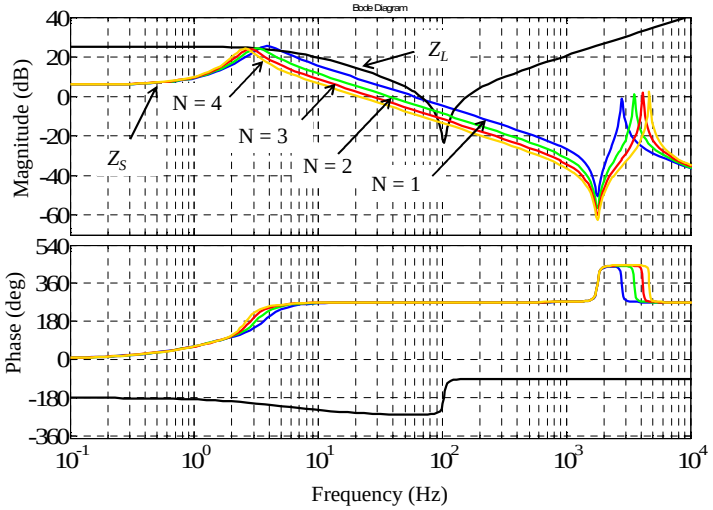

Figure 6.8. Bode plot for parallel sources with the fixed global droop gain (k_t = 2).

If the multiple sources work in parallel with the same individual droop gain (k_i = 2), the global droop gain k_t increases with the increasing number of parallel sources as expected from (6-11). For this case, the Bode diagram is shown in Figure 6.9(a). It is seen that at low frequency the source impedance decreases, and at the same load conditions the bus voltage drop decreases under parallel circumstances in comparison with a single module. Also, the resonance peak is reduces with the decrease of global droop gain (k_t). Similarly as shown in Figure 6.8, it can be seen that within the 100 Hz control bandwidth of the load, the phase diagram shows -180º. Indicating a negative impedance charactieristic within the load control bandwidth. As shown in Figure 6.9(b), load impedance magnitude increases with the increase of the number of parallel modules, which indicates that the system stability is improved if parallel sources are working with the identical individual droop gain (k_i).

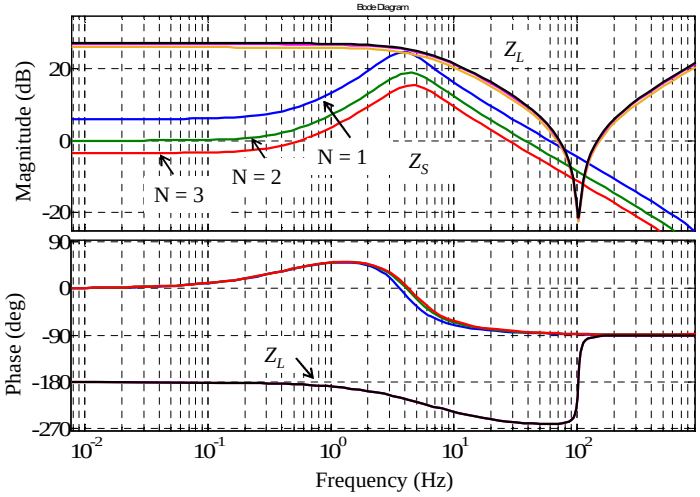

(a)

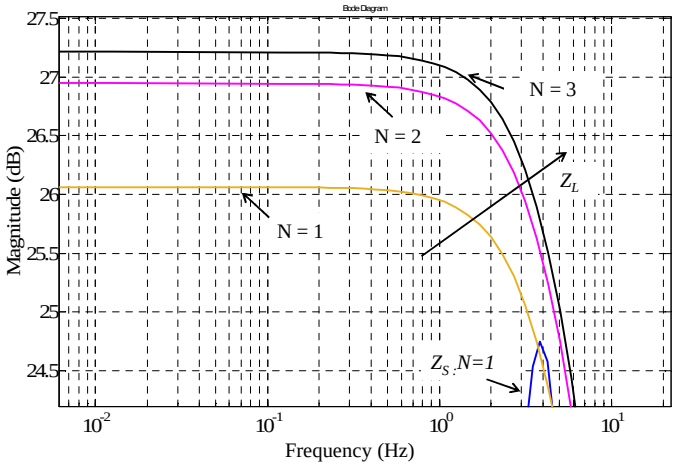

(b)

Figure 6.9. Bode plot for parallel sources with the same individual droop gain. (a) Zoomed area for source impedances. (b) Zoomed area for load impedances.

The Nyquist stability criterion has been widely accepted for stability analysis. Figure 6.10 shows the Nyquist plots of the minor loop gain ($T_{MLG} = Z_{S\_P}/Z_L$) for the current-mode droop-controlled system under a buck converter controlled at 6 kW. If each individual droop gain is set to 1, the global droop gain k_t decreases with an increasing number of parallel sources. As a consequence, the main bus voltage increases and the magnitude of the load impedance reduces, which is helpful for improving stability. In order to highlight the benefit of paralleling, the single source system is designed unstable on purpose. It can also be seen from the Nyquist diagram in Figure 6.10(a) that the single source EPS encircles the critical point (-1,

j0) and the Nyquist contour moves further towards the RHP with the increase number of parallel sources. This indicates that a higher stability margin is achieved by increasing the number of parallel modules.

Figure 6.10(b) shows the Nyquist plots of the minor loop gain for the current-mode droop-controlled system with identical global droop gain. It can be seen that the Nyquist contour moves towards right with increased number of parallel sources, which reveals that system stability could be still improved.

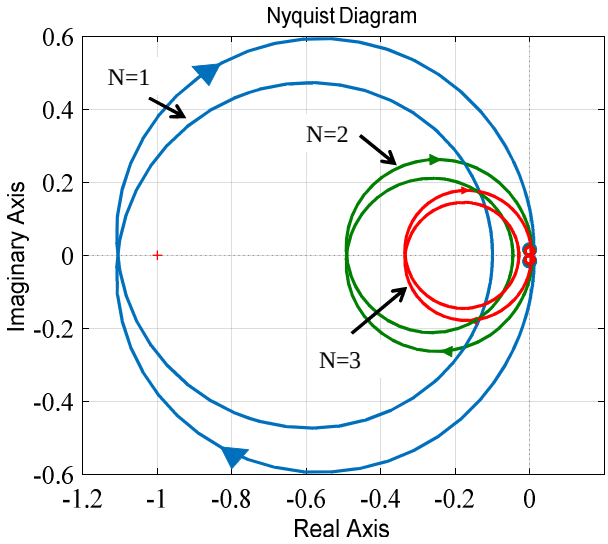

(a)

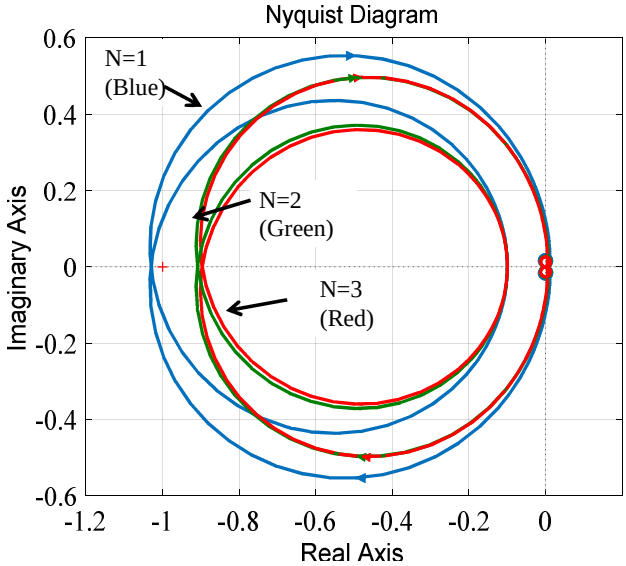

(b)

Figure 6.10. Nyquist contours for the current-mode droop-controlled systems (a) k_i = 1. (b) k_t = 1.

6.5.2 Voltage Mode System

For a 6kW CPL, the Nyquist diagrams of the minor loop gain for a voltage-mode droop-controlled system are shown in Figure 6.11. The overview of the Nyquist contour is shown in Figure 6.11(a) and it can be clearly seen from the zoomed version in Figure 6.11(b) that the Nyquist contour of the single source system encircles (-1, j0) whilst the system with more parallel sources does not encircle the critical point. This indicates that the stability is improved by increasing the number of modules with the same individual droop gain.

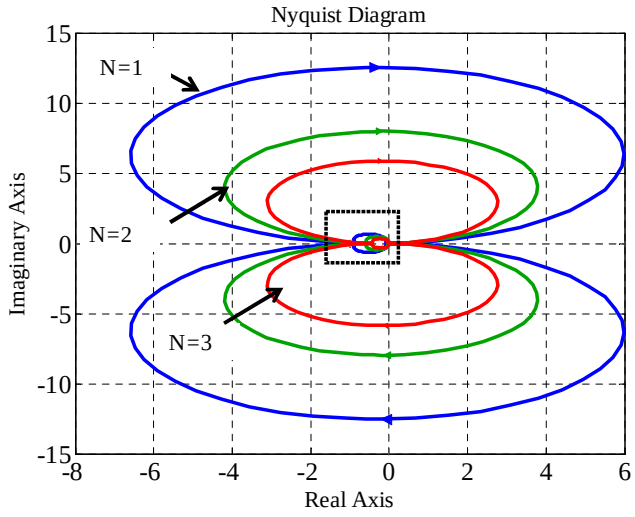

(a)

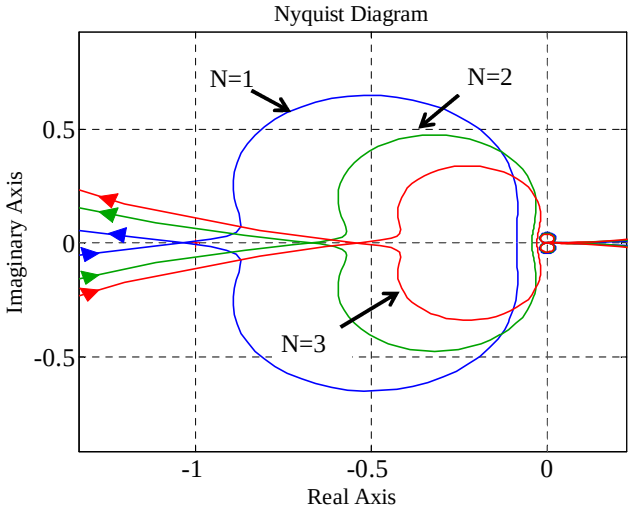

(b)

Figure 6.11. Nyquist contours for the voltage-mode droop-controlled system with individual droop gain k_i = 1. (a) Overview. (b) Zoomed part around (-1, j0).

In addition, Figure 6.12 shows the Nyquist contours of the voltage-mode droop-controlled system with fixed global droop gain. It is shown that the real-axis crossing points move to the right with anincreasing number of parallel sources, indicating that under parallel operation, with the same global droop gain, the system shows a larger stability margin.

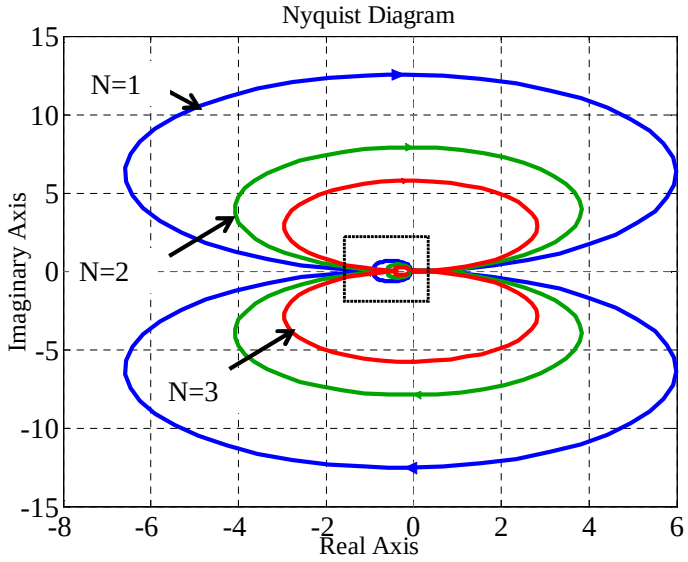

(a)

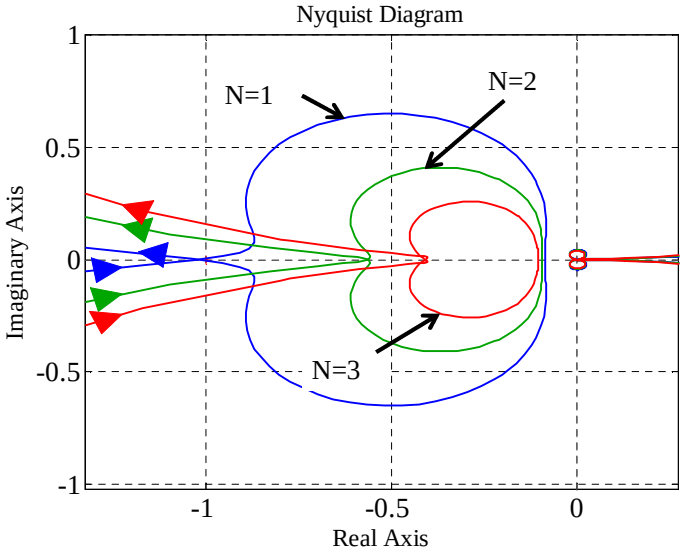

(b)

Figure 6.12. Nyquist contours for the voltage-mode droop-controlled system with global droop gain k_t = 1. (a) Overview. (b) Zoomed part around (-1, j0).

To summarise, the global droop gain is an important factor when evaluating the stability of a multiple source EPS feeding a single bus. With an increased number of parallel modules, the global droop gain reduces and as a consequence, the stability margin is improved for both current-mode and voltage-mode droop control. For both modes, paralleling sources while maintaining fixed global droop gain shows a higher stability margin than the single source system having identical droop characteristics.

6.6 Simulation Results

To support the theoretical analysis of the multi-system, time domain simulations have been conducted in Matlab/Simulink. The effect of the global droop gain and load sharing ratio among the parallel sources on the stability has been validated.

6.6.1 Effect of Global Droop Gain

Figure 6.13 shows simulation results for global droop gain variation. As seen, CPL power increases step-wise by 0.02s until t = 0.1s. Prior to t = 0.12s, the generator G_1 provides the full power to the bus to meet the load demand. It can be seen that the DC bus voltage reduces with the increasing load current and the steady state values match the droop characteristic. At t = 0.12s, the generator G_2 is connected to the grid with the same droop coefficient as G_1 ($k_1 = k_2 = 1/8$). As a result, the global droop gain k_t is changed to a smaller value of 1/16, according to (6-12), which results in smaller voltage drop at the bus under the same load power. The bus voltage changes from 260.4V to 265.3V after G_2 is connected. The results are in agreement with the discussion about the global droop gain in Section 6.4.

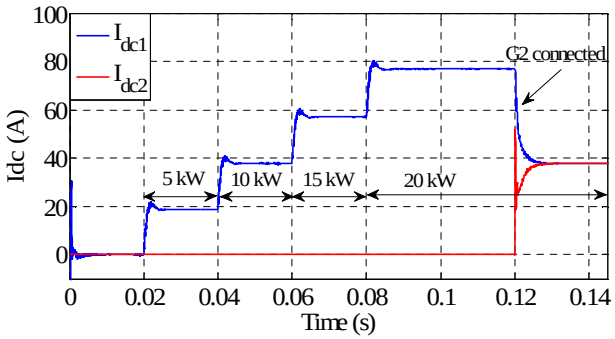

(a)

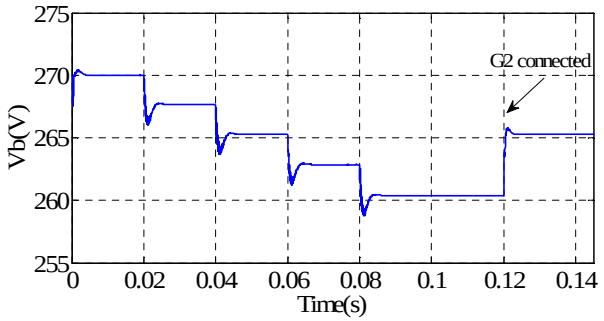

(b)

Figure 6.13. Simulation results of the connection of G_2. (a) DC current waveforms. (b) Bus voltage waveforms.

6.6.2 Effect of Load Sharing Ratio

To support the analysis in Section 6.5, the simulations in this subsection will show the varying load sharing ratio among the parallel sources whilst keeping the main bus voltage fixed. Figure 6.14 presents simulation results for the variation of the power sharing ratio between the two generators. The global droop gain is fixed to 1/16. Different ratios are tested, as shown in Figure 6.14(a), and corresponding different individual droop gains are calculated according to (6-13). This shows that the bus voltage is fixed although the current sharing varies between the parallel modules. System stability is not determined by the load sharing proportion among the sources. Again, this is in line with the analysis in Section 6.5.

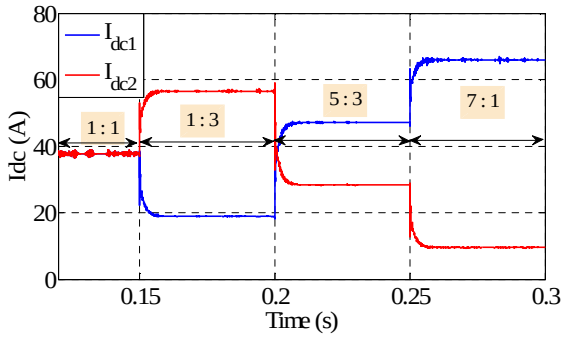

(a)

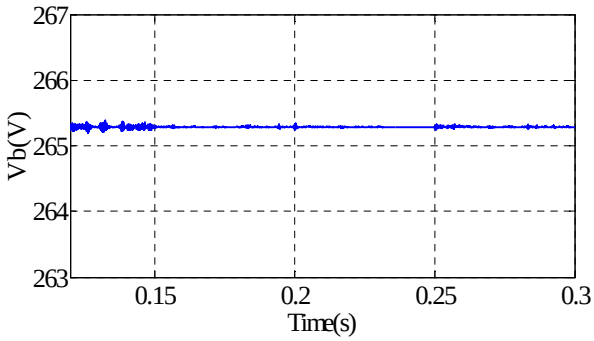

(b)

Figure 6.14. Simulation results of a variation of load sharing ratio. (a) DC current waveforms. (b) Bus voltage waveforms.

The simulation results show that the global droop gain can be used as the factor to determine the main bus V-I characteristic. With fixed global droop gain different power sharing ratio can be achieved. It is in accordance with the analysis in Subsections 6.3 and 6.4.

6.7 Chapter Summary

This chapter extends the stability analysis to the generalised multiple source multiple loads-based single bus EPS. An equivalent impedance model for the parallel sources and parallel loads are developed, based on which of the equivalent source impedance and load admittance are derived. A stability evaluation of parallel source based EPS configuration has been conducted in this chapter. The main findings can be summarised as follows:

1) global droop gain, a crucial factor to show the main bus V-I characteristic, was proposed in this paper to compare and analyse the stability of a multi-source multi-load system. It has been shown both analytically and experimentally that parallel operation improves system stability for both droop strategies;

2) a different power sharing ratio will affect the distribution losses. Assuming the condition that each generator can supply enough power to feed the load, the optimal power sharing ratio has been discussed to minimise distribution loss: The source with same length of feeders provides identical power whilst the long length of feeders provide less power;

3) when the sources have identical AC fundamental frequency and control dynamics, the power sharing ratio among the sources has an insignificant effect on the stability. When the sources are divided into low and high frequency sources, the low frequency source would provide more power in order to make the overall system stable.

Chapter 7 Proposed Voltage Compensation Method

This chapter analyses a proposed novel voltage compensation method (secondary control) for the droop-controlled DC EPS. The method significantly reduces the voltage regulation and simultaneously establishes the desirable load power sharing among the sources. The concept of the global droop gain proposed in Chapter 4 is revisited in this Chapter to facilitate the analysis of the proposed secondary control method. With the concept of the global droop gain, the main DC bus V-I characteristic can be derived under any load circumstance. The working principle of the method and the optimal droop gain settings to reduce the distribution losses are discussed. Simulation results are provided to confirm the effectiveness and performance of the proposed method.

7.1 Introduction

For a droop-controlled system, there is a trade-off between droop coefficients and voltage regulation [173]-[175]. High droop gain can guarantee precise power sharing among the sources while the voltage regulation performance is poor, i.e., voltage drop is high under high droop gains. In order to maintain the bus voltage for droop-controlled DC MEA EPS, a conventional method is to employ a secondary control to compensate the voltage drop. The principle of the secondary control is shown in Figure 7.1.

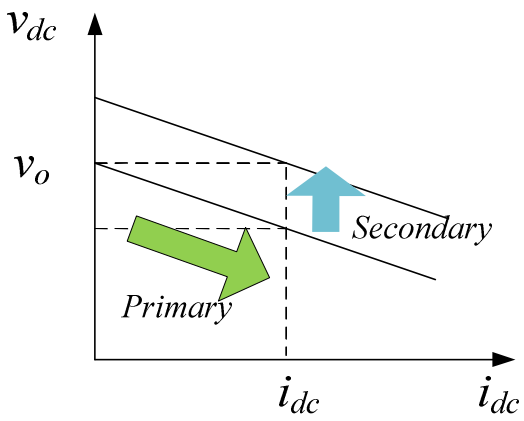

Figure 7.1. Secondary control on DC voltage restoration.

In [176] a three level control structure is proposed so that good load sharing performance and improved voltage regulation can be achieved simultaneously as shown in Figure 7.2. Secondary control is implemented by means of a voltage PI controller to eliminate the voltage deviation owing to voltage droop.

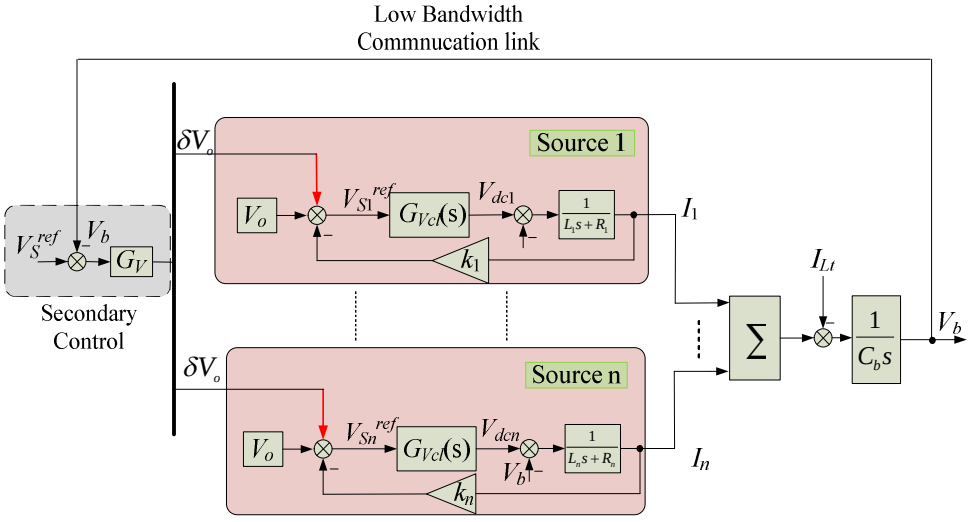

Figure 7.2. Hierarchical control structure for voltage compensation.

For the excitation system, reactive droop compensation and/or line drop compensation can be employed to compensate the voltage drop at the AC terminal. Reference [177] shows the load compensation in the excitation system so that a norminal AC terminal voltage operation is guaranteed. Nevertheless, this method is not applicable to a multiple-source based DC system. An enhanced droop method with improved voltage regulation is proposed in [178]. Average current and voltage is controlled by PI controllers and desired voltage compensation values to eliminate

the voltage deviation are obtained. However, the communications between the modules are still needed to generate desired compensation values. In addition, PI controllers are required to regulate the average voltage and current. In [179] large droop gain is recommended to overcome the load sharing error caused by line resistance and average current is used to modify each droop characteristic line so that each droop line is shifted up by a same amount with the increase of the load. However the average current needs to be computed and the choice of shift value becomes important but these are not easily implemented in practice. So far, a voltage compensation method, presented in previous literature, is based on the communication line and/or additional PI controller [176]-[179].

In contrast to conventional voltage restoration methods, an improved voltage compensation method in EPS without communication link is proposed in [180], however this study is limited to EPS with tightly regulated power electronic converters or motor drives behaving as CPLs. This chapter extends this voltage compensation method for droop-controlled EPS with mixed load types, including both CPLs and resistive or constant impedance loads (CILs).

Table 7-1 Comparison of exsiting voltage compensation approach in DC EPS

Method	Centralised controller	Low bandwidth communication line	PI controller	Average voltage/current calculation
[175]	No	Yes	Yes	No
[176]	Yes	Yes	Yes	No
[178]	No	Yes	Yes	Yes
[179]	No	Yes	No	Yes
Proposed approach	No	No	No	No

Table 7-1 shows a comparison of the existing secondary control methods in the DC system. It can be clearly seen that the prevous methods either rely on the digital

communication line, or on additional PI controllers, to maintain the norminal voltage. In contrast, the proposed compensation method has the following advantages [184]:

- load sharing accuracy is guaranteed and improves under higher droop gain
- no extra controllers and communication between the sources are needed
- voltage regulation can be realised even if the compensation gain cannot be quickly updated
- performance of the current sharing and voltage regulation are also good under most fault conditions
- system stability is not compromised or guaranteed with the proposed method
- the total load current and output current for each source is reduced for the same power, hence the efficiency of the system is increased due to reduced losses in lines and sources.For the machine-based generation system, the resistive loss in the machine is reduced and the overload capacity is increased to some extent.

In a voltage droop-controlled system the selection of droop gain is important since it impacts not only on the load sharing accuracy but also on the voltage regulation. Droop settings based on the reduction of generation cost are discussed in [181] and [182]. The generation costs include levelised capital, maintenance, and fuel cost, and the greenhouse emission penalty/incentive of each distributed generator (DG). To reduce this total generation cost, an autonomous droop scheme is proposed, in which resulting power sharing is decided by the individual DG generation costs. In [183] the droop gain for each terminal in the MTDC grids is obtained through a cost function which takes into account the power flow error, voltage deviation and distribution loss. However, distribution loss reduction based droop gain setting strategies for multi-generator based single bus DC EPS have not been investigated with the voltage restoration method. It is of interest to design proper droop gains to minimise the distribution loss when the DC terminal voltage restores to the nominal value. To fill this gap, this chapter considers optimal droop gain selection for parallel modules based on the minimisation of line losses within the proposed voltage compensation approach.

The main contributions can be highlighted as follows:

- an enhanced voltage compensation method to eliminate the voltage deviation in the droop-controlled EPS.
- a method for optimal droop gain selection based on the criteria of distribution loss minimisation is analysed.

The following sections will address the proposed method in detail.

7.2 Enhanced Voltage Restoration Method

7.2.1 Operating Principle

According to the droop control approach, the DC bus voltage will reduce according to the increase of the load power/current. In order to reduce the voltage drop under heavy loads this section proposes an enhanced voltage compensation method. This is illustrated by Figure 7.3 for voltage-mode and in Figure 7.4 for current-mode droop-controlled EPS. The method restores the terminal voltage to its nominal value autonomously. The G_V(s) in Figure 7.3 and G_C(s) in Figure 7.4 represent the control dynamics for the i^{th} converter in voltage-mode and current-mode, respectively. A feedforward term is added to the terminal voltage reference for each module which can be expressed as follows:

$$\Delta V = I_{Lt} k_t \tag{7-1}$$

where I_{Lt} is the total load current. It is easily implemented since only the load current needs to be measured and no DC voltage controller is in need. If multiple loads are in presence and distributed among the EPS, the total load current measurement can be obtained at the main feeders (if this exists) which supplies the power to all loads.

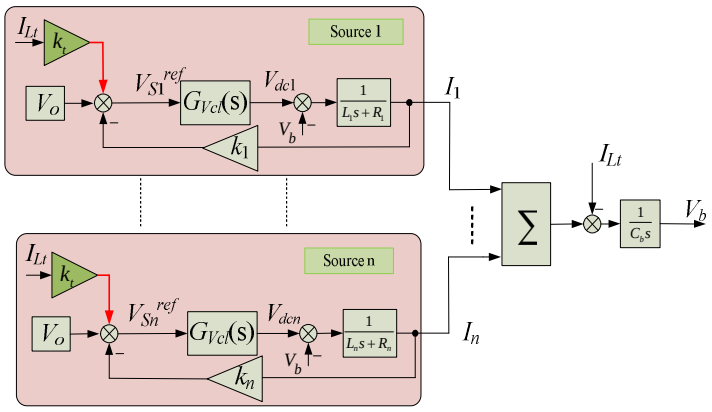

Figure 7.3. Proposed voltage compensation method for voltage-mode controlled converter [184].

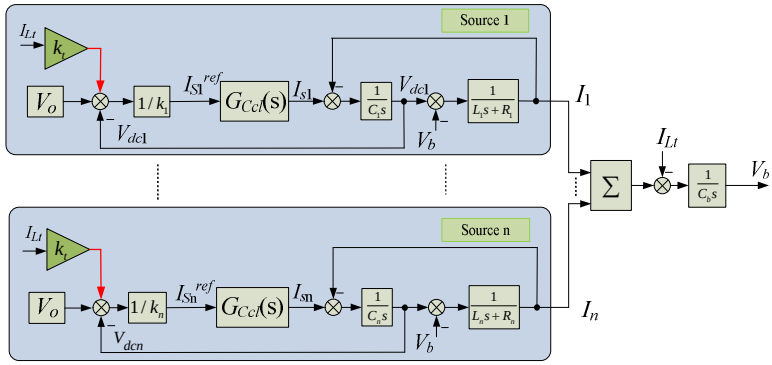

Figure 7.4. Proposed voltage compensation method for current-mode controlled converter [184].

Loads in typical EPS can be divided into three categories: CIL, CPL, CCL (constant current load). Resistive loads are considered as a typical representative of CIL. Its impedance is invariant with the applied voltage and current. As for the CIL, when the bus voltage is increased to the nominal voltage after the proposed voltage compensation method is applied, the total load current will increase accordingly. Therefore, the DC current flowing thorough each module will also increase. For the CPL, since the current is inversely proportional to the voltage, the demanding load current is reduced with the increase of bus voltage.

The working principle of the proposed compensation method under different load types is illustrated in Figure 7.5. The main bus V-I characteristic is represented by the straight line with slope k_t. Under conventional droop control, the operating point is shown as $\mathbf{op_0}$. After the voltage restoration technique is implemented, the operating point moves to $\mathbf{op_1}$, $\mathbf{op_2}$, and $\mathbf{op_3}$ for CPL, CCL, and CIL, respectively. It can be clearly seen that the DC current at $\mathbf{op_1}$ is smaller than $\mathbf{op_0}$, which indicates

that the proposed method can significantly reduce the total load current for pure CPL conditions. For the CCL, the operating point is relocated at **op$_2$** where the current is identical to the case at **op$_0$**. When the proposed method is applied for CIL, a new equilibrium point **op$_3$** is obtained and, as a result, the DC voltage is increased. In general, at any load condition, the voltage deviation (ΔV) caused by the conventional droop characteristic is compensated for. The terminal voltage is restored to its nominal value and meantime the droop slope is kept as before, which guarantees the load sharing performance.

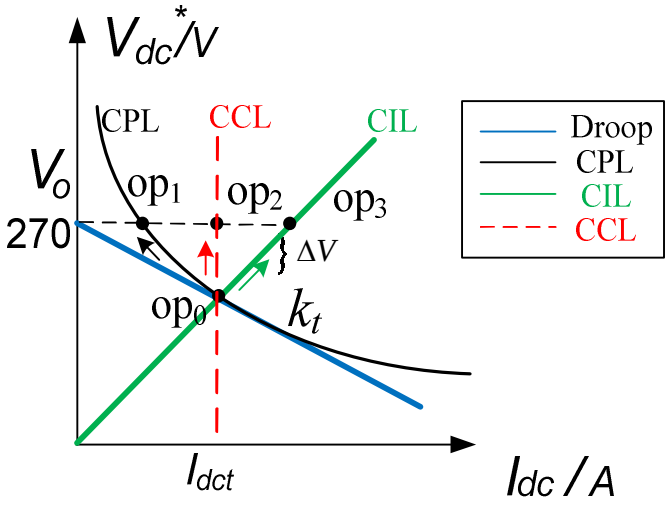

Figure 7.5. Operating mechanism of the proposed voltage compensation method under different loads.

7.2.2 Fault Scenario

If the outage of one source or multiple sources occurs, the others will share the load power according to their individual droop gains. The proportional power sharing among the remaining sources is still ensured in this case as the individual droop gains are fixed. If the feedforward gain k_t can be updated in time, the bus voltage will still be restored to its nominal value. On the other hand, if the feedforward gain k_t cannot be updated instantly, the influence of k_1 is still active in computing the global droop gain k_t, which results in a smaller k_t than the real value as indicated from (6-11) and (6-12). Thus, the compensation voltage ΔV is not high enough to

fully compensate for the bus voltage drop, whereas the voltage deviation can still be reduced using this approach.

7.2.3 Effect on PMSG-based System

If this voltage compensation method is applied in the DC EPS fed by PMSGs operating in flux weakening mode, the proposed voltage compensation method will effectively reduce the stator loss and increase the overload capacity. This section addresses this feature in detail.

Consider an EPS with a surface-mounted PMSG (i.e. the machine inductances in the *d*-axis and *q*-axis are identical, $L_d = L_q = L_S$). The maximum phase current $I_c^{\max}$ is defined by the inverter and machine ratings; the maximum voltage $V_c^{\max}$ is dependent on voltage in the DC-link and on the selected modulation method. The voltage and current limitations are:

$$\begin{cases} \omega_e \sqrt{(L_s I_q)^2 + (L_s I_d + \varphi_m)^2} \le V_c^{\max} \\ \sqrt{I_d^2 + I_q^2} \le I_c^{\max} \end{cases} \tag{7-2}$$

These limits can be represented by circles as shown in Figure 7.6; the current limit circle centre is at the origin and the voltage limit circles are centred with respect to the point ($-\varphi_m/L_s$, 0) with a radius of V_c^{max}/ω_e. Figure 7.6 illustrates the effect of the proposed voltage restoration method of the operation of PMSG. As the radius of the voltage limit circle is proportional to the converter AC voltage under the given generator speed, which has a linear relationship with DC voltage, the voltage limit circle will increase when the proposed voltage compensation method is employed. The threshold AC voltage for flux weakening is increased correspondingly under the same load power and generator speed. As a result, less negative de-fluxing current (I_d) is needed if the compensation method is activated. In this case, more I_q can be applied for the account of reduced I_d, or more EPS load can be supplied before the inner current loop of PMSG control hits the limit. It helps to increase the overload capacity of the machine. As shown in Figure 7.6, the equilibrium point changes to $\mathbf{E_2}$ from $\mathbf{E_1}$ when the proposed method is implemented. Hence, the stator current of the PMSG decreases and the resistive losses within the machine reduce.

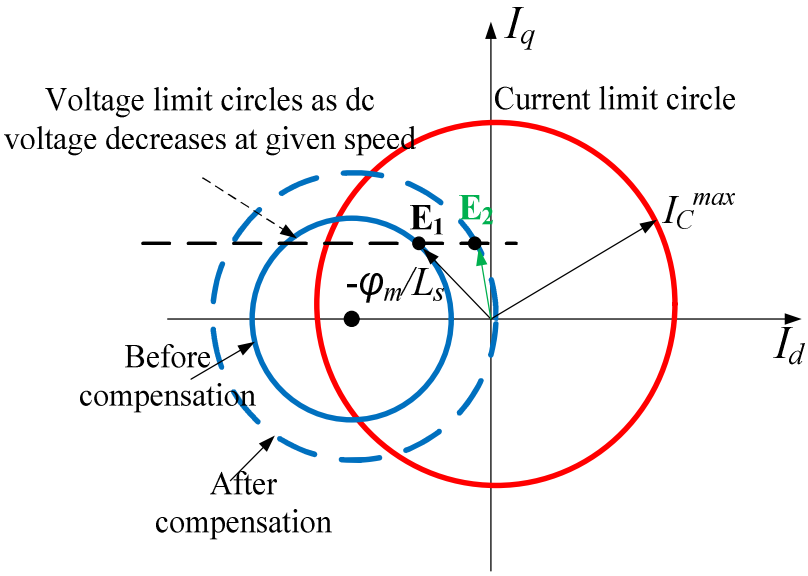

Figure 7.6. The effect of the proposed method on PMSGs-based system.

In summary, the proposed voltage compensation method can reduce the voltage deviation, improve the load sharing accuracy indirectly, and increase the overload capacity of the PMSG-based generation system.

7.3 Distribution Loss Reduction Based Droop Scheme

As discussed above, the proposed compensation method can reduce the total load current of CPL and, correspondingly, the branch current may be reduced. Hence the proposed approach can help minimise the distribution losses and as a result, increase the system efficiency in comparison with the conventional droop control method. This section discusses the optimal droop settings to minimise distribution losses when the proposed voltage compensation method is implemented.

As illustrated in Figure 7.5, after compensation the total load current will increase for CIL but reduce for CPL. Since the current of CCL does not change after the compensation, CIL and CPL are taken into account for further discussion. The total load current before compensation I_{Lt1} is written as (7-3),

$$I_{Lt1} = \frac{V_{b1}}{R_{res}} + \frac{P_{cpl}}{V_{b1}} \tag{7-3}$$

where P_{cpl} is the CPL power and R_{res} is the resistance of CIL.

After the proposed compensation method is applied, the total load current I_{Lt2} can be calculated again as follows:

$$I_{Lt2} = \frac{V_o}{R_{res}} + \frac{P_{cpl}}{V_o} \tag{7-4}$$

where V_o is 270V (nominal voltage). Following earlier discussions, the compensation method will increase the load current on CIL but reduce the current on CPL.

7.3.1 Optimal Global Droop Gain Setting

In order to analyse the distribution losses, the difference of the total load current between (7-3) and (7-4) can be initially expressed as follows:

$$I_{Lt1} - I_{Lt2} = (\frac{V_{b1} - V_o}{V_{b1}})(\frac{V_{b1}}{R_{res}} - \frac{P_{cpl}}{V_o}) \tag{7-5}$$

As illustrated in Figure 7.5, V_{b1} is less than V_o.

$$V_{b1} = V_o - k_t I_{Lt1} \tag{7-6}$$

Thus the following condition should be satisfied to ensure that the load current is reduced after compensation:

$$\frac{V_{b1}}{R_{res}} - \frac{P_{cpl}}{V_o} < 0 \tag{7-7}$$

Combining (7-3) and (7-6), the bus voltage before compensation is obtained as follows,

$$V_{b1} = \frac{R_{res}V_o + \sqrt{-4k_t P_{cpl} R_{res}(k_t + R_{res}) + V_o^2 R_{res}^{\ 2}}}{2(k_t + R_{res})} \tag{7-8}$$

Global droop gain settings can be optimised by solving (7-7) and (7-8), yielding,

$$
\begin{aligned}
&if \quad \frac{V_o^2}{3R_{res}} < P_{cpl} \le \frac{V_o^2}{R_{res}}, \quad \frac{-P_{cpl}R_{res}+V_o^2}{P_{cpl}+\frac{V_o^2}{R_{res}}} < k_t \le \frac{-R_{res}}{2}+\frac{1}{2}\sqrt{\frac{P_{cpl}R_{res}^2+R_{res}V_o^2}{P_{cpl}}} \\
&if \quad P_{cpl} > \frac{V_o^2}{R_{res}}, \ 0 < k_t \le \frac{-R_{res}}{2}+\frac{1}{2}\sqrt{\frac{P_{cpl}R_{res}^2+R_{res}V_o^2}{P_{cpl}}}
\end{aligned} \tag{7-9}
$$

If P_{res} is defined as the power of CIL at the nominal voltage as

$$
P_{res} = \frac{V_o^2}{R_{res}} \tag{7-10}
$$

a ratio "*r*" between the power of CPL and CIL can be defined here,

$$
r = \frac{P_{cpl}}{P_{res}} \tag{7-11}
$$

As a result, the global droop gain can be expressed as follows:

$$
\begin{cases} if \quad \frac{1}{3} < r \le 1, \\ R_{res}\frac{1-r}{1+r} < k_t \le \frac{R_{res}}{2}\left(\sqrt{1+\frac{1}{r}}-1\right) \end{cases}, \qquad \begin{cases} if \quad r > 1, \\ 0 < k_t \le \frac{R_{res}}{2}\left(\sqrt{1+\frac{1}{r}}-1\right) \end{cases} \tag{7-12}
$$

The minimum total load current can be achieved based on the following global droop gain settings, which can be regarded as the optimal droop gain $k_{\text{t\_optimal}}$,

$$
if \ \ P_{cpl} > \frac{1}{3}P_{res}, \quad k_{t\_optimal} = \frac{R_{res}}{2}\left(\sqrt{1+\frac{1}{r}}-1\right) \tag{7-13}
$$

From (7-13), it can be concluded that the optimal droop gain cannot be obtained if the CPL power is less than one third of the CIL power. It can be easily explained as follows. As the proposed compensation method improves the bus voltage regulation reduces the CPL current. However this approach increases the CIL current due to the increase of the bus voltage. If the CPL power is too small, the current that decreases in the CPL is less than the current increaseing in the CIL. Overall, the total load is increased in this case. Thus, the prerequisite for the obtainable optimal droop gain is that the CPL power needs to be higher than one third of CIL power. In real EPS,

quantities of motor drives and tightly controlled power electronic converters are in presence. Therefore, this condition is usually satisfied.

7.3.2 Optimal Individual Droop Gain Setting

The EPS main bus voltage is dependent only on the global droop gain while the branch current for each module is determined by the ratio of individual droop gains. The designer can regulate each source current by tuning the individual droop constants. In other words, different sets of droop gain settings (different power sharing ratio) can yield identical global droop gain. To find the optimal individual droop gain settings, line losses-prioritised analysis on the individual droop coefficient is performed in this subsection. Assuming that n modules are working in parallel, the i^{th} module shares n_i ($n_i < 1$) part of the total load. Here n_i is the weighting factor of the injecting current from i^{th} source.

Thus, the current sharing ratio among the parallel modules can be expressed as:

$$\begin{aligned} &I_1 : I_2 : \cdots : I_n = n_1 : n_2 : \cdots : n_n \\ &Condition : n_1 + n_2 + \cdots + n_n = 1 \end{aligned} \tag{7-14}$$

To make things simpler and to consider the practical location of the main generators in the MEA, it is assumed that the cable resistance connected with each source to the load is identical (R_c). Now the optimisation task is formulated as in:

$$\begin{aligned} &\min(P_{Lineloss}) = \min[I_{Lt}^2 R_c (n_1^2 + n_2^2 + \cdots + n_n^2)] \\ &n_1 + n_2 + \cdots + n_n = 1 \end{aligned} \tag{7-15}$$

By solving (7-15), the losses can be further minimised on the condition that each module shares the load current equivalently, i.e., ($n_1 = n_2 = \ldots = n_n$).

Therefore, the individual droop gain can be optimised as the followings:

$$k_{i\_optimal} = \frac{k_{t\_optimal}}{1/n} = n * k_{t\_optimal} \tag{7-16}$$

where n is the number of parallel modules in the system.

To make a short conclusion here, the proposed voltage compensation method can reduce the distribution losses of the system in presence of large quantity of CPL. With this approach, the high droop gain can be applied for each parallel module and as a result, the power sharing is guaranteed without any additional control.

7.4 Stability Assessment

The stability of using the proposed voltage compensation method is assessed in this section by using state-space modelling. Both normal scenario and fault scenario is also considered.

7.4.1 Normal Scenario

Since CPLs may result in EPS instability, a stability assessment of the proposed voltage compensation method is of great importance. This section investigates the transient behaviour and EPS stability of the proposed method. Based on the equivalent circuit diagrams shown in Figure 7.7, and using a first-order lag to represent the control dynamics (see Figure 7.8), the corresponding state space model in small-signal manner and state variables are shown as below:

$$\begin{cases} \dot{\Delta x} = A\Delta x \\ \dot{\Delta x} = A_{Compen}\Delta x \end{cases} \quad (x = \left[v_b, v_1, v_2, \cdots, v_n, i_1, i_2, \cdots, i_n, i_{s1}, i_{s2}, \cdots, i_{sn}\right]^T) \qquad (7\text{-}17)$$

where A and A_{compen} denote the state matrix of the system with conventional droop control and the system with proposed voltage compensation method respectively; v_b stands for the bus voltage; v_1, v_2 ,…, v_n represents the local DC terminal voltage; i_1, i_2,…,i_n stands for the line current; i_{s1}, i_{s2}, …, i_{sn} indicates the source current. The details of the state matrix A and A_{compen} are shown below.

$$A=\begin{bmatrix} \frac{P_{cpl}}{C_b V_b^2}-\frac{1}{C_b R_{res}} & 0_{1*n} & \left(\frac{1}{C_b} \ * \ * \ * \ \frac{1}{C_b}\right) & 0_{1*n} \\ 0_{n*1} & 0_{n*n} & \begin{pmatrix} -\frac{1}{C_1} & & \\ & \ddots & \\ & & -\frac{1}{C_n} \end{pmatrix} & \begin{pmatrix} \frac{1}{C_1} & & \\ & \ddots & \\ & & \frac{1}{C_n} \end{pmatrix} \\ \begin{pmatrix} -\frac{1}{L_1} \\ \vdots \\ -\frac{1}{L_n} \end{pmatrix} & \begin{pmatrix} \frac{1}{L_1} & & \\ & \ddots & \\ & & \frac{1}{L_n} \end{pmatrix} & \begin{pmatrix} -\frac{R_1}{L_1} & & \\ & \ddots & \\ & & -\frac{R_n}{L_n} \end{pmatrix} & 0_{n*n} \\ 0_{n*1} & \begin{pmatrix} -\frac{1}{\tau_1 k_1} & & \\ & \ddots & \\ & & -\frac{1}{\tau_n k_n} \end{pmatrix} & 0_{n*n} & \begin{pmatrix} -\frac{1}{\tau_1} & & \\ & \ddots & \\ & & -\frac{1}{\tau_n} \end{pmatrix} \end{bmatrix} \tag{7-18}$$

$$A_{Compen}=\begin{bmatrix} \frac{P_{cpl}}{C_b V_b^2}-\frac{1}{C_b R_{res}} & 0_{1*n} & \left(\frac{1}{C_b} \ * \ * \ * \ \frac{1}{C_b}\right) & 0_{1*n} \\ 0_{n*1} & 0_{n*n} & \begin{pmatrix} -\frac{1}{C_1} & & \\ & \ddots & \\ & & -\frac{1}{C_n} \end{pmatrix} & \begin{pmatrix} \frac{1}{C_1} & & \\ & \ddots & \\ & & \frac{1}{C_n} \end{pmatrix} \\ \begin{pmatrix} -\frac{1}{L_1} \\ \vdots \\ -\frac{1}{L_n} \end{pmatrix} & \begin{pmatrix} \frac{1}{L_1} & & \\ & \ddots & \\ & & \frac{1}{L_n} \end{pmatrix} & \begin{pmatrix} -\frac{R_1}{L_1} & & \\ & \ddots & \\ & & -\frac{R_n}{L_n} \end{pmatrix} & 0_{n*n} \\ \begin{pmatrix} -\frac{1}{\tau_1 k_1}(\frac{1}{R_{res}}-\frac{P_{CPL}}{V_b^2})k_t \\ \vdots \\ -\frac{1}{\tau_n k_n}(\frac{1}{R_{res}}-\frac{P_{CPL}}{V_b^2})k_t \end{pmatrix} & \begin{pmatrix} -\frac{1}{\tau_1 k_1} & & \\ & \ddots & \\ & & -\frac{1}{\tau_n k_n} \end{pmatrix} & 0_{n*n} & \begin{pmatrix} -\frac{1}{\tau_1} & & \\ & \ddots & \\ & & -\frac{1}{\tau_n} \end{pmatrix} \end{bmatrix} \tag{7-19}$$

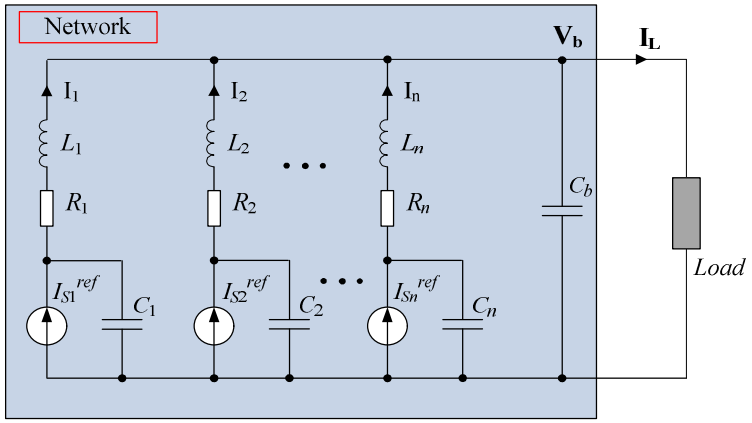

Figure 7.7. Equivalent circuit diagram.

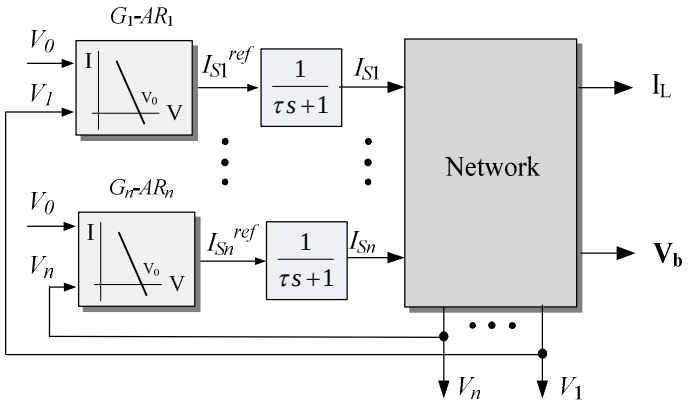

Figure 7.8. Droop control and control dynamic mimic.

Comparing the eigenvalues of the matrix A and A_{compen}, Figure 7.9 shows the dominant eigenvalues of twin and triple sources operating in parallel under the load of 2 kW CPL and 47 Ω CIL (1.55 kW CIL). It can be seen that the load specification matches the requirement that CPL power exceeds 1/3 of the CIL power. In addition, the values chosen are consistent with the experimental setup discussed in Chapter 8. It can be seen that the eigenvalues of the system with the proposed method are almost identical to the system without the proposed method but one eigenvalue slightly moves towards the left. It reveals that the proposed voltage compensation method does not compromise the stability of original system.

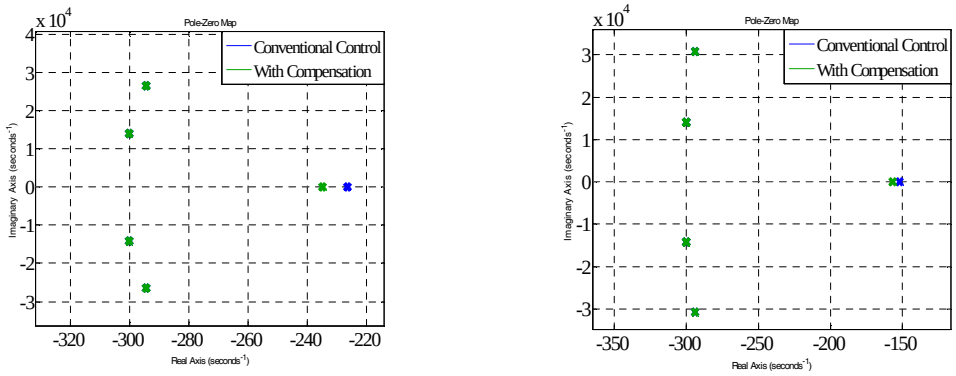

(a) (b)

Figure 7.9. Dominant eigenvalues of parallel-source paralleling system. (a) Twin sources. (b) Three Sources.

7.4.2 Fault Scenario

The fault scenario is also considered in the three source system. When one source fails, the desired compensation gain k_t should be computed based on the remaining two active sources. However, if the desired global droop cannot be updated in real time, the droop gain of the lost source still participates in the global droop gain (k_t) calculation, As a result a smaller k_t, which can be defined as the out-of-date compensation, is used in the feedforward link shown in Figure 7.3. Figure 7.10 shows the eigenvalues of the fault scenario. The system with the updated compensation and out-of-date compensation does not show much difference in terms of stability, which indicates that the system stability is still ensured with out-of-date compensation.

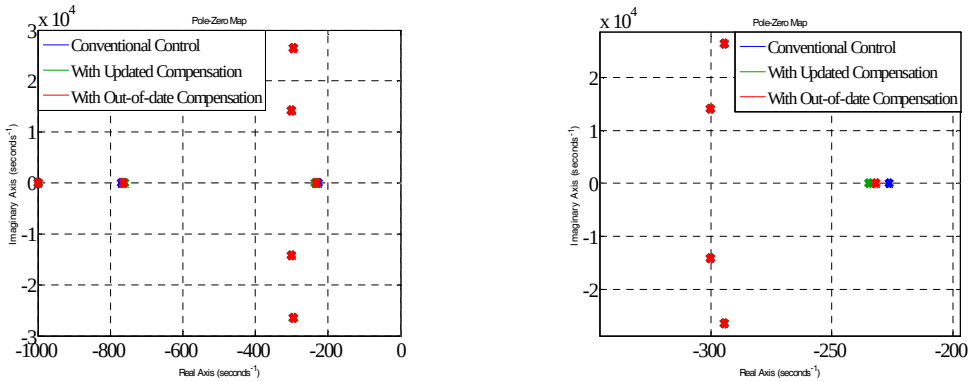

(a) (b)

Figure 7.10. Eigenvalues of fault scenario. (a) Overall plot. (b) Zoomed area of dominant poles.

Figure 7.11 shows the eigenvalue loci for varying global droop gain when the proposed compensation method is activated. It can be seen that dominant poles will move towards the RHP as the global droop gain increases, which indicates that the system stability is degraded with the increase of the global droop gain. However, system stability is still guaranteed with large global droop gain settings. Therefore, it also demonstrates the feasibility of the proposed voltage compensation method under large droop gain settings.

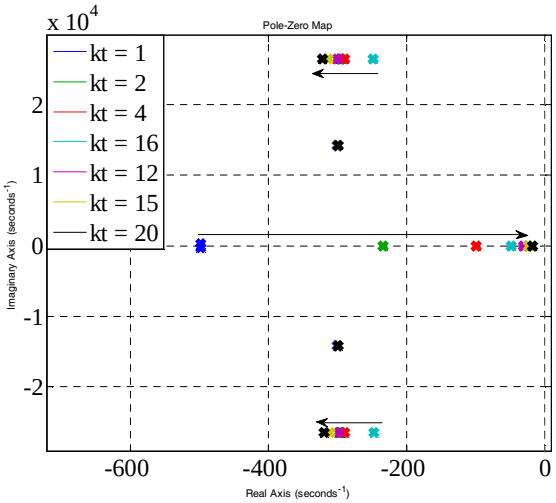

Figure 7.11. Eigenvalues loci for proposed compensation method with varying global droop gain.

To summarise this subsection, the proposed compensation method does not deteriorate the system stability under normal or fault scenarios. Even if the global droop gain is not fully updated, stable EPS operation is still guaranteed with the proposed method.

7.5 Simulation Results

To support the analytical analysis of the proposed voltage restoration method, a DC EPS with three power sources isolated by three transformers and converters working in parallel, as shown in Figure 7.12, is modelled in Matlab/Simulink. A DC/DC converter is tightly controlled to represent a CPL.The topology can be regarded as a fundamental representation of more complex MEA EPS.

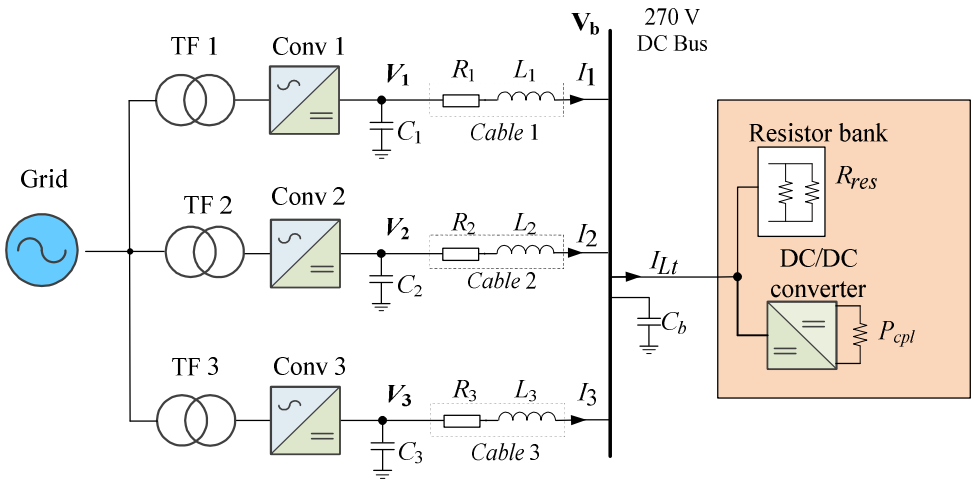

Figure 7.12. Schematic of the simulated system.

7.5.1 Normal Scenario

If a small droop gain is applied, the voltage drop at the main bus is small even at heavy loads due to stiff global droop characteristic. However, the current sharing ratio is not exactly 1:2:1 as desired because the cable resistances influence the accuracy of the current sharing, according to (4-8). Therefore, the individual droop gains were set to 8, 4 and 8 respectively to satisfy the condition $k_i >> R_c$. The global droop gain, according to (6-12), equals 2. Figure 7.13 shows simulation results based on these settings. It is seen that the bus voltage reduces with the increase of the CPL power and the steady-state values are consistent with the specified bus voltage/current characteristics. The dashed lines show the results when the proposed compensation method is employed. It can be seen from Figure 7.13(a) that the current sharing ratio is 1:2:1. The proportional load sharing is guaranteed under the proposed compensation method. The performance of current sharing is also good when the load sheds as confirmed by the scenario when the resistive load is switched off (t = 0.4 s). According to (7-12) in order to reduce distribution losses, the global droop gain (k_t) should be less than 7.8135 in the presence of a 2kW load, so the global droop gain setting in this simulation was set to 2 to match the condition. Above t = 0.2s, the current of each module is reduced and consequently, the line losses are reduced when the proposed compensation method is applied. This is in accordance with the analysis in Subsection 7.2. As shown in Figure 7.13(b), the bus voltage in steady-state is kept at rated value.

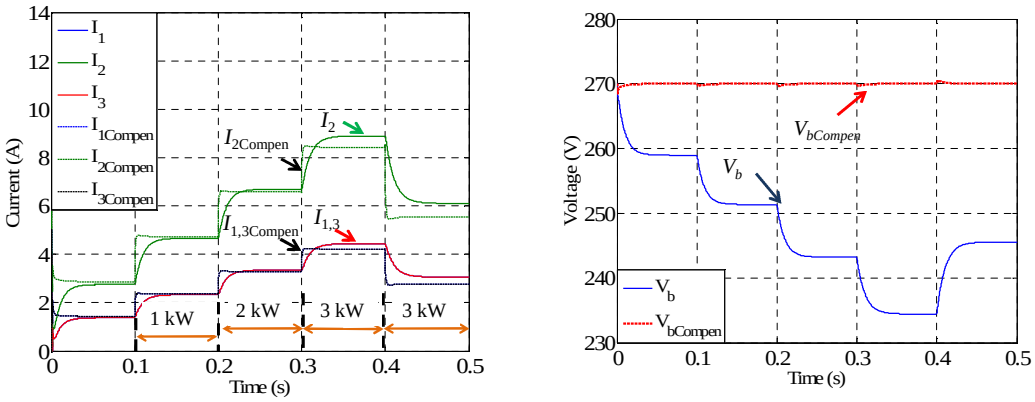

(a) (b)

Figure 7.13. Simulation results of the parallel system with unequal current sharing ($k_1 = k_3 = 8$, $k_2 = 4$). (a) DC currents. (b) Bus voltage.

Figure 7.14 shows the DC current and bus voltage when the individual gain is set to 6 for all converters (equal sharing case). The global droop gain is still 2 as in the previous case. It can be seen from Figure 7.14(a) that the equal current sharing among the three modules is achieved irrespective of whether the compensation method is activated. Similar to the results in Figure 7.13, the transmission line losses is decreased after CPL reaches 2kW.

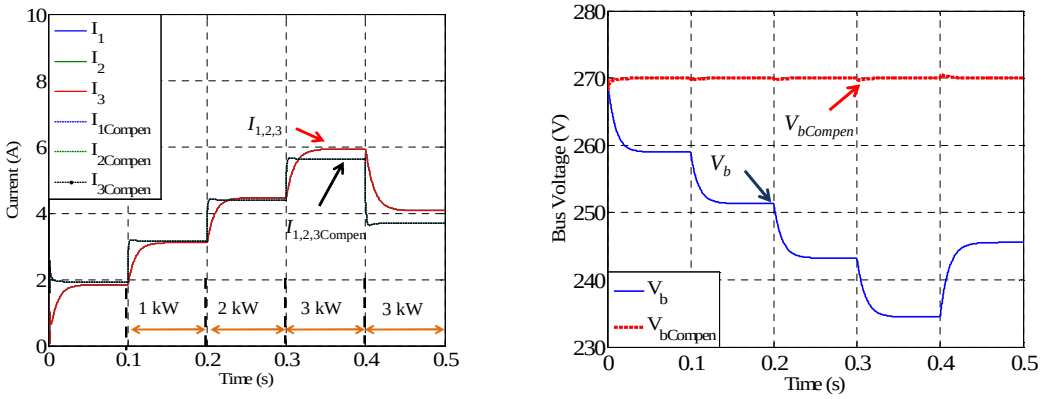

(a) (b)

Figure 7.14. Simulation results of the parallel system with equal current sharing ($k_1 = k_2 = k_3 = 6$). (a) DC current. (b) Bus voltage.

7.5.2 Fault Scenario

A source fault scenario was simulated to test the robustness of the proposed method. Prior to t = 0.6s, three converters work in parallel to share the load power (3kW CPL) at the desired ratio 1:2:1 (k_1 = k_3 = 8, k_2 = 4). At t = 1.2s, source 3 is disconnected from the system and it can be seen from Figure 7.15 that converters 1 and 2 take full responsibility of providing power to meet the load demand after the loss of converter 3. Meanwhile the compensation method is still active and the compensation gain k_t is still 2 (not updated in real time). The bus voltage drops from a nominal voltage to 262V at steady state, indicating that the proposed method still compensates for the bus voltage drop to some extent. When the global droop gain is updated under new EPS conditions (k_t = 8/3) at t = 1s, it is seen that the bus voltage is restored to 270V. When the proposed compensation method is deactivated after t = 1.2s (conventional droop scheme), the bus voltage will further drop to 237V in steady state.

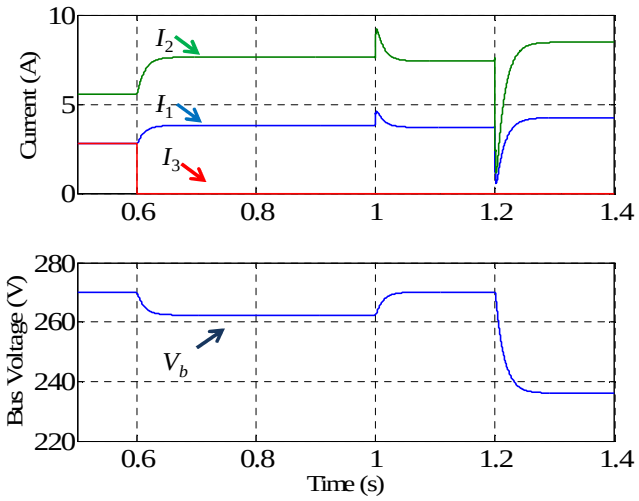

Figure 7.15. Simulation results at fault scenario ((k_1 = k_3 = 8, k_2 = 4).

This simulation confirms that the proposed compensation method is robust and performs well under the fault scenario. It is in accordance with the analysis in Subsection 7.2.2. Even if the global droop gain is not real-time updated, the voltage deviation can still be reduced compared to the case without the proposed approach.

7.6 Chapter Summary

A novel voltage compensation method for the droop-controlled DC EPS is proposed in this chapter. The main findings of this chapter can be highlighted as follows:

1) the method significantly reduces the voltage regulation and simultaneously establishes the desirable load power sharing among the sources. The proposed approach is easily implemented since no extra controllers or communication lines are needed, hence the advantages of a droop-controlled EPS such as reliability and modularity are retained.

2) it has also been shown that the method reduced the total load current and output currents of each source, leading to improved EPS efficiency due to reduced losses in lines and in sources. Moreover, application of this method increases the overload capacity of EPS generators controlled by power electronic converters.

3) also, this chapter has derived the criteria of optimal global droop selection for distribution losses minimisation in the presence of CPL and CIL. Based on this, the individual droop settings are investigated to minimise the distribution losses further in the parallel source system.

4) the performance of the proposed method under EPS fault scenarios has been demonstrated. The voltage deviation at the main bus still can be compensated for and partly restored when the global droop gain is not updated in time.

5) the system stability has also been examined under normal and fault scenarios and it has been demonstrated that the proposed method does not deteriorate the system stability.

Chapter 8 Experimental Validation

This chapter describes the test platform in the lab and presents the experimental results to support the theoretical analysis.

8.1 Lab Prototype

To validate the foregoing theoretical analysis, a prototype consisting of three parallel active front-end converters to mimic three sources in the EPS was built in the laboratory. Figure 8.1 presents the overview of the experimental setup. The test rig layout is depicted in Figure 8.2. The power converter (SEMIKRON's IGBTS Power Stack-SEMIKUBE: SKM400GB12E4 [185]) is connected to DSP/FPGA board through an interface board shown in Figure 8.1. Meanwhile, the sensor signals (voltage sensor/current sensor) are sent back from the converter to the microprocessor by means of the interface boards. Control algorithms are implemented based on a TI microprocessor TMS320F6713. A DC/DC converter (buck converter) with resistor is tightly regulated in constant power mode (within the control bandwidth). The system parameters are listed in Table 8-1.

Table 8-1 Parameters for experimental system

Category	Parameter	Value
Three phase grid	Grid source voltage	415 V line-to-line RMS
Transformer	Transformer	415 V/160 V, Y-Y
AC side inductor	AC side inductor	1.2 mH
Resistive load	Resistance	47 Ω
DC/DC converter	Converter load	23.5 Ω
	Inductor	3.4 mH
Converter	Switching frequency	10 kHz
	Local capacitor	1.2 mF
DC link	DC link capacitor	1.2 mF
	DC link bus voltage	270 V

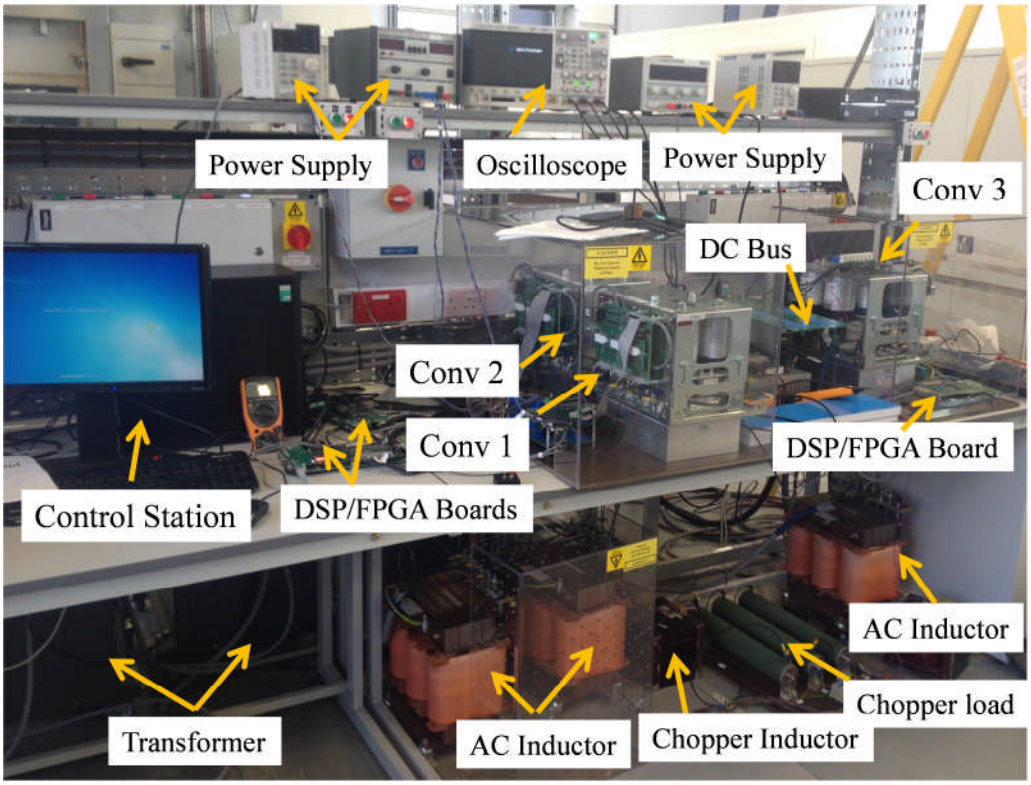

Figure 8.1. Experimental setup.

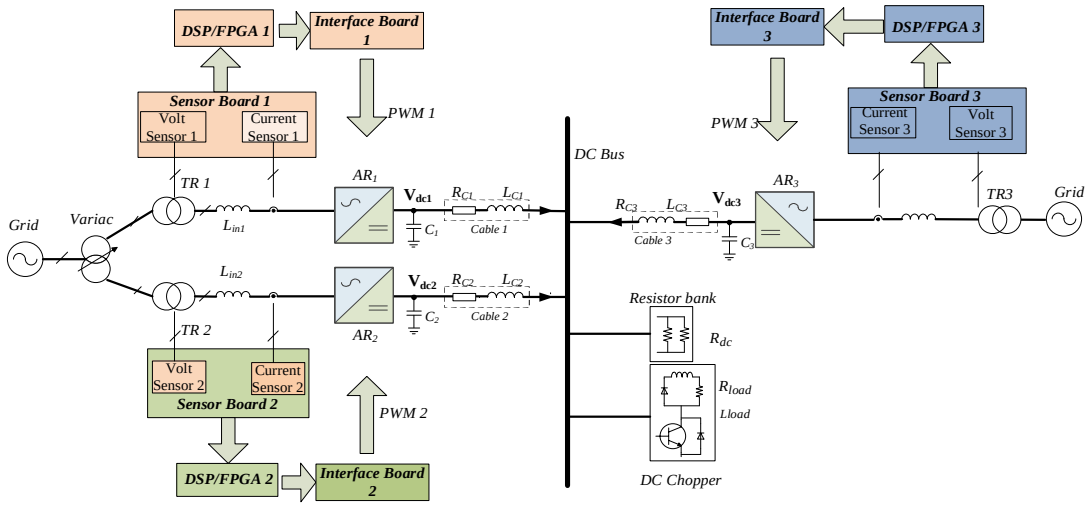

Figure 8.2. Test rig layout.

8.1.1 Control Platform

As shown in Figure 8.3, the control platform consists of a TIDSK 6713 board, an Actel FPGA ProAsic3 A3P400 board and an HPI daughter card.

The C6713 DSK (DSP Starter Kit) is a Texas Instruments development board based on a TMS320C6713 floating-point DSP. The FPGA board has ten 12-bit A/D channels, 50 MHz clock, ten fibre optics outputs. The communication between the DSK board and the FPGA card is carried out through the DSK 80-pin EMIF connectors, which allow a daughter card to have access to the DSP data and address buses, power supply, reading/writing control signals, timers, clocks and interrupts.

The HPI daughter card, developed by Educational DSP, allows the control program to be loaded into the DSK and enables a bi-directional data transfer between the host PC and the DSP via a USB connection. Matlab is used to monitor the variables of the control program.

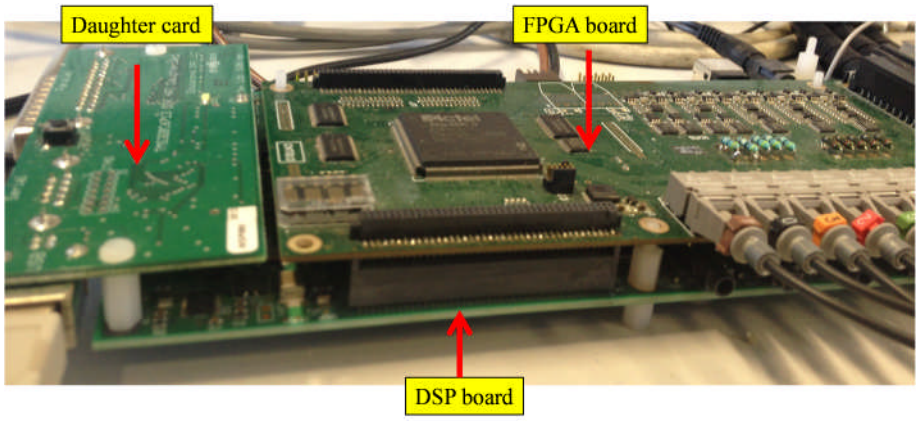

Figure 8.3. Control platform.

The interface board is utilised to provide an interface between the SEMIKUBE and the control platform. This sends the PWM signals from the DSP/FPGA to the converter and receives the sensor signal from the SEMIKUBE, then sends the corresponding conditioning sensor signals to DSP/FPGA.

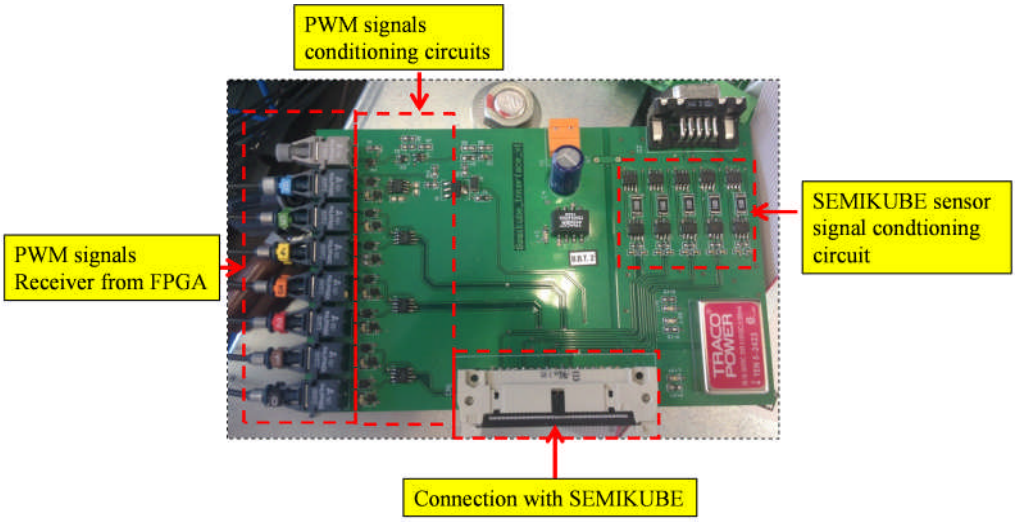

Figure 8.4. The interface board.

8.1.2 IGBT Power Stack

The power stack used in the system is a SEMIKUBE. It integrates the circuit to sense current via external current sensors, heat sink temperature via external temperature sensor, andDC-link voltage. The over current, over temperature protection has also been integrated in the driver board.

The IGBT power stack (SEMIKUBE) is shown in Figure 8.5 with the full bridge IGBT module (SKM400GB12E4) shown in Figure 8.6. The IGBT driver board is shown in Figure 8.5(b).

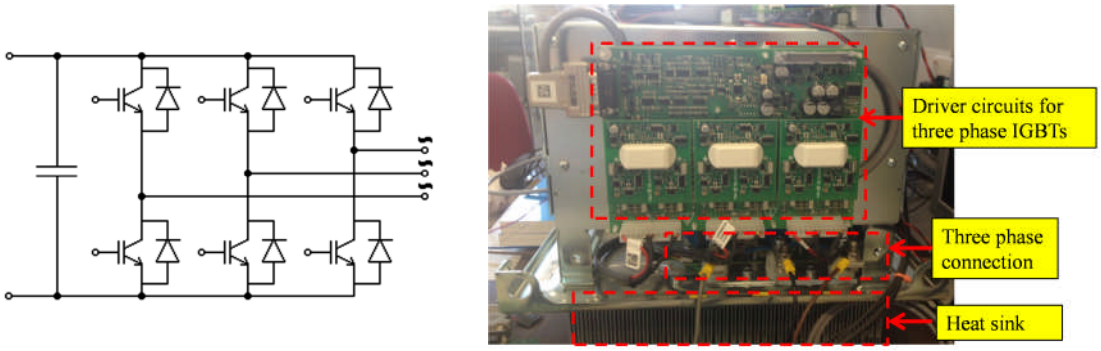

(a) (b)

Figure 8.5. SEMIKUBE power stack. (a) Schematic. (b) Prototype.

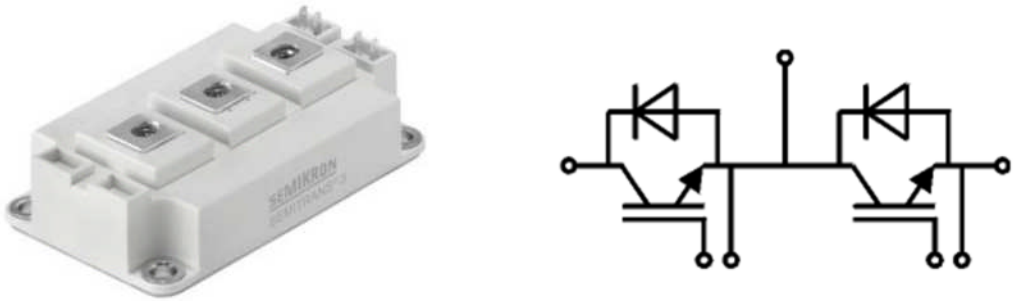

(a) (b)

Figure 8.6. IGBT modules. (a) Prototype. (b) Schematic.

Three sources are isolated through the 50/60 Hz transformers as shown in Figure 8.7.

Figure 8.7. Isolation transformers.

8.1.3 DC/DC Converter

As shown in Figure 8.2, the load consists of a buck converter and a resistor bank. The IGBT S_1 and the diode D_1 are integrated in the module DYNEX DIM200WLS12-A000 [186] as shown in Figure 8.8(b). As shown in Figure 8.8(a), the module includes half bridge, chopper, dual, single and bi-directional switch configurations. The IGBT switch has the following electrical ratings: maximum collector-emitter voltage V_{CES} = 1200 V, maximum continuous collector current I_c = 200 A.

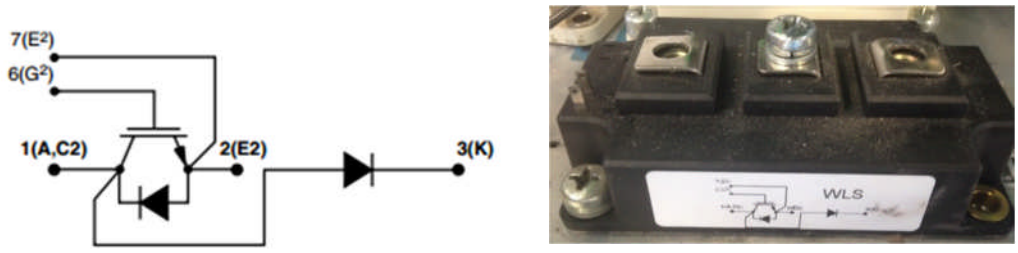

(a) (b)

Figure 8.8. Switch for the buck converter.

The inductor L_{DC} and the load of the buck converter R_{DC} is shown in Figure 8.9 and Figure 8.10, respectively. The resistor load, consisting of three resistors of 1kW ratings at 240V, is located in the cabinet, as shown in Figure 8.11.

Figure 8.9. DC choke of the buck converter.

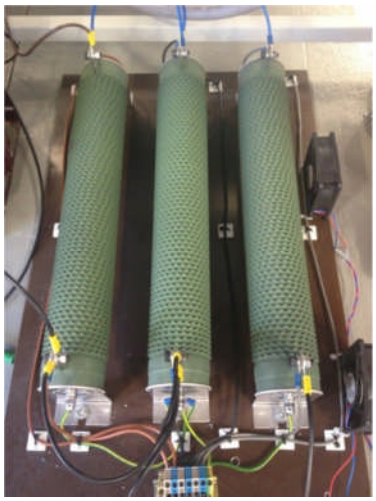

Figure 8.10. Load of the buck converter.

Figure 8.11. Resistor bank.

8.1.4 Sensor Board

The sensor board shown below measures the three phase current/voltage, DC link current. The voltage transducer LEM LV 25-P [187] and current transducer LA 55-P [188] are used for the voltage and current measurements, respectively, as shown in Figure 8.12. The measurement range of the voltage transducer LV25-P is 10V to 500V and the measuring range of the current transducer LA 55-P is -70A to 70A.

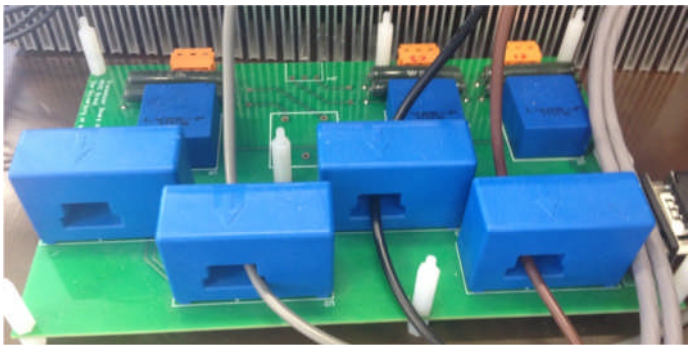

Figure 8.12. Sensor board.

8.2 Experimental Results Overview

After reviewing the experimental platform developed in the lab, this section gives an overview of the experimental results which are shown in subsequent sections (Section 8.3-8.6). Section 8.3 presents the steady-state power sharing performance. Sections 8.4 and 8.5 deal with the stability tests of the EPS with single source/multiple sources. Section 8.6 shows the effectiveness and performance of the proposed voltage compensation method. The experimental results can be summarised as follows:

(1) Section 8.3 shows the steady-state performance sharing approaches to support Chapters 4 and 6.

- varying global droop gain with fixed power sharing ratio is presented to support the analysis in Section 6.3
- fixed global droop gain with varying power sharing ratio is also tested to support the analytical results in Section 4.4
- fault scenario with source contingency is shown to see the robustness of the droop control approaches which is in alignment with the discussion in Section 4.4

(2) Section 8.4 shows the stability study of the single source based EPS to support the analysis in Chapter 5.

- Impact of parameters (control bandwidth and droop gain) in single source based EPS is shown to support the analysis in Section 5.4.

(3) Section 8.5 shows the stability study of the multi-source based EPS to support the analysis in Chapter 6.

- results of multiple sources based EPSs are provided to support the stability improvement of parallel operation in Sections 6.4 and 6.5

(4) Section 8.6 shows the results of the proposed voltage compensation method to confirm the theoretical analysis in Chapter 7.

- the equal sharing case and unequal sharing case are presented to demonstrate the effectiveness of the proposed voltage compensation method

- the distribution losses of the results are also analysed to show the loss reduction with the proposed method, which supports the analysis in Section 7.3.

- fault scenario test is conducted to confirm the good performance of the proposed method under fault conditions, which supports the analysis in Section 7.4.

8.3 Steady State Validation-Multiple Sources Operation

This subsection will present experimental results to support the steady-state values of the multi-source operation. In terms of the steady-state value demonstration, the current-mode (LVF) and voltage-mode system give the same performance, thus, either can be used as a representative. The following tests in this section are based on the current-mode system.

8.3.1 Varying Global Droop Gain Test

The first experiment was conducted to show the impact of global droop gain on the steady-state performance (voltage and current response). The buck converter is tightly controlled at 2.6 kW. With the presence of a 2.6 kW CPL, the two converters are then operated in parallel with identical individual droop gain, as shown in Table 8-2, to achieve equal power sharing. From Figure 8.13, the bus voltage decreases as the global droop gain k_t increases and the currents injected by Conv 1 and Conv 2 are identical. As before, the DC bus voltage-current characteristic is in accordance with the expectations.

Table 8-2 Varying global droop gains in Figure 8.13

Global droop gain (k_t)	k_1	k_2
1	2	2
1.5	3	3
2	4	4

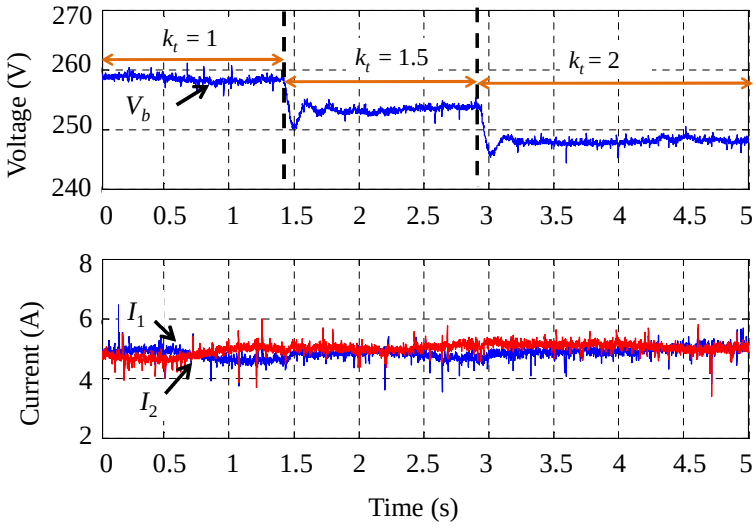

Figure 8.13. Experimental result with global droop gain variation.

8.3.2 Varying Power Sharing Ratio Test

In the next experimental result depicted in Figure 8.14, the global droop gain k_t is fixed to 1 and kept constant, however the sources current sharing ratio was varied –

i.e. the individual droop gains are varied as listed in Table 8-3. As can be observed, the steady state bus voltage is not affected by the step changes in the sharing ratio, but the load current provided by Conv 1 and Conv 2 varies according to the set ratio. As before, the results are consistent with the theoretical analysis.

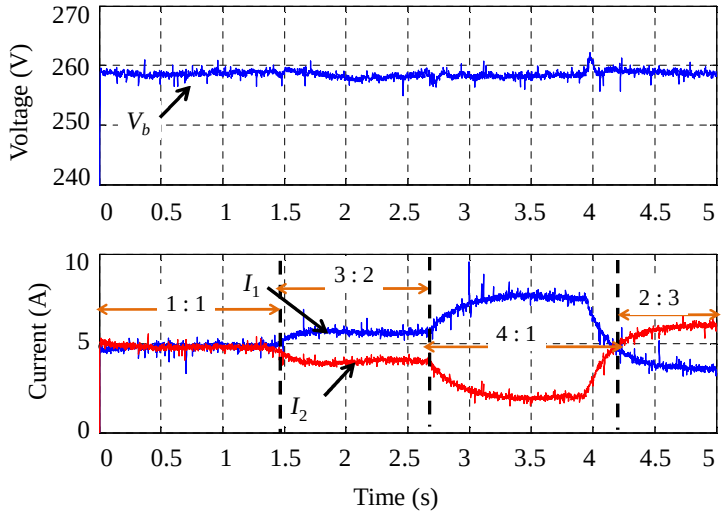

Figure 8.14. Experimental result with varying power sharing ratio.

Table 8-3 Varying power sharing ratio in

Power sharing ratio (I_1 : I_2)	k_1	k_2
1:1	1/0.5	1/0.5
3:2	1/0.6	1/0.4
4:1	1/0.8	1/0.2
2:3	1/0.4	1/0.6

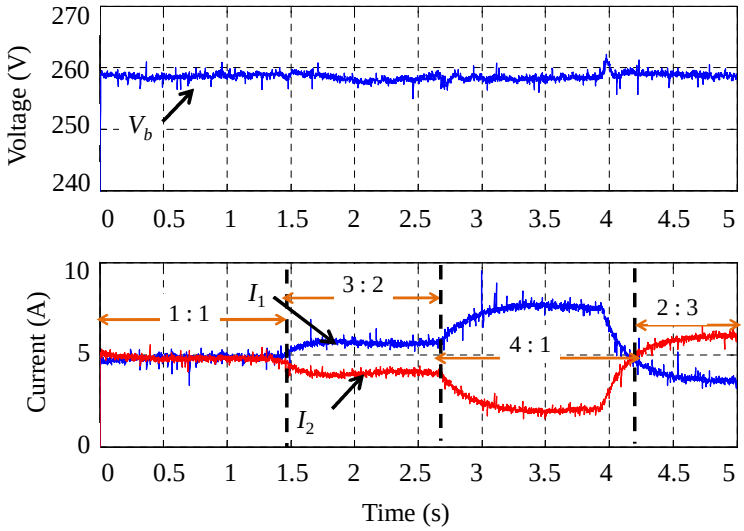

Figure 8.15. Experimental result with power sharing ratio variation.

8.3.3 Fault Scenario

Figure 8.16 shows the effect of parallel sources operation on the steady-state voltages and currents. The individual droop gain for each source is set to k_i = 1.5 and the common bus is loaded with a 2.6 kW CPL. Before $t = t_1$, only Conv 1 is active and connected to the DC bus. The steady-state bus voltage is 254.6V and the load current is 10.2A. The voltage and current values agree with the droop characteristic. At $t = t_1$, Conv 2 connects in parallel with Conv1. According to (6-11), the global droop gain increases to k_t = 0.75, and it can be seen that the main bus voltage increases to 262V, and the total load current is 9.95 A. This is in alignment with the global droop gain discussion in Chapter 6.

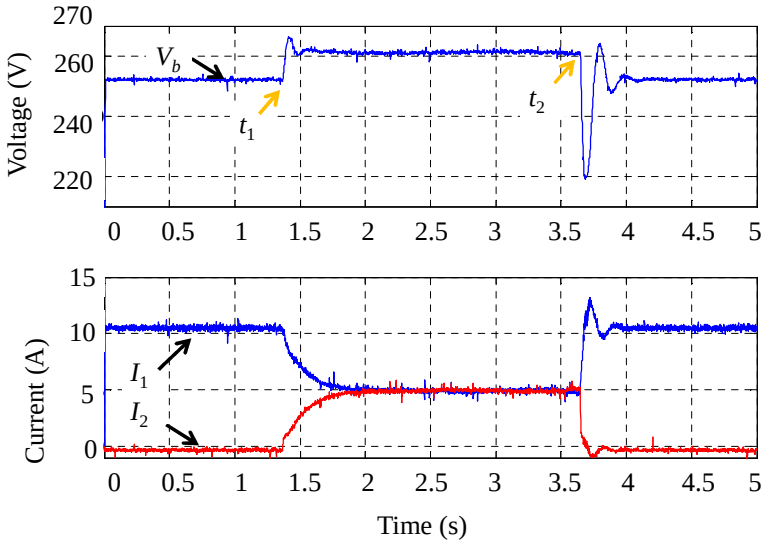

Figure 8.16. Experimental result for integration of parallel sources.

Overall, the presented experimental results demonstrate the knowledge of the proposed global droop gain, which provides an efficient tool to analyse the main bus voltage-current characteristic. It can be seen that different power sharing ratio among the parallel sources can be obtained whilst keeping the main bus voltage invariant.

8.4 Stability Validation-Single Source Operation

After validating the steady-state values, the stability condition has been experimentally tested including the effect of the control bandwidth, droop gain and load power, Considering different stability conditions for current-mode and voltage-mode droop control approach (as can be predicted from the discussion in Chapter 5), experiments were conducted for current-mode and voltage-mode, respectively.

8.4.1 Current-Mode System

8.4.1.1 Different Control Bandwidth

As discussed in Section 5.4, the I_{dc} control bandwidth affects the system stability. This subsection conducts the experimental test with different control bandwidths to see the effect of the I_{dc} control bandwidth on the current-mode system stability. Droop gain k_1 is set to 2. Figure 8.17(a) shows the response to the increase of the

CPL power of a system with 5Hz local I_{dc} control bandwidth, demonstrating degradation of the dynamic performance at high power, until the instability in a form of 3Hz oscillation occurs at 3kW. This shows that the high CPL deteriorates the system stability and demonstrates the effect of a low frequency resonance peak at f_{res1} under low bandwidth control. Figure 8.17(b) shows that the system can be stabilised by increasing the control bandwidth (50Hz) and the dynamic response is also improved.

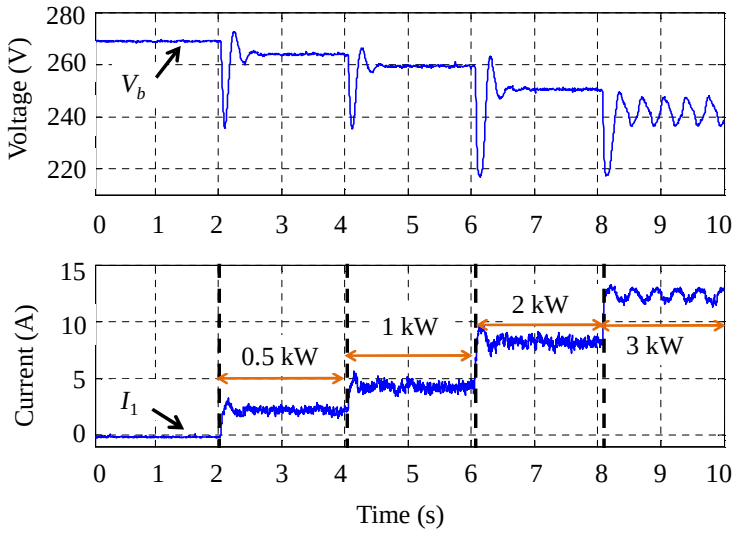

(a)

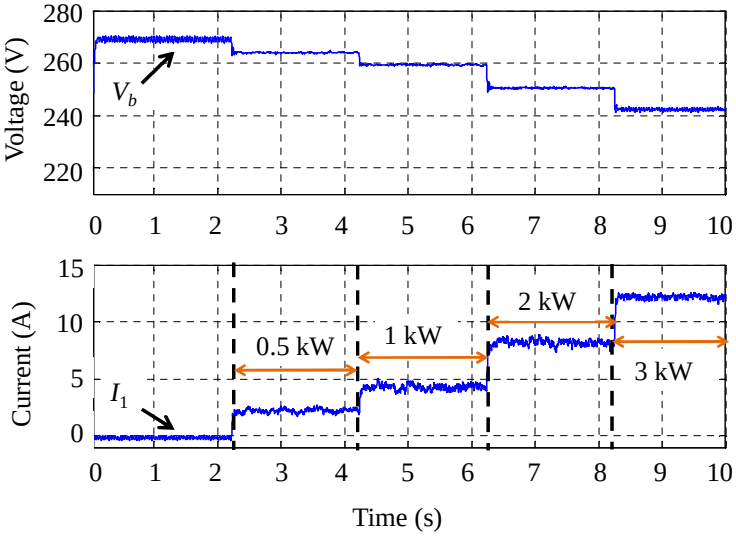

(b)

Figure 8.17. Experimental results with different local control bandwidth. (a) 5Hz control bandwidth. (b) 50Hz control bandwidth.

Figure 8.18 shows the effect of the I_{dc} control bandwidth on stability when the system is loaded with 3kW CPL. It can be observed that with the reasonable increase of I_{dc} control bandwidth, the oscillation of the bus voltage is attenuated although high frequency noise exists in high control bandwidth systems. These results match the effect of control bandwidth on stability discussed in Section 5.4.5.

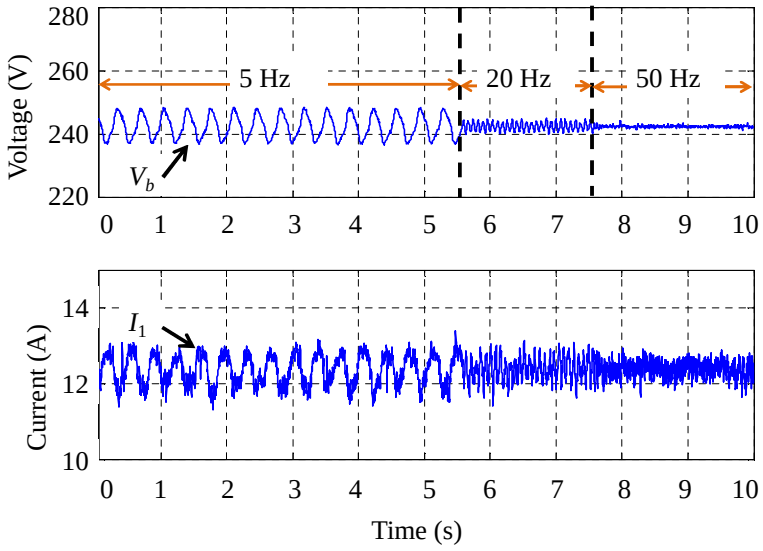

Figure 8.18. Experimental result for varying I_{dc} control bandwidth (5 - 50 Hz).

8.4.1.2 Different Droop Gain

The effect of droop gain on the system stability is tested and the experimental result is shown in Figure 8.19 by varying k_1 from 1 to 0.03.When k_1 becomes equal to 0.03, the system becomes unstable due to the non-minimum phase property and the protection stops the system. The result matches the stability prediction regarding the effect of droop gain in section 5.6.

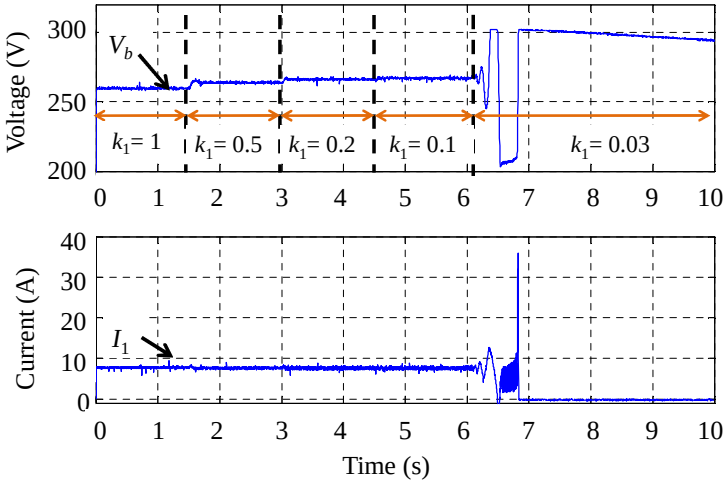

Figure 8.19. Experimental results with varying droop gain.

8.4.2 Voltage-Mode System

The voltage-mode droop control strategy (shown in Figure 5.4) has also been tested with a single converter to observe the effect of the V_{dc} control bandwidth, and the droop gain, on the system stability.

8.4.2.1 Different Control Bandwidth

As discussed in Section 5.4.7, due to the RHP zero, the V_{dc} control bandwidth needs to be limited for stable operation. Figure 8.20 shows the experimental results with different V_{dc} control bandwidths. It can be seen that with a 10Hz control bandwidth the system is stable over a CPL power ranging from 0 to 3kW whilst with a 100Hz control bandwidth the system shows significant oscillation when the load is around 3kW.

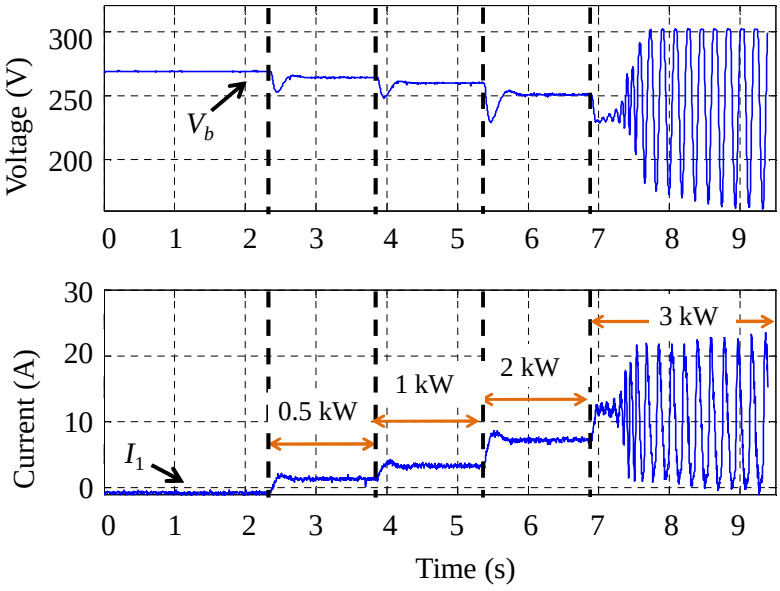
Voltage (V)
300
250
200
V_b
0 1 2 3 4 5 6 7 8 9
Current (A)
30
20
10
0
I_1
0.5 kW
1 kW
2 kW
3 kW
0 1 2 3 4 5 6 7 8 9
Time (s)

(a)

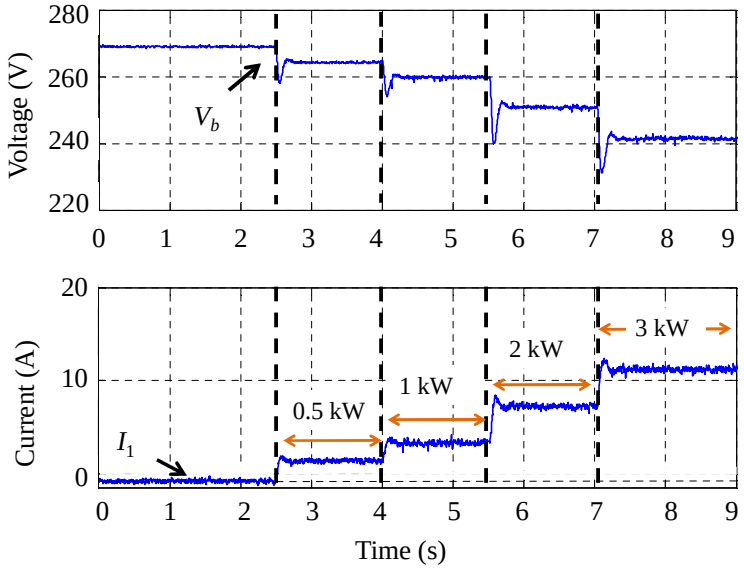
Voltage (V)
280
260
240
220
V_b
0 1 2 3 4 5 6 7 8 9
Current (A)
20
10
0
I_1
0.5 kW
1 kW
2 kW
3 kW
0 1 2 3 4 5 6 7 8 9
Time (s)

(b)

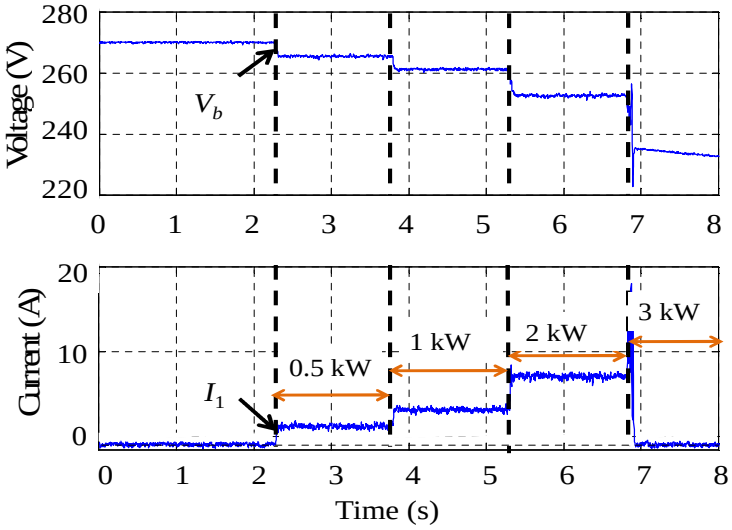

(c)

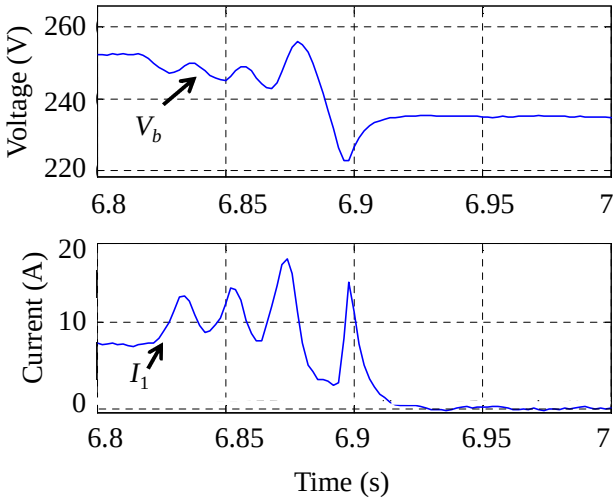

(d)

Figure 8.20. Experimental result with different control bandwidth. (a) 5Hz; (b) 10Hz; (c)100Hz; (d) Zoomed of oscillation part in (c).

8.4.2.2 Different Droop Gain

Since the droop gain belongs to a feedforward path in the voltage-mode droop control scheme, the system stability is not degraded by small droop gains. It can be seen from Figure 8.21 that under voltage-mode droop control the system shows stability improvement under small droop gains in comparison with *current-mode* droop control (see Figure 8.19). Again, this result is in accordance with the theoretical discussions in Section 5.4.6.

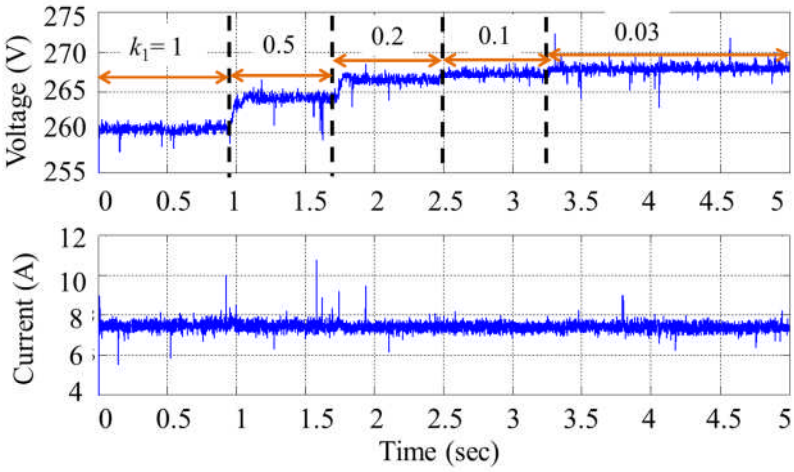

Figure 8.21. Experimental results with varying droop gain at 10Hz control bandwidth.

As a short summary of Section 8.4, the presented experimental results show the impact of control bandwidth and droop gain on the stability in respective current-mode and voltage mode system, which supports the analysis in Chapter 5.

8.5 Stability Validation-Multiple Sources Operation

Parallel operations of multiple sources with identical global droop gain and individual droop gain have been tested respectively to support the analysis in Chapter 6.

8.5.1 Fixed Global Droop Gain

Parallel operation of multiple sources with fixed global droop gain has also been tested to validate the expected stability improvements. The experimental results are shown in Figure 8.22. It can be seen in Figure 8.22(a) that under single source operation the system becomes unstable under a CPL of 6kW. However, with the same global droop gain, stable operations of a twin source system and three source system are achieved, as shown in Figure 8.22(b) and (c). The experimental results verify the discussion of system stability under parallel operation in Chapter 6, and confirm that using the current-mode droop control approach, parallel operation with identical global droop gain can improve the system stability.

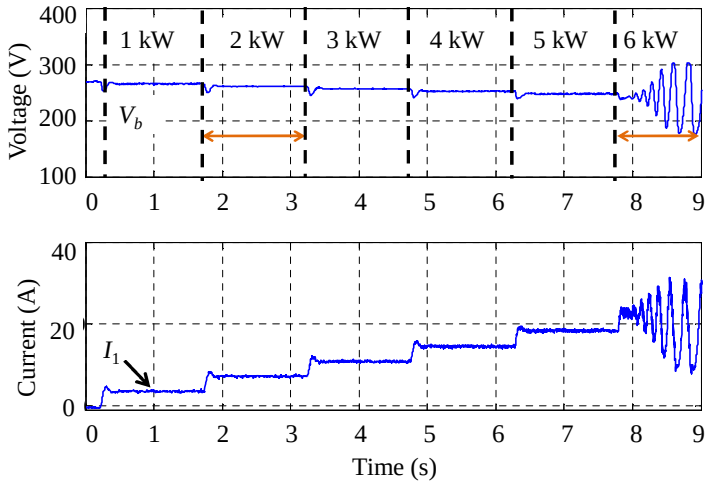
1 kW
2 kW
3 kW
4 kW
5 kW
6 kW
Voltage (V)
V_b
Current (A)
I_1
Time (s)

(a)

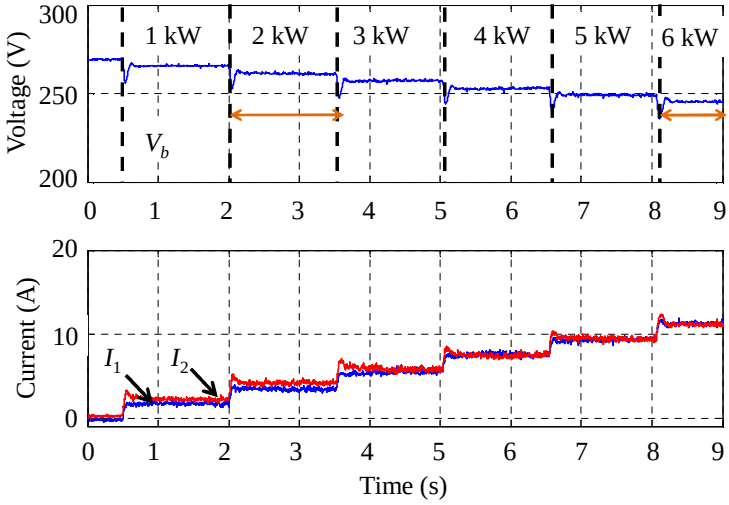
1 kW
2 kW
3 kW
4 kW
5 kW
6 kW
Voltage (V)
V_b
Current (A)
I_1
I_2
Time (s)

(b)

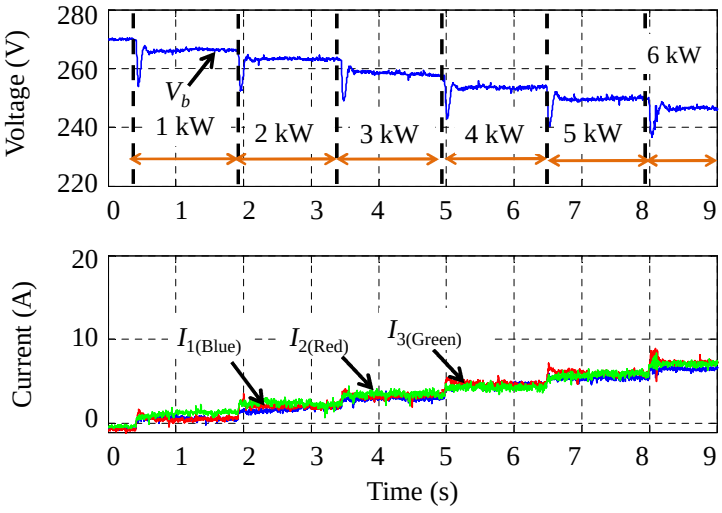
6 kW
V_b
1 kW
2 kW
3 kW
4 kW
5 kW
Voltage (V)
Current (A)
$I_{1(Blue)}$
$I_{2(Red)}$
$I_{3(Green)}$
Time (s)

(c)

Figure 8.22. Experimental results for parallel operation using the current-mode approach under 50Hz control bandwidth. (a) Single source operation: Conv 1 operates at k_1 = 1, and Conv 2, 3 are disconnected. (b) Twin sources operation: Conv 1, 2 operate at $k_1 = k_2 = 2$ (k_t = 1). (c) Three sources operation: Conv 1, 2, 3 operate at $k_1 = k_2 = k_3 = 3$ (k_t = 1).

8.5.2 Fixed Individual Droop Gain

The effect of parallel operation with the same individual droop gain (k_i = 1) has been also tested and the results are shown in Figure 8.23. As discussed in Chapter 6, the global droop gain reduces as the numbers of parallel modules with the same individual droop constant increases. The overall source impedance reduces and consequently, stability is improved by parallel operation. In Figure 8.23, at t = 0s, the load is set at 3kW and only Conv 1 is operating. The instability point is predicted at 6kW CPL (see Figure 8.22(a)). At t = 1.1 s, Conv 2 is connected and begins to operate in parallel with Conv 1. As a result, the global droop gain reduces and the bus voltage increases. It can be seen that the twin source system is stable below 7kW of CPL. This result demonstrates that compared with single source operation, parallel operation with the same individual droop gains significantly improves the system stability.

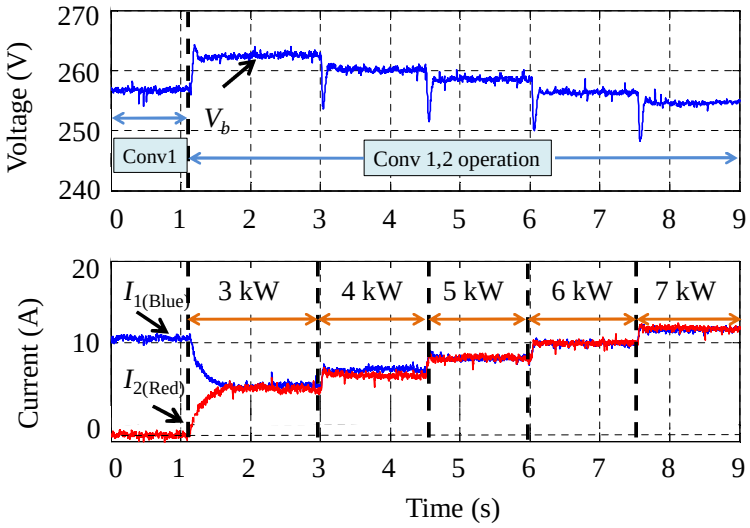

Figure 8.23. Experiment result for parallel sources with identical individual droop gains ($k_1 = k_2$ = 1, k_t = 0.5).

8.5.3 Different AC Fundamental Frequencies

In the following test, the CHROMA and a VARIABLE AUTOTRANSFORMER are connected to Conv 1 and Conv 2 respectively and both sources are operated at different frequencies (400Hz and 50Hz) to mimic the HP and LP generators. The influence of different power sharing ratios on the system stability has been tested and the result is shown in Figure 8.24. Figure 8.24(a) shows pure 230V/200Hz sinusoidal AC voltage which is generated from CHROMA and 50Hz AC voltage (distorted due to the VARIABLE AUTOTRANSFORMER). It can be seen from Figure 8.24(b) that the system is stable until 5kW CPL is applied when the ratio between HP and LP channel is 3:7 whilst oscillation and instability occurs at higher load condition (see Figure 8.24(c)-(d)). This indicates that the overall system stability will be upgraded if the LP channel shares more power. Furthermore, it is consistent with the theoretical analysis in Section 6.4.

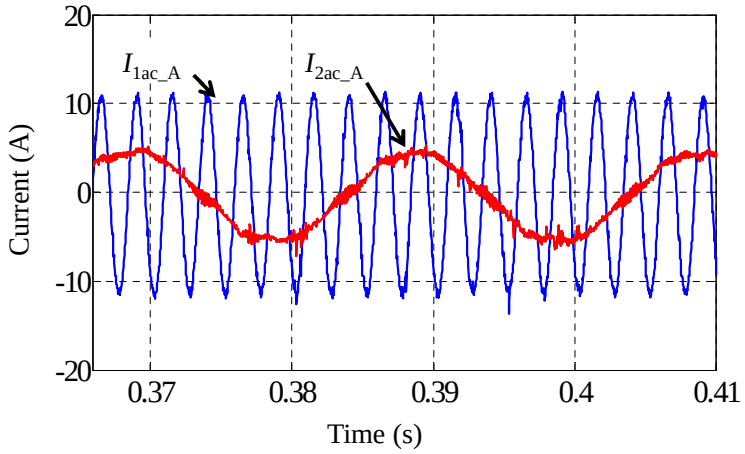

(a)

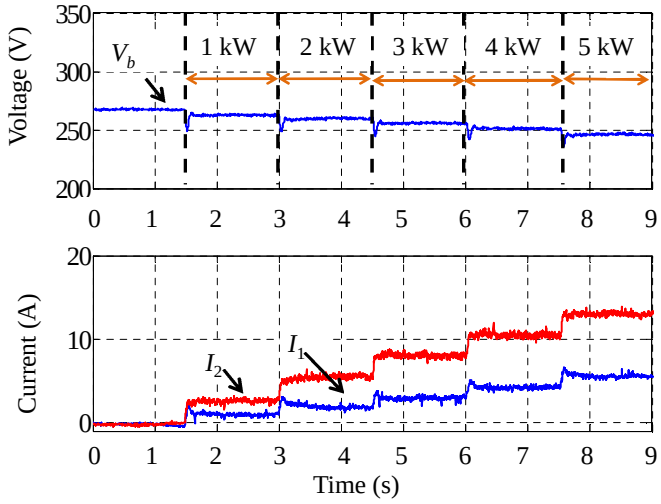
Voltage (V)
V_b
1 kW
2 kW
3 kW
4 kW
5 kW
Current (A)
I_2
I_1
Time (s)

(b)

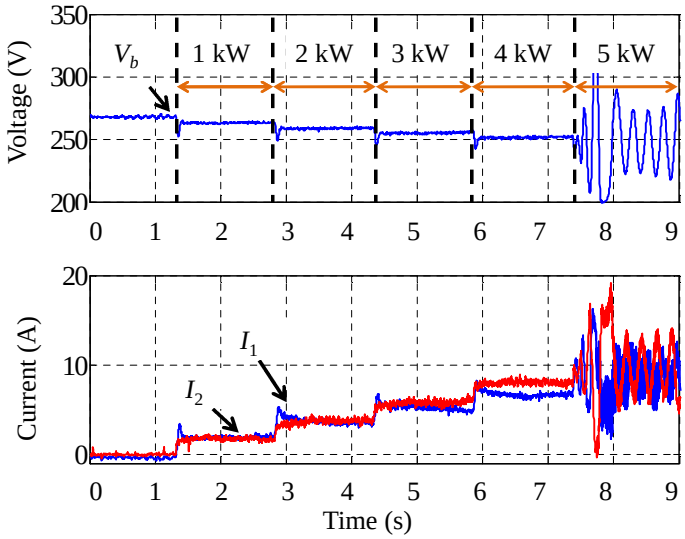
Voltage (V)
V_b
1 kW
2 kW
3 kW
4 kW
5 kW
Current (A)
I_1
I_2
Time (s)

(c)

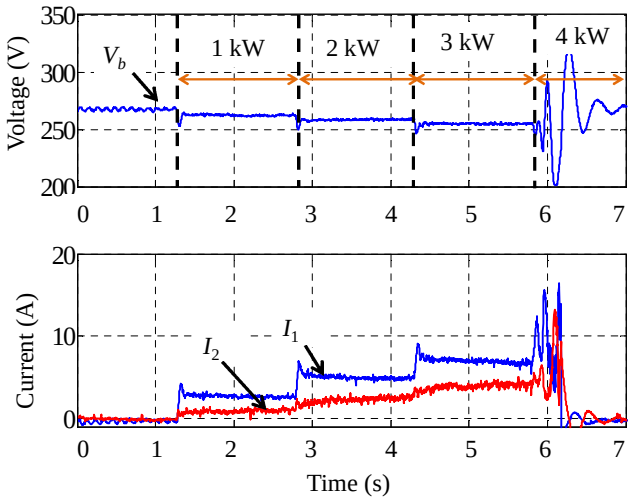

(d)

Figure 8.24. Experimental results for power sharing between different AC frequencies. (a) 400Hz and 50Hz AC fundamental frequencies (mimic HP and LP generators respectively); (b) power sharing between HP: LP = 3:7; (c) power sharing between HP: LP = 1:1; (d) power sharing between HP: LP = 7:3.

As a short summary of Section 8.5, the presented experimental results demonstrates the stability improvement of parallel source operation and show the stability issue of power sharing among LP and HP systems. It supports the analysis in Chapter 6.

8.6 Proposed Voltage Compensation Method

8.6.1 Unequal Power Sharing Case (Case 1)

First of all, pure CPL is used as the load to justify the effectiveness of the proposed method. If a small droop gain is applied, the voltage drop at the main bus is small even at heavy loads due to the stiff global droop characteristic. However, the current sharing ratio is not exactly 1:2:1 as desired because the cable resistances influence the accuracy of the current sharing, according to (4-8). Therefore, the individual droop gain for each converter is 8, 4 and 8 respectively to satisfy the condition $k_i >> R_c$. The global droop gain, according to (6-12), becomes equal to 2. Figure 8.25 shows the effect of the proposed voltage compensation method of the test rig with pure CPL (4 kW). It can be seen that below t = 2.5s, the DC bus voltage is 235V and DC current of each module injected to the main bus are 4.2A, 8.4A and 4.2A,

respectively. After the proposed voltage compensation approach is implemented at t = 2.5s, the main bus voltage recovers to 270V and the branch current is 3.8A, 7.6A and 3.8A, respectively. The practical result agrees with the distribution loss-based analysis in subsection 7.4.

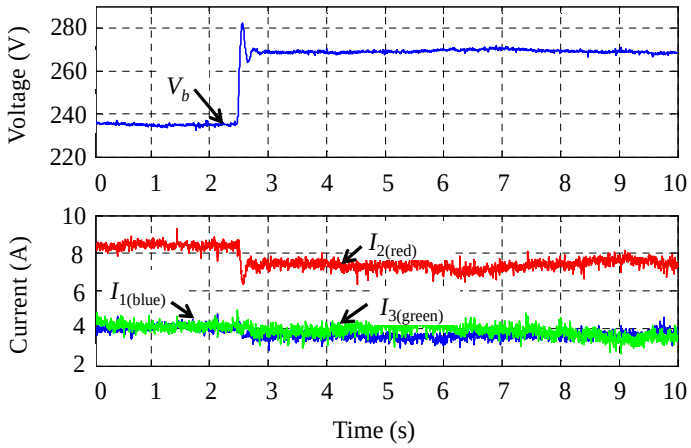

Figure 8.25. Experimental result for the proposed compensation method with unequal load sharing ($k_1 = k_3 = 8$, $k_2 = 4$).

8.6.2 Equal Power Sharing Case (Case 2)

In Case 2 the global droop gain (k_t) at the main bus is still set to 2, but the individual droop gains are set to 6 for each converter. Thus, the current ratio among three sources is expected to be 1:1:1.

Figure 8.26 shows the experimental result for unequal power sharing case. Below t = 4s, a conventional droop control method is employed and it can be seen that DC currents injected to the main bus are 5.65A each which satisfies the desired ratio 1:1:1. The bus voltage is maintained at 235V since the global droop gain is identical to Case 1.On activation of the proposed voltage compensation method at t = 4s the main bus voltage recovers to 270V. The current sharing ratio among three converters is still 1:1:1, whilst the branch current of each module is reduced to 4.95A. This result is consistent with the theoretical analysis: the proposed restoration method facilitates reducing the distribution losses. As listed in Table 8-4, the distribution loss under the equal sharing condition is less than for the unequal sharing case. For the unequal sharing case, the distribution loss is reduced by 18.8% after the proposed

compensation approach is applied. Similarly, it can be calculated that for the equal sharing case, compared to the case before the voltage compensation, the distribution loss can be reduced by 23.6% after the proposed voltage compensation is activated. Thus, it is in accordance with the discussion about the impact of power sharing ratio in Subsection 7.4.

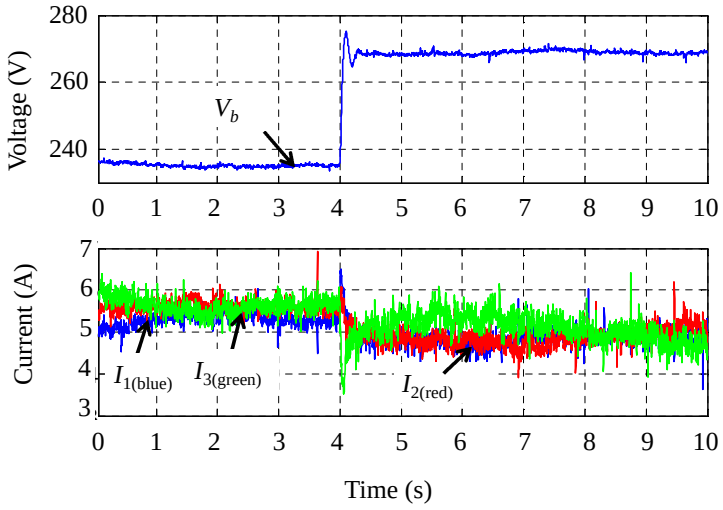

Figure 8.26. Experimental result for the proposed compensation method with equal load sharing (k_1 = k_2 = k_3 = 6).

Table 8-4 Branch current and distribution loss for case 1 and case 2

Case (sharing ratio)	Case 1 (1:2:1)	Case 2 (1:1:1)
Branch current before compensation (I_1 / I_2 / I_3)	4.2 A / 8.4 A / 4.2 A	5.65 A / 5.65 A/ 5.65 A
Branch current after compensation (I_1 / I_2 / I_3)	3.8 A / 7.6 A / 3.8 A	4.95 A / 4.95 A / 4.95 A
Distribution loss before compensation	21.2 W	19.1 W
Distribution loss after compensation	17.3 W	14.6 W

8.6.3 Fault Scenario

The fault scenarios have been tested to validate the robustness of the proposed voltage compensation method including both equal and unequal power sharing cases.

Figure 8.27 shows the experimental result for a fault scenario in unequal power sharing among the test case (the same as Case 1). Prior to t = 0.6 s, three converters are operated in parallel with different individual droop gains ($k_1 = k_3 = 8$, $k_2 = 4$).

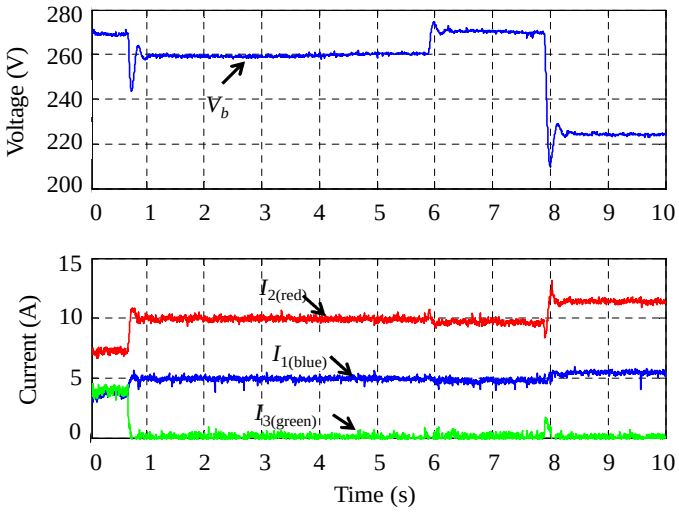

Figure 8.27. Experimental result for fault scenario with unequal power sharing.

Once the proposed voltage restoration method is activated, the bus voltage is 270V initially. At t = 0.6s, the outage of Conv 3 occurs and as a consequence Conv 1 and Conv 2 take responsibility for feeding the load. Between t = 0.6s and 5.9s, the global droop gain is not updated, thus the main bus voltage drops to 260V. The global droop gain is updated for the working converters (Conv 1, 2) at t = 5.9s, it is seen that the main bus voltage recovers to approximately 270V and the current sharing between Conv 1 and Conv 2 is still 1:2. After t = 7.9s, the proposed compensation method is deactivated and the bus voltage reduces further to 225V. The robustness of the proposed method and effective voltage restoration is demonstrated here.

Figure 8.28 demonstrates the feasibility of the proposed voltage compensation method in the fault scenario under equal sharing case (the same as Case 2). Conv 1 and Conv 2 take the full responsibility of providing power to meet the load demand

after the loss of Conv 3 at t = 1.7s. The bus voltage drops from the nominal voltage to 253V at steady state, indicating that the proposed method still compensates for the bus voltage drop to some extent but cannot fully compensate the voltage deviation since the global droop gain under new EPS conditions is not updated (k_t = 2). When the global droop gain is updated at t = 7.2s (k_t = 8/3), the main bus voltage restores to its nominal value. At t = 9.1s, the proposed method is deactivated and the bus voltage the drops to 218V. These results confirm that the proposed restoration approach can effectively reduce the voltage deviation under faulty conditions even if the global droop gain cannot be updated in time.

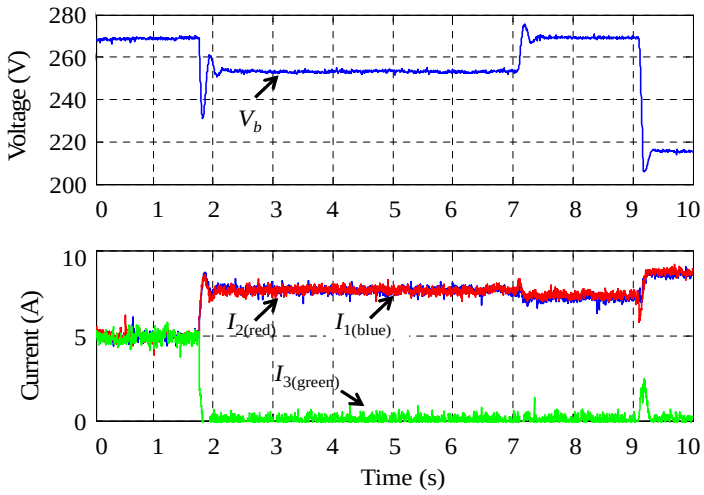

Figure 8.28. Experimental result for fault scenario with equal power sharing.

8.6.4 Mixed Load

In order to validate the feasibility of the proposed voltage restoration method for the generalised load condition, the mixed load of CPL and 47 Ω CIL (1.55 kW at 270V) is used below. Droop gain settings are identical with those in Case 1. As shown in Figure 8.29(a), the initial voltage is 258V since the resistive load is always connected to the system and is consuming power. With the increase of the CPL power, the bus voltage is reduced and the current-voltage relationship matches the droop characteristic settings. Figure 8.29(b) shows the counterpart experiment result with the proposed voltage compensation method.

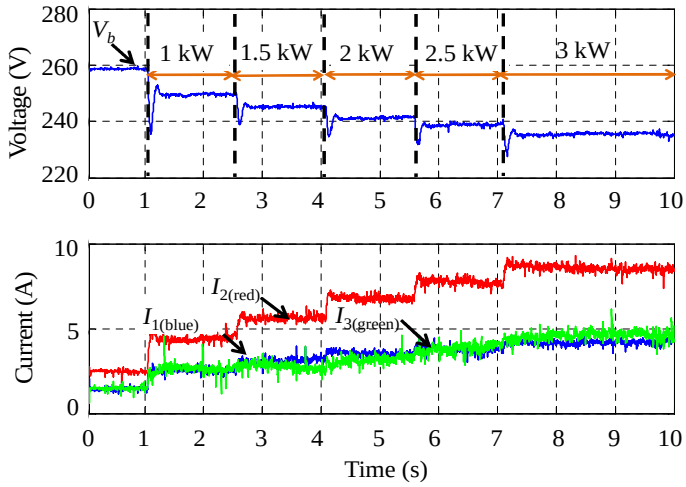

(a)

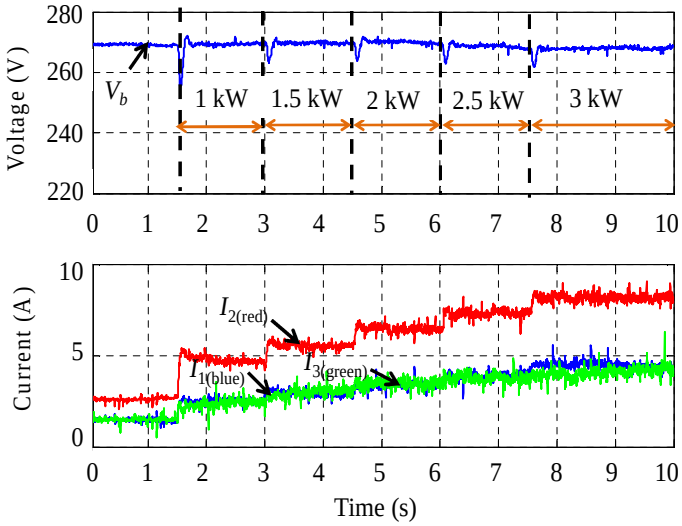

(b)

Figure 8.29. Experimental result of mixed load with unequal power sharing using (a) conventional droop control method. (b) proposed compensation method.

Table 8-5 shows a comparison of the experimental results shown in Figure 8.29 and simulation results shown in Figure 7.13. It can be seen that the error between simulation and experimental result for 0 kW, 1 kW, 2 kW, 3 kW CPL is 3.3%, 2.1%, 1.45%, 1.2%, respectively. The good agreement demonstrates the effectiveness of the simulation model and experimental system.

Table 8-5 Comparison between simulation and experimental results under unequal power sharing case (k_t = 2 (k_1 = k_3 = 8, k_2 = 4))

Load condition (Before compensation)	Simulation-Branch current (I_1 / I_2 / I_3)	Experiment-Branch current (I_1 / I_2 / I_3)
CPL (0 kW) + CIL	1.4 A / 2.8 A / 1.4 A	1.4 A / 2.7 A / 1.4 A
CPL (1 kW) + CIL	2.35 A / 4.7 A / 2.35 A	2.4 A / 4.8 A / 2.4 A
CPL (2 kW) + CIL	3.45 A / 6.9 A / 3.45 A	3.4 A / 6.8 A / 3.4 A
CPL (3 kW) + CIL	4.25 A / 8.5 A / 4.25 A	4.3 A / 8.6 A / 4.3 A
Load condition (After compensation)	Simulation-Branch current (I_1 / I_2 / I_3)	Experiment-Branch current (I_1 / I_2 / I_3)
CPL (0 kW) + CIL	1.5 A / 3 A / 1.5 A	1.5 A / 3 A / 1.5 A
CPL (1 kW) + CIL	2.5 A / 5 A / 2.5 A	2.45 A / 4.9 A / 2.45 A
CPL (2 kW) + CIL	3.35 A / 6.7 A / 3.35 A	3.3 A / 6.5 A / 3.3 A
CPL (3 kW) + CIL	4.16 A / 8.28 A / 4.16 A	4.15 A / 8.3A / 4.15 A

The equal sharing results for the mixed load are shown in Figure 8.30. It can be seen that the bus voltage restores to 270V in the presence of mixed loads when the proposed voltage compensation method is activated.

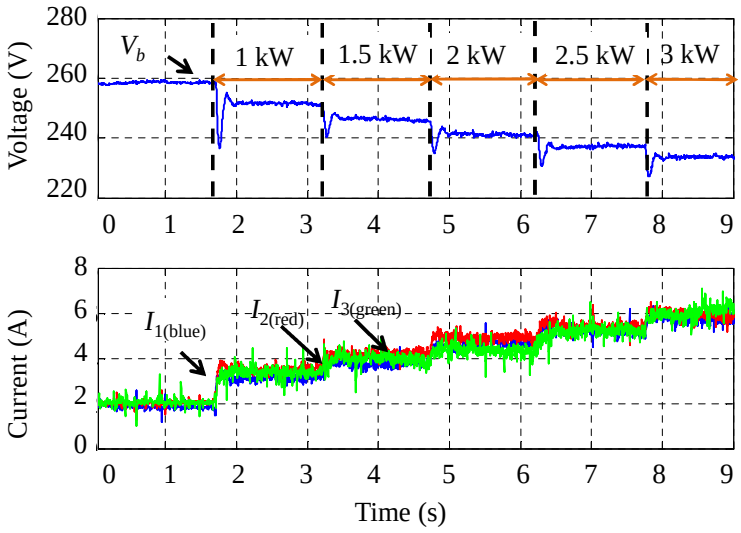

(a)

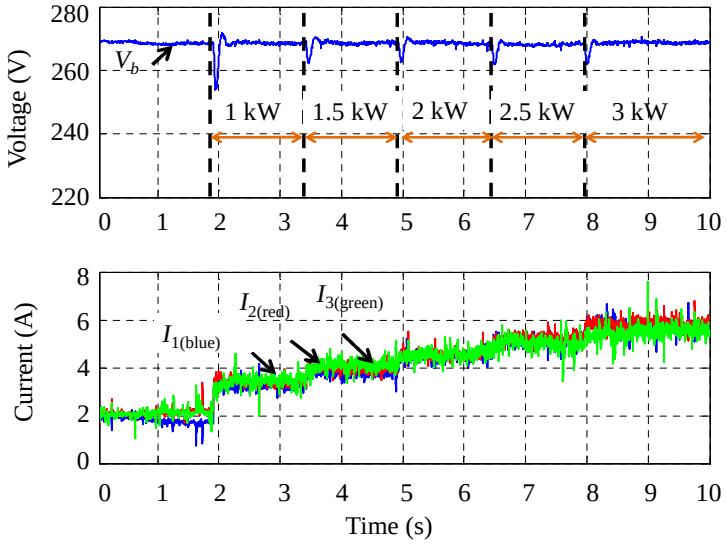

(b)

Figure 8.30. Experimental result of mixed load with equal power sharing. (a) conventional droop control method. (b) proposed compensation method.

Table 8-6 shows a comparison of the experimental results shown in Figure 8.30 and simulation results shown in Figure 7.14. It can be seen that the error between simulation and experimental result for no-load, 1 kW, 2 kW and 3 kW CPL is 1.03%, 0.4%, 0.3% and 0.16% respectively. It indicates that the experimental result matches with the theoretical analysis and simulations very well.

Table 8-6 Comparison between simulation and experimental results under unequal power sharing case (k_t = 2 ($k_1 = k_2 = k_3$ = 6))

Load condition (Before compensation)	Simulation-Branch current (I_1 / I_2 / I_3)	Experiment-Branch current (I_1 / I_2 / I_3)
CPL (0 kW) + CIL	1.85 A each	1.84 A each
CPL (1 kW) + CIL	3 A each	3.2 A each
CPL (2 kW) + CIL	4.5 A each	4.48 A each
CPL (3 kW) + CIL	5.9 A each	5.85 A each
Load condition (After compensation)	Simulation-Branch current (I_1 / I_2 / I_3)	Experiment-Branch current (I_1 / I_2 / I_3)
CPL (0 kW) + CIL	1.93 A each	1.95 A each
CPL (1 kW) + CIL	3.45 A each	3.4 A each
CPL (2 kW) + CIL	4.4 A each	4.39 A each
CPL (3 kW) + CIL	5.71 A each	5.7 A each

The branch currents under different loading scenarios are illustrated in Table 8-7. It can be seen that when the resistive load dominates, the branch current is increased after using the proposed compensation method. However, when the CPL power is increasing and becoming dominant, the branch current is reduced. This is in alignment with the analysis in Section 7.4.

Table 8-7 Branch current for mixed load

Load condition (Unequal sharing)	Branch current before compensation (I_1 / I_2 / I_3) k_t = 2 (k_1 = k_3 = 8, k_2 = 4)	Branch current after compensation (I_1 / I_2 / I_3) k_t = 2 (k_1 = k_3 = 8, k_2 = 4)
CPL (0 kW) + CIL	1.4 A / 2.6 A / 1.4 A	1.5 A / 3 A / 1.5 A
CPL (2 kW) + CIL	3.4 A / 6.8 A / 3.4 A	3.3 A / 6.5 A / 3.3 A
CPL (3 kW) + CIL	4.3 A / 8.6 A / 4.3 A	4.15 A / 8.3A / 4.15 A
Load condition (Equal sharing)	Branch current before compensation (I_1 / I_2 / I_3) k_t = 2 (k_1 = k_2 = k_3 = 6)	Branch current after compensation (I_1 / I_2 / I_3) k_t = 2 (k_1 = k_2 = k_3 = 6)
CPL (0 kW) + CIL	1.84 A each	1.95 A each
CPL (2 kW) + CIL	4.48 A each	4.39 A each
CPL (3 kW) + CIL	5.85 A each	5.7 A each

8.7 Chapter Summary

This chapter describes the test platform in the lab and presents experimental results. The single source operation with varying droop gain and power sharing ratio (Chapter 4) has been validated. Also, the effect of droop gain and control bandwidth of the current-mode and voltage-mode (Chapter 5) has been shown. The multi-source operation (Chapter 6) has been demonstrated. In addition, the feasibility and effectiveness of the proposed voltage compensation method (Chapter 7) has been proved.

Summarising, the reported experimental results in this chapter have confirmed all the key theoretical findings of this Thesis.

Chapter 9 Conclusion and Future Work

9.1 Conclusion

The thesis provides insight into designing a stable multiple sources based DC EPS for the future MEA.

(1) The power sharing performance among the parallel sources are analysed with the inclusion of cables. Different load sharing methods are reviewed and droop control approaches are finally selected due to their modularity, reliability and absence of communication link.

(2) An impedance-based approach provides the framework for tuning the key parameters including component parameters (cable impedance, cable length), operating parameters (generator speed, load power), control parameters (local control bandwidth, droop gain) of the DC EPS in MEA and this can easily be used to predict the conditions under which the system becomes unstable.

(3) A novel voltage compensation (secondary control) method is proposed to reduce the voltage deviation and simultaneously improve the power sharing performance.

In Chapter 3 a comparison of the single generation channel is performed. Eigenvalue sensitivity and participation factors are utilised to assess the effect of machine and control parameters, as well as system operating conditions, on EPS stability. Repeat computation for the eigenvalues with varying parameters is avoided which not only predicts the movement of the dominant modes of the system but also reduces the

computation burden. It shows that the cabling model is crucial since a model without cable may lead to some misleading, even opposite results. The chapter lays the theoretical foundation for the consideration of cables in the subsequent chapters.

In Chapter 4, power sharing performance of the droop control approaches are discussed and compared. Current-mode droop control uses a DC current controller to regulate the injected current from each terminal based on the voltage measurements. In contrast, voltage-mode droop control regulates the terminal voltage based on current measurements. The current-mode droop control approaches can be divided into local voltage feedback and global voltage feedback, depending on the voltage measurement point. The effect of the cable impedance on the steady-state power sharing is also taken into account. Among the current-mode droop control schemes, GVF shows better power sharing performance but additional sensors or communication lines are needed which compromise the modularity and reliability of droop control. The normal scenario and fault scenario has been investigated. It is confirmed that all droop approaches are robust to the source contingencies, i.e., the other active sources can share the load power proportionally according to their individual droop settings.

In Chapter 5 the stability of the single source based EPS is investigated. The main findings are highlighted as follows:

(1) When utilising the current-mode droop control, increased DC current control bandwidth is helpful for stability enhancement of the system. However, the upper boundary of the DC current control bandwidth is limited by the RHP zero. For the current-mode droop-controlled system, the DC voltage dynamics are affected by the DC current control bandwidth and the droop gain. It has been demonstrated that increasing the droop gain will reduce the voltage loop bandwidth.

(2) In contrast to a current-mode approach, voltage-mode droop control regulates the terminal voltage based on current measurements. The RHP zero results in the V_{dc} controller having high gain instability i.e. the system will easily become unstable when the V_{dc} controller has a high gain. When utilising the voltage-mode droop control, the voltage loop bandwidth is mainly determined by the voltage controller rather than the droop gain.

(3) Assuming the existence of a steady state operating point and the absence of source/load impedance interactions, an upper boundary for the droop gain can be defined in both techniques. Under the current-mode droop control, a lower boundary is imposed due to the RHP zero, whilst the voltage-mode droop control is feasible for wider droop gain settings even under zero droop gain (constant DC voltage control).

Hence, before analysing the complex multi-source multi-load system, Chapter 5 analyses the system stability condition in a single source based EPS by investigating the effect of parameters such as control bandwidth, droop gain, load power, machine speed, etc.

In Chapter 6 the stability analysis is extended to a generalised multi-source multi-load based EPS. Equivalent source and load impedance has been derived for current-mode and voltage-mode system. Global droop gain, a crucial factor to show the main bus V-I characteristic, was proposed to compare and analyse the stability of multi-source multi-load system.

Different power sharing ratios will affect the distribution losses. Assuming the condition that each generator can supply the power to feed the load, the optimal power sharing ratio has been discussed to minimise the distribution loss: The source with the same length of feeders provides identical power whilst the long length of feeders provides less power.

When the sources have identical AC fundamental frequency and control dynamics, the power sharing ratio among the sources has insignificant effect on stability. When the sources are divided into low frequency and high frequency sources, the low frequency source would provide more power in order to make the overall system stable.

It has been shown both analytically and experimentally that parallel operation improves the system stability for both droop strategies

In Chapter 7 an improved voltage regulation method in multi-source based DC electrical power system for the more electric aircraft is proposed. Since no extra

communication line and controllers are required, the proposed method is easily implemented and also increases the system modularity and reliability. The proposed approach effectively improves the load sharing accuracy under high droop gain circumstances with consideration of cable impedance. By using the proposed approach the DC distribution losses can be reduced. Furthermore, optimal droop gain settings are investigated and the selections of individual droop gains as well as the proportional power sharing ratio have been described. In addition, application of this method increases the overload capacity of EPS generators controlled by power electronic converters.

Finally, experimental validation has been performed in Chapter 8.

9.2 Achievement Summary

The thesis provides an insightful view on the modelling, control, and stability analysis of a multi-generator based DC electrical power system for future more electric aircraft. The following points summarise the achievements presented in this thesis:

Appropriate power sharing is of importance in such a multi-generator based power system. Droop control has been widely used due to its reliability and modularity. A comparative stability analysis of different droop control approaches has been proposed to investigate the stability discrepancy. It provides a guideline to select proper droop control approaches in DC EPS.

In order to overcome the drawback of droop control (high voltage regulation under heavy load condition), a novel voltage compensation method is proposed in this thesis. The method can implement nominal voltage operation at the main DC bus while also ensuring the approporiate power sharing among the sources. A main perceived advantage of this method is its extremely elegant and easy implementation since it does not require additional rigorous PI controllers and average current/voltage calculation. The main drawback of this method is that communications are still required to calculate the total current for multiple load conditions in a large scale system. However it is also true that due to the requirement

of monitoring, conditioning, and protection in modern power system, the communication line is widely used especially in large-scale systems. Thus, with the assistance of communication, the proposed compensation method is still feasible at no extra cost.

A large scale power system analysis method, modal analysis, has been implemented to study system stability in the small scale MEA EPS. Participation factor and eigenvalues analysis identify the critical mode of the system, analyse the eigenvalues movement and therefore predict the system stability under parameters variation. The method is applicable into large scale power systems with an increased number of parallel sources.

Overall, the comprehensive analysis conducted in this thesis offers insightful guidance for parameter optimisation and system stability prediction in multiple source/generator based DC MEA EPS. The context of the work can also be considered to be a challenging case of a DC MG in islanding mode since generation, and distribution, power electronic interfaced converters are regulated in an intelligent manner.

9.3 Future Works

Although the work in this thesis has addressed several research subjects in the field of power management, control and stability of power-electronic converter interfaced EPS, there are possible points which could be investigated further.

(1) Active damping methods to improve the system stability

In order to improve the system damping, there are several possibilities. One of the examples of the first solution is designing the control of the load converter with very low bandwidth so that the negative impedance characteristic is reduced. This can be effective but results in poor dynamic performance for the converters. The other approach is to incorporate a passive damping network to stabilise the system [189], [190]. The extra hardware and space required can be expensive and the system efficiency may be reduced. Alternatively, the active damping methods [191]-[198]

are attractive since they do not change the hardware circuit. The main idea is to stabilise the system by implementing a feedback on the load control to improve the stability margins. Thus, possible active damping methods can be investigated to improve the system stability.

(2) Coordinated control and integration of energy storage system into the existing topology

Energy storage system (ESS) is of interest which may help reduce the generator ratings, improve the transients, provide the additional power and adjust the power flow to meet the load demand. The coordinated control of a DC EPS with an energy storage system for future MEA could be discussed. Coordination between the generators and ESS can be realised by proposing control methods in order to avoid repetitive charging and discharging for the battery and to minimise corresponding losses for the ESS.

(3) Optimal operation investigation in multiple generator based system

Considering the converter, generator and distribution line losses, a proper power management scheme, i.e., an optimised operation mode would be found which minimise the system losses and maximise efficiency. Taking two sources systems as an example, it is assumed that the full-load power is within the capacity of single source. In order to feed the fix amount load, there are several choices to achieve this objective 1) single source operation; 2) twin source operation with equivalent sharing ratio; 3) twin source operation with inequivalent sharing ratio.

A generalised loss model including the converter loss and line loss can be developed Regarding losses reduction, a set of optimal reference values are derived to minimise the power losses including the line losses and converter losses. Based on the developed model, an optimal algorithm can be proposed as below:

Step 1) Find a preliminary optimal number N of VSCs participating in optimisation control to realise the loss minimisation.

Step 2) Find the feasible operating points within the system constraints and check the stability by eigenvalues and check the system modulation to see if it is unstable or over-modulated.

Step 3) If the system is not stable (some of the eigenvalues are in the RHP) or over-modulated, go back to Step 1 to find another optimal number (N-1 or N+1)

The abovementioned ideas could be interesting for the future studies in further improvement to the MEA electrical power system.

Appendix A Reference Frame Transformation

There are three reference frames widely used: natural (abc), stationary (αβ), synchronous rotating (dq). Clarke's and Park's transformations are widely used in many studies on synchronous and asynchronous machines. The aim of Clarke's transformation is to project the three-phase quantities onto a stationary two-axis reference frame, i.e., transform the variables from the natural reference frame to the stationary frame. Whereas Park's transformation transforms the variables from the stationary reference frame onto a rotating two-axis reference frame.

A.1 Clarke Transformation

The Clarke transformation converts balanced three-phase quantities into balanced two-phase quadrature quantities. In order to make the transformation invertible, the zerosequence component is usually added, then Clarke's transformation matrix can be expressed by

$$x_{\alpha\beta 0} = T_{\alpha\beta 0} x_{abc} = K_c \begin{bmatrix} 1 & -\frac{1}{2} & -\frac{1}{2} \\ 0 & \frac{\sqrt{3}}{2} & -\frac{\sqrt{3}}{2} \\ \frac{1}{2} & \frac{1}{2} & \frac{1}{2} \end{bmatrix} x_{abc} \qquad \text{(A.1-1)}$$

where $x_{\alpha\beta0}$ is the quantity in the stationary reference frame and x_{abc} is the quantity in the natural reference frame. $T_{\alpha\beta0}$ is the transformation matrix and K_c is a constant depending on the principle of the transformation (will be discussed later).

The inverse Clarke's transformation can be expressed as follows:

$$x_{abc} = T_{\alpha\beta0}^{-1} x_{\alpha\beta0} = \frac{2}{3} K_c^{-1} \begin{bmatrix} 1 & 0 & 1 \\ -\frac{1}{2} & \frac{\sqrt{3}}{2} & 1 \\ -\frac{1}{2} & -\frac{\sqrt{3}}{2} & 1 \end{bmatrix} x_{\alpha\beta0} \tag{A.1-2}$$

A.2 Park Transformation

The Park transformation converts vectors in a balanced two-phase orthogonal stationary system into an orthogonal rotating reference frame. By rotating the stationary reference frame over angle θ, the variables defined in the stationary reference frame $x_{\alpha\beta}$ can be turned into a rotating frame x_{dq} as below,

$$x_{dq} = \begin{bmatrix} \cos\theta & \sin\theta \\ -\sin\theta & \cos\theta \end{bmatrix} x_{\alpha\beta} \tag{A.2-1}$$

The above transformation from an αβ reference frame to a dq reference frame is called Park's transformation and its inverse can be written as

$$x_{\alpha\beta} = \begin{bmatrix} \cos\theta & -\sin\theta \\ \sin\theta & \cos\theta \end{bmatrix} x_{dq} \tag{A.2-2}$$

Combing (A.1-2) and (A.2-1), the three-phase abc frame can be directly transformed into the two phase dq frame by

$$x_{dq0} = T_{dq0} x_{abc} = K_c \begin{bmatrix} \cos\theta & \cos(\theta - \frac{2}{3}\pi) & \cos(\theta + \frac{2}{3}\pi) \\ -\sin\theta & -\sin(\theta - \frac{2}{3}\pi) & -\sin(\theta + \frac{2}{3}\pi) \\ \frac{\sqrt{2}}{2} & \frac{\sqrt{2}}{2} & \frac{\sqrt{2}}{2} \end{bmatrix} x_{abc} \quad \text{(A.2-3)}$$

Similarly, the inverse yields,

$$x_{abc} = T_{dq0}^{-1} x_{dq0} = \frac{2}{3} K_c^{-1} \begin{bmatrix} \cos\theta & -\sin\theta & \frac{\sqrt{2}}{2} \\ \cos(\theta - \frac{2}{3}\pi) & -\sin(\theta - \frac{2}{3}\pi) & \frac{\sqrt{2}}{2} \\ \cos(\theta + \frac{2}{3}\pi) & -\sin(\theta + \frac{2}{3}\pi) & \frac{\sqrt{2}}{2} \end{bmatrix} x_{dq0} \quad \text{(A.2-4)}$$

It is worth noting that different K_c values can lead to differenet conventions which are summarised as follows:

$$\begin{aligned} &K_c = \frac{2}{3}, \quad \text{amplitude invariant} \\ &K_c = \sqrt{\frac{2}{3}}, \quad \text{power invariant} \\ &K_c = \frac{\sqrt{2}}{3}, \quad \text{RMS variant} \\ &K_c = 1, \quad \text{1.5*amplitude invariant} \end{aligned} \quad \text{(A.2-5)}$$

In this thesis, the amplitude invariant principle is used and K_c is chosen as 2/3. Under the amplitude invariant convention, the active power P and reactive power Q can be expressed as

$$\begin{aligned} P &= \frac{3}{2}(v_d i_d + v_q i_q) \\ Q &= \frac{3}{2}(v_d i_q - v_q i_d) \end{aligned} \quad \text{(A.2-6)}$$

By applying the Clarke and Park Transformation, three time-varying quantities are transformed into two non time-varying quantities. Linear control methods such as PI

control can be easily used in a synchronously rotating dq reference frame. Therefore, this action favours the analysis of the electrical power system and the development of control system.

Appendix B State-Space Model for Modal Analysis

B.1 System Parameters and Symbols

The symbols used in the elements of the state matrix are illustrated as follows:

1) Control parameters:

Stator current loop	Proportional gain	K_{idp}, K_{iqp}	0.8785
	Integral gain	K_{idi}, K_{iqi}	3908
Flux weakening control	Proportional gain	K_{vcp}	0
	Integral gain	K_{vci}	5000
I_{dc} control	Proportional gain	K_{iop}	0.4
	Integral gain	K_{ioi}	600

2) Generator parameters:

PMSG	Machine resistor	R_{s1}	1.058 mΩ
	Machine inductor in d-axis	Ld	99μH
	Machine inductor in q-axis	Lq	99μH
	Flux linkage of permanent magnet	φ_m	0.03644V*s/rad

3) Cable parameters:

Cable	Local capacitor	C_i	1mF
	Cable resistor	R_{ci}	3mΩ
	Cable inductor	L_{ci}	1μH

4) Operating points:

I_d: d-axis current;

I_q: q-axis current;

V_d: stator voltage in d-axis;

V_q: stator voltage in q-axis;

V_c: stator voltage;

V_{dc1}: voltage across the local capacitor;

V_b: bus voltage (voltage of the bus capacitor);

ww: electrical speed of the generator.

B.2 State Matrix A_c of the Single Generator System

The state matrix A of the single generator system without DC cable is a submatrix of A_c which is also shown below. The State-space for single generation channel is also shown:

$$A_C = \begin{bmatrix} A & F_1 & F_2 \\ L & -\frac{R_{c1}}{L_{c1}} & -\frac{1}{L_{c1}} \\ 0 & \frac{1}{C_b} & -\frac{1}{C_b} * ((\frac{2}{R_{res}} - \frac{P_{cpl}}{V_b^2})) \end{bmatrix} \quad \text{(B-1)}$$

where

$$A = \begin{bmatrix} A_{11} & A_{12} & A_{13} & A_{14} & A_{15} & A_{16} & A_{17} \\ A_{21} & A_{22} & A_{23} & A_{24} & A_{25} & A_{26} & A_{27} \\ A_{31} & A_{32} & A_{33} & A_{34} & A_{35} & A_{36} & A_{37} \\ A_{41} & A_{42} & A_{43} & A_{44} & A_{45} & A_{46} & A_{47} \\ A_{51} & A_{52} & A_{53} & A_{54} & A_{55} & A_{56} & A_{57} \\ A_{61} & A_{62} & A_{63} & A_{64} & A_{65} & A_{66} & A_{67} \\ A_{71} & A_{72} & A_{73} & A_{74} & A_{75} & A_{76} & A_{77} \end{bmatrix} \quad \text{(B-2)}$$

$$F_1 = \begin{bmatrix} B_{11} \\ B_{21} \\ B_{31} \\ B_{41} \\ B_{51} \\ B_{61} \\ B_{71} \end{bmatrix}, \; F_2 = \begin{bmatrix} AVB_1 \\ AVB_2 \\ AVB_3 \\ AVB_4 \\ AVB_5 \\ AVB_6 \\ AVB_7 \end{bmatrix}, \; L = \begin{bmatrix} \frac{1}{L_{C1}} & 0 & 0 & 0 & 0 & 0 & 0 \\ 0 & 0 & 0 & 0 & 0 & 0 & 0 \end{bmatrix} \quad \text{(B-3)}$$

The elements are presented as follows:

A11=-((3*Id*Vd)/(2*C1*Vdc1^2)) + (3*Id*Kf1*Kidp*Kvcp*Vc)/(2*C1*Vdc1*(-Vc+Kidp*Kvcp*Vd))-(3*Iq*Vq)/(2*C1*Vdc1^2)+(3*0*Kiop*Kiqp*(-Iq*Vc+Iq*Kidp*Kvcp*Vd-Id*Kidp*Kvcp*Vq))/(2*C1*Vdc1*(Vc-Kidp*Kvcp*Vd));

A12=(3*Vd)/(2*C1*Vdc1)-(3*Id*Kidp*Vc)/(2*C1*Vdc1*(-Vc+Kidp*Kvcp*Vd))+(3*Ld*(-Iq*Vc+Iq*Kidp*Kvcp*Vd-Id*Kidp*Kvcp*Vq)*ww)/(2*C1*Vdc1*(Vc-Kidp*Kvcp*Vd));

A13=(3*Vq)/(2*C1*Vdc1)-(3*Kiqp*(-Iq*Vc+Iq*Kidp*Kvcp*Vd-Id*Kidp*Kvcp*Vq))/(2*C1*Vdc1*(Vc-Kidp*Kvcp*Vd))-(3*Id*Lq*Vc*ww)/(2*C1*Vdc1*(-Vc+Kidp*Kvcp*Vd));

A14=(3*Id*Kidp*Vc)/(2*C1*Vdc1*(-Vc+Kidp*Kvcp*Vd));

A15=(3*Kiqp*(-Iq*Vc+Iq*Kidp*Kvcp*Vd-Id*Kidp*Kvcp*Vq))/(2*C1*Vdc1*(Vc-Kidp*Kvcp*Vd));

A16=(3*Id*Vc)/(2*C1*Vdc1*(-Vc+Kidp*Kvcp*Vd));

A17=(3*(-Iq*Vc+Iq*Kidp*Kvcp*Vd-Id*Kidp*Kvcp*Vq))/(2*C1*Vdc1*(Vc-Kidp*Kvcp*Vd));

A21=-((Kf1*Kidp*Kvcp*Vc)/(Ld*(-Vc+Kidp*Kvcp*Vd))) + (0*Kidp*Kiop*Kiqp*Kvcp*Vq)/(Ld*Vc*(1-(Kidp*Kvcp*Vd)/Vc));

A22=-(Rs1/Ld) +(Kidp*Vc)/(Ld*(-Vc+Kidp*Kvcp*Vd)) + (Kidp*Kvcp*Vq*ww)/(Vc*(1 - (Kidp*Kvcp*Vd)/Vc));

A23=-((Kidp*Kiqp*Kvcp*Vq)/(Ld*Vc*(1-(Kidp*Kvcp*Vd)/Vc)))+(Lq*ww)/Ld + (Lq*Vc*ww)/(Ld*(-Vc+Kidp*Kvcp*Vd));

A24=-(Kidp*Vc)/(Ld*(-Vc+Kidp*Kvcp*Vd));

A25=(Kidp*Kiqp*Kvcp*Vq)/(Ld*Vc*(1-(Kidp*Kvcp*Vd)/Vc));

A26=-Vc/(Ld*(-Vc+Kidp*Kvcp*Vd));

A27=(Kidp*Kvcp*Vq)/(Ld*Vc*(1-(Kidp*Kvcp*Vd)/Vc));

A31=0;

A32=0;

A33=-(Kiqp/Lq+Rs1/Lq);

A34=0;

A35=Kiqp/Lq;

A36=0;

A37=1/Lq;

A41=Kf1*Kvci+(Kf1*Kidp*Kvci*Kvcp*Vd)/(Vc-Kidp*Kvcp*Vd)+(0*Kiop*Kiqp*Kvci*Vq)/(Vc-Kidp*Kvcp*Vd);

A42=-((Kidp*Kvci*Vd)/(Vc-Kidp*Kvcp*Vd))+(Kvci*Ld*Vq*ww)/(Vc-Kidp*Kvcp*Vd);

A43=-((Kiqp*Kvci*Vq)/(Vc-Kidp*Kvcp*Vd))-(Kvci*Lq*Vd*ww)/(Vc-Kidp*Kvcp*Vd);

A44=(Kidp*Kvci*Vd)/(Vc-Kidp*Kvcp*Vd);

A45=(Kiqp*Kvci*Vq)/(Vc-Kidp*Kvcp*Vd);

A46=(Kvci*Vd)/(Vc-Kidp*Kvcp*Vd);

A47=(Kvci*Vq)/(Vc-Kidp*Kvcp*Vd);

A51=0;

A52=0;

A53=0;

A54=0;

A55=0;

A56=0;

A57=0;

A61=Kf1*Kidi*Kvcp+(Kf1*Kidi*Kidp*Kvcp^2*Vd)/(Vc-Kidp*Kvcp*Vd)+(0*Kidi*Kiop*Kiqp*Kvcp*Vq)/(Vc-Kidp*Kvcp*Vd);

A62=-Kidi-(Kidi*Kidp*Kvcp*Vd)/(Vc-Kidp*Kvcp*Vd)+(Kidi*Kvcp*Ld*Vq*ww)/(Vc-Kidp*Kvcp*Vd);

A63=-((Kidi*Kiqp*Kvcp*Vq)/(Vc-Kidp*Kvcp*Vd))-(Kidi*Kvcp*Lq*Vd*ww)/(Vc-Kidp*Kvcp*Vd);

A64=Kidi+(Kidi*Kidp*Kvcp*Vd)/(Vc-Kidp*Kvcp*Vd);

A65=(Kidi*Kiqp*Kvcp*Vq)/(Vc-Kidp*Kvcp*Vd);

A66=(Kidi*Kvcp*Vd)/(Vc-Kidp*Kvcp*Vd);

A67=(Kidi*Kvcp*Vq)/(Vc-Kidp*Kvcp*Vd);

A71=0;

A72=0;

A73=-Kiqi;

A74=0;

A75=Kiqi;

A76=0;

A77=0;

B11= (-(1/C1)-(3*Kiop*Kiqp*(-Iq*Vc+Iq*Kidp*Kvcp*Vd-Id*Kidp*Kvcp*Vq))/(2*C1*Vdc1*(Vc-Kidp*Kvcp*Vd)))

B21=-((Kidp*Kiop*Kiqp*Kvcp*Vq)/(Ld*Vc*(1-(Kidp*Kvcp*Vd)/Vc)));

B31=-1/Lq*Kiqp*Kiop;

B41=-(Vq*Kiqp*Kiop*Kvci)/((Vc-Vd*Kidp*Kvcp));

B51=-Kioi;

B61=-Kidi*Kiop*Kiqp*Kvcp*Vq/((Vc-Vd*Kidp*Kvcp));

B71=-Kiop*Kiqi;

AVB1= (3* kD1*Kiop*Kiqp*(-Iq*Vc+Iq*Kidp*Kvcp*Vd-Id*Kidp*Kvcp*Vq))/(2*C1*Vdc1*(Vc-Kidp*Kvcp*Vd));

AVB2= (kD1*Kidp*Kiop*Kiqp*Kvcp*Vq)/(Ld*Vc*(1-(Kidp*Kvcp*Vd)/Vc));

AVB3= kD1*Kiop*Kiqp/Lq;

AVB4= (kD1*Kiop*Kiqp*Kvci*Vq)/(Vc-Kidp*Kvcp*Vd);

AVB5= kD1*Kioi;

AVB6= (kD1*Kidi*Kiop*Kiqp*Kvcp*Vq)/(Vc-Kidp*Kvcp*Vd);

AVB7= kD1*Kiop*Kiqi;

Appendix C State-Space Model for Source Impedance Computation

C.1 State-space modelling for current-mode LVF droop-controlled system

The LVF state-space model is shown in C.1-1,

$$\begin{aligned} \dot{\Delta x} &= A_{LVF}\Delta x + B_{LVF}\Delta u \\ \Delta y &= C_{LVF}\Delta x \end{aligned} \tag{C.1-1}$$

where the state matrices (A_{LVF}, B_{LVF}, C_{LVF}) are shown as follows:

$$A_{LVF} = \begin{bmatrix} 0 & 0_{1*n} & \begin{pmatrix} \frac{1}{C_b} & * & * & * & \frac{1}{C_b} \end{pmatrix} & 0_{1*n} \\ 0_{n*1} & 0_{n*n} & \begin{pmatrix} -\frac{1}{C_1} & & \\ & \ddots & \\ & & -\frac{1}{C_n} \end{pmatrix} & \begin{pmatrix} \frac{1}{C_1} & & \\ & \ddots & \\ & & \frac{1}{C_n} \end{pmatrix} \\ \begin{pmatrix} -\frac{1}{L_1} \\ \vdots \\ -\frac{1}{L_n} \end{pmatrix} & \begin{pmatrix} \frac{1}{L_1} & & \\ & \ddots & \\ & & \frac{1}{L_n} \end{pmatrix} & \begin{pmatrix} -\frac{R_1}{L_1} & & \\ & \ddots & \\ & & -\frac{R_n}{L_n} \end{pmatrix} & 0_{n*n} \\ 0_{n*1} & \begin{pmatrix} -\frac{1}{T_1 k_1} & & \\ & \ddots & \\ & & -\frac{1}{T_n k_n} \end{pmatrix} & 0_{n*n} & \begin{pmatrix} -\frac{1}{T_1} & & \\ & \ddots & \\ & & -\frac{1}{T_n} \end{pmatrix} \end{bmatrix} \tag{C.1-2}$$

$$B_{LVF}=\begin{bmatrix}\frac{1}{C_b} & 0 & 0 & \bullet & \bullet & \bullet & 0\end{bmatrix},\ C_{LVF}=\begin{bmatrix}1 & 0 & 0 & \bullet & \bullet & \bullet & 0\end{bmatrix}$$

where T_i is the time constant, k_i is the droop gain, R_i is the feeder resistance, L_i is the feeder inductance, C_i is the local capacitance of the ith module, n is the number of parallel modules.

C.2 State-space modelling for current-mode GVF droop-controlled system

The GVF state-space model is shown as

$$\begin{aligned}\dot{\Delta x} &= A_{GVF}\Delta x + B_{GVF}\Delta u\\ \Delta y &= C_{GVF}\Delta x\end{aligned} \tag{C.2-1}$$

where the state matrices (A_{GVF}, B_{GVF}, C_{GVF}) are shown as follows:

$$A_{GVF}=\begin{bmatrix} 0 & 0_{1*n} & \begin{pmatrix}\frac{1}{C_b} & * & * & * & \frac{1}{C_b}\end{pmatrix} & 0_{1*n}\\ 0_{n*1} & 0_{n*n} & \begin{pmatrix}-\frac{1}{C_1} & & & \\ & \bullet & & \\ & & \bullet & \\ & & & -\frac{1}{C_n}\end{pmatrix} & \begin{pmatrix}\frac{1}{C_1} & & & \\ & \bullet & & \\ & & \bullet & \\ & & & \frac{1}{C_n}\end{pmatrix}\\ \begin{pmatrix}-\frac{1}{L_1}\\ \bullet\\ \bullet\\ \bullet\\ -\frac{1}{L_n}\end{pmatrix} & \begin{pmatrix}\frac{1}{L_1} & & & \\ & \bullet & & \\ & & \bullet & \\ & & & \frac{1}{L_n}\end{pmatrix} & \begin{pmatrix}-\frac{R_1}{L_1} & & & \\ & \bullet & & \\ & & \bullet & \\ & & & -\frac{R_n}{L_n}\end{pmatrix} & 0_{n*n}\\ \begin{pmatrix}-\frac{1}{T_1k_1}\\ \bullet\\ \bullet\\ \bullet\\ -\frac{1}{T_nk_n}\end{pmatrix} & 0_{n*n} & 0_{n*n} & \begin{pmatrix}-\frac{1}{T_1} & & & \\ & \bullet & & \\ & & \bullet & \\ & & & -\frac{1}{T_n}\end{pmatrix}\end{bmatrix} \tag{C.2-2}$$

$$B_{GVF}=\begin{bmatrix}\frac{1}{C_b} & 0 & 0 & \bullet & \bullet & \bullet & 0\end{bmatrix},\ C_{GVF}=\begin{bmatrix}1 & 0 & 0 & \bullet & \bullet & \bullet & 0\end{bmatrix}$$

C.3 State-space modelling for voltage-mode droop-controlled system

The voltage-mode state-space model is shown in (C.3-1),

$$\begin{aligned} \dot{\Delta x} &= A_V \Delta x + B_V \Delta u \\ \Delta y &= C_V \Delta x \end{aligned} \tag{C.3-1}$$

where the state matrices (A_V, B_V, C_V) are shown as follows:

$$A_V = \begin{bmatrix} 0 & \left(\frac{1}{C_b}, \cdots \frac{1}{C_b}\right) \\ \begin{pmatrix} -\frac{1}{L_1} \\ \bullet \\ \bullet \\ \bullet \\ -\frac{1}{L_n} \end{pmatrix} & \begin{pmatrix} -\frac{R_1}{L_1} & & & \\ & \bullet & & \\ & & \bullet & \\ & & & \bullet \\ & & & -\frac{R_n}{L_n} \end{pmatrix} \end{bmatrix} \tag{C.3-2}$$

$$B_V = \begin{bmatrix} \frac{1}{C_b} & 0 & 0 & \bullet & \bullet & \bullet & 0 \end{bmatrix}, \quad C_V = \begin{bmatrix} 1 & 0 & 0 & \bullet & \bullet & \bullet & 0 \end{bmatrix}$$

References

[1] J. A. Rosero, J. A. Ortaga, E. Aldabas, and L. Romeral, “Moving towards a more electric aircraft,” *IEEE Aerosp. Electron. Syst. Mag.*, vol. 22, no. 3, pp. 3–9, Mar. 2007.

[2] Cleansky project, http://www.cleansky.eu.

[3] K. Emadi and M. Ehsani, “Aircraft power systems: technology, state of the art, and future trends,” *IEEE Aerosp. Electron. Syst. Mag.*, vol. 15, no. 1, pp. 28–32, Jan. 2000.

[4] Y. Tao, "Development of dynamic phasors for the modelling of aircraft electrical power systems," PhD Dissertation, University of Nottingham, 2013.

[5] R. K. Agarwal, “Recent advances in aircraft technology”, Ch 13. Power generation and distribution system for a more electric aircraft- A review, pp. 289–308, Feb. 2012.

[6] K. Rajashekara, “Power conversion technologies for automotive and aircraft systems,” *IEEE Electrif. Mag*., pp. 50–60, Jun. 2014.

[7] M. Sinnett, “787 No-bleed systems: saving fuel and enhancing operational efficiencies”, *Boeing Aero Mag*., vol. 4, pp. 6–11, 2007.

[8] X. Roboam, B. Sareni, and A. D. Andrade, “More electricity in the air: toward optimized electrical networks embedded in more-electrical aircraft,” *IEEE Ind. Electron. Mag.*, vol. 6, no. 4, pp. 6–17, Dec. 2012.

[9] GaN based power devices: cost-effective revolutionary performance, http://www.infineon.com/dgdl/560pee0811.pdf?fileId=5546d462533600a4015356925db52b5d.

[10] Chris Gerada, “High performance electrical machines for electrical propulsion,” Presentaion on future power train conference, Feb. 2014.

[11] B. Mecrow, J. Cullen and P. Mellor, “Editorial - Electrical machines and drives for the more electric aircraft,” *IET Elec. Power Appl*., vol. 5, no. 1, pp. 1–2, Jan. 2011.

[12] B. H. Nya, J. Brombach, and D. Schulz, “Benefits of higher voltage levels in aircraft electrical power systems,” in *Proc. Electrical Systems for Aircraft, Railway and Ship Propulsion (ESARS)*, Bologna, Oct. 2012, pp. 1–5.

[13] J.C. Swierczek, F. Moller, C. Saudemont, R. Meuret, and B. Robyns, “Power management of a regenerative local HVDC aircraft network using supercapacitors,” in *Proc. of the 15th International Power Electronics and Motion Control Conference, EPE-PEMC 2012 ECCE Europe*, Novi Sad, Serbia, 2012.

[14] MOET EU Project, (2006). [Online]. Available:http://www.eurtd.com/moet.

[15] T. Dragicevic, J. M. Guerrero, and J.C. Vasquez, “A distributed control strategy for coordination of an autonomous LVDC microgrid based on power-line signaling,” *IEEE Trans. Ind. Electron.*, vol. 61, no. 7, pp. 3313–3326, Jul. 2014.

[16] K. Sun, L. Zhang, Y. Xing, and J. M. Guerrero, “A distributed control strategy based on DC bus signaling for modular photovoltaic generation systems with battery energy storage,” *IEEE Trans. Power Electron.*, vol. 26, no. 10, pp. 3032–3045, Oct. 2011.

[17] L. Xu and D. Chen, “Control and operation of a DC microgrid with variable generation and energy storage,” *IEEE Trans. Power Electron*., vol. 26, no. 4, pp. 2513–2522, Oct. 2011.

[18] X. Yu, A. M. Khambadkone, H. Wang, and S. T. S. Terence, “Control of parallel-connected power converters for low-voltage microgrid-Part I: A hybrid control architecture,” *IEEE Trans. Power Electron.*, vol. 25, no. 12, pp. 2962–2970, Dec. 2010.

[19] H. Wang, A. M. Khambadkone, and X. Yu, “Control of parallel-connected power converters for low-voltage microgrid-Part II: Dynamic electrothermal modeling,” *IEEE Trans. Power Electron.*, vol. 25, no. 12, pp. 2971–2980, Dec. 2010.

[20] J. Xiao, P. Wang, and L. Setyawan, “Implementation of multiple-slack-terminal DC microgrids for smooth transitions between grid-tied and islanded states,” *IEEE Trans. Smart Grid*, vol. 7, no. 1, pp. 273–281, Jan. 2016.

[21] US Patent, “Integrated electrical power extraction for aircraft engines,” US7468561 B2, Dec. 2008, available at http://www.google.co.uk/patents/US7468561.

[22] K. Areerak, “Modelling and stability analysis of aircraft power systems,” PhD Dissertation, The University of Nottingham, Oct. 2009.

[23] D. Marx, P. Magne, B. Nahid-Mobarakeh, S. Pierfederici, and B. Davat, “Large signal stability analysis tools in DC power systems with constant power loads and variable power loads—A review,” *IEEE Trans. Power Electron.*, vol. 27, no. 4, pp. 1773–1787, Apr. 2012.

[24] P. E. Gartz, “Commercial systems development in a changed world,” *IEEE Trans. Aerosp. Electron. Syst.*, vol. 33, no. 2, pp. 632–636, Apr. 1997.

[25] D. Izquierdo, R. Azcona, F. J. L. Cerro, C. Fernández, and B. Delicado, “Electrical power distribution system (HV270DC), for application in more electric aircraft,” in *Proc. IEEE Appl. Power Electron. Conf. Exhib*., 2010, pp. 1300–1305.

[26] A. Eid, H. El-Kishky, M. Abdel-Salam, and T. El-Mohandes, “Modeling and characterization of an aircraft electric power system with a fuel cell equipped APU paralleled at main ac bus,” in *Proc. IEEE Conf. Int. Power Modulator High Voltage*, 2010, pp. 229–232.

[27] R. E. J. Quigley, “More electric aircraft,” *Proc. 8th the Applied Power Electronics Conference and Exposition, APEC’93*, 1993, pp. 906–911.

[28] P. Wheeler and S. Bozhko, “The more electric aircraft: technology and challenge,” *IEEE Electrif. Mag*., vol. 2, no. 4, pp. 6–12, Dec. 2014.

[29] R. Abdel-Fadil, A. Eid, and M. Abdel-Salam, “Electrical distribution power systems of modern civil aircrafts,” *Proc. 2nd International Conference on Energy Systems and Technologies*, Cairo, Egypt, Feb. 2013, pp. 1–10.

[30] Ian Moir and A. Seabridge, “Aircraft systems: Mechanical, electrical, and avionics susbsystems integration, third edition,” John Wiley & Sons, 2008.

[31] V. Biagini, P. Zanchetta, M. Odavic, M. Sumner, and M. Degano, “Control and modulation of a multilevel active filtering solution for variable-speed constant-frequency more-electric aircraft grids,” *IEEE Trans. Ind. Informat*., vol. 9, no. 2, pp. 600–608, Jun. 2013.

[32] M. Olaiya and N. Buchan, “High power variable frequency generator for large civil aircraft,” in *Proc. IET Elect. Mach. Syst. More Elect. Aircr*., 1999, pp. 1–4.

[33] Department of Defense of United States of America, “Department of defense interface standard–aircraft electric power characteristics,” Military Std. MIL-STD-704F, USA, Mar. 2004.

[34] I. Moir and A. Seabridge, Aircraft Systems: Mechanical, Electrical and Avionics Subsystems Integration: Wiley, 2008.

[35] B. S. Bhangu and K. Rajashekara, “Electric starter generators: The integration into gas turbine engines,” *IEEE Ind. Appl. Mag.*, vol. 20, no. 2, pp. 14–22, Apr. 2014.

[36] N. Fernando, G. Vakil, P. Arumugam, E. Amankwah, C. Gerada, and S. Bozhko, “Impact of soft magnetic material on design of high speed permanent magnet machines,” *IEEE Trans. Ind. Electron*., vol. PP, no. 99, pp. 1-1, 2016.

[37] M. E. Elbuluk and M. D. Kankam, “Potential starter/generator technologies for future aerospace applications,” *IEEE Aerosp. Electron. Syst. Mag.*, vol. 12, no. 5, pp. 24–31, May 1997.

[38] Z. Yang, F. Shang, I. P. Brown, and M. Krishnamurthy, “Comparative study of interior permanent magnet, induction, and switched reluctance motor drives for EV and HEV applications,” *IEEE Trans. Transp. Electrif*. vol. 1, no. 6, pp. 245–254, Oct. 2015.

[39] US Patent, “Three phase flux switching generator in a three stage wound field synchronous machine,” US2015097372 A1, available at http://www.google.co.uk/patents/US7468561.

[40] I. Alan and T. A. Lipo, “Starter/generator employing resonant-converter-fed induction machine. I. Analysis,” *IEEE Trans. Aerosp. Electron. Syst.*, vol. 36, no. 4, pp. 1309–1328, Oct. 2000.

[41] I. Alan and T. A. Lipo, “Starter/generator employing resonant-converter-fed induction machine. II. Hardware prototype,” *IEEE Trans. Aerosp. Electron. Syst.*, vol. 36, no. 4, pp. 1319–1329, Oct. 2000.

[42] R. Bojoi, A. Cavagnino, A. Tenconi, and S. Vaschetto, “Control of shaft-line-embedded multiphase starter/generator for aero-engine,” *IEEE Trans. Ind. Electron.*, vol. 63, no. 1, pp. 641–652, Jan. 2016.

[43] E. Ganev, “Selecting the best electric machines for electrical power-generation systems: High-performance solutions for aerospace more electric architectures,” *IEEE Electrification Magazine*, vol. 2, no. 4, pp. 13–22, Dec. 2014.

[44] S. R. Jones and B. T. Drager, “Sensorless switched reluctance starter/generator performance,” *IEEE Ind. Appl. Mag.*, vol. 3, pp. 33–38, Nov/Dec. 1997.

[45] D. J. Powell, G. W. Jewell, S. D. Calverley and D. Howe, “Iron loss in a modular rotor switched reluctance machine for the “More-Electric” aero-engine,” *IEEE Trans. Magn.*, vol. 41, no. 10, pp. 3934–3936, Oct. 2005.

[46] N. Schofield and S. Long, “Generator operation of a switched reluctance starter/generator at extended speeds,” *IEEE Trans. Veh. Technol.*, vol. 58, no. 1, pp. 48–56, Jan. 2009.

[47] A. Griffo, D. Drury, T. Sawata, and P. H. Mellor, “Sensorless starting of a wound-field synchronous starter/generator for aerospace applications,” *IEEE Trans. Ind. Electron.*, vol. 59, no. 9, pp. 3579–3587, Sep. 2012.

[48] S. Fang, Q. Liu, H. Lin, and S. L. Ho, “A novel flux-weakening control strategy for permanent-magnet actuator of vacuum circuit breaker,” *IEEE Trans. Ind. Electron*., vol. 63, no. 4, pp. 2275–2283, Mar. 2016.

[49] J. Wei, Q. Deng, B. Zhou, M. Shi, and Y. Liu, “The control strategy of open-winding permanent magnet starter-generator with inverter-rectifier topology,” *IEEE Trans. Ind. Inform.*, vol. 9, no. 2, pp. 983–991, May 2013.

[50] J. Legranger, G. Friedrich, S. Vivier, and J. C. Mipo, “Combination of finite-element and analytical models in the optimal multidomain design of machines: application to an interior permanent-magnet starter generator,” *IEEE Trans. Ind. Appl.*, vol. 46, no. 1, pp. 232–239, Jan./Feb. 2010.

[51] C. F. Wang, M. J. Jin, J. X. Shen, and C. Yuan, “A permanent magnet integrated starter generator for electric vehicle onboard range extender application,” *IEEE Trans. Magn.*, vol. 48, no. 4, pp. 1625–1628, Apr. 2012.

[52] L. Chedot, G. Friedrich, J. M. Biedinger, and P. Macret, “Integrated starter generator: The need for an optimal design and control approach. application to a permanent magnet machine,” *IEEE Trans. Ind. Appl.*, vol. 43, no. 2, pp. 551–559, Mar./Apr. 2007.

[53] C. Liu, K. T. Chau, and J. Z. Jiang, “A permanent-magnet hybrid brushless integrated starter–generator for hybrid electric vehicles,” *IEEE Trans. Ind. Electron.*, vol. 57, no. 12, pp. 4055–4064, Dec. 2010.

[54] H. Abu-Rub, M. Malinowski, and K. Al-Haddad, “Power electronics for renewable energy systems, transportation and industry applications,” IEEE Wiley, Jul. 2014.

[55] Cleansky. AEGART Project Summary. Available: http://cordis.europa.eu/result/rcn/143557_en.html. Accessed: 11/11/2015.

[56] 787 Electrical system, http://787updates.newairplane.com/787-Electrical-Systems/787-Electrical-System#

[57] T. Dragicevic, X. Lu, J. Vasquez, and J. Guerrero, “DC microgrids–Part I: A review of control strategies and stabilization techniques,” *IEEE Trans. Power Electron.*, vol. 31, no. 7, pp.4876-4891, Sep. 2016.

[58] N. Hur and K. Nam, “A robust load-sharing control scheme for parallel connected multisystems,” *IEEE Trans. Ind. Electron.*, vol. 47, no. 4, pp. 871–879, Aug. 2000.

[59] X. Sun, Y.-S. Lee, and D. Xu, “Modeling, analysis, and implementation of parallel multi-inverter system with instantaneous average-current-sharing scheme,” *IEEE Trans. Power Electron*., vol. 18, no. 3, pp. 844–856, May 2003.

[60] J. M. Guerrero, L. Hang, and J. Uceda, “Control of distributed uninterruptible power supply systems,” *IEEE Trans. Ind. Electron.*, vol. 55, no. 8, pp. 2845–2859, Aug. 2008.

[61] S. Luo, Z. Ye, R. Lin, and F. C. Lee, “A classification and evaluation of paralleling methods for power supply modules,” in *Proc. 30th Power Electronic Specialists Conference, IEEE*, vol. 2, 1999, pp. 901–908.

[62] S. K. Mazumder, M. Tahir, and K. Acharya, “Master–slave current sharing control of a parallel DC–DC converter system over an RF communication interface,” *IEEE Trans. Ind. Electron*., vol. 55, no. 1, pp. 59–66, Jan. 2008.

[63] H.H.C. Iu, V. Pjevalica, and B. Robert, “Implementation of a simple rotating master control scheme for parallel converters,” in *Proc. Power Electronics Specialists Conference, 2004. PESC 04. 2004 IEEE 35th Annual*, Jun. 2004, pp.1494–1499.

[64] S. Pan and P. K. Jain, "A precisely-regulated multiple output forward converter with automatic master-slave control," in *Proc. Power Electronics Specialists Conference, 2005. PESC 05. 2005 IEEE 36th Annual*, Jun. 2005, pp.969–975.

[65] F. Valenciaga and P. F. Puleston, "Supervisor control for a stand-alone hybrid generation system using wind and photovoltaic energy," *IEEE Trans. Energy Convers*., vol. 20, no. 2, pp. 398–405, Jun. 2005.

[66] F. Valenciaga and P. F. Puleston, "High-order sliding control for a wind energy conversion system based on a permanent magnet synchronous generator," *IEEE Trans. Energy Convers*., vol. 23, no. 3, pp. 860–867, Sep. 2008.

[67] S. K. Mazumder, M. Tahir, and K. Acharya, "Master-slave current-sharing control of a parallel DC-DC converter system over an rf communication interface," *IEEE Trans. Ind. Electron*., vol. 55, no. 1, pp. 59–66, Jan. 2008.

[68] G. Byeon, T. Yoon, S. Oh, and G. Jang, "Energy management strategy of the DC distribution system in buildings using the EV service model," *IEEE Trans. Power Electron*., vol. 28, no. 4, pp. 1544–1554, Apr. 2013. 69

[69] B. Wang, M. Sechilariu, and F. Locment, "Intelligent DC microgrid with smart grid communications: Control strategy consideration and design," *IEEE Trans. Smart Grid*, vol. 3, no. 4, pp. 2148–2156, Dec. 2012.

[70] C. Xianghui, C. Jiming, X. Yang, and S. Youxian, "Building-environment control with wireless sensor and actuator networks: Centralized versus distributed," *IEEE Trans. Ind. Electron*., vol. 57, no. 11, pp. 3596–3605, Nov. 2010.

[71] A. P. Martins, A. S. Carvalho, and A. S. Araújo, "Design and implementation of a current controller for the parallel operation of standard UPSs," in *Proc. IEEE IECON*, 1995, pp. 584–589.

[72] R. Olfati-Saber and R. M. Murray, "Consensus problems in networks of agents with switching topology and time-delays," *IEEE Trans. Autom. Control*, vol. 49, no. 9, pp. 1520–1533, Sep. 2004.

[73] Z. Meng, W. Ren, Y. Cao, and Z. You, "Leaderless and leader-following consensus with communication and input delays under a directed network topology," *IEEE Trans. Syst. Man, Cybern. B, Cybern*., vol. 41, no. 1, pp. 75–88, Feb. 2011.

[74] F. L. Lewis, Z. Qu, A. Davoudi, and A. Bidram, "Secondary control of microgrids based on distributed cooperative control of multi-agent systems," *IET Gener. Transmiss. Distrib.*, vol. 7, no. 8, pp. 822–831, 2013.

[75] H. Behjati, A. Davoudi, and F. Lewis, "Modular DC-DC converters on graphs: Cooperative control," *IEEE Trans. Power Electron*., vol. 29, no. 12, pp. 6725–6741, Dec. 2014.

[76] V. Nasirian, S. Moayedi, A. Davoudi, and F. Lewis, “Distributed cooperative control of DC Microgrids,” *IEEE Trans. Power Electron*., vol. 30, no. 4, pp. 2288–2303, Apr. 2015.

[77] L. Meng, X. Zhao, F. Tang, M. Savaghedi, T. Dragicevic, J.C. Vasquez, and J. M. Guerrero, “Distributed voltage unbalance compensation in islanded microgrids by using a dynamic consensus algorithm,” *IEEE Trans. Power Electron*., vol. 31, no. 1, pp. 827–838, Jan. 2016.

[78] L. Meng, T. Dragicevic, J. Roldán-Pérez, J. C. Vasquez, and J. M. Guerrero, “Modeling and sensitivity study of consensus algorithm-based distributed hierarchical control for DC microgrids,” *IEEE Trans. Smart Grid*, vol. 7, no. 3, pp. 1504–1515, May 2016.

[79] J. M. Guerrero, J. C. Vasquez, J. Matas, L. Vicuña G., et al, “Hierarchical control of droop-controlled AC and DC microgrids—A general approach toward standardization,” *IEEE Trans. Ind. Electron*., vol. 58, no. 1, pp. 158–172, Jan. 2011.

[80] J. M. Guerrero, M. Chandorkar, T.-L. Lee, and P. C. Loh, “Advanced control architectures for intelligent microgrids—Part I: decentralized and hierarchical Control,” *IEEE Trans. Ind. Electron*., vol. 60, no. 4, pp. 1254–1262, Apr. 2013.

[81] T. M. Haileselassie and K. Uhlen, “Impact of DC line voltage drops on power flow of MTDC using droop control,” *IEEE Trans. Power Syst.*, vol. 27, no. 1, pp. 1441–1449, Aug. 2012.

[82] N. R. Chaudhuri and B. Chaudhuri, “Adaptive droop control for effective power sharing in Multi-Terminal DC (MTDC) grids,” *IEEE Trans. Power Syst.*, vol. 28, no. 1, pp. 21–29, Feb. 2013.

[83] H. Kakigano, Y. Miura, and T. Ise, “Distribution voltage control for DC microgrids using fuzzy control and gain-scheduling technique,” *IEEE Trans. Power Electron*., vol. 28, no. 5, pp. 2246–2258, May 2013.

[84] S. Anand, B. G. Fernandes, and J. M. Guerrero, “Distributed control to ensure proportional load sharing and improve voltage regulation in low-voltage DC microgrids,” *IEEE Trans. Power Electron.*, vol. 28, no. 4, pp. 1900–1913, Apr. 2013.

[85] J. M. Guerrero, J. Vasquez, and R. Teodorescu, “Hierarchical control of droop-controlled DC and AC microgrids—A general approach towards standardization,” in *Proc. 35th Annu. Conf. IEEE Ind. Electron*., Nov. 2009, pp. 4305–4310.

[86] J. Kim, H. Choi, and B. H. Cho, “A novel droop method for converter parallel operation,” *IEEE Trans. Power Electron*., vol. 17, no. 1, pp. 25–32, Jan. 2002.

[87] T. S. Kwon and S. K. Sul, “Novel anti-windup of a current regulator of a surface-mounted permanent-magnet motor for flux weakening control,” *IEEE Trans. Ind. Appl*., vol. 42, no. 5, pp. 1293–1300, Sep./Oct. 2006.

[88] T.-S. Kwon, G.-Y. Choi, M.-S. Kwak, and S.-K. Sul, “Novel flux-weakening control of an IPMSM for quasi six-step operation,” *IEEE Trans. Ind. Appl*., vol. 44, no. 6, pages 1722–1731, Nov./Dec., 2008.

[89] Y. Zhang, L. Xu, M. K. Güven, S. Chi, and M. Illindala, “Experimental verification of deep field weakening operation of a 50-kW IPM machine by using single current regulator,” *IEEE Trans. Ind. Appl*., vol. 47, no. 1, pp. 128–133, Jan./Feb. 2011.

[90] B. Sarlioglu and C.T. Morris, “More electric aircraft: Review, challenges, and opportunities for commercial transport aircraft,” *IEEE Trans. Transp. Electrif.*, vol. 1, no. 1, pp.54–64, Jun. 2015.

[91] A. Emadi, A. Khaligh, C. Rivetta, and G. Williamson, “Constant power loads and negative impedance instability in automotive systems: Definition, modeling, stability, and control of power electronic converters and motor drives,” *IEEE Trans. Veh. Technol.*, vol. 55, no. 4, pp. 1112–1125, Jul. 2006.

[92] A. Rahimi and A. Emadi, “Active damping in DC/DC power electronic converters: A novel method to overcome the problems of constant power loads,” *IEEE Trans. Ind. Electron.*, vol. 56, no. 5, pp. 1428–1439, May 2009.

[93] M. Kabalan, P. Singh, and D. Niebur, “Large signal Lyapunov-based stability studies in microgrids: A review,” *IEEE Trans. Smart Grid*, vol. 99, no. 99, pp. 1-1, 2016.

[94] P. Kundur et.al, “Definition and classification of power system stability IEEE/CIGRE joint task force on stability terms and definitions,” *IEEE Trans. Power Syst.*, vol. 19, no. 3, pp. 1387–1401, Aug. 2004.

[95] P. W. Sauer and M. A. Pai, *Power System Dynamics and Stability*. Champaign, IL, USA: Stipes, 2006.

[96] W. Du, J. Zhang, Y. Zhang, and Z. Qian, “Stability criterion for cascaded system with constant power load,” *IEEE Trans. Power Electron*., vol. 28, no. 4, pp. 1843–1851, Apr. 2013.

[97] A. Griffo and J. Wang, “Large signal stability analysis of ‘more electric’ aircraft power systems with constant power loads,” *IEEE Aerosp. Electron. Syst. Mag*., vol. 48, no. 1, pp. 477–489, Jan. 2012.

[98] D. Marx, P. Magne, B. Nahid-Mobarakeh, S. Pierfederici, and B. Davat, “Large signal stability analysis tools in DC power systems with constant power loads and

variable power loads-A review," *IEEE Trans. Power Electron*., vol. 27, no. 4, pp. 1773–1787, Apr. 2012.

[99] S. Sonmez and S. Ayasun, "Stability region in the parameter space of PI controller for a single-area load frequency control system with time delay," *IEEE Trans. Power Syst*., vol. 31, no. 1, pp. 829–830, Jan. 2016.

[100] B.-F. Wu, H.-I. Chin, J.-W. Perng, and T.-T. Lee, "Robust control design for perturbed systems by frequency domain approach," *IEEE Trans. Veh. Technol*., vol. 56, no. 5, pp. 2893–2901, Sep. 2007.

[101] B. Demirel, and L. Güvenc, "Parameter space design of repetitive controllers for satisfying a robust performance requirement," *IEEE Trans. Automat. Contr*., vol. 55, no. 8, pp. 1893–1899, Aug. 2010.

[102] D. Siljak, "Parameter space methods for robust control design: a guided tour," *IEEE Trans. Automat. Contr*., vol. 34, no. 7, pp. 674–688, Jul. 1989.

[103] M. Cespedes and J. Sun, "Impedance modeling and analysis of grid-connected voltage-source converters," *IEEE Trans. Power Electron*., vol. 29, no. 3, pp.1254–1261, Mar. 2014.

[104] A. Radwan and Y. Mohamed, "Assessment and mitigation of interaction dynamics in hybrid AC/DC distribution generation systems," *IEEE Trans. Smart Grid*, vol. 3, no. 3, pp. 1382–1393, Sep. 2012.

[105] F. Gao, X. Zheng, and S. Bozhko, "Stability assessment of a droop-controlled multi-generator system in the more electric aircraft using parameter space approach," *accepted for presentation in ECCE 2016, IEEE Energy Conversion Congress & Expo*, Milwaukee, USA, Sep. 2016.

[106] W.U.N. Fernando, M. Barnes, and O. Marjanovic, "Direct drive permanent magnet generator fed AC-DC active rectification and control for more-electric aircraft engines," *IET Electr. Power Appl.*, vol. 5, no. 1, pp. 14-27, 2011.

[107] A. Griffo and J. Wang, "Stability analysis of 'more electric' aircraft hybrid electrical power systems," in *Electrical Machines and Systems (ICEMS), 2011 International Conference on*, Beijing, 2011, pp. 1-8.

[108] K-N. Areerak, T. Wu, S. V. Bozhko, G. M. Asher, and D. W. P. Thomas, "Aircraft power system stability study including effect of voltage control and actuators dynamic," *IEEE Trans. Aerosp. Electron. Syst*., vol. 47, no. 4, pp. 2574–2589, Oct. 2011.

[109] K-N. Areerak, S. V. Bozhko, G. M. Asher, L. De Lillo, and D. W. P. Thomas, "Stability study of a hybrid AC-DC more-electric aircraft power system," *IEEE Trans. Aerosp. Electron. Syst*., vol. 48, no. 1, pp. 329–347, Jan. 2012.

[110] L. Han, J. Wang, and D. Howe, “Small-signal stability studies of a 270V DC more-electric aircraft power system,” *Power Electronics, Machines and Drives, 2006. The 3rd IET International Conference on*, The Contarf Castle, Dublin, Ireland, 2006, pp. 162–166.

[111] R.D. Middlebrook, “Input filer consideration in design and application of switching regulators,” in *Proc. IEEE IAS Annu. Meet*., Chicago, USA, Oct. 1976, pp. 336–382.

[112] J. A. Abu Qahouq and V. Arikatla, “Online closed-loop autotuning digital controller for switching power converters,” *IEEE Trans. Ind. Electron*., vol. 60, no. 5, pp. 1747–1758, May 2013.

[113] J. Morroni, R. Zane, and D. Maksimovic, “Design and implementation of an adaptive tuning system based on desired phase margin for digitally controlled DC-DC converters,” *IEEE Trans. Power Electron*., vol. 24, no. 2, pp. 559–564, Feb. 2009.

[114] X. Feng, J. Liu, and F. C. Lee, “Impedance specifications for stable DC distributed power systems,” *IEEE Trans. Power Electron*., vol. 17, no. 2, pp. 157–162, Aug. 2002.

[115] X. Wang, R. Yao, and F. Rao, “Three-step impedance criterion for small-signal stability analysis in two-stage DC distributed power systems,” *IEEE Power Electron. Lett*., vol. 1, no. 3, pp. 83–87, 2003.

[116] S. D. Sudhoff, S. F. Glover, P. T. Lamm, D. H. Schmucker, and D. E. Delisle, “Admittance space stability analysis of power electronic systems,” *IEEE Trans. Aerosp. Electron. Syst*., vol. 36, no. 3, pp. 965–973, 2000.

[117] C. M. Wildrick, F. C. Lee, B. H. Cho, and B. Choi, “A method of defining the load impedance specification for a stable distributed power system,” *IEEE Trans. Power Electron*., vol. 10, no. 3, pp. 280–285, May 1995.

[118] S. D. Sudhoff and J. M. Crider, “Advancements in generalized immittance based stability analysis of DC power electronics based distribution systems,” in *Proc. IEEE ESTS*, Apr. 2011, pp. 207–212.

[119] X. Feng, Z. Ye, K. Xing, F. C. Lee, and D. Borojevic, “Impedance specification and impedance improvement for DC distributed power system,” in *Proc. 30th IEEE PESC*, Jun./Jul. 1999, vol. 2, pp. 889–894.

[120] X. Feng, Z. Ye, K. Xing, F. C. Lee, and D. Borojevic, “Individual load impedance specification for a stable DC distributed power system,” in *Proc. 14th Annu. IEEE APEC Expo*., Mar. 1999, vol. 2, pp. 923–929.

[121] A. Riccobono and E. Santi, "Comprehensive review of stability criteria for DC power distribution systems," *IEEE Trans. Ind. Appl.*, vol. 50, no. 5, pp. 3525–3535, Sep./Oct. 2014.

[122] B. Wen, D. Boroyevich, R. Burgos, P. Mattavelli, and Z. Shen, “Small-signal stability analysis of three-phase AC systems in the presence of constant power loads based on measured d-q frame impedances,” *IEEE Trans. Power Electron*., vol. 30, no. 10, pp. 5952–5963, Oct. 2015.

[123] B. Wen, D. Dong, D. Boroyevich, R. Burgos, P. Mattavelli, and Z. Shen, “Impedance-based analysis of grid-synchronization stability for three-phase paralleled converters,” *IEEE Trans. Power Electron*., vol. 31, no. 1, pp. 26–38, Jan. 2016.

[124] B. Wen, D. Boroyevich, R. Burgos, Z. Shen, and P. Mattavelli, "Impedance-based analysis of active frequency drift islanding detection for grid-tied inverter system," *IEEE Trans. Ind. Appl.*, vol. 52, no. 1, pp. 332–341, Jan./Feb. 2016.

[125] B. Wen, D. Boroyevich, R. Burgos, P. Mattavelli, and Z. Shen, "Analysis of D-Q small-signal impedance of grid-tied inverters," *IEEE Trans. Power Electron*., vol. 31, no. 1, pp. 675–687, Jan. 2016.

[126] L. H. Hassan, M. Moghavvemi, H. A. F. Almurib, K. M. Muttaqi, and V. G. Ganapathy, “Optimization of power system stabilizers using participation factor and genetic algorithm,” *Int. J. Elect. Power Energy Syst.*, vol. 55, pp. 668–679, Feb. 2014.

[127] Y. Mishra, S. Mishra, M. Tripathy, N. Senroy, and Z. Y. Dong, “Improving stability of a DFIG-based wind power system with tuned damping controller,” *IEEE Trans. Energy Convers.*, vol. 24, no. 3, pp. 650–660, Sep. 2009.

[128] B. Mehta, P. Bhatt, and V. Pandya, “Small signal stability analysis of power systems with DFIG based wind power penetration,” *Int. J. Elect. Power Energy Syst.*, vol. 58, pp. 64–74, Jun. 2014.

[129] F. Mei and B. Pal, “Modal analysis of grid-connected doubly-fed induction generators,” *IEEE Trans. Energy Convers.*, vol. 22, no. 3, pp. 728–736, Sep. 2007.

[130] L. Fan, C. Zhu, Z. Miao, and M. Hu, “Modal analysis of a DFIG-based wind farm interfaced with a series compensated network,” *IEEE Trans. Energy Convers.*, vol. 26, no. 4, pp. 1010–1020, Dec. 2011.

[131] D. Gautam, V. Vittal, and T. Harbour, “Impact of increased penetration of DFIG-based wind turbine generators on transient and small signal stability of power systems,” *IEEE Trans. Power Syst.*, vol. 24, no. 3, pp. 1426–1434, Aug. 2009.

[132] H. K. Nam and Y. K. Kim, “A new eigen-sensitivity theory of augmented matrix and its applications to power system stability,” *IEEE Trans. Power Syst.*, vol. 15, no. 1, pp. 363–369, Feb. 2000.

[133] K. W. Wang and C. Y. Chung, “Multi-machine eigenvalue sensitivities of power system parameters,” *IEEE Trans. Power Syst.*, vol. 15, no. 2, pp. 741–747, May 2000.

[134] L. Yang, Z. Xu, J. Ostergaard, Z. Y. Dong, K. P. Wong, and X. Ma, “Oscillatory stability and eigenvalue sensitivity analysis of a DFIG wind turbine system,” *IEEE Trans. Energy Convers.*, vol. 26, no. 1, pp. 328–339, Mar. 2011.

[135] S. Eftekharnejad, V. Vittal, G. T. Heydt, B. Keel, and J. Loehr, “Small signal stability assessment of power systems with increased penetration of photovoltaic generation: a case study,” *IEEE Trans. Sust. Energy*, vol. 4, no. 4, pp. 960–967, Oct. 2013.

[136] Y. Tang, P. Ju, H. He, C. Qin, and F. Wu, “Optimized control of DFIG-based wind generation using sensitivity analysis and particle swarm optimization,” *IEEE Trans. Smart Grid*, vol. 4, no. 1, pp. 509–520, Mar. 2013.

[137] F. Wu, X. Zhang, K. Godfrey, and P. Ju, “Small signal stability analysis and optimal control of a wind turbine with doubly fed induction generator,” *IET Gener. Transm. Distrib.*, vol. 1, no. 5, pp. 757–760, Sep. 2007.

[138] L. Rouco and F. L. Pagola, “An eigenvalue sensitivity approach to location and controller design of controllable series capacitors for damping power system oscillations,” *IEEE Trans. Power Syst.*, vol. 12, no. 4, pp. 1660–1666, Nov. 1997.

[139] A. Griffo and J. Wang, “Modeling and stability analysis of hybrid power systems for the more electric aircraft,” *Elec. Power Syst. Res.*, vol. 82, no. 1, pp. 59–67, Jan. 2012.

[140] K-N. Areerak, T. Wu, S. V. Bozhko, G. M. Asher, and D. W. P. Thomas, “Aircraft power system stability study including effect of voltage control and actuators dynamic,” *IEEE Trans. Aerosp. Electron. Syst.*, vol. 47, no. 4, pp. 2574–2589, Oct. 2011.

[141] K-N. Areerak, S. V. Bozhko, G. M. Asher, L. De Lillo, and D. W. P. Thomas, “Stability study of hybrid AC-DC more-electric aircraft power system,” *IEEE Trans. Aerosp. Electron. Syst.*, vol. 48, no. 1, pp. 329–347, Jan. 2012.

[142] F. Gao, X. Zheng, S. Bozhko, C. Hill, and G. Asher, “Modal analysis of a PMSG-based dc electrical power system in the more electric aircraft using eigenvalues sensitivity,” *IEEE Trans. Transp. Electrif.*, vol. 1, no. 1, pp. 65–76, Jun. 2015.

[143] P. C. Krause, O. Wasynczuk, and S. D. Sudhoff, “Analysis of electric machinery and drive system,” *Wiley-IEEE Press*, 2002.

[144] W. Leonhard, “Adjustable-speed ac drives,” *Proc of IEEE*, vol. 76, no. 4, pp. 455–471, 1988.

[145] S. Yeoh, F. Gao, S. Bozhko, and G. Asher, “Control design for PMM-based starter generator system for more electric aircraft,” in *16th IEEE European Conference on Power Electronics and Applications(EPE)*, Lappeenranta, Finland, Aug. 2014, pp. 1–10.

[146] C. T. Pan and J. H. Liaw, “A robust field-weakening control strategy for surface-mounted permanent-magnet motor drives,” *IEEE Trans. Energy Convers*., vol. 20, no. 4, pp. 70–709, Dec. 2005.

[147] A. Yazdani and R. Iravani, “Voltage-sourced converters in power systems: Modeling, control and applications,” IEEE Willey Press, 2010.

[148] L. Han, J. Wang, and D. Howe, “Small-signal stability studies of a 270V dc more-electric aircraft power system,” in *Proc. Power Electronics Machines and Drives 2006. The 3rd IET International Conference (PEMD)*, Apr. 2006, pp. 197–201.

[149] X. Lu, J. M. Guerrero, K. Sun, and J. C. Vasquez, “An improved droop control method for DC microgrids based on low bandwidth communication with DC bus voltage restoration and enhanced current sharing accuracy,” *IEEE Trans. Power Electron*., vol. 29, no. 4, pp. 1800–1812, Apr. 2014.

[150] F. Gao, Y. Gu, S. Bozhko, G. Asher, and P. Wheeler, “Analysis of droop control methods in DC microgrids,” in *Proc. 16th IEEE European Conference on Power Electronics and Applications(EPE-ECCE’ Europe)*, Lappeenranta, Finland, Aug. 2014, pp. 1–9.

[151] K. Rouzbehi, A. Miranian, A. Luna, and P. Rodriguez, “DC voltage control and power sharing in Multiterminal DC grids based on optimal DC power flow and voltage-droop strategy,” *IEEE J. Emerg. Sel. Topics Power Electron*., vol. 2, no. 4, pp. 1171–1180, Dec. 2014.

[152] W. Wang, M. Barnes, O. Marjanovic, and O. Cwikowski, “Impact of DC breaker systems on Multiterminal VSC-HVDC stability,” *IEEE Trans. Power Del.*, vol. 31, no. 2, pp. 769–779, Apr. 2016.

[153] X. Lu, J. M. Guerrero, K. Sun, J.C. Vasquez, R. Teodorescu, and L. Huang, “Hierarchical control of parallel AC-DC converter interfaces for hybrid microgrids,” *IEEE Trans. Smart Grid*, vol. 5, no. 2, pp. 683–692, Mar. 2014.

[154] J. Beerten and R. Belmans, “Analysis of power sharing and voltage deviations in droop-controlled DC grids,” *IEEE Trans. Power Syst*., vol. 28, no. 4, pp. 4588–4597, Nov. 2013.

[155] C. Wan, M. Huang, C. K. Tse, and X. Ruan, “Effects of interaction of power converters coupled via power grid: a design-oriented study,” *IEEE Trans. Power Electron*., vol. 30, no. 7, pp. 3589–3600, Jul. 2015.

[156] F. Gao, X. Zheng, S. Bozhko, C. Hill, and G. Asher, “Modal analysis of a PMSG-based DC electrical power system in the more electric aircraft using eigenvalues sensitivity,” *IEEE Trans. Transp. Electrif*., vol. 1, no. 1, pp. 65–76, Jun. 2015.

[157] F. Gao, S. Bozhko, A. Costabeber, C. Patel, P. Wheeler, C. I. Hill, and G. Asher, "Comparative stability analysis of droop control approaches in voltage source converters-based DC microgrids," *IEEE Trans. Power Electron*., vol. 99, no. 99, pp. 1-1, 2016.

[158] J. Sun, "Impedance-based stability criterion for grid-connected inverters," *IEEE Trans. Power Electron*., vol. 26, no. 11, pp. 3075–3078, Nov. 2011.

[159] F. Liu, J. Liu, H. Zhang, and D. Xue, "Stability issues of Z+Z type cascade system in hybrid energy storage system (HESS)," *IEEE Trans. Power Electron*., vol. 29, no. 11, pp. 5846–5859, Nov. 2014.

[160] X. Zhang, X. Ruan, and C. K. Tse, "Impedance-based local stability criterion for DC distributed power systems," *IEEE Trans. Circuits Syst. I, Reg. Papers*, vol. 62, no. 3, pp. 916–925, Mar. 2015.

[161] X. Wang, F. Blaabjerg, and W. Wu, "Modeling and analysis of harmonic stability in an AC power-electronics-based power system," *IEEE Trans. Power Electron*., vol. 29, no. 12, pp. 6421–6432, Dec. 2014.

[162] L. Xu, L. Fan, and Z. Miao, "DC impedance-model-based resonance analysis of a VSC-HVDC system," *IEEE Trans. Power Del*., vol. 3, no. 3, pp. 1221–1230, Jun. 2015.

[163] Y. Gu, W. Li, and X. He, "Frequency-coordinating virtual impedance for autonomous power management of DC microgrid," *IEEE Trans. Power Electron*., vol. 30, no. 4, pp. 2328–2337, Apr. 2015.

[164] T. Dragicevic, J. Guerrero, J. Vasquez, and D. Skrlec, "Supervisory control of an adaptive-droop regulated dc microgrid with battery management capability," *IEEE Trans. Power Electron.*, vol. 29, no. 2, pp. 695–706, Feb. 2014.

[165] S. Anand and B. Fernandes, "Reduced-order model and stability analysis of low-voltage dc microgrid," *IEEE Trans. Ind. Electron.*, vol. 60, no. 11, pp. 5040–5049, Nov. 2013.

[166] W. Wang, A. Beddard, M. Barnes, and O. Marjanovic, "Analysis of active power control for VSC–HVDC," *IEEE Trans. Power Del.*, vol. 29, no. 4, pp.1978–1988, Aug. 2014.

[167] P. Karlsson and J. Svensson, "DC bus voltage control for a distributed power system," *IEEE Trans. Power Electron.*, vol. 18, no. 6, pp. 1405–1412, Nov. 2003.

[168] D. Kim, D. Son, and B. Choi, "Input impedance analysis of PWM DC-to-DC converters," in *Proc. 21st Annu. IEEE Appl. Power Electron. Conf. Expo. (APEC)*, Mar. 2006, pp. 19–23.

[169] S. Skogestad and I. Postlethwaite, *Multivariable Feedback Control: Analysis and Design*, 2nd ed. Hoboken, NJ, USA: Wiley, 2005.

[170] C. Gavriluta, I. Candela, A. Luna, A. Gomez-Exposito, and P. Rodriguez, "Hierarchical control of HV-MTDC systems with droop-based primary and OPF-based secondary," *IEEE Trans. Smart Grid*, vol. 6, no. 3, pp.1502–1510, May 2015.

[171] J. Cao, W. Du, H. F. Wang, and S. Q. Bu, "Minimization of transmission loss in meshed AC/DC grids with VSC-MTDC networks," *IEEE Trans. Power Electron*., vol. 28, no. 3, pp. 3047–3055, Aug. 2013.

[172] A. de la Villa Jaen, E. Acha, and A. G. Exposito, "Voltage source converter modeling for power system state estimation: STATCOM and VSC-HVDC," *IEEE Trans. Power Syst*., vol. 23, no. 4, pp. 1552–1559, Nov. 2008.

[173] J. M. Guerrero, M. Chandorkar, T.-L. Lee, and P. C. Loh, "Advanced control architectures for intelligent microgrids—Part I: Decentralized and hierarchical control," *IEEE Trans. Ind. Electron.*, vol. 60, no. 4, pp. 1254–1262, Apr. 2013.

[174] N. R. Chaudhuri and B. Chaudhuri, "Adaptive droop control for effective power sharing in multi-terminal dc (MTDC) grids," *IEEE Trans. Power Syst.*, vol. 28, no. 1, pp. 21–29, Feb. 2013.

[175] P. Wang, X. Lu, X. Yang, W. Wang, and D. Xu, "An improved distributed secondary control method for DC microgrids with enhanced dynamic current sharing performance," *IEEE Trans. Power Electron.*, vol. 31, no. 9, pp. 6658–6673, Sep. 2016.

[176] T. Dragicevic, J. C. Vasquez, J. M. Guerrero, and D. Skrlec, "Advanced LVDC electrical power architectures and microgrids: A step toward a new generation of power distribution networks," *IEEE Electrifi. Mag*. vol. 2, no. 1, pp. 54–65, Mar. 2014.

[177] IEEE Std 421.5-2005 (Revision of IEEE Std 421.5-1992), "IEEE recommended practice for excitation system models for power system stability studies," pp. 1–93, Apr. 2006.

[178] X. Lu, J. M. Guerrero, K. Sun, and J. C. Vasquez, "An improved droop control method for dc microgrids based on low bandwidth communication with dc bus voltage restoration and enhanced current sharing accuracy," *IEEE Trans. Power Electron.*, vol. 29, no. 4, pp. 1800–1812, Apr. 2014.

[179] S. Anand, B. G. Fernandes, and J. M. Guerrero, "Distributed control to ensure proportional load sharing and improve voltage regulation in low voltage DC microgrids," *IEEE Trans. Power Electron.*, vol. 28, no. 4, pp. 1900–1913, Apr. 2013.

[180] F. Gao, S. Bozhko, G. Asher, and P. Wheeler, "An improved voltage compensation method for droop-controlled system in DC microgrid," in *Proc. Industrial Electronics Society, 40th Annual Conference of the IEEE (IECON 2014)*, Dallas, USA, Nov. 2014, pp.1240–1246.

[181] I. U. Nutkani, P. Wang, P. C. Loh, and F. Blaabjerg, “Cost-based droop scheme for DC microgrid,” in *Proc. Energy Conversion Congress and Exposition (ECCE)*, IEEE, Pittsburgh, USA, Sep. 2014, pp.765–769.

[182] I. U. Nutkani, P. C. Loh, P. Wang, and F. Blaabjerg, “Autonomous droop scheme with reduced generation cost,” *IEEE Trans. Ind. Electron.*, vol. 61, no. 12, pp. 6803–6811, Dec. 2014.

[183] X. Zhao and K. Li, “Droop setting design for multi-terminal HVDC grids considering voltage deviation impacts,” *Elect. Power Syst. Res.*, vol. 123, pp. 67–75, Feb. 2015.

[184] F. Gao, S. Bozhko, G. Asher, P. Wheeler, and C. Patel, “An improved voltage compensation approach in a droop-controlled DC power system for the more electric aircraft,” *IEEE Trans. Power Electron.*, vol. 31, no. 10, pp. 7369–7383, Oct. 2016.

[185] SEMIKUBE IGBT Converter, http://www.semikron.com/products/product-lines/semikube.html.

[186] DYNEX, IGBT Chopper Module, http://www.farnell.com/datasheets/50923.pdf.

[187] LEM, *Voltage Transducer LV 25-P*, LV 25-P datasheet, http:// www.lem.com.

[188] LEM, *Current Transducer LA 25-P*, LA 25-P datasheet, http:// www.lem.com.

[189] R.N. Beres, X. Wang, F. Blaabjerg, M. Liserre, and C.L. Bak, “Optimal design of high-order passive-damped filters for grid-connected applications,” *IEEE Trans. Power Electron.*, vol. 31, no. 3, pp. 2083–2098, Mar. 2016.

[190] W. Wu, Y. He, T. Tang, and F. Blaabjerg, “A new design method for the passive damped LCL and LLCL filter-based single-phase grid-tied inverter,” *IEEE Trans. Ind. Electron.*, vol. 60, no. 10, pp. 4339–4350, Oct. 2013.

[191] P. Magne, B. Nahid-Mobarakeh, and S. Pierfederici, “General active global stabilization of multiloads dc-power networks,” *IEEE Trans. Power Electron.*, vol. 27, no. 4, pp. 1788–1798, Apr. 2012.

[192] X. Liu, A. Forsyth, and A. Cross, “Negative input-resistance compensator for a constant power load,” *IEEE Trans. Ind. Electron.*, vol. 54, no. 6, pp. 3188–3196, Dec. 2007.

[193] X. Liu and A.J. Forsyth, “Input filter state feed-forward stabilising controller for constant power load systems,” *IET Electr. Power Appl.*, vol. 2, no. 5, pp. 306–315, 2008.

[194] P. Magne, B. Nahid-Mobarakeh, and S. Pierfederici, “Active stabilization of DC microgrids without remote sensors for more electric aircraft,” *IEEE Trans. Ind. Appl.*, vol. 27, no. 4, pp. 1788–1798, Apr. 2012.

[195] A. B. Awan, S. Pierfederici, B. Nahid-Mobarakeh, and F. Meibody-Tabar, “Active stabilization of a poorly damped input filter supplying a constant power load,” in *Proc. ECCE*, Sep. 2009, pp. 2991–2997.

[196] A. M. Rahimi, G. A. Williamson, and A. Emadi, “Loop-cancellation technique: A novel nonlinear feedback to overcome the destabilizing effect of constant-power loads,” *IEEE Trans. Veh. Technol*., vol. 59, no. 2, pp. 650–661, Feb. 2010.

[197] A. Rahimi and A. Emadi, “Active damping in dc/dc power electronics converters: a novel method to overcome the problems of constant power loads,” *IEEE Trans. Ind. Electron*., vol. 56, no. 5, pp. 1428–1439, May 2009.

[198] J. Wang and D. Howe, “A power shaping stabilizing control strategy for dc power systems with constant power loads,” *IEEE Trans. Power Electron*., vol. 23, no. 6, pp. 2982–2989, Nov. 2008.